Relationships Between the Photochemical and Photophysical Properties of Dissolved Organic Matter

by

Garrett McKay
BA Chemistry, California State University Long Beach, 2011
MS Chemistry, California State University Long Beach, 2013

A thesis submitted to the
Faculty of the Graduate School of the
University of Colorado in partial fulfillment
of the requirements for the degree of
Doctor of Philosophy
Department of Civil, Environmental, and Architectural Engineering
2017

This thesis entitled:
Relationships Between the Photochemical and Photophysical Properties of Dissolved Organic Matter

written by Garrett McKay
has been approved for the
Department of Civil, Environmental, and Architectural Engineering

_____
Fernando Rosario-Ortiz (chair)

_____
Karl G. Linden

_____
Joseph N. Ryan

_____
Charles M. Sharpless

_____
Silvio Canonica

Date: _____

A final copy of this thesis has been examined by the signatories, and we
find that both the content and the form meet acceptable presentation standards
of scholarly work in the abovementioned discipline

ABSTRACT

McKay, Garrett (PhD, Environmental Engineering)

Relationships between the photochemical and photophysical properties of dissolved organic matter

Thesis directed by Associate Professor Fernando L. Rosario-Ortiz

Naturally occurring dissolved organic matter (DOM) is a major constituent in aquatic water bodies, including lakes, rivers, estuaries and bays, and the open ocean. DOM is often the primary absorber of sunlight in these systems. This absorption of light leads to excited electronic states of DOM molecules that subsequently undergo photophysical and photochemical processes to form transient reactive intermediates (RI), such as the hydroxyl radical ($^{\bullet}$OH), singlet oxygen, and triplet state DOM. Because of DOM's complexity, it is difficult to obtain a precise description of the photophysical and photochemical processes that occur in DOM. The goal of this thesis is to better understand the origin of both DOM's optical properties and the mechanisms of $^{\bullet}$OH formation from DOM photolysis.

After an introduction of the topic of DOM optical properties and photochemistry, the relationship between DOM molecular weight and photophysics/photochemistry is evaluated. Although this initial study seemed to provide evidence for the charge-transfer (CT) model for DOM photophysics, later studies examining the effect of temperature and solvent polarity on DOM absorbance and fluorescence indicated that CT interactions are likely not playing a dominant role in DOM. Specifically, absorption and emission position were insensitive to changing temperature and solvent polarity, contrary to hypotheses based donor-acceptor complexes of organic molecules.

The photochemical formation of $^\bullet$OH from DOM was also investigated. The quantum yield for $^\bullet$OH formation from DOM was shown to be temperature-dependent and described by the Arrhenius equation. The activation energies of different isolates for $^\bullet$OH formation correlated to DOM physicochemical properties, such as molecular weight. In addition, the temperature-independence for photohydroxylation of a $^\bullet$OH probe compound by p-benzoquinone, a model photosensitizer in DOM, was consistent with this species forming a quinone-water exciplex and not free $^\bullet$OH. Finally, a long-term monitoring study of the Florida Everglades was conducted to assess the ability to model $^\bullet$OH formation using DOM physicochemical parameters. $^\bullet$OH quantum yields were poorly modeled by all factors investigated, indicating that $^\bullet$OH precursors comprise a small and variable portion of the overall DOM pool.

DEDICATION

This thesis is dedicated to Lauren McKay, for her continued love and support and making my graduate education possible.

ACKNOWLEDGMENTS

I am grateful for all of those who have helped me achieve my goal of earning a PhD. My family, for their love and support. My grandparents, for giving me the means to pursue a college education. And especially my wife, Lauren, who has listened to me practice more talks on the topic of dissolved organic matter then anyone should.

I am also grateful to my advisors who inspired me to pursue research. Steve Mezyk at CSU Long Beach, my undergraduate and masters advisor, introduced me to research and I will always be grateful for that opportunity. I would also like to acknowledge my committee members: Karl Linden, Joseph Ryan, Charles Sharpless, and Silvio Canonica. Their support and constructive comments on my research significantly improved this thesis. Finally, I would like to acknowledge my advisor, Fernando Rosario-Ortiz. I have been fortunate enough to know Fernando since I was an REU student in his lab, some 7 years ago. Over this time, I have learned an incredible amount about science, the research process, and striking a good work-life balance from Fernando. I am very grateful for his support of me over the years, both profesionally and personally.

TABLE OF CONTENTS

LIST OF TABLES

LIST OF FIGURES

Figure 4.1. Scheme depicting the possible photophysical processes of CDOM, including local excited (LE) states and charge-transfer (CT) interactions and the expected effects of temperature, solvent polarity, and viscosity on CDOM absorption (a-c) and fluorescence (d-f). Scenarios are depicted for independent D and A molecules (a, d), covalently tethered D and A (b, e) and conjugated D and A moieties (c, f). Only some of the critical dependencies are indicated. For example, the wavelength of fluorescence ($h\nu_{F,CT}$) is dependent on solvent viscosity due to dipole reorientation effects.(Lakowicz, 1999) Note also that temperature also perturbs solvent viscosity

1. Introduction

1.1. Motivation

The chemistry involving naturally occuring dissolved organic matter (DOM) influences a great number of environmental and engineered systems (Thurman, 1985). As the largest pool of carbon in aquatic ecosystems, DOM is present in all lakes, rivers, and streams, although its quality and quantity varies significantly amongst these systems. DOM is best described as a mixture of chemical structures containing primarily C, O, and N (typically < 5% N, S combined) and contains aromatic, carbonyl, quinoidal, hydroxy, and phenolic functional groups in a multitude of different structural arrangements.

Amongst its many properties, DOM binds both protons and metal ions (Driver and Perdue, 2015; Perdue and Ritchie, 2003; Reuter and Perdue, 1977; Ritchie and Perdue, 2003), participates in environmental redox reactions (Aeschbacher et al., 2010; Fimmen et al., 2007), and absorbs and emits light in the UV and visible regions of the spectrum (Ghassemi and Christman, 1968). Carboxylic acids and phenols are the main acidic functional groups in DOM (Ritchie and Perdue, 2003), which experimentally has pK_a values ~ 4 and 10 (compared to ~ 4.5 9.9 for carboxylic acids and phenols, respectively). Phenols and similar electron-rich aromatic structures act as electron-donors (Aeschbacher et al., 2012a), whereas quinone moieties are thought to be the primary electron accepting moieties in DOM (Aeschbacher et al., 2010). Choromophoric units within DOM include aromatic ketones, aldehydes, and esters; quinones; phenols, poly phenols, and alkoxy phenols; hydroxy benzoic acids and hydroxybenzoates; coumarins; flavones; among many other possibilities (Aiken, 2014). Many of these chromophores also comprise fluorescent DOM, with notable exceptions being aromatic

1

ketones/aldehydes and quinones, which are rapidly converted to their excited triplet state following light absorption (Turro et al., 2012).

This thesis presents research focused on the photophysical and photochemical prroperties of DOM and the relationships between these properties. Absorption of light by DOM is a prerequisite to formation of photochemically produced reactive intermediates (RI) (Leifer, 1988), transient photooxidants such as the hydroxyl radical, singlet oxygen, and triplet excited states. These RI play an important role in the chemistry of environmental systems (Figure 1.1), including pollutant transofrmation (Zepp and Cline, 1977), the global carbon cycle (Cory et al., 2014; Ward and Cory, 2016), and trace metal cycling (Southworth and Voelker, 2003; Vermilyea and Voelker, 2009; Zepp et al., 1992).
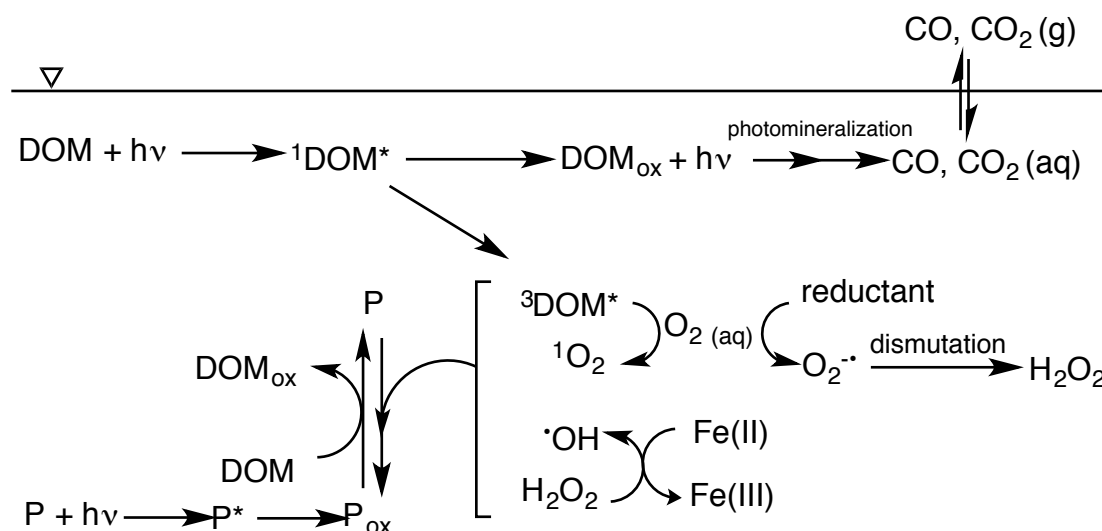
Figure 1.1. Scheme depicting some of the relvant photochemical reactions occuring in aquatic environmental systems. P represents a generalized organic pollutant.

The optical and photochemical properties of DOM have been a topic of study starting in the 1960s and 1970s. By the end of the 1980s, many pioneering studies by Kotzias, Zika, Cooper, Zepp, Hoigné, and many others, resulted in much of the mechanistic information shown in Figure 1.1 (Cooper et al., 1988; Haag et al., 1984; Haag and Höigne, 1985; Kotzias et al., 1987a;

1987b; Zepp et al., 1981a; 1981b; Zepp and Schlotzhauer, 1981). Of course, these initial studies' data also resulted in many future research questions, many of which involve linking the chemical composition of DOM with its observed photophysical and photochemical properties and, in addition, how these properties are related. A study by Ziechman in the 1970s (Ziechmann, 1972) suggested that a large portion of DOM optical properties (absorbance and fluorescence) arose from donor-acceptor (DA) complexes in DOM, leading to absorption into and emission from charge-transfer (CT) excited states ($[D^+A^-]^*$). Studies by Langford in the 1980s and 1990s further examined this idea, with an additional emphasis on the role of exciplexes (Ariese et al., 2004; Power and Langford, 1988; Z.-D. Wang et al., 1990). In 2004, del Vecchio and Blough put forward a more comprehensive CT model for DOM optical properties, in which DA complexes played a prevalent role (Del Vecchio and Blough, 2004). Subsequent work by del Vecchio and Blough, Sharpless, and others has resulted in a general acceptance of the CT model in the research community (Boyle et al., 2009; Dalrymple et al., 2010; Ma et al., 2010; Sharpless, 2012; Sharpless and Blough, 2014). The CT model has also been used as a broad framework to explain the photochemistry of DOM (Sharpless and Blough, 2014).

Although much is known about DOM photophysics and photochemistry, there are still many unanswered questions. Although the CT model has been generally embraced, it has never been tested from a fundamental chemistry perspective, leading some to doubt its role in DOM photophysics. In addition, many details surrounding DOM photochemical pathways are unclear. In particular, the photochemical formation of the hydroxyl radical from DOM is poorly understood both in terms of reaction mechanisms for its formation as well as the physicochemical properties of DOM that describe its propensity to be produced upon light absorption.

3

1.2. Research Objectives

The overall goal of this thesis is to understand the molecular basis for DOM photophysical and photochemical properties. The specific research objectives of this thesis are twofold. First, I wanted to test the validity of the CT model for DOM photophysics under conditions commonly used in physical chemistry studies. Second, I sought to better understand the formation of the hydroxyl radical from DOM photolysis, focusing specifically on apportioning known formation mechanisms. As a follow up to this second objective, I sought to determine a set of physicochemical properties of DOM that could be used hydroxyl radical formation in the environment. Although these objectives may seem esoteric, there is a real need for understanding the molecular basis of DOM photophysics and photochemistry. For example, online sensing of absorbance and fluorescence is used in engineered and natural systems to track DOM quality and quantity over a wide range of conditions. The analysis and assumptions used in relating this data to DOM behavior in the environment requires an overarching model (e.g. CT model), which could potentially result in erroneous conclusions if an incorrect model is used.

As often happens, the research direction of this thesis shifted. Specifically, my initial plan of study concerned $^{\bullet}$OH formation from DOM photolysis. The research project that ultimately was developed into Chapter 3 represents a change in focus from DOM photochemistry to DOM photophysics, which is the focus of Chapters 4 and 5. Although this shift was welcomed and allowed me to pursue more knowledge of the CT model, it resulted in a number of questions proposed in my comprehensive examination being left unanswered. This is dissapointing, but I am confident that these questions will be addressed in the near future.

1.3. Thesis Organization

This thesis is organized based on the above research objectives. Each chapter represents a stand alone publication that is either published (Chapters 2, 3, 6, and 7) or in review/under revision/to be submitted (Chapters 4, and 5). The Appendices represent the Supporting Information associated with each chapter beginning with Chapter 3 (e.g. Appendix A is the Supporting Information for Chapter 3). The Chapter/Appendix combinations have been largely unaltered from the format in which they were originally submitted, revised, or published, and consequently there is some overlap of content between these sections. Chapters 2 through 5 focus on the origin of the photophysical properties of DOM. Chapters 6 through 7 focus on formation of the hydroxyl radical from DOM photolysis. There is some overlap of these concepts in Chapter 3. The final chapter provides overall conclusions and the future outlook for research in this field. A summary of the chapters is given below.

Chapter 2 is a review article focusing on DOM optical properties and photochemistry. Particular attention was given to the role of DOM molecular weight as this parameter is has been consistently shown to result in systematic changes to these properties.

Chapter 3 explores the role of DOM molecular weight in more detail. Specifically, a key supporting point of the CT model for DOM is related to observation that higher molecular weight DOM tends to exhibt differences from lower molecular weight DOM (e.g. increased visible absorbance). The results of this publication provide strong evidence for this idea in the case of an exemplar DOM isolate, Suwannee River Fulvic Acid.

Chapter 4 tests the CT model for DOM using methods commonly employed in the physical organic chemistry field (e.g. solvatochromism). Contrary to Chapter 3 and the current CT model

for DOM, the results in this Chapter were not consistent with a significant role for DA complexes in DOM photophysics.

Chapter 5 examines the temperature-dependence of the fluorescence quantum yield for DOM. The data are analyzed using a simple photophysical model and the Arrhenius equation and the results show evidence that higher molecular weight DOM has faster rates of radiationless decay than lower molecular weight DOM.

Chapter 6 presents a study of the temperature-dependence of the quantum yield for hydroxyl radical formation. Activation parameters for the formation of hydroxyl radical are derived from the Arrhenius equation and related to DOM physicochemical properties. Various perturbations to the system are utilized in an attempt to assess the importance of possible hydroxyl radical formation mechanisms.

Chapter 7 presents a collaborative study with Professor Rudolf Jaffé at Florida International University on the optical and photochemical properties of whole water DOM samples from the Florida Everglades. This study sought to relate DOM photochemical properties for samples collected from a long term monitoring study. With regards to hydroxyl radical, the results indicate that unlike other reactive intermediates, hydroxyl radical formation was poorly modeled by all physicochemical properties examined, suggesting that hydroxyl radical precursors represent a small fraction of the overall DOM pool.

2. Photochemical Reactivity of Organic Matter and its Size Fractions

2.1. Abstract

The photochemical reactions that occur in natural water bodies play an important role in many biogeochemical processes, such as global carbon cycling and the fate of organic contaminants. Photochemically active compounds found in these systems include nitrate, nitrite, and dissolved organic matter (DOM). DOM is a major constituent in the water matrix and thus its photochemical reactions are central to understanding the photochemistry of natural waters. DOM is colored (typically yellow to brown) and absorbs light in the ultraviolet and visible range. Formation of excited states following DOM absorption leads to (sensitized) production of reactive intermediates, such as singlet oxygen, organic peroxyl radicals, hydrogen peroxide, hydroxyl radical, and excited triplet states. As DOM is a complex, heterogeneous material, a complete mechanistic understanding of these species' production has been difficult to obtain. The aim of this chapter is to develop a framework for understanding the mechanism of sensitized reactive intermediate production from DOM, with special attention to the role of the molecular size of DOM.

2.2. DOM in the environment

Dissolved organic matter (DOM), defined as the pool of carbonaceous compounds found ubiquitously in aqueous environments, represents the largest pool of reduced carbon in the biosphere (Hedges et al., 1997). DOM has been characterized as a complex mixture of organic compounds of varying molecular weight and composition, ranging from simple molecules

composed of carbon, hydrogen and oxygen to more complex structures where heteroatoms such as nitrogen and sulfur are incorporated (Leenheer and Croue, 2003).

Based on its source and subsequent physicochemical properties, DOM observed in surface waters can be classified into three main pools. These include terrestrial or allochthonous and aquatic or autochthonous DOM (McKnight et al., 2001; Yamashita et al., 2008). Both of these sources are considered to be end-members of geochemical importance and are frequently used to define boundaries with respect to the observed physicochemical properties of DOM in aquatic systems. A third component observed in surface waters is the material derived from wastewater processes, referred to as effluent organic matter (EfOM). EfOM is composed of oxidized, recalcitrant DOM from drinking water sources as well as soluble microbial products, a byproduct of biological treatment of wastewater (Shon et al., 2006). The chemical composition of DOM includes lignin-type compounds, sugars, peptides, and polysaccharides; with phenolic, quinone, ketone, aldehyde, aromatic, carboxylic acid, amide, ester, and ether functional groups.

2.2.1 Molecular composition of DOM

The structural characterization of DOM has fascinated researchers since the published molecular formula of a humic substance ($C_{40}H_{30}O_{15}$) in 1840 (Mulder, 1840). Historically, DOM has been quantified as dissolved or total organic carbon (DOC or TOC) (Krogh and Keys, 1934; Menzel and Vaccaro, 1964). DOM has been represented as a combination of both humic and non-humic material (Hedges et al., 1997; Leenheer and Croue, 2003), with the humic material, commonly known as humic substances (HS) accounting for as much as 80% of the total DOM in fresh waters (Leenheer and Croue, 2003; Steinberg, 2008). HS are further classified into fulvic acid (FA) and humic acid (HA), based on their solubility at different pHs and chemical

composition. The non-humic component of DOM includes proteins, carbohydrates, and other organic compounds including low molecular weight acids.

The number of studies focusing on EfOM has lagged behind the progress made on DOM. However, analysis of the properties of EfOM suggest that it behaves differently from DOM. Briefly, the composition of EfOM could be sub-divided into three main groups: (1) background DOM originating from water supplies: (2) soluble microbial by-products (SMPs) produced during biological wastewater treatment: and (3) natural and synthetic trace chemicals (Shon et al., 2006). In terms of mass contribution, SMPs will dominate over the background DOM. The trace chemicals will contribute a minor part to the overall mass. SMPs are produced during biological processes in wastewater treatment plants and are divided into two categories: biomass-associated products (BAP) and utilization-associated products (UAP) (Namkung and Rittmann, 1986). UAP are a result of microbial substrate intake, which is proportional to the amount of substrate available in the system, and BAP is a result of microbial endogenous decay, which correlates to biomass concentration in the biological reactor (Barker and Stuckey, 1999; Krogh and Keys, 1934; Menzel and Vaccaro, 1964; Shon et al., 2006). Operational parameters such as sludge retention time, organic loading rate, hydraulic retention time, and process temperature can alter the properties of SMPs, therefore impacting the overall chemistry of EfOM (Barker and Stuckey, 1999; Grebel et al., 2010; Keen et al., 2014; Rosario-Ortiz et al., 2008).

In the past decade, DOM has been characterized using a wide array of analytical techniques, such as three-dimensional fluorescence excitation-emission spectroscopy (Birks, 1970), high and ultra-high resolution mass spectrometry(Stenson et al., 2003; Stubbins et al., 2012), and NMR (carbon, nitrogen and phosphorous) (Maie et al., 2006). These techniques have allowed researchers to obtain chemical formulas and additional information with regards to chemical

functionalities. For example, Stenson et al. used Fourier transform ion cyclotron resonance mass spectrometry (FTICR-MS) to determine the molecular formulas for 4626 individual components of Suwannee River Fulvic Acid (SRFA) and compared these data to degraded lignin (Stenson et al., 2003). This technique has also been applied to EfOM and shown that it has more diverse functional groups than DOM isolates from natural samples (Birks, 1970). Furthermore, FTICR-MS has been used to characterize/compare EfOM derived from different activated sludge processes based on the measured mass spectra (Tseng et al., 2013).

The apparent molecular weight (AMW) of DOM has consistently been of interest to scientists and engineers examining the impact of DOM on natural and engineered processes (Dong et al., 2010; Tang et al., 2010). Multiple techniques have been used to measure this property, including vapor pressure osmometry (Cronan and Aiken, 1985; Hayes et al., 1989), size exclusion chromatography (SEC) (Chin et al., 1994), small angle X-ray scattering (Hayes et al., 1989) and ultracentrifugation (Visser, 1985). Early on, researchers had a fairly good understanding of the molecular weight range (700-10,000 Da published in 1968)(Ghassemi and Christman, 1968) of DOM and its metal-complexing abilities (Reuter and Perdue, 1977; Shapiro, 1964). Based on all of the above techniques, the average molecular weight of DOM molecules is likely around 1 kDa (Perdue and Ritchie, 2003).

In addition, size fractionation of bulk DOM into its AMW fractions has been utilized as a tool to evaluate the physiochemical properties of DOM. Size fractionation has been performed using UF membranes(Dong et al., 2010; Mostafa et al., 2014a; Mostafa and Rosario-Ortiz, 2013), as well as by dialysis and SEC (Richard et al., 2004). These techniques have provided greater insight into the physicochemical properties of DOM, which in turn has allowed for more advanced study of its photophysical and photochemical properties.

2.3. Photophysics of DOM

The first law of photochemistry states that the rate of direct photoreaction of a chemical is a function of the rate of light absorption. Therefore, in order to describe the photochemical properties of DOM and its molecular weight fractions, we start by describing the basic photophysical processes that are in effect when DOM interacts with light. The potential photophysical processes upon DOM light absorption are shown in Figure 2.1. The initially formed singlet excited state, $^1DOM^*$, can undergo various processes, including internal conversion (IC), fluorescence (F), and intersystem crossing (ISC), which leads to a triplet excited state, $^3DOM^*$. Compared to individual organic molecules, DOM exhibits some complex optical properties that are difficult to describe. The difficulty is compounded by DOM's heterogeneity and inexact knowledge of its structure. In the following sections, a framework will be developed for understanding the photophysics of DOM light absorption and luminescence so as to understand its photochemical pathways.

As light absorption is the initial step in the population of excited states that lead to reactive intermediates, it is useful to develop a framework for explaining this initial photophysical step. First, the types of chromophores in DOM and their electronic transitions as individual moieties will be discussed. We will subsequently review the relationships between absorption spectra and DOM physicochemical properties.

2.4. Light Absorption

Absorbance spectra of simple inorganic and organic compounds derive from energy differences between the lowest vibrational state of the electronic ground state and different vibrational states of higher electronic states. In aqueous solutions, vibrational structure is lost and mainly broad absorption bands are observed. For DOM, however, absorbance decreases

exponentially (i.e. no prominent absorption bands) from ~ 200-600 nm. Importantly, DOM spectra share these characteristics, regardless of source and physicochemical properties.
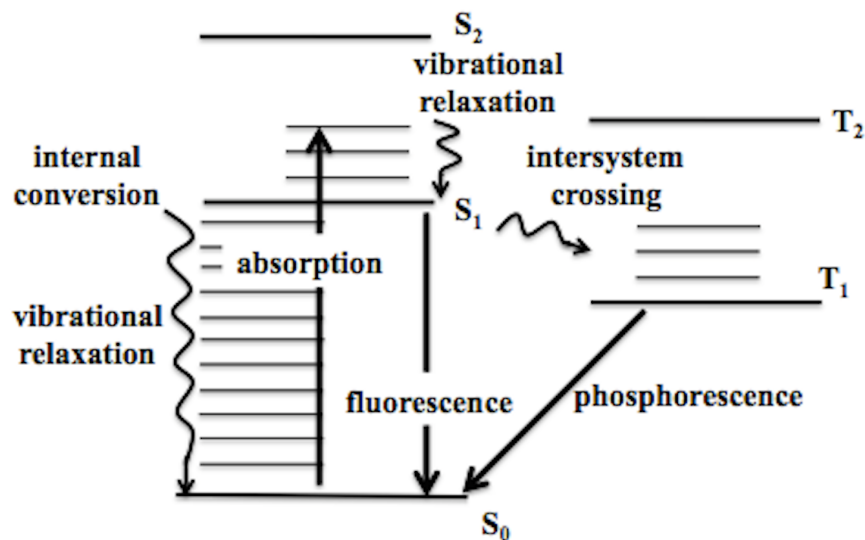
Figure 2.1. Simplified Jablonski diagram representing the photophysical processes possible for DOM.

The most likely chromophores in DOM include various carbonyl-containing groups and aromatic rings. Electronic transitions in these groups involve excitation of electrons in non-bonding or π bonding orbitals to a π^* anti-bonding orbital (either $n \rightarrow \pi^*$ or $\pi \rightarrow \pi^*$). With respect to carbonyl compounds, the $n \rightarrow \pi^*$ transition is lower in energy than the $\pi \rightarrow \pi^*$ transition, but is also forbidden and therefore less intense. For example, Fig. 2 shows the maximum molar absorption coefficient (ε_{max}) for the $n \rightarrow \sigma^*$ and $\pi \rightarrow \pi^*$ transitions for acetone and 3-buten-2-one. If one considers the UV-visible spectrum of DOM to be due to individual chromophores, extremely conjugated carbonyl and olefin compounds would need to be present in order to achieve absorption into the near UV and visible wavelength range (e.g. the λ_{max} of β-Carotene which has 11 conjugated carbon-carbon double bonds is 452 nm).

6

$$\pi \longrightarrow \pi^* \qquad \varepsilon_{189nm} = 900 \qquad \varepsilon_{213nm} = 7100$$

$$n \longrightarrow \sigma^* \qquad \varepsilon_{280nm} = 12 \qquad \varepsilon_{320nm} = 27$$
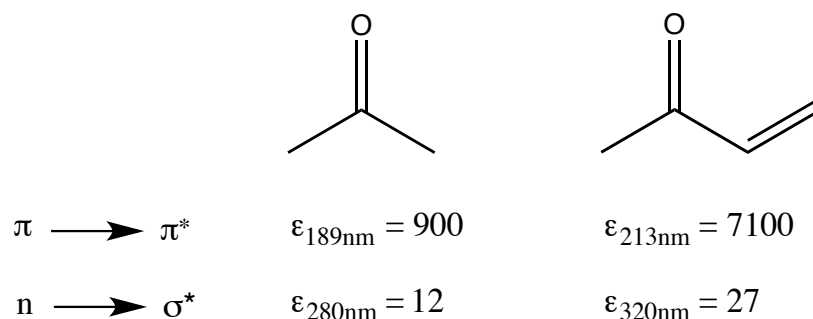
Figure 2.2.Maximum absorption coefficients (units of $M^{-1}cm^{-1}$) for acetone and 3-buten-2-one.
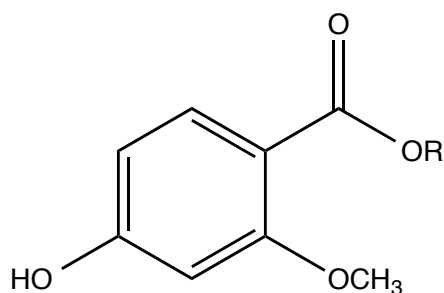
λ_{max} = 230 nm (parent chromophore) + 25 nm (*p*-OH) + 7 nm (*m*-OCH$_3$) = 262 nm

Figure 2.3.Calculation of maximum absorption wavelength for a typical DOM moiety based on empirical rules for benzoyl derivatives.

Aromatic structures represent the other potential chromophore ($\pi \rightarrow \pi^*$ transition) in DOM. Sharpless and Blough have suggested that all DOM absorption and photochemistry results from these structures (Sharpless and Blough, 2014), though this does not exclude carbonyl compounds conjugated to aromatic rings (e.g. aromatic ketones) (Canonica, 2007; Canonica et al., 2006; 2000). It has been suggested that lignin is a primary DOM-precursor in both marine DOM (Boyle et al., 2009) as well as terrestrial DOM (SRFA) (Stenson et al., 2003). Lignin contains linked aromatic rings substituted with hydroxyl, alkoxy, and carboxyl groups that are electronically isolated by *o*-ether linkages. Empirical rules have been developed for benzoyl derivatives (present in lignin), correlating structure with λ_{max}. For example, consider Fig. 3 in which a benzoyl ring is substituted with a *p*-hydroxy and *m*-alkoxy group. Even with the

presence of these electron-donating substituents, the calculated λ_{max} is only 262 nm. This value is in good agreement with the λ_{max} of 282 nm measured in lignin obtained from an un-treated wood powder.[51] Fused aromatic and heteroaromatic rings (e.g. anthracene and quinolone) have absorption bands that extend into the near UV (e.g. log ε of quinolone is ~ 3.1 at 310 nm).

Many parameters have been used to characterize DOM absorption spectra. For example, the spectral slope parameter (S), obtained from exponential fitting of the absorption spectrum, provides a quantitative measure of how rapidly absorption decreases as a function of wavelength. The E2:E3 and E4:E6 ratio (ratio of absorption at 254 nm to that at 365 nm and 465 nm to that at 665 nm, respectively) are other quantitative parameters used to describe that rate of absorbance decrease as a function of wavelength. Previous work by our group (E. Lee et al., 2013; Mostafa and Rosario-Ortiz, 2013) and others (Boyle et al., 2009; Helms et al., 2008) has shown that S increases and E2:E3 increases with decreasing molecular size fractions of DOM. Addition of simple organic acids to DOM decreases its molecular size (shown by SEC), apparently by disrupting hydrophobic interactions, which in turn leads to a decrease in UV-visible absorbance (Piccolo, 2001). In addition, reduction of DOM with borohydride as well as photobleaching results in a preferential loss of visible absorption (Ma et al., 2010).

Our initial discussion of DOM chromophores highlighted that, except for very conjugated structures, absorption occurs mainly below 300 nm. If it is assumed that DOM absorption spectra are due to a superposition of individual chromophores, highly conjugated or heteroaromatic structures need be present in order to explain DOM's absorbance in the near UV and visible region of the spectrum. However, research suggests that these structures are not prevalent in DOM. It has recently been proposed that the complex optical properties of DOM result from intramolecular charge transfer (CT) complexes (Dalrymple et al., 2010; Del Vecchio and

8

Blough, 2004; Sharpless and Blough, 2014). According to this model, intramolecular electron donors (D) and acceptors (A) within DOM can interact to form a donor-acceptor complex (D + A ⇌ DA). CT complexes (D^+A^-) can form directly upon excitation of ground state DA

$$DA + h\nu \rightarrow D^+A^- \qquad\qquad \text{Equation 2.1}$$

or following conversion of a singlet or triplet excited state (Birks, 1970).

$$DA + h\nu \rightarrow {}^1(DA)^* \qquad\qquad \text{Equation 2.2}$$

$${}^1(DA)^* \rightarrow D^+A^- \qquad\qquad \text{Equation 2.3}$$

$${}^1(DA)^* \rightarrow {}^3(DA)^* \qquad\qquad \text{Equation 2.4}$$

$${}^3(DA)^* \rightarrow D^+A^- \qquad\qquad \text{Equation 2.5}$$

Additionally, CT states could be formed by electron transfer from short-range (but non-complexed) excited state donors and acceptors (Turro et al., 2012):

$$D^* + A \rightarrow D^{\bullet+} + A^{\bullet-} \qquad\qquad \text{Equation 2.6}$$

$$D + A^* \rightarrow D^{\bullet+} + A^{\bullet} \qquad\qquad \text{Equation 2.7}$$

For DOM, the CT state is represented by ${}^1DOM^{+\bullet/-\bullet}$, signifying a di-radical charge separation. Presence of short-range, CT interactions between electron-rich donors and electron-poor acceptors are capable of producing lower energy electronic transitions, thus, explaining the near UV and visible absorption properties of DOM. Assuming that lignin is the main DOM precursor, it is likely that hydroxy/methoxy substituted aromatics (e.g. phenols, methoxylated phenols) act as donors while carbonyl-containing structures (e.g. quinone, triplet aromatic ketones/aldehydes) act as acceptors. It is well known that triplet aromatic ketones ($E^0{}_{red} \sim 1.7$ V) oxidize electron-rich phenols (Canonica et al., 2000), and that DOM inhibits oxidation of electron-rich phenols (Canonica and Laubscher, 2008). Furthermore, kraft lignin (containing donor phenolic groups)

and 3,5-di-*tert*-butyl-1,2-benzoquinone (an electron acceptor) interact to produce a CT absorption band (Furman and Lonsky, 1988).

The CT model could also explain correlations between DOM physicochemical and optical properties. Observations of an inverse dependence of S on molecular weight are explained by the greater likelihood of CT interactions present for larger DOM molecules. Conversely, lower molecular weight DOM, having a less aggregated structure, should have less CT interactions. An alternative explanation to the CT model is that higher molecular weight DOM molecules absorb more, possibly due to a greater degree of π electron conjugation.

2.5. Luminescence

Following excitation to a singlet excited state, ^{1}DOM* can undergo many photophysical processes (Figure 2.1). Vibrational relaxation of ^{1}DOM* from an excited vibrational state to the ground vibrational state of an excited electronic state occurs quickly (within picoseconds). The possible fates of ^{1}DOM* are reaction, fluorescence, internal conversion, or intersystem crossing.

The lifetime of ^{1}DOM* (τ_{1DOM*}) is related to the sum of its decay processes:

$$\tau_{1_{DOM*}} = (k_f^0 + k_{ic}^0 + k_{isc}^0)^{-1}$$
Equation 2.8

Because of its short lifetime, it is intuitively unlikely that ^{1}DOM* has significant intermolecular reactions. However, research investigating the effect of halide quenching on DOM excited states and reactive intermediates has shown that photochemical production of hydroxyl radical ($^{\bullet}$OH) is correlated to fluorescence quantum yields (i.e. τ_{1DOM*}), but not triplet state quantum yields (Glover and Rosario-Ortiz, 2013). This does not exclude intramolecular electron transfer reactions, which as previously discussed could lead to CT states within DOM molecules.

Fluorescence quantum yields for DOM range from ~ 0.1-2% depending on the sample and excitation wavelength (Boyle et al., 2009; Del Vecchio and Blough, 2004). Interestingly, DOM

fluorescence spectra do not seem to follow Kasha's rule, which establishes that fluorescence is expected to originate from the lowest vibrational excited state and thus a molecule will exhibit identical emission wavelength and quantum yield regardless of excitation wavelength. For simple organic molecules, Kasha's rule is explained by rapid (picosecond) internal conversion or vibrational relaxation of higher excited states to the lowest electronic excited state.

Model DOM compounds (Canonica, 2007; Canonica et al., 2006; 2000), DOM isolates (Xu et al., 2011), and EfOM (Dong et al., 2015) have been shown, in some cases, to increase the degradation rate of organic pollutants (relative to direct photolysis in pure water), apparently by oxidation by ^{3}DOM*. It is therefore necessary to understand the rate of intersystem crossing as a function of AMW. Although the intersystem crossing quantum yields for DOM are difficult to measure these values are expected to be near 0.3-1, as evidenced by experimental measurements (Bruccoleri et al., 1990) and the expectation that carbonyls, a potentially important chromophore, have intersystem crossing values near unity (Lamola and Hammond, 1965).

Phosphorescence of DOM (^{3}DOM* → ^{1}DOM) is weakly allowed by spin-orbit mixing and time-resolved measurements estimate ^{3}DOM* lifetimes of ~ 1-100 μs (Sharpless and Blough, 2014). Some studies have reported direct observation of ^{3}DOM* (Cottrell et al., 2013; Fischer et al., 1985; Power et al., 1986). Notably, there is some debate over whether the transient species observed in these studies is actually ^{3}DOM* (though no other suggestion for the transient has been advanced) as it was not quenched by alkyl phenols, a well-known ^{3}DOM* quencher. However, the apparent ^{3}DOM* signal is quenched by sorbic acid, a known triplet state quencher (Cottrell et al., 2013).

2.6. Photochemical Formation of Reactive Intermediates

The photosensitized formation of reactive intermediates from DOM is a potential source of organic pollutant degradation in natural systems (e.g. estuaries, treatment ponds, rivers, lakes). Reactive intermediates include $^{\bullet}OH$, singlet oxygen ($^1O_2$), and $^3DOM^*$. In addition, photoionization of DOM can produce the aqueous electron, $e^-_{(aq)}$, however, dissolved oxygen ([O_2] ~ 200 μM) effectively scavenges all $e^-_{(aq)}$ to form $O_2^{\bullet-}$ (k ~ 2 x 10^{10} $M^{-1}s^{-1}$) (Buxton et al., 1988). Other photochemical intermediates and products include H_2O_2 and peroxyl radicals ($ROO^{\bullet}$).

The specific mechanism for the formation of reactive intermediates is described below using DOM as the starting material. After DOM absorbs light and electrons are promoted to an excited state, the system could return to the ground state following emission (fluorescence). A fraction of the chromophores that were excited could also go through intersystem crossing and form an excited triplet state ($^3DOM^*$). The excited triplet state can be quenched by molecular oxygen, which results in the formation of $^1O_2$ (Zepp et al., 1977).

$$^3O_2 + {}^3DOM^* \rightarrow {}^1O_2 + {}^1DOM \qquad \text{Equation 2.9}$$

Due to the relatively low energy of $^1O_2$ (94 kJ mol^{-1}) this reaction occurs readily and it has been suggested that $^1O_2$ is essentially a probe for $^3DOM^*$ (Sharpless and Blough, 2014).

The formation of $^{\bullet}OH$ occurs through the photochemical reactions of DOM, however, the source of this radical is still under investigation (Gan et al., 2008; Page et al., 2011; Pochon et al., 2002; Vaughan and Blough, 1998). For $^{\bullet}OH$, at least two general pathways have been suggested: an H_2O_2-dependent and H_2O_2-independent pathway. In addition there is evidence that both free $^{\bullet}OH$ is produced as well as lower-energy hydroxylating species. The H_2O_2-independent pathway is often portrayed as a $^3DOM^*$ or a low-energy hydroxylating species abstracting

hydrogen from water. This mechanism has been demonstrated for the reaction of photochemically excited 2-methyl-1,4,-benzoquinone with water, in which a non-free $^•$OH hydroxylating species (possibly a quinone-water exciplex) capable of transferring $^•$OH (Pochon et al., 2002). Oxidation of water has yet to be shown, however. Studies of OH$^•$ production from DOM isolates using different probes and quenchers show that the H_2O_2-dependent pathway accounts for ~ 0-50% of OH$^•$ production and that some probes (e.g. terephthalate and benzoate) are not specific for free $^•$OH (Page et al., 2011).

Direct detection of reactive intermediates using time-resolved techniques is difficult, though some studies have utilized laser flash photolysis methods. Steady-state measurements using probe compounds is common. An excellent review of these methods has been written by Blough and Zepp (Blough and Zepp, 1995) and the reader is referred there for complete details. In brief, $^1O_2$ is commonly measured by its reaction with dienes (dimethyl furan or furfuryl alcohol). Steady-state concentrations of $^1O_2$ are calculated from the rate of diene loss and the known rate constant for the reaction between $^1O_2$ and the specific probe. Dienes (e.g. sorbic acid) are also used to probe ^{3}DOM* production rates (Parker et al., 2013) and energies (Zepp et al., 1985). As ^{3}DOM* is a strong oxidant, alkylated phenols such as 1,3,5-trimethylphenol and 2,4,6-trimethylphenol are also commonly used to measure production rates of triplet states. Many probes have been used to monitor $^•$OH production rates, though it has been shown that hydroxylated products can result from hydroxylating species other than OH$^•$ (Page et al., 2011).

2.7. Observations for bulk DOM

Production of reactive intermediates from bulk DOM samples has been well studied for the past few decades. Specifically, many studies have quantified the production rate and quantum yield of reactive intermediates for natural samples of varying origin, while others have sought

mechanistic understanding. Closely tied to the formation of reactive intermediates are the optical properties of DOM.

For $^1O_2$, quantum yields on the order of 0.6-6% have been reported for various natural water samples (Dalrymple et al., 2010; Haag et al., 1984; Peterson et al., 2012), from which steady-state concentrations can be calculated if the spectral irradiance is known. $OH^\bullet$ formation rates from DOM photolysis are on the order of 10^{-12} to 10^{-11} M s^{-1} (Mopper and Zhou, 1990; Vaughan and Blough, 1998; Vione et al., 2006), while quantum yields for this species are less commonly reported. However, values of 1.1 to 3.0 x 10^{-4} for three ocean waters and 7.5 x 10^{-5} for SRFA have been measured irradiating at 320 nm (Vaughan and Blough, 1998). This same study measured nine $^\bullet$OH quantum yields for SRFA over 290-360 nm, finding an average value of 5.4 x 10^{-5}. In particular, the $^\bullet$OH quantum yield of SRFA peaked around 310 nm, and decreased at shorter and longer wavelengths. Steady state concentrations of ^{3}DOM are estimated at 10^{-15} to 10^{-13} M (Zepp et al., 1985). In addition, a pioneering study by Zepp et al. estimated ^{3}DOM* energy levels up to 250 kJ mol^{-1} for natural samples and DOM isolates (Zepp et al., 1985). With respect to quantum yields and steady-state concentrations of reactive intermediates, wastewater-derived EfOM has been shown to have higher values relative to DOM isolates, potentially due to non-humic material produced in water treatment (Dong and Rosario-Ortiz, 2012; E. Lee et al., 2013; Mostafa and Rosario-Ortiz, 2013).

In an effort to chemically alter the photosensitizing moieties of DOM, Mostafa and Rosario-Ortiz treated bulk EfOM with oxidizing NaOCl and O_3 (Mostafa and Rosario-Ortiz, 2013). A decrease in absorbance and increase in E2:E3 accompanied DOM oxidation and resulted in an increase in singlet oxygen quantum yield. The decrease in absorbance is explained by oxidation of light-absorbing aromatic rings and olefins. The increase in singlet oxygen quantum yield

indicates either the relative non-importance of the oxidized aromatic/olefin moieties as sensitizers in $^1O_2$ formation or a decrease in molecular weight following oxidation. Conversely, Sharpless treated DOM isolates with reducing NaBH$_4$ (Sharpless, 2012). While a decrease in absorbance was noted, there was no apparent decrease in singlet oxygen quantum yield. These observations support the idea that, while chemical alteration of both electron donors (aromatics/olefins) and acceptors (carbonyls) may disrupt CT interactions and thus decrease absorbance, mainly carbonyl-containing compounds (acceptors) mediate the formation of $^1O_2$.

Correlations between production of reactive intermediates and optical properties of bulk DOM samples have been reported for a variety of samples. Firstly, the correlation of singlet oxygen quantum yield to absorbance parameters (S, E2:E3, specific absorption coefficients)(Dalrymple et al., 2010; Haag and Höigne, 1986; Mostafa and Rosario-Ortiz, 2013; Peterson et al., 2012; Sharpless, 2012) probably reflects an increase in CT interactions in DOM with lower S and E2:E3. An increase in formation of CT complexes may decrease the efficiency of ^{3}DOM* formation (through production of CT states following absorption of a photon or reaction of ^{1}DOM* → DOM$^{•+/•-}$ and ^{3}DOM* → DOM$^{•+/•-}$) (Sharpless and Blough, 2014). Since ^{3}DOM* is the precursor to $^1O_2$, a decrease in singlet oxygen quantum yield would follow. A few studies report a positive correlation between fluorescence quantum yield and hydroxyl radical quantum yield (Glover and Rosario-Ortiz, 2013; E. Lee et al., 2013; Richard et al., 2004), although it is unclear whether this relationship is due to molecular size parameters or some involvement of ^{1}DOM* in OH$^•$ production (E. Lee et al., 2013; Richard et al., 2004).

With respect to DOM source, it has been shown that EfOM has larger quantum yields for reactive intermediates formation than DOM isolates (Dong and Rosario-Ortiz, 2012). As noted in section 2, EfOM is comprised of recalcitrant DOM from drinking water sources, SMPs, and trace

organic contaminants. Organic contaminants in EfOM should have no contribution due to their very low concentration. It is possible that the difference in apparent quantum yields is due to the oxidation of DOM during chlorination in drinking water treatment. In fact, a positive correlation has been shown between oxidant dose and singlet oxygen quantum yield (Mostafa and Rosario-Ortiz, 2013), with the reason being attributed to either a decrease in molecular weight following oxidation or a chemical change in the sensitizing chromophores. The presence of SMPs in EfOM may also cause this increase, though apparent quantum yields of reactive intermediates from SMPs have not been measured.
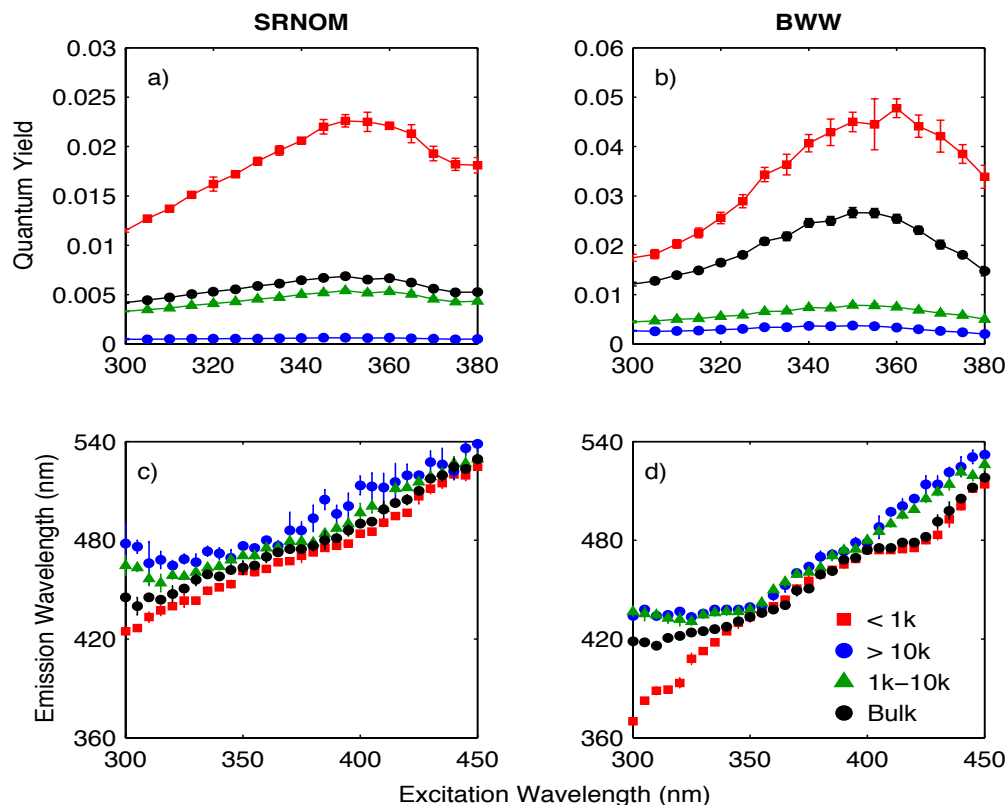
Figure 2.4. Fluorescence quantum yields as a function of excitation wavelength is presented for each size fraction in a) SRNOM and b) Boulder waste water (BWW). Peak emission wavelength as a function of excitation wavelength is depicted for each size fraction for c) SRNOM and d) BWW. Figure taken from Mostafa et al (Mostafa et al., 2014a).

2.8. Observations from different molecular weight fractions

Relatively few studies exist on the effect of molecular weight on reactive intermediates formation (Haag and Höigne, 1986; E. Lee et al., 2013; Mostafa et al., 2014a; Mostafa and Rosario-Ortiz, 2013; Richard et al., 2004; Z.-D. Wang et al., 1990), however, there is a consistent trend of increasing apparent quantum yield for fluorescence and all reactive intermediates with decreasing size. The results from these studies will be summarized in this section and a framework for understanding the physical and chemical basis will be developed.

Wang et al. used ultrafiltration to separate a fulvic acid isolate and observed higher fluorescence intensities for lower AMW fractions, which were attributed to CT interactions within the DOM. This observation has been confirmed by further studies utilizing ultrafiltration

17

for both EfOM (E. Lee et al., 2013; Mostafa et al., 2014a) and a DOM isolate (Mostafa et al., 2014a). Figure 2.4 shows the fluorescence quantum yields for different AMW fractions of Suwannee River NOM (SRNOM) and an EfOM sample as a function of excitation wavelength. As shown, the fluorescence quantum yields are higher for EfOM than for SRNOM. The bottom part of the figure shows the peak emission wavelength as a function of excitation wavelength. A monotonic increase of the emission versus the excitation, as observed for SRNOM, has been used to rationalize charge transfer interactions for DOM (Del Vecchio and Blough, 2004). However, for EfOM, the monotonic increase in emission versus excitation is only observed for the lower AMW fraction. For the larger AMW fraction and bulk sample, there is a deviation at excitation wavelengths below 350 nm. Below this wavelength, it appears the fluorescence is following Kasha's rule, indicating differences in photophysical behavior and suggesting the presence of individual compounds that will also impact photochemical properties. The same deviation is observed between 400-420 nm excitation for smaller EfOM AMW fractions.

The increase in fluorescence quantum yield for lower AMW fractions could be due to either lower degrees of quenching of ^{1}DOM* or intrinsic fluorescence ability. For example, larger molecular weight DOM molecules may have a more aggregated three dimensional structure (Dong et al., 2010; McKay et al., 2011), which would promote intramolecular quenching of ^{1}DOM*, resulting in a decrease in fluorescence quantum yield. Alternatively, lower AMW fractions could contain more potent fluorophores. However, considering that more conjugated structures generally have higher fluorescence quantum yields (Turro et al., 2012), and that higher AMW fractions might be expected to have more conjugated structures relative to low AMW fractions, the first explanation (quenching of ^{1}DOM*) seems more likely.
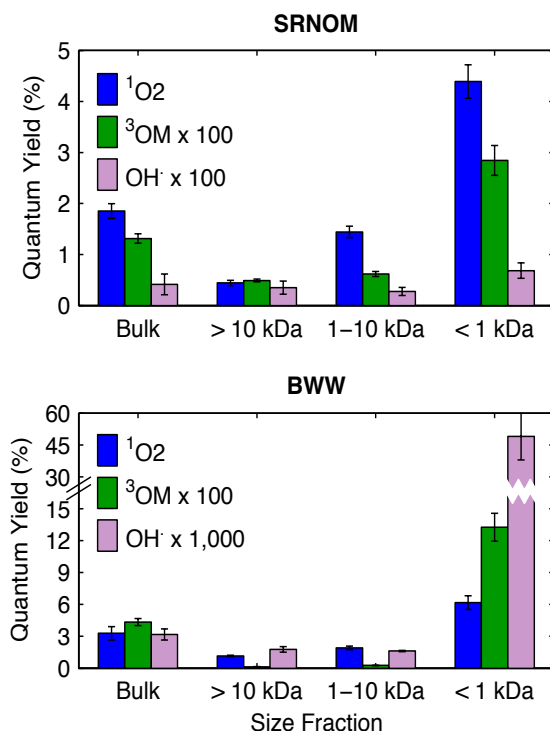
Figure 2.5. Quantum yields for the formation of reactive intermediates ($^{1}O_{2}$, $^{3}DOM^*$, $OH^{\bullet}$), for different size fractions normalized to the values of the unfractionated samples of SRNOM and an EfOM sample. Quantum yields are reported as % to facilitate the display of the data. Figure adapted from Mostafa et al. 2014 (Mostafa et al., 2014a).

With respect to reactive intermediates, an early study by Haag and Hoigné (Haag and Höigne, 1986) used gel permeation chromatography to separate DOM samples into apparent molecular weight fractions and quantified steady state $^{1}O_{2}$ concentrations ($[^{1}O_{2}]_{ss}$). Their results showed that 100-500 Da fractions had consistently higher, or at least equal, $[^{1}O_{2}]_{ss}$ as bulk samples. Richard et al. used SEC-Page to separate DOM isolate standards and soil DOM extracts in order to determine the effect of AMW on fluorescence and photosensitizing ability (Richard et al., 2004). Similar to previous studies, fluorescence intensity was increased in low relative to high AMW fractions. Degradation of fenuron and 2,4,6-trimethylphenol (TMP), known to react with $^{3}DOM^*$ (Canonica et al., 2006; 2000), was also increased in low AMW fractions, suggesting an increase in reactive intermediates formation. Rosario-Ortiz et al. have carried out

systematic studies on the effect of AMW on reactive intermediates quantum yields (E. Lee et al., 2013; Mostafa et al., 2014a; Mostafa and Rosario-Ortiz, 2013); the general results are summarized in Fig. 5, which shows the apparent quantum yields for SRNOM and an EfOM sample. The bulk EfOM sample had higher quantum yields for the formation of $OH^{\bullet}$, $^{1}O_{2}$, and $^{3}DOM^{*}$ compared to DOM (Mostafa et al., 2014a). After fractionation into different AMW fractions, the lower AMW fractions of EfOM still had higher quantum yields than for DOM. In addition it is observed that the components associated with the lower AMW fraction of EfOM are much more reactive towards the formation of reactive intermediates. This fraction could be enriched in SMPs. The work done on AMW fractions could be rationalized by expecting that lower AMW components will have molecules with excited states separated by larger energy gaps, compared to larger (and more highly conjugated) components with faster internal conversion kinetics. It could also be that there are inherent differences in chromophore composition, and higher SMP reactivity overall.

It should be noted that the chemical probe used to measure $^{1}O_{2}$, furfuryl alcohol (FFA), is hydrophilic and is limited to reaction with bulk, aqueous phase $^{1}O_{2}$ and not $^{1}O_{2}$ in the DOM microenvironment (Latch and McNeill, 2006). Therefore, an increase in singlet oxygen quantum yields may reflect the greater amount of $^{1}O_{2}$ escaping the DOM microenvironment (and reaching the bulk phase) before being quenched by DOM as would be expected with smaller molecular size DOM molecules. However, the fact that $^{3}DOM^{*}$ quantum yields (measured by TMP, a more hydrophobic probe) positively correlate with singlet oxygen quantum yields suggests another explanation, namely, that $^{3}DOM^{*}$ itself (and not $^{1}O_{2}$ alone) may undergo intramolecular quenching. Higher AMW DOM has a more aggregated three-dimensional structure (see section 5) and thus increased intramolecular quenching is expected in these fractions.

Two studies have reported an increase in hydroxyl radical quantum yield with decreasing AMW (E. Lee et al., 2013; Mostafa et al., 2014a). In both instances, a concomitant increase in fluorescence quantum yield was observed in low AMW fractions. Sharpless and Blough have suggested that this is an indication of fewer CT interactions in low AMW fractions (Sharpless and Blough, 2014). This seems plausible, as CT interactions would provide a relaxation pathway for excited state DOM molecules, which play a role in formation of $^\bullet$OH.

2.9. Scavenging of reactive intermediates by DOM

Central to the understanding of photochemical production of reactive intermediates from DOM photolysis is the recognition that DOM is reactive towards these very same reactive intermediates. In principle, both inter- and intramolecular reaction of reactive intermediates with DOM are possible. Wenk et al. have studied quenching of model triplet excited states (quinones and aromatic ketones) by bulk DOM standards (Wenk et al., 2013), finding that only neutral or cationic sensitizers were quenched, likely due to complexation of these molecules by DOM. Based on rate constants measured for this system in aerated solution where triplet states are deactivated via reaction with oxygen, intermolecular quenching is insignificant below DOM concentrations 22-72 mg_C L^{-1}, which is far below that of most natural systems. Intramolecular quenching of ^{3}DOM* has not yet been investigated and remains a possible pathway for ^{3}DOM* loss.

Other reactive intermediates have high reactivity with DOM, including $^\bullet$OH (Dong et al., 2010; Rosario-Ortiz et al., 2008; Westerhoff et al., 2007) and ^{1}O$_2$ (Cory et al., 2009). Scavenging of these species by DOM can affect their steady-state concentrations and thus their ability to degrade organic contaminants. Rate constants for the reaction of $^\bullet$OH and ^{1}O$_2$ with DOM are on the order of 10^{8-9} and 10^5 $M_C^{-1}s^{-1}$, respectively, where M_C is the molar concentration of carbon.

21

Dong et al. showed that lower AMW fractions of EfOM were more reactive towards OH$^{\bullet}$ on a per carbon basis, explaining the result as geometric affect. In short, if high AMW fractions contain more aggregated three-dimensional structures, some carbon atoms are likely inaccessible to OH$^{\bullet}$. Conversely, less aggregated, low AMW fractions having a higher surface area-to-carbon atom ratio would exhibit higher reactivities on a molar basis based on this geometric effect.

2.10.   Conclusions

Throughout this chapter, we have developed a framework for understanding the photophysical and photochemical processes in the complex material that is DOM. There are a few main conclusions that can be derived. One is that the optical properties (absorbance, fluorescence, phosphorescence) in DOM are influenced by interactions within DOM molecules. This may be influenced by the so-called charge transfer interactions as well as by molecular size. In addition, photochemical production of reactive intermediates (as well as fluorescence) clearly varies with molecular size. It is difficult at this point, however, to distinguish whether this is due to strictly molecular size (e.g. intramolecular quenching) or differences in chemical composition between the different fractions. More experiments are needed to clarify this matter. For example, reduction of molecular size fractions with borohydride to yield DOM with the same electron donating or accepting capacity would allow examination based solely on molecular size. Conversely, chemically modifying the same molecular fraction, or bulk DOM sample, via chemical or electrochemical oxidation or reduction would provide insight into the effects of chemical composition. In the context of natural systems, knowing the molecular size of the DOM in the system should provide a good surrogate to the expected steady-state concentrations of reactive intermediates and thus provide estimations of indirect organic pollutant degradation rates.

3. Investigation of the Coupled Effects of Molecular Weight and Charge Transfer Interactions on the Optical and Photochemical Properties of Dissolved Organic Matter

3.1. Abstract

We studied the formation of photochemically produced reactive intermediates (RI) from dissolved organic matter (DOM). Specifically, we focused on the effects of variable molecular weight and chemical reduction on the optical properties of DOM (absorbance and fluorescence) and the formation of singlet oxygen ($^1O_2$), DOM triplet excited states ($^3DOM^*$), and the hydroxyl radical ($^\bullet OH$). The data are largely evaluated in terms of a charge transfer (CT) model, but deficiencies in the model to explain the data are pointed out when evident. Two sets of samples were studied that were subjected to different treatments; the first set included secondary-treated wastewaters and a wastewater-impacted stream, the second was a DOM isolate. Treatments included size fractionation and chemical reduction using sodium borohydride. Taken as a whole, the results demonstrate that decreasing molecular weight and borohydride reduction work in opposition regarding quantum efficiencies for $^1O_2$ and $^3DOM^*$ production, but in concert for fluorescence and $^\bullet OH$ production. The optical and photochemical data provide evidence for a limited role of CT interactions occurring in lower molecular weight DOM molecules. In addition, the data suggest that the observed optical and photochemical properties of DOM are a result of multiple populations of chromophores and that their relative contribution is changed by molecular weight fractionation and borohydride reduction.

3.2. Introduction

The fate and transport of organic contaminants in aquatic systems is an important research topic in the field of environmental engineering and chemistry. Contaminant removal and transformation mechanisms in these environments include sorption, biotransformation, volatilization, and many abiotic chemical reactions. One reactive pathway for contaminant degradation is through direct or sensitized photolysis (Leifer, 1988). Direct photolysis of a contaminant occurs due to absorption of light by that chemical, which may induce its degradation. Sensitized degradation (commonly known as indirect photolysis) of a contaminant can occur through production of reactive intermediates (RI) following absorption of light by chemical sensitizers. Multiple chemical compounds can act as sensitizers in aquatic systems, such as nitrate (NO_3^-), nitrite (NO_2^-), and dissolved organic matter (DOM) (Leifer, 1988).

DOM has been recognized as a significant absorber of light and sensitizer leading to RI formation in aquatic systems as well as some atmospheric systems (Ghassemi and Christman, 1968; Phillips and Smith, 2014; Vione et al., 2014). Absorption of light by DOM produces a variety of RI such as singlet oxygen ($^1O_2$), DOM triplet excited states ($^3DOM^*$), hydrogen peroxide (H_2O_2), and the hydroxyl radical ($^\bullet OH$) (Blough and Zepp, 1995; Canonica et al., 1995; Cooper et al., 1988; Dong and Rosario-Ortiz, 2012; Fischer et al., 1985; Glover and Rosario-Ortiz, 2013; E. Lee et al., 2013; Mostafa et al., 2014b; Mostafa and Rosario-Ortiz, 2013; Zepp et al., 1977). These species can oxidize or reduce organic contaminants (Canonica et al., 2006; 2000; Wenk et al., 2015), inactivate pathogens (Jasper et al., 2013; Kadir and Nelson, 2014), and are involved in carbon cycling in aquatic systems (Gao and Zepp, 1998). Although many studies have examined the photochemical formation of RI, there are still unanswered questions

regarding the underlying mechanisms. Some of these mechanisms and knowledge gaps are reviewed below.

Equations 3.1-3.3 illustrate the formation of ^{3}DOM* and ^{1}O$_2$.

$$DOM + h\nu \rightarrow {^1}DOM* \qquad\qquad\qquad \text{Equation 3.1}$$

$$^1DOM* \xrightarrow{k_{isc}} {^3}DOM* \qquad\qquad\qquad \text{Equation 3.2}$$

$$^3DOM* + O_2 \xrightarrow{Y} {^1}O_2 + DOM \qquad\qquad\qquad \text{Equation 3.3}$$
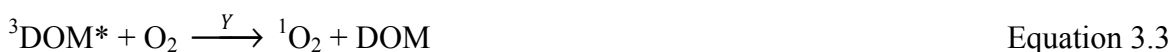
where k_{isc} is the rate of intersystem crossing and Y is the yield of ^{1}O$_2$ from quenching of ^{3}DOM* by O$_2$. Although the energy difference between ^{1}O$_2$ and its triplet ground state is only 94 kJ mol$^-$^{1}, only approximately 30-50% of the ^{3}DOM* pool is thought to contribute to ^{1}O$_2$ formation (Sharpless and Blough, 2014). It was shown that ~ 50% of ^{3}DOM* derived from commercial and isolated humic substances as well as natural water samples had energies of at least 250 kJ mol^{-1} (Zepp et al., 1985).

The formation of $^•$OH from DOM photolysis is less well understood because typically used probes can be oxidized by other, unknown photooxidants. Indeed, combined use of arene probe compounds and methane has shown that DOM photolysis produces a combination of free $^•$OH and so-called low energy hydroxylators (McKay and Rosario-Ortiz, 2015; Page et al., 2011). The exact identity of these latter species are unknown, but two possibilities are water-quinone exciplexes (Gan et al., 2008) or DOM radicals (Sharpless and Blough, 2014). Furthermore, the sources of free $^•$OH in this system are not known. In both DOM isolates and natural waters, some free $^•$OH is attributable to the photo-Fenton reaction, but this can not account for all of it (Page et al., 2011; Vermilyea and Voelker, 2009; White et al., 2003). Recent work suggests that hydroxy aromatic acids may be important sources of free $^•$OH from DOM photolysis (Sun et al., 2015).

Various models have been proposed to explain the photophysical and photochemical properties of DOM. One model that has received much attention in recent years is that of charge transfer (CT) interactions, recently reviewed by Sharpless and Blough (2014) (Sharpless and Blough, 2014). In this model, electron-rich donors (D groups) and electron-poor acceptors (A), which are thought to be in close proximity within a DOM molecule, can interact in the ground or excited state via partial or full transfer of an electron (from D to A) to form a CT state, (D^+ / A^-). D and A groups are thought to result from the oxidation of lignin precursors, and model compounds for typical D and A groups are hydroxylated/alkoxylated aromatics and aromatic ketones/aldehydes or quinones, respectively. It is thought that presence of CT states provides: (i) lower energy electronic transitions (excitation into CT states), thereby explaining the long wavelength absorption of DOM (Del Vecchio and Blough, 2004; Ma et al., 2010); (ii) a deactivation pathway for local singlet excited states ($^1DOM^* \rightarrow DOM^{\bullet+/\bullet-}$) (Boyle et al., 2009; Del Vecchio and Blough, 2004; Ma et al., 2010), thereby explaining long wavelength fluorescence at short excitation wavelengths; (iii) a relaxation pathway for local triplet excited states ($^3DOM^* \rightarrow DOM^{\bullet+/\bullet-}$) (Parker et al., 2013). Two different notations will be used for CT complexes in this paper: one is $DOM^{\bullet+/\bullet-}$ and the other is (D^+ / A^-). Additional details regarding CT are given in 8; also see references (Sharpless and Blough, 2014) and (Dalrymple et al., 2010; Sharpless, 2012) for information on these two notations, respectively. Although additional studies have indicated other physical bases for some of these processes (Latch and McNeill, 2006), there has yet to be a comprehensive model for DOM photophysics and photochemistry proposed other than CT interactions. For example, in contrast to the CT model, it could be assumed that DOM's photochemical and photophysical behavior results from a superposition of individual chromophores, where the behavior of the whole is the average of its components.

Another important variable influencing DOM photophysics and photochemistry is the molecular weight distribution of DOM molecules (Frimmel et al., 1987; E. Lee et al., 2013; McKay et al., 2011; McKay and Rosario-Ortiz, 2015; Mostafa and Rosario-Ortiz, 2013; Richard et al., 2004). DOM of lower molecular weight exhibits increased spectral slopes (S) (Boyle et al., 2009; Mostafa et al., 2014a; Peuravuori and Pihlaja, 1997; Yacobi et al., 2003), E2/E3 values (Abs_{250}/Abs_{365}) (Boyle et al., 2009; Mostafa and Rosario-Ortiz, 2013; Peuravuori and Pihlaja, 1997; Yacobi et al., 2003), and increased fluorescence, $^1O_2$, $^3DOM*$, and $^\bullet OH$ quantum yields (E. Lee et al., 2013; Mostafa et al., 2014a; Mostafa and Rosario-Ortiz, 2013). S and E2/E3 are thus thought of as surrogates for molecular weight and (indirectly) the prevalence of CT interactions. Although the relationship between molecular weight and S or E2/E3 has been documented for some time, the specific physical bases have not been firmly established. Based on a negative correlation between S and average gel permeation chromatography retention time, Boyle et al. (2009) suggested that higher molecular weight DOM has on average a greater number and variety of CT interactions that are possible within the larger size ensemble (Boyle et al., 2009). While conceptually possible, this idea is difficult to verify and assumes a consistent functional group composition between molecular weight fractions, which may not be the case (Aeschbacher et al., 2010; Richard et al., 2004). Indeed, the relationships between DOM optical properties, photochemistry, and molecular weight are not completely understood. For example, it is unknown whether size-fractionation, either by biological/photochemical (e.g. photobleaching) or intentioned (e.g. SEC or ultrafiltration) means, produces samples of identical chemical composition to that of the un-fractionated sample. This has been noted in previous studies (E. Lee et al., 2013; Mostafa and Rosario-Ortiz, 2013) and an important knowledge gap remains.

27

Therefore, we have studied the relationship between DOM molecular weight and its optical and photochemical properties for both whole water samples (secondary-treated wastewaters and a wastewater-impacted stream) as well as an isolated terrestrial fulvic acid from the Suwannee River. A solar simulator was used to measure "environmental" quantum yields (for simplicity the term quantum yield, Φ, will be used). Chemical (base modification and coagulation with alum) and physical (size-fractionation using an ultrafiltration membrane) treatments were used to examine the effect of molecular weight. Aliquots of the molecular weight fractions obtained by ultrafiltration were chemically reduced with borohydride to decouple the effects of molecular weight and carbon oxidation state. Base modification, coagulation, and ultrafiltration are shown below to lower the average molecular weight of each DOM sample. This relates to the CT model because lower molecular weight DOM molecules are hypothesized to be less able (probabilistically) to form CT states. Reduction with borohydride affects DOM photophysics via a distinctly different mechanism. Borohydride-reduction reduces carbonyl groups to alcohols ($R_2C=O \rightarrow R_2CHOH$), which decreases the number of A groups within DOM molecules. As a result, the CT model would again predict that borohydride-treated DOM is less able to form CT states.

Some of the data are interpreted in light of the CT model, but deficiencies in the ability of this model to explain the data are discussed. In addition to providing new insight into the photophysical and photochemical processes of DOM, the data presented here will be useful for wastewater treatment systems employing lime softening (mimicked by base modification) or coagulation in assessing the photochemical activity of discharged effluents.

3.3. Materials and Methods

3.3.1 Samples

Suwannee River Fulvic Acid (SRFA, 1S101F) was purchased from the International Humic Substances Society. Three secondary treated wastewaters were used: Boulder Wastewater (BWW); Orange County Water District (OCWD), as produced by the Orange County Sanitation District and used by OCWD as influent to an advanced wastewater recycling facility; and Longmont (LM) wastewater. An additional sample was collected from Boulder Creek (BC) at 75th and Jay St. (Boulder, CO). Additional sample details are provided in Appendix A. Samples were collected in pre-combusted (550 °C for 4 hours in a muffle furnace) amber glass bottles, filtered with pre-combusted and rinsed (1 L Milli-Q water, 18 MΩ-cm) 0.7 μm GF/F filters, and stored at 4 °C. Water quality data are presented in Table A.1. Sample pH adjustment when indicated was performed with concentrated phosphoric acid or sodium hydroxide.

3.3.2 Experimental matrix

It should be made explicit at this point that all treatments were not performed on every sample because of the inherent differences in the samples (isolates versus more complex natural and anthropogenic sources). Two wastewaters (BWW and OCWD) and the wastewater-impacted stream (BC) were subjected to base modification, one wastewater (LM) was subjected to coagulation with alum, and SRFA was subjected to both ultrafiltration and reduction with borohydride. There are a few reasons for this. First, we demonstrate that base modification, coagulation with alum, and ultrafiltration all show results characteristic of high molecular weight removal. Base modification and coagulation with alum both resulted in coagulation of organic matter and ultrafiltration is a well-documented size fraction technique. Because the effects

29

following each treatment were similar, we did not perform all size fractionation procedures on each sample (e.g. coagulation of OCWD or SRFA). We chose to reduce only SRFA molecular weight fractions with borohydride, and not wastewater samples, due to the complex background matrix of inorganic constituents in wastewater. This choice seems justified based on the fact that most of the papers reporting CT interactions in DOM use SRFA as an exemplar (Boyle et al., 2009; Del Vecchio and Blough, 2004; Golanoski et al., 2012; Ma et al., 2010; Zhang et al., 2012) and that the results for SRFA appear to be general across DOM of different types and origins (Ma et al., 2010; Sharpless, 2012).

3.3.3 Base modification and coagulation procedure

Two chemical size-fractionation procedures were used. The first was a base modification process in which the pH of a 1 L aliquot was quickly (less than one minute) adjusted to 11.0 ± 0.2 and stirred for one hour at a constant rate, which resulted in formation of a gray precipitate. After one hour, the solution was filtered and the solution pH was adjusted to 7.2. Non-base-modified samples were also adjusted to pH 7.2 to remove the effect of pH on measured optical and photochemical properties. As shown in Table A.1, this process resulted in significant coagulation of organic matter for wastewater samples ($\sim 13\%$ and 10% reduction in DOC for BWW and OCWD, respectively), but less for the wastewater-impacted river water ($\sim 3\%$ reduction in DOC). The minimal change in DOC, optical properties, and SEC chromatograms for the BC sample that underwent minimal coagulation is taken as evidence that the structure of the organic matter was unchanged after adjustment to pH 11.

Coagulation of LM wastewater with aluminum sulfate hexadecahydrate (alum) ($Al_2(SO_4)_3 \cdot 16H_2O$) was performed using a jar tester (Phipps & Bird) in 1 L volumes at doses of 0, 30, 60, 90, and 120 mg alum L^{-1}. Following coagulant injection, samples were rapidly mixed

(290 rpm for 1 minute), followed by two flocculation phases (10 minutes at 55 rpm and 10 minutes at 20 rpm), and a sedimentation period (30 to 60 minutes with no mixing). The supernatant was filtered through 1.5 and 0.7 μm GF/F filters in series and adjusted to pH 7.2. Chemical analyses, fluorescence measurements, and photochemical experiments were performed within one week of coagulation.

3.3.4 Borohydride reduction procedure

SRFA was dissolved in 10 mM phosphate buffer at a concentration of 80 mg L^{-1} (43.2 mg$_C$ L^{-1}) by stirring overnight. After filtering, this solution was fractionated by passing the 80 mg L^{-1} solution through a 5-kDa membrane (Millipore, USA) to obtain a <5K (permeate) and >5K (retentate) fraction. Aliquots pre-saturated with N$_2$ (30 min.) were reduced with NaBH$_4$ (30 mg NaBH$_4$ per mg DOM) under N$_2$. NaBH$_4$ was added over a period of 5 to 10 minutes and the reaction mixture was stirred vigorously for 3 hours. The mixture was re-saturated with breathing quality air (28% O$_2$/72% N$_2$, Airgas) after dilution with buffer to ~ 10 mg$_C$ L^{-1} and the solution pH was adjusted to 3 and then re-adjusted to 7.2. The long reaction time as well as the absence of hydrogen (H$_2$) evolution after adjustment to acidic pH was taken as evidence of no residual borohydride. Absorbance spectra of the reduced and native samples were monitored throughout the course of study (Figure A.1) and did not change.

3.3.5 Analytical Methods

Dissolved organic carbon (DOC) content of filtered samples was measured after acidification to pH < 2 with phosphoric acid with a TOC-V$_{SCH}$ (Shimadzu Corp.) analyzer using a non-purgeable organic carbon method. The accuracy and precision of 1.4 and 3.0 mg$_C$ L^{-1} potassium hydrogen phthalate standards were within 5% throughout the course of this study.

Nitrate (NO_3^-) and nitrite (NO_2^-) were analyzed by the Laboratory for Environmental and Geological Sciences (LEGS) at CU Boulder using ion chromatography. Total iron was measured by LEGS using atomic emission spectroscopy (AES), with a reported detection limit of 0.002 ppm. Absorbance was measured in triplicate with a Cary Bio 100 (Agilent Technologies, CA) from 200-800 nm in a 1 or 5 cm quartz cuvette and baseline corrected to deionized water. Fluorescence was measured in triplicate on a Fluoromax-4 (Horiba) with excitation wavelengths ranging from 240 to 550 nm in 10 nm increments and emission scans collected from 300 to 700 nm in 2 nm increments (Cawley et al., 2015). The bandpass for both excitation and emission monochromators was 5 nm and the integration time was 0.25 s. Raw fluorescence data were corrected using the method of Murphy et al. (2010) (Murphy et al., 2010) and quantum yields were calculated by using quinine sulfate as a reference standard following the method of Cawley et al. (2015) (Cawley et al., 2015). In many cases, samples were diluted for fluorescence measurements such that the maximum emission intensity was less than 2×10^6 counts per second to avoid detector saturation. Size exclusion chromatography (SEC) was performed using previously described methods (Dong et al., 2010).

3.3.6 Photochemical measurements.

Data shown in figures and tables represents an average of at least duplicate irradiations and error bars represent two standard deviations (*s*). Samples were irradiated using an Oriel 94041A Solar Simulator (Newport Corp.) with an AM 1.5 filter in clear, borosilicate glass vials laid flat in a water-jacketed petri dish that was cooled with a chiller to 20 ± 2 °C. Lamp spectra were measured with an Ocean Optics USB 2000 spectroradiometer. Probe compounds used for the detection of RI have been described previously and details are provided in Appendix A. A lamp spectrum and description of the polychromatic quantum yield calculation is also described in

Appendix A (Figure A.2). Polychromatic quantum yields are denoted from this point on as Φ_f, Φ_{1O2}, and Φ_{OH} for fluorescence, $^1O_2$, and $^\bullet OH$, respectively, while f_{TMP} represents the TMP degradation efficiency (at $[TMP]_0 = 5$ µM).

3.4. Results

3.4.1 DOM size characterization.

SEC data is plotted in Figure A.3 to Figure A.5. The data generally show results consistent with a decrease in apparent molecular weight upon base modification, coagulation, and ultrafiltration (average retention times given in Table A.2). Coagulation and ultrafiltration have previously been shown to remove high molecular weight molecules from DOM (Korshin et al., 2009; Thurman et al., 1982). It is important to note that E2/E3 values, which have a negative correlation with molecular size, increased as a result of each of these treatments, which corroborates the SEC measurements.

A critical assumption in the use of borohydride is that neither borohydride nor OH⁻ ions from the high pH it causes induces reactions involving esters (e.g. hydrolysis), which would result in lower molecular weight compounds. SEC was used to test for this and the data for each fraction pre- and post-reduction are shown in Figure A.5. Although a peak at a retention time of ~ 45 minutes appears in all reduced samples, there is essentially no change in average retention time and thus borohydride reduction can be considered, at a first approximation, as a means to examine the effect of oxidation state independent of molecular weight (see 8 for additional discussion).

3.4.2 Optical changes following phsysicochemical treatments.

Base modification, coagulation, and ultrafiltration all caused changes in absorption that have been attributed to removal of high molecular weight DOM (see E2/E3 values in Table 3.1). Figure 3.1 shows the molar absorptivity (units of M_C^{-1} cm^{-1}) and fraction molar absorptivity remaining for samples subjected to each of these treatments (see also Figure A.6 and Figure A.7). All samples exhibited a preferential decrease in molar absorptivity with increasing wavelength into the visible region of the spectrum, as does borohydride-treated SRFA (Figure 3.2 and (Ma et al., 2010)). The ratio of reduced to native molar absorptivity decreases systematically for each molecular weight fraction to ~ 450 nm, with varying behavior at longer wavelengths. Molar absorptivity is used because of varying carbon concentrations across samples.
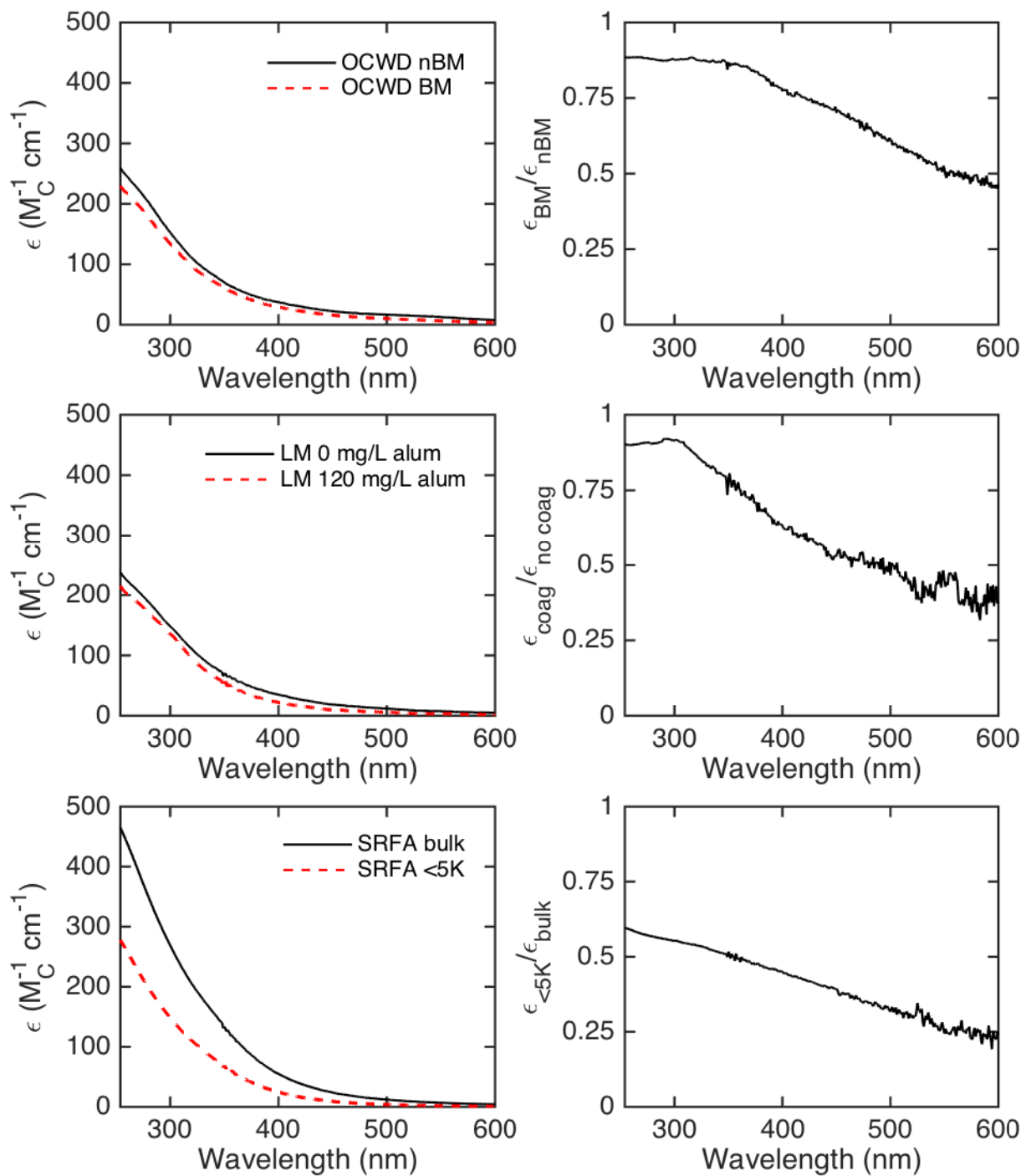
Figure 3.1. Carbon-based molar absorptivities plotted from 254 to 600 nm for for wastewater samples and size-fractionated SRFA. (Right panels) Fraction of remaining absorptivity based on data in left panels. Absorbance scans collected with a 1 cm pathlength. [DOC] ~ 5-10 mg L^{-1}.
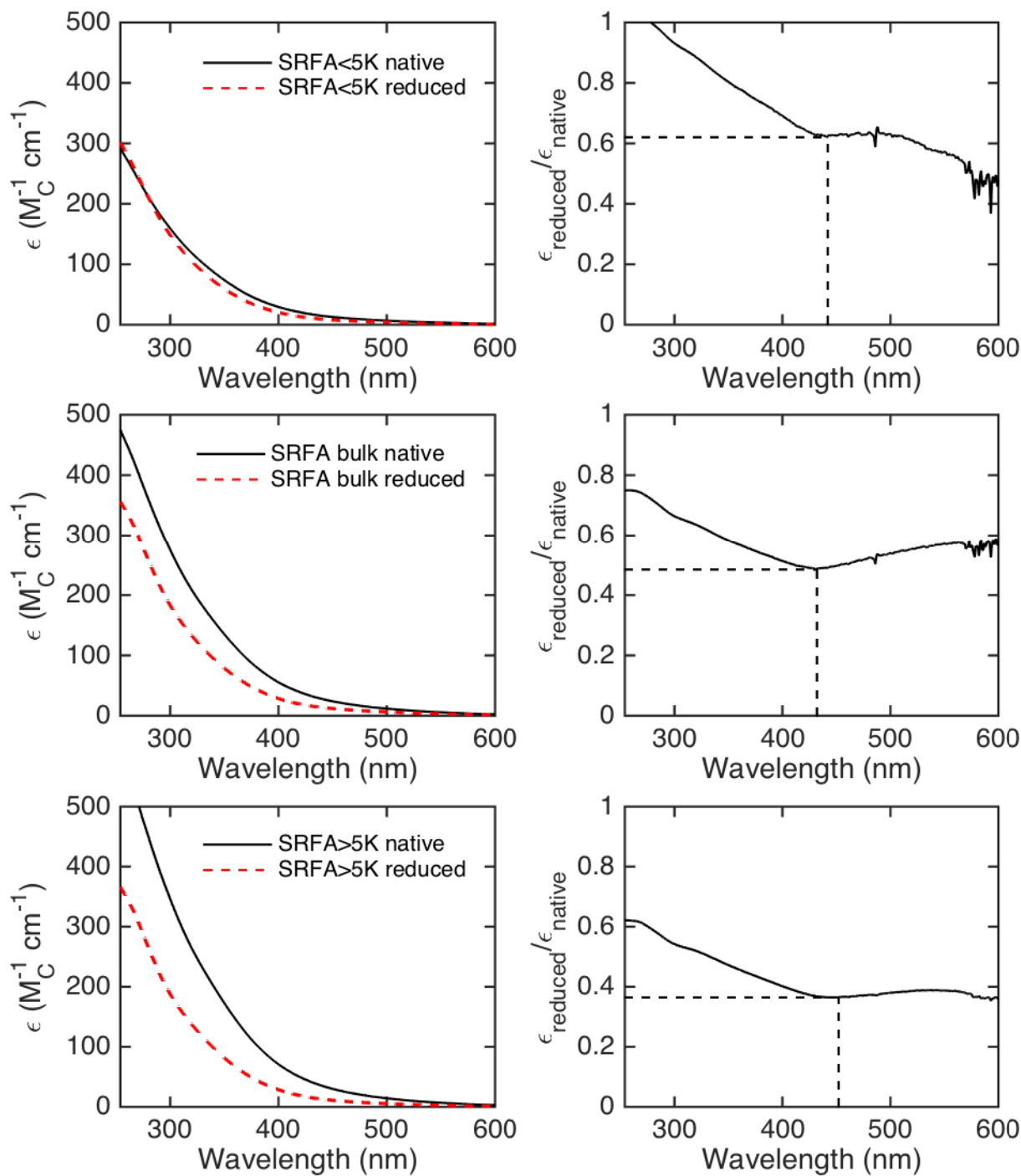
Figure 3.2. Carbon-based molar absorptivities for SRFA plotted from 254 to 600 nm for SRFA <5K, unfractionated, and >5K before and after reduction with sodium borohydride. (Right panels) Fractional absorptivity remaining based on data in left panels. Dashed line represents local $f_{a,min}$ and λ_{min} as described in text ($f_{a,min}$, λ_{min}): SRFA >5K (0.389, 452 nm), SRFA (0.485, 432 nm), SRFA <5K (0.620, 442 nm). Absorbance scans collected with a 5 cm path length. [DOC] ~ 10 mg L^{-1}.

36

Φ_f as a function of excitation wavelength for LM wastewater and SRFA is shown in and Figure 3.3, respectively. Maximum Φ_f values and their corresponding excitation wavelengths (λ_{max}) are listed in Table 3.1. Apparent quantum yields for all samples in this study.. Similar to previous studies, Φ_f was increased by removal of high molecular weight DOM by coagulation(Korak, 2014) and ultrafiltration (M.-H. Lee and Hur, 2013; Mostafa et al., 2014a) as well as by reduction with borohydride (Ma et al., 2010). λ_{max} did not change for SRFA after reduction with borohydride (except by + 70 nm for the >5K fraction). Reduction resulted in a significant increase in Φ_f for all samples. A greater relative difference is observed with increasing molecular weight, but a greater absolute difference is seen with decreasing molecular weight (see Table A.3). Finally, the maximum Φ_f for SRFA is in good agreement with the data reported in Ma et al. (2010) (Ma et al., 2010).

There are clear differences between wastewater and SRFA samples regarding the Φ_f-λ_{max} relationship. Figure A.8 and Figure 3.3 show that Φ_f varies more strongly with excitation wavelength for LM wastewater than for SRFA (regardless of molecular weight fraction or carbon oxidation state). This is not just a scaling issue; the ratio of max to min Φ_f is consistently ~ 3 for LM wastewater and less than ~ 2 for SRFA. Also, λ_{max} is ~ 20 nm shorter for LM wastewater than SRFA. Whole water EfOM samples (and their corresponding fluorescence properties) are much more heterogeneous than the SRFA isolate (Henderson et al., 2009). In previous work, fluorescence properties of EfOM have been explained in part by individual fluorophores as opposed to the CT model (Mostafa et al., 2014a).
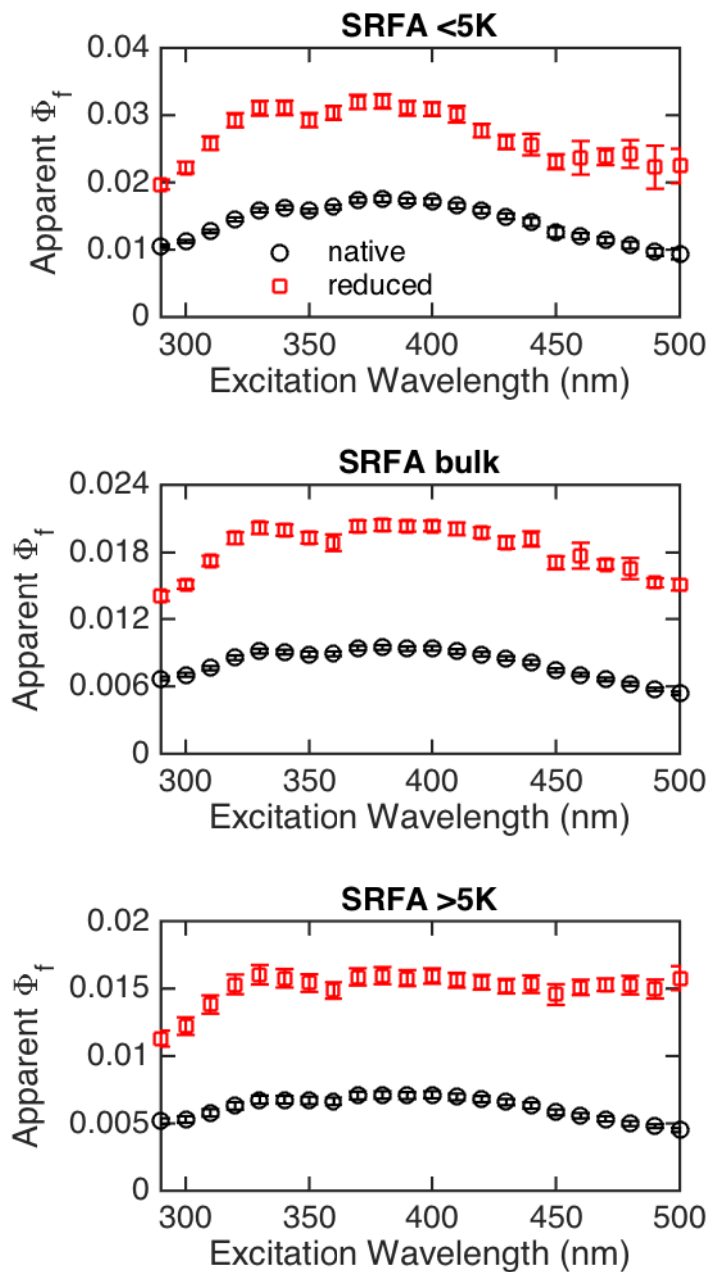
Figure 3.3. Apparent fluorescence quantum yields for native and borohydride reduced SRFA molecular weight fractions. [DOC] ~ 4 mg L^{-1}.

3.4.3 Changes in RI quantum yields following phsysicochemical treatments.

Φ_{1O2}, f_{TMP}, and Φ_{OH} were measured for each of the samples described in this study (Table Table 3.1).

Table 3.1. Apparent quantum yields for all samples in this study.

Sample	Treatment	E2/E3	λ_{max}	Φ_f	Φ_{1O2}	f_{TMP} (M^{-1})	$\Phi_{OH} \times 10^5$
			Fluorescence		Reactive Intermediates		
BC	none	5.56	380	0.0570 ± 0.0024	0.0365 ± 0.015	88.9 ± 7.8	0.98 ± 0.05
BC	pH adjustment	5.61	380	0.0579 ± 0.0044	0.0382 ± 0.001	81.4 ± 1.2	1.00 ± 0.50
BWW	none	5.25	370	0.0211 ± 0.0012	0.0277 ± 0.005	37.1 ± 3.8	3.97 ± 0.74
BWW	pH adjustment	5.79	380	0.0270 ± 0.0032	0.0358 ± 0.007	69.2 ± 2.6	4.81 ± 0.74
OCWD	none	5.01	360	0.0251 ± 0.0018	0.0261 ± 0.001	118.9 ± 0.2	26.28 ± 2.07
OCWD	pH adjustment	5.14	370	0.0295 ± 0.0012	0.0371 ± 0.005	136.4 ± 37.5	35.37 ± 0.74
LM	none	4.59	360	0.0285 ± 0.0012	0.0236 ± 0.003	23.0 ± 2.7	6.13 ± 0.95
LM	30 mg alum/L	4.88	370	0.0330 ± 0.0016	0.0278 ± 0.002	28.7 ± 2.8	7.02 ± 0.45
LM	60 mg alum/L	5.21	370	0.0396 ± 0.0018	0.0300 ± 0.004	49.0 ± 4.2	8.25 ± 0.81
LM	90 mg alum/L	5.37	370	0.0428 ± 0.0022	0.0352 ± 0.004	66.3 ± 1.8	9.22 ± 0.66
LM	120 mg alum/L	5.51	370	0.0456 ± 0.0022	0.0363 ± 0.001	79.1 ± 2.7	10.85 ± 0.49
SRFA <5K	fractionation	5.46	390	0.0176 ± 0.001	0.0298 ± 0.004	40.7 ± 4.7	1.71 ± 0.50
SRFA <5K	fractionation and reduction	7.37	390	0.0321 ± 0.0022	0.0256 ± 0.000	30.1 ± 0.2	2.85 ± 0.74
SRFA	fractionation	4.73	390	0.0095 ± 0.0004	0.0181 ± 0.001	25.7 ± 1.2	1.58 ± 0.07
SRFA	fractionation and reduction	6.36	390	0.0204 ± 0.001	0.0164 ± 0.000	25.0 ± 0.7	2.02 ± 0.43
SRFA >5K	fractionation	4.57	410	0.0071 ± 0.0006	0.0154 ± 0.001	21.5 ± 2.5	1.10 ± 0.37
SRFA >5K	fractionation and reduction	6.33	340	0.0160 ± 0.0014	0.0152 ± 0.001	17.1 ± 1.6	1.91 ± 0.45

The Φ_{OH} values here represent a combination of free $^\bullet$OH and low energy hydroxylators because benzene may also be oxidized by the latter species (McKay and Rosario-Ortiz, 2015) Table 3.1 shows RI quantum yields for BWW, OCWD, and BC pre- and post-base modification and demonstrates an increase in Φ_{1O2}, f_{TMP}, and Φ_{OH} for BWW and OCWD, but not BC. Figure 3.4 shows RI quantum yields for coagulated LM wastewater plotted versus coagulant dose (note that greater coagulant doses resulted in increased E2/E3). Φ_{1O2}, f_{TMP}, and Φ_{OH} increased systematically as a result of all water treatment processes. These results are consistent with previous reports, which demonstrate similar changes in RI quantum yields with changes in DOM molecular weight obtained by different processes (e.g. gel electrophoresis, ultrafiltration) as well as changes in E2/E3 for non (size) fractionated samples and DOM isolates (Bodhipaksha et al., 2015; E. Lee et al., 2013; Mostafa et al., 2014a; Richard et al., 2004).

In an attempt to decouple the effect of molecular weight and carbon oxidation state on RI quantum yields, Φ_{1O2}, f_{TMP}, and Φ_{OH} for SRFA molecular weight fractions before and after reduction with sodium borohydride were measured (Table 3.1). Previous studies have examined

the effect of borohydride reduction on Φ_{1O2} and f_{TMP} for DOM isolates that have not undergone size fractionation (Golanoski et al., 2012; Sharpless, 2012; Zhang et al., 2012). Similar to Sharpless (2012), we saw no significant change in Φ_{1O2} for bulk SRFA (Sharpless, 2012). However, there was a significant (one-tailed t-test, $\alpha = 5\%$) decrease for SRFA <5K. This result was paralleled by f_{TMP} values except that there was also a significant difference for the >5K fraction. A significant (one-tailed t-test, $\alpha = 5\%$) increase in Φ_{OH} was observed for each molecular weight fraction after borohydride reduction.
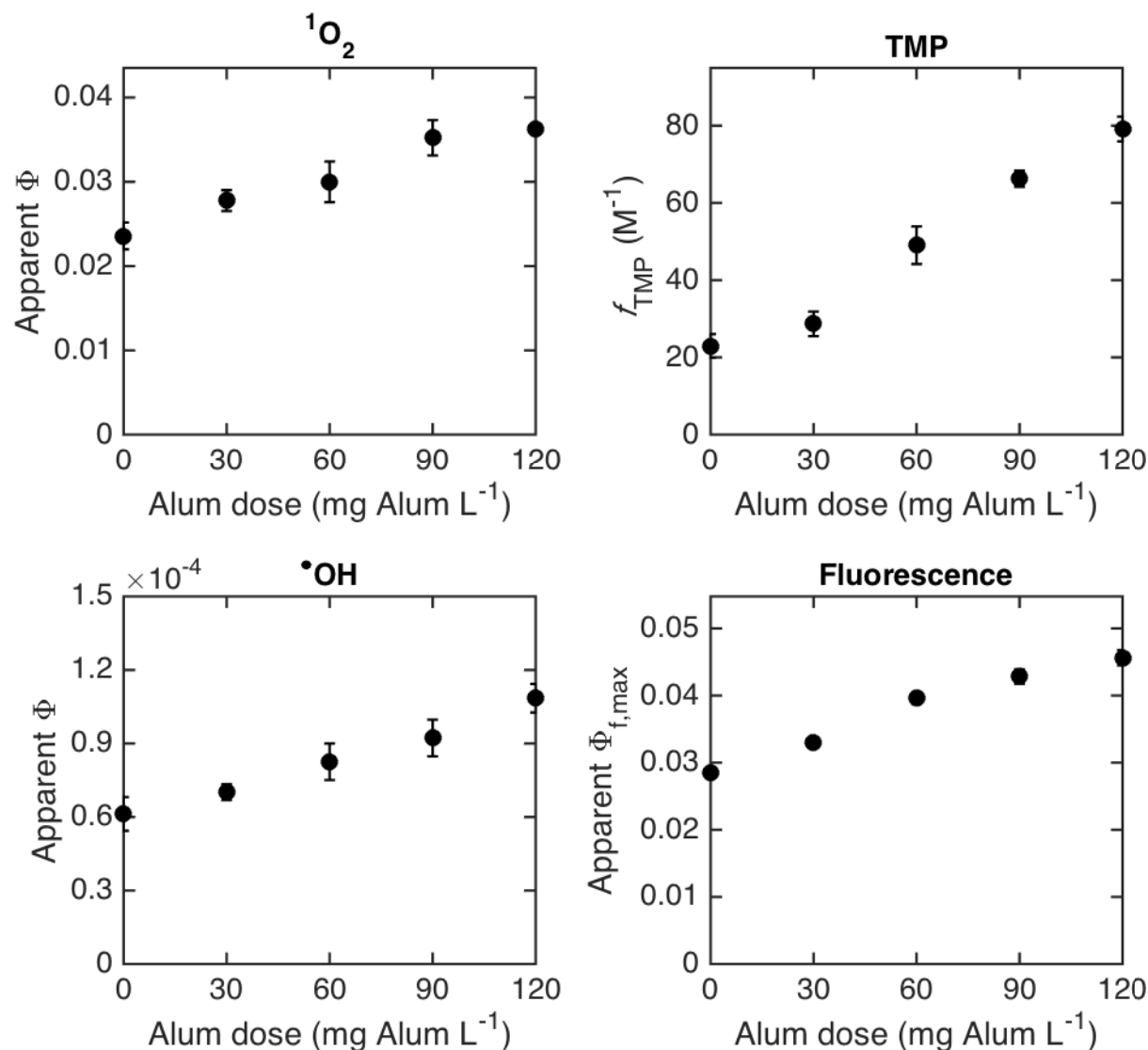
Figure 3.4. Apparent quantum yields for $^1O_2$, $^{\bullet}OH$, fluorescence, and TMP degradation efficiencies for LM wastewater pre- and post-coagulation with Alum. Data points are averages of duplicate runs and error bars represent two standard deviations.

3.5. Discussion

The following discussion seeks to interpret the observed results in light of the different models (i.e. superposition of chromophores, CT) that could be used when studying the photophysics and photochemistry of DOM.

3.5.1 Absorbance and fluorescence spectroscopy.

The presence and preferential relative removal of long wavelength absorption in this study and others seems to provide evidence for the CT model. This is because the types of chromophores necessary for these low-energy transitions (characteristic of very conjugated π systems) are likely nonexistent or exist at low concentrations within DOM. As a result, the transitions are assigned to excitation into CT states, which would also have high extinction coefficients (Del Vecchio and Blough, 2004; Ma et al., 2010; Sharpless and Blough, 2014). This preferential removal of long wavelength absorption was observed for wastewater samples undergoing base modification and coagulation (Figure 3.1) and SRFA following ultrafiltration and borohydride reduction (Figure 3.2). In the CT model, a reasonable quantitative measure for the proportion of CT interactions is the minimum value of fractional absorptivity remaining following borohydride reduction, $f_{a,min}$, which can be defined as

$$f_{a,min} = \left. \frac{\varepsilon_{red}}{\varepsilon_{nat}} \right|_{\lambda_{min}}$$

Equation   3.4

where λ_{min} is defined as

$$\left. \frac{d(\varepsilon_{red}/\varepsilon_{nat})}{d\lambda} \right|_{\lambda_{min}} = 0$$

Equation 3.5

A lesser $f_{a,min}$ indicates more CT removal while a greater $f_{a,min}$ indicates less CT removal. Because of the varying behavior at $\lambda > 450$ nm, a local $f_{a,min}$ was calculated. As shown in Figure 3.2, the effect of reduction was more pronounced in higher molecular weight fractions, exhibited by a decreasing $f_{a,min}$ with increasing molecular weight. Absorbance data were collected with a 5 cm pathlength for this analysis and the absorbance was always greater than the quantitation limit (average of water blank + $10s \simeq 0.0013$) at wavelengths shorter than 700 nm. The reduction

procedure was repeated on a different size-fractionated SRFA solution (Figure A.9) with similar qualitative results. Other potential metrics to quantify CT loss are provided in Appendix A (Table A.3, Figure A.10).

DOM optical properties do not generally depend on concentration, so CT contacts are assumed to be *intramolecular* (Summers et al., 1987); however, the ability of DOM molecules to form these associations based on known DOM molecular weights has not been discussed. An analysis based on SRFA molecular weight and ^{13}C-NMR estimation of functional groups is presented in 8. This analysis indicates that for multiple CT contacts to exist in SRFA (based on the number of A groups) esters and carboxylic acids must be able to act as A groups. The prevailing CT model states that only ketone or aldehyde carbonyl groups are acceptors (Sharpless and Blough, 2014). It is thus noteworthy that borohydride is usually not able to reduce esters and carboxylic acids.

The percent change in maximum Φ_f for reduced SRFA increased with increasing molecular weight fraction. This result is consistent with the idea that there are fewer CT interactions in the <5K fraction because [1]DOM* inactivation into CT bands would be in competition with fluorescence. However, one issue that should be noted is that Φ_f values for each fraction are relatively constant with excitation wavelength, especially for excitation wavelengths > 350 nm, before and after borohydride-reduction (see Figure 3.3 contrasted to (Ma et al., 2010)). It would thus seem that DOM fluorescence is obeying Kasha's rule (Φ_f independent of excitation wavelength), in contrast to that described by the CT model (Del Vecchio and Blough, 2004). While excitation into CT bands and subsequent charge-recombination-induced luminescence can occur at these longer excitation wavelengths, it is unlikely that the process would occur with similar efficiency as fluorescence at shorter wavelengths. This is a subject for future research.

As noted above, the explanation put forth by Boyle et al. (2009) (Boyle et al., 2009) that fewer and less varied CT interactions are possible in low molecular weight DOM is conceptually sound but lacks experimental support. The $f_{a,min}$ values and percent increase in maximum Φ_f (see Table A.3 for values) following borohydride reduction of the SRFA molecular weight fractions reported here strongly support this conclusion.

3.5.2   Change in RI quantum yields following physicochemical treatments.

The trend of increasing Φ_{1O2}, f_{TMP}, and Φ_{OH} with decreasing molecular weight is consistent with other reports in the literature (Dalrymple et al., 2010; E. Lee et al., 2013; Mostafa et al., 2014a; Mostafa and Rosario-Ortiz, 2013; Richard et al., 2004). This study shows for the first time that these effects occur following two commonly used water treatment processes – base modification (to mimic lime softening) and coagulation. Based on the consistent increase in SEC retention time and increase in E2/E3 values following these treatments, it is thought that the physical basis for the increase in RI quantum yields observed here is strongly linked to decreases in molecular weight. However, we note that in the case of coagulation with alum, the potential effect of Al-DOM complexes on the photophysics and photochemistry cannot be ruled out (although the residual Al concentrations were < 0.03 mg/L, see Table A.1). Additional discussion is provided in Appendix A.

The experiments involving reduction of SRFA size fractions represent an attempt to decouple the effects of molecular weight and CT interactions on DOM's optical and photochemical properties. There are two important results from photochemical studies of these samples: (i) that Φ_{1O2} decreased following borohydride reduction only for SRFA < 5K and (ii) that Φ_{OH} increased following borohydride reduction for all molecular weight fractions. Under the CT model, D and A groups can form CT interactions in either the ground or excited electronic

state, which would lessen the ability of these moieties to act independently. Similar to the model of Blough and Sharpless (Dalrymple et al., 2010; Del Vecchio and Blough, 2004; Sharpless, 2012; Sharpless et al., 2014) we propose that three distinct pools of chromophores best describe the photophysics and photochemistry of DOM: D groups, A groups, and CT groups. D and A groups can exist in close proximity within DOM molecules, but have the ability to absorb light and lead to (productive) photochemical reactions. CT groups are those coupled D and A groups that have either ground or excited state CT character and their excitation does not lead to photochemical reactions that generate RI. CT character is defined as the contribution of the no-CT-state and CT-state wavefunctions to the ground and excited state complexes (see 8 for additional discussion) (Mulliken, 1952).

Considering the results for Φ_{1O2}, fewer potential CT interactions as the result of decreased molecular weight or reduction would decrease the rate of Equation 3.6 and Equation 3.7 and increase the rate of Equation 3.8 through Equation 3.10.

$$^1(D + A) + h\nu \rightarrow {}^1(D^+ / A^-) \qquad \text{direct excitation into CT states} \qquad \text{Equation 3.6}$$

$$^1(D^* + A) \rightarrow {}^1(D^+ / A^-) \qquad \text{decay into CT states} \qquad \text{Equation 3.7}$$

$$^1(D + A) + h\nu \rightarrow {}^1(D^* + A) \qquad \text{excitation of local donors} \qquad \text{Equation 3.8}$$

$$^1(D^* + A) \rightarrow {}^1(D + A^*) \qquad \text{energy transfer between D and A} \qquad \text{Equation 3.9}$$

$$^1(D + A^*) \rightarrow {}^3(D + A^*) + O_2 \quad \rightarrow {}^1O_2$$

$$\text{intersystem crossing and quenching by } O_2 \quad \text{Equation 3.10}$$
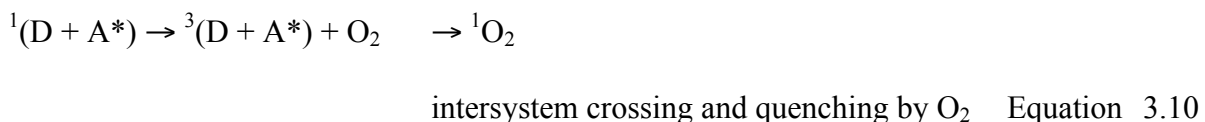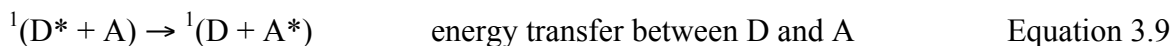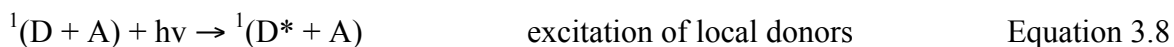
A possible explanation for the decrease in Φ_{1O2} and f_{TMP} for the <5K fraction after reduction is derived from the result that lower molecular weight DOM has, on average, a fewer number of CT interactions. With this in mind, a reasonable hypothesis is that any non-reduced A groups are less conformationally able to couple to D groups either in the ground or excited state, decreasing

the proportion of light absorbed by CT groups in the reduced < 5K sample. Another possibility, though also speculative, is that reduction of ketones and aldehydes to alcohols via borohydride increases the ability of $^1O_2$ to diffuse from the hydrophobic DOM core, which would result in a greater observed Φ_{1O2} (as measured by the aqueous-phase probe compound FFA) (Latch and McNeill, 2006). This change in three-dimensional configuration could occur, for example, due to increased hydrogen bonding between water and newly formed hydroxyl groups.

It is interesting that borohydride reduction increases Φ_{OH} regardless of molecular weight fraction. That the behavior of $^\bullet OH$ is distinct from that of $^1O_2$ and $^3DOM^*$ following borohydride reduction is similar to behavior observed for the quenching of these RI by halides (Glover and Rosario-Ortiz, 2013). In this instance, Φ_{OH} increased with increased halide concentrations, whereas Φ_{1O2} and f_{TMP} decreased, indicating different precursors. In addition, the consistent increase in Φ_{OH} suggests that reduction of O_2 or H_2O_2 by CT states ($DOM^{\bullet+/\bullet-} + O_2/H_2O_2 \rightarrow {}^\bullet OH$) is an insignificant source of $^\bullet OH$ (Sharpless and Blough, 2014). A likely reason for this observation is that hydroxyaromatic acids (potential D groups) are significant sources of free $^\bullet OH$, as was recently reported (Sun et al., 2015). Reduction of carbonyl-containing A groups would allow D groups, which are not reducible by borohydride, to be excited into local excited states as opposed to CT bands, increasing the rate of $^1(^*D + A)$ formation. Furthermore, the correlation between Φ_f and Φ_{OH} (Figure 3.5) suggests that either $^1DOM^*$ is a precursor to $^\bullet OH$ or that its deactivation into CT states is in competition with decay into $^\bullet OH$ precursors, for example, DOM radicals (Equation 3.11 through Equation 3.14).

$$^1DOM^* \rightarrow R^\bullet + DOM^\bullet \qquad\qquad \text{Equation 3.11}$$

$$^1DOM^* \rightarrow {}^3DOM^* \rightarrow R^\bullet + DOM^\bullet \qquad\qquad \text{Equation 3.12}$$

$$R^\bullet \rightarrow\rightarrow {}^\bullet OH \qquad\qquad \text{Equation 3.13}$$
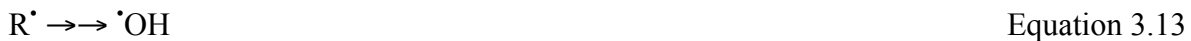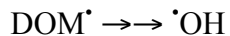
$$DOM^{\bullet} \rightarrow\rightarrow {}^{\bullet}OH \qquad\qquad\qquad \text{Equation 3.14}$$
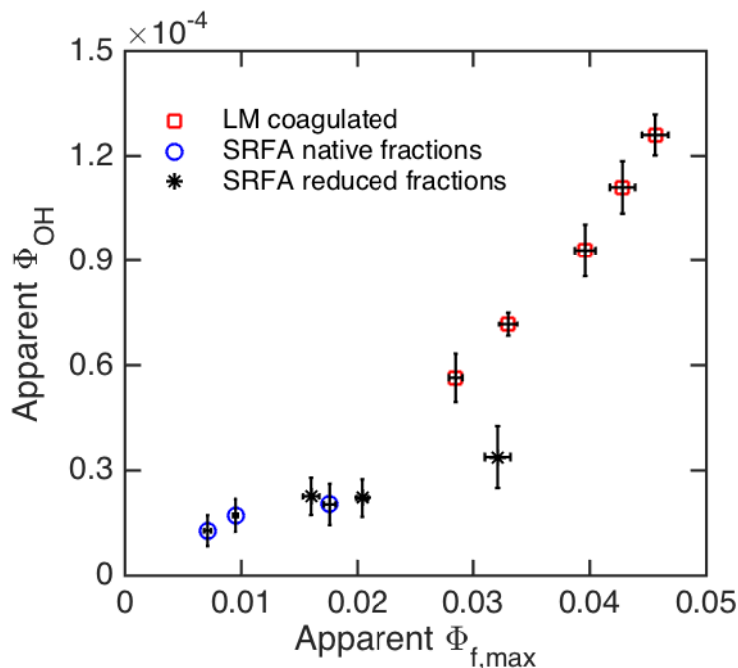
Figure 3.5. Correlation between ${}^{\bullet}OH$ and maximum fluorescence quantum yields. Data are a combination of SRFA molecular weight fractions before and after reduction with borohydride and LM wastewater at each coagulation dose. See Table 1 for max fluorescence quantum yields and the wavelengths at which they occur.

Excitation into CT bands would also compete with photoionization and subsequent reaction of $DOM^{\bullet+}$ with water, a potential (although speculative) source of ${}^{\bullet}OH$ (Equation 3.15 through Equation 3.17).

$$DOM + h\nu \rightarrow DOM^{+\bullet} + e^- \qquad\qquad\qquad \text{Equation 3.15}$$

$$DOM^{+\bullet} + H_2O \rightarrow [DOM\text{--}OH_2]^{+\bullet} \qquad\qquad\qquad \text{Equation 3.16}$$

$$[DOM\text{--}OH_2]^{+\bullet} \rightarrow DOM + H^+ + {}^{\bullet}OH \qquad\qquad\qquad \text{Equation 3.17}$$

Reduction of A groups by borohydride would decrease the rate of reaction 6 and thus increase the rate of Equation 3.15 through Equation 3.17. ${}^1DOM^*$ is not directly responsible for ${}^{\bullet}OH$ production as its lifetime is too short (Turro et al., 2012). Therefore, it seems that that a dominant control on Φ_{OH} is the ability of D groups to act as independent chromophores. Additional

evidence for involvement of DOM radicals and radical cations comes from the fact that apparent activation energies for $^{\bullet}$OH production from DOM photolysis are on the order of $\sim$ 15 to 30 kJ mol^{-1} (McKay and Rosario-Ortiz, 2015), which are typical of radical reactions (Buxton et al., 1988). Importantly, the results presented in Figure 3.4 and Table 3.1 demonstrate that decreasing molecular weight and chemical reduction work in concert to produce greater Φ_{OH}.

3.6. Environmental Implications

The results presented here have significant consequences on the photochemical processes occurring in natural and engineered aquatic systems. This is clearly demonstrated by the increase in Φ_{1O2}, f_{TMP}, and Φ_{OH} after applying two commonly used water treatment technologies (base modification to mimic lime softening and coagulation). Receiving water bodies heavily impacted by wastewater undergoing these treatment processes could expect greater RI steady state concentrations and potentially increased contaminant removal, although other factors such as changes in light absorption and scavenging of RI by DOM would need to be considered.

Another finding of this research is that the correlations between RI quantum yields and E2/E3 (Figure A.11) may be more sample specific than previously demonstrated (Dalrymple et al., 2010; Mostafa and Rosario-Ortiz, 2013; Peterson et al., 2012; Sharpless et al., 2014). Other studies have reached this conclusion. In particular, Sharpless et al. (2014) observed different dependencies (slopes) between Φ_{1O2} and E2/E3 for photo-oxidized humic substances of varying origin (Sharpless et al., 2014) compared to previous reports (Dalrymple et al., 2010; Mostafa and Rosario-Ortiz, 2013; Peterson et al., 2012). An earlier study by Peterson et al. (2012) showed that this same relationship for water samples collected over a multi-year timeframe from Lake Superior was weaker than that observed by Dalrymple et al. (2010) (again, in terms of the linear regression slope) (Peterson et al., 2012). One contrasting point, however, is that Mostafa and

Rosario-Ortiz observed a relationship between Φ_{1O2} and E2/E3 for wastewater samples between that of Peterson et al. and Dalrymple et al. (slope of 0.72 vs. 0.61 and 0.87). The correlations between Φ_{1O2} and E2/E3 observed in this study as well as those just mentioned are summarized in Table A.5.

Considering the current study, although physical and chemical treatments applied to these samples caused systematic changes in fluorescence and RI quantum yields that correlated in expected ways with E2/E3, these correlations did not hold across all samples and all treatments, exemplified by Figure A.11and Table A.5. While E2/E3 may be a useful surrogate for assessing DOM molecular weight and predicting RI quantum yields, this relationship is highly specific on the sample type and treatment. An additional aspect relating to our study in the context of water treatment applications is that coagulated or base modified wastewater and borohydride-treated SRFA are not best characterized as natural samples. Of all the RI shown in Figure A.11, Φ_{1O2} correlates the best with E2/E3. Finally, linear regression of Φ_{1O2} to E2/E3 for the samples in our study, besides reduced SRFA (which could be considered the least natural sample) yields a relationship of Φ_{1O2} (%) = 1.59×E2/E3 – 5.29 (R^2 = 0.733, slope p < 0.0001, intercept p < 0.01).

4. The Case Against Charge Transfer Interactions in Dissolved Organic Matter Photophysics

4.1. Abstract

The optical properties of dissolved organic matter influence chemical and biological processes in all aquatic ecosystems. Organic matter optical properties have been attributed to a charge-transfer model in which donor-acceptor complexes play a primary role. This model was evaluated by measuring the absorbance and fluorescence response of organic matter isolates to perturbations in solvent temperature, viscosity, and polarity, which affect the position and intensity of spectra for known donor-acceptor complexes of organic molecules. Absorbance and fluorescence spectral shape were unaffected by these perturbations, indicating that the distribution of absorbing and emitting species was unchanged. These results call into question the wide applicability of the charge-transfer model for explaining organic matter optical properties and suggest that future research should explore other models for organic matter photophysics.

4.2. Introduction

Organic matter, the complex mixture of organic compounds present in terrestrial and aquatic ecosystems, is an active component of the global carbon cycle (Cory et al., 2014; Opsahl and Benner, 1997). Organic matter in aquatic systems is derived from allochthonous sources, such as the leaching of plant material and soil organic matter, as well as autochthonous sources, such as microbial exudates and other cellular components (Thurman, 1985) Dissolved organic matter (DOM), constitutes the fraction of organic matter dissolved in aquatic systems and is ubiquitous in inland and marine waters.(Thurman, 1985) The variety of organic matter sources and

environmental transformation mechanisms results in a diverse collection of chemical functionalities that consequently play significant roles in aquatic systems. The importance of DOM has led to the development of a suite of characterization methods to understand both its chemistry and function in the environment (Aiken et al., 1992; Chin et al., 1994; McKnight et al., 2001; Ritchie and Perdue, 2003; Stenson et al., 2003). DOM also has important public health implications due to the formation of toxic disinfection byproducts in drinking water (Rook, 1977).

Chromophoric DOM (CDOM) is the light-absorbing fraction of DOM and is the main absorber of sunlight in aquatic systems (Bricaud et al., 1981; Ghassemi and Christman, 1968; Zepp and Cline, 1977), thus influencing the dynamics of photosynthetic organisms in these environments. An abundance of evidence suggests that aromatic, phenolic, and carbonyl-containing groups are the main chromophoric units in CDOM (Sharpless and Blough, 2014). CDOM absorbance spectra are characterized by an exponential decrease in absorbance with increasing wavelength. CDOM fluorescence is characterized by significant Stokes shifts and relatively small fluorescence quantum yields (Φ_f) that exhibit a maximum Φ_f of approximately 1-3% at an excitation wavelength (λ_{ex}) of ~350 nm and decrease monotonically with increasing λ_{ex} (Del Vecchio and Blough, 2004). CDOM absorbance and fluorescence have been used remotely, *in situ*, and in whole water samples to track organic matter concentration, composition, and dynamics at varying spatial and temporal scales (Brezonik et al., 2015; Coble et al., 1990; Peterson et al., 2012). In addition, CDOM photophysical properties influence many processes in aquatic photochemistry, including the fate of environmental contaminants (Vione et al., 2014) and the oxidation and mineralization of organic matter (Cory et al., 2014).

Despite its importance, the photophysics of CDOM optical properties is not fully understood, due in part to the complexity of CDOM and its structural variability. Two models have been applied to CDOM. The first states that observed CDOM optical properties are a superposition of non-interacting chromophores ($a(\lambda) = \sum_{i=1}^{N} a_i(\lambda)$; where a_i is absorbance). Alternatively, an interaction model has been proposed in which electron rich donors (D) associate with electron poor acceptors (A) to form complexes capable of undergoing charge-transfer excitation (D + A $\rightleftharpoons$ DA + hν $\rightarrow$ [D$^+$A$^-$]*).(Del Vecchio and Blough, 2004; Sharpless and Blough, 2014) This model states that CDOM optical properties include contributions from individual chromophores in addition to DA complexes ($a(\lambda) = \sum_{i=1}^{N} a_i(\lambda) + \sum_{i}^{N} \sum_{j \neq i}^{N} a_{i,j}(\lambda)$ where $a_{i,j}$ refers to absorbance due to interacting chromophores).

Many studies have adopted the charge-transfer (CT) model as a broad framework for interpreting CDOM optical properties and photochemistry in aquatic systems (Dalrymple et al., 2010; Maizel and Remucal, 2017; Sharpless et al., 2014; Sharpless and Blough, 2014). The CT model has also been applied to organic matter sources other than aquatic CDOM, including soil (Sharpless et al., 2014) and atmospheric (Phillips and Smith, 2014) systems. The humic and fulvic acid fractions of soil organic matter are typically more aromatic and higher in molecular weight than their aquatic counterparts, which according to the CT model, explains their more intense color. Recent studies of atmospheric systems containing so-called brown carbon, a mixture of compounds resulting from biomass burning that has important implications in radiative forcing, have suggested that CT interactions may play a role (Laskin et al., 2015; Lin et al., 2016; Phillips and Smith, 2014). Some atmospheric studies have drawn verbatim from the CT model developed for aquatic CDOM, arguing that brown carbon optical properties are

completely explained by CT interactions (Phillips et al., 2017; Phillips and Smith, 2015; 2014). Taken together, it is not well understood whether the similarities in optical properties observed between these different pools of organic matter can be explained by the CT model or by the superposition model, especially because of the known differences in structure between aquatic CDOM and these other organic matter sources.

4.3. Testing the Working CT Model

Some of the key aspects of the CT model are shown in Figure 1. There are three possible arrangements of D and A groups that show CT behavior. First, D and A groups may be independent molecules that associate to form a ground state intermolecular DA complex with a characteristic CT absorbance (Figure 4.1). Examples of this type include complexes between acceptors, such as electron-poor quinones (e.g., chloranil) or alkenes (e.g., tetracyanoethylene), and electron-rich aromatics (e.g., hexamethylbenzene) or amines (Rathore et al., 1997). Second, D and A groups may be tethered, but are otherwise electronically independent, non-conjugated moieties, such as in naphthalene-pyridinium or porphyrin-quinone systems (Figure 4.1b) (Le et al., 2000; Mori and Inoue, 2005; Siemiarczuk et al., 1983). These groups could form intramolecular DA complexes that exist in equilibrium with their respective D and A groups. Finally, the D and A moieties may be linked as interacting, conjugated groups, such as *p*-cyano-*N,N*-dialkylanilines (Grabowski et al., 2003) or pyridinium *N*-phenolate betaine dyes (Figure 4.1c) (Machado et al., 2014). Fluorescence can occur from each of these CT excited states, which could form as a result of excited state electron or proton transfer from a local excited (LE) state D or A moiety.

Each of these arrangements has an expected sensitivity to solvent conditions, including temperature, solvent polarity, and solvent viscosity, which can be used to test for the presence of

53

these complexes. In fact, a common test for the presence of CT states is the role of solvent

polarity on the observed position and intensity of spectral transitions.(Foster, 1969)

Figure 4.1. Scheme depicting the possible photophysical processes of CDOM, including local excited (LE) states and charge-transfer (CT) interactions and the expected effects of temperature, solvent polarity, and viscosity on CDOM absorption (a-c) and fluorescence (d-f). Scenarios are depicted for independent D and A molecules (a, d), covalently tethered D and A (b, e) and conjugated D and A moieties (c, f). Only some of the critical dependencies are indicated. For example, the wavelength of fluorescence ($h\nu_{F,CT}$) is dependent on solvent viscosity due to dipole reorientation effects.(Lakowicz, 1999) Note also that temperature also perturbs solvent viscosity and solvent polarity and is thus expected to have effects beyond DA complex equilibrium position.

To investigate the CT model for CDOM photophysics, a diverse set of organic matter

isolates was examined, including isolates from soil (ESHA, PPHA, PPFA), terrestrial aquatic

(SRFA, NRFA, SRHA, SRNOM, MRNOM, NRNOM, YHPOA), and microbial/marine (PLFA, GMHPOA, POFA) sources. (Appendix B provides additional details on sources and isolation procedures.) With respect to the soil isolates, we note that it is common practice to extract soil organic matter into aqueous solution to characterize its optical properties using similar approaches as aquatic organic matter. Optical properties (absorbance and fluorescence spectra; fluorescence quantum yields) were measured as a function of temperature (-10–70 °C), solvent viscosity (0.38–1.31 cP), and solvent polarity (dielectric constant, 8–80). This paper compares the results obtained following these perturbations with the hypotheses shown in Figure 4.1 developed for well-defined DA complexes of organic molecules (Foster, 1969), thus providing a direct assessment of the CT model's ability to explain CDOM optical properties.

4.4. Materials and Methods

4.4.1 Experimental Matrix.

Thirteen DOM isolates were studied (see Table B.2 for a list of sample names and sources). Absorbance spectra of all isolates were measured on a Cary Bio 100 UV-VIS spectrophotometer (Agilent). Fluorescence spectra were measured for all thirteen isolates using an Aqualog spectrofluorometer (Horiba Scientific) in H_2O, ACN, and THF. Temperature-dependent absorbance and fluorescence spectra were measured on a subset ($n=10$) of these samples using a Fluoromax-4 spectrofluorometer (Horiba Scientific), and absorbance and fluorescence spectra at varying temperature/glycerol combinations were measured on a subset ($n=4$) of these samples on the Fluoromax-4.

4.4.2 Preparation of solutions.

Aqueous stock solutions (~ 100-300 mg isolate L^{-1}) were prepared by dissolving isolates in lab grade water and adjusting to pH 7.0 using 0.1 M NaOH. Samples were maintained at this pH for two days, after which they were filtered through 0.7 µm glass fiber filters (muffled at 500 ºC for 4 hr). These stocks were used to prepare dilute solutions in H_2O, ACN, and THF for absorbance and fluorescence measurements. For aqueous solutions, a target concentration of ~ 4 mg_C L^{-1} was used. For organic solvent-based solutions, a standard dilution factor was applied across all isolates (%v/v = 95/5 organic/water). Spectroscopic grade glycerol was used to alter the viscosity during some experiments; the exact volume percent of glycerol was determined using its density. All solutions were well mixed prior to analysis. For temperature-dependent studies, samples were prepared in 10 mM phosphate buffer at pH 7.2. Control experiments indicated no difference in absorbance or fluorescence spectra between buffered and unbuffered solutions. Once prepared, samples were stored in muffled, amber glass bottles at 4°C.

Dissolved organic carbon (DOC) concentrations of stock solutions (diluted from ~ 100-300 mg L^{-1} to ~ 1-4 mg_C L^{-1}) and aqueous dilutions were measured using a total organic carbon analyzer (M5310C, Sievers) that utilizes UV-persulfate oxidation. Potassium hydrogen phthalate was used as a QA/QC standard. DOC concentrations measured on the aqueous dilutions were used to calculate molar extinction coefficients for these samples on a molar carbon basis, whereas molar extinction coefficients for organic solvent-based measurements were calculated using DOC concentrations determined for stock solutions and known dilution factor.

4.4.3 Data collection and processing.

Absorbance spectra were collected on a Cary-100 Bio UV-Vis spectrophotometer from 800-200 nm and baseline corrected to the appropriate solvent. Fluorescence spectra were collected on

the Fluoromax-4 spectrofluorometer at excitation wavelengths from 240-550 nm. Emission intensity was collected from 300-800 nm using a 0.25 s integration time and a 5 nm bandpass for both excitation and emission monochromators. Fluorescence spectra were collected on the Aqualog spectrofluorometer at excitation wavelengths from 240-600 nm and a bandpass of 5 nm. Emission intensity for this instrument was collected using a charge-coupled device (CCD) at 4.64 nm/pixel leading to an emission scan range of 245 to 824 nm. Integration times varied depending on sample but did not exceed 10 s. Fluorescence intensity for both instruments was collected in signal over reference (S/R) mode. Fluorescence data were corrected according to published methods incorporating instrument-specific correction factors, blank subtraction, inner filter correction and Raman normalization (Murphy et al., 2010). Table B.3 provides a comparison of the Fluoromax-4 and Aqualog instruments.

Absorbance spectra were collected in triplicate and fluorescence spectra were collected in either duplicate or triplicate. Although the Aqualog measures absorbance and fluorescence spectra simultaneously, the Aqualog absorbance data were not used due to unacceptable coefficients of variance (>10%) and consequently large propagated errors in Φ_f at longer excitation wavelengths.

E2/E3, $S_{300-600}$, S_R, and FI were calculated as previously described (McKnight et al., 2001; Peuravuori and Pihlaja, 1997; Twardowski et al., 2004). Fluorescence quantum yields were calculated as previously described (Cawley et al., 2015) with some modifications that are explained in Appendix B.
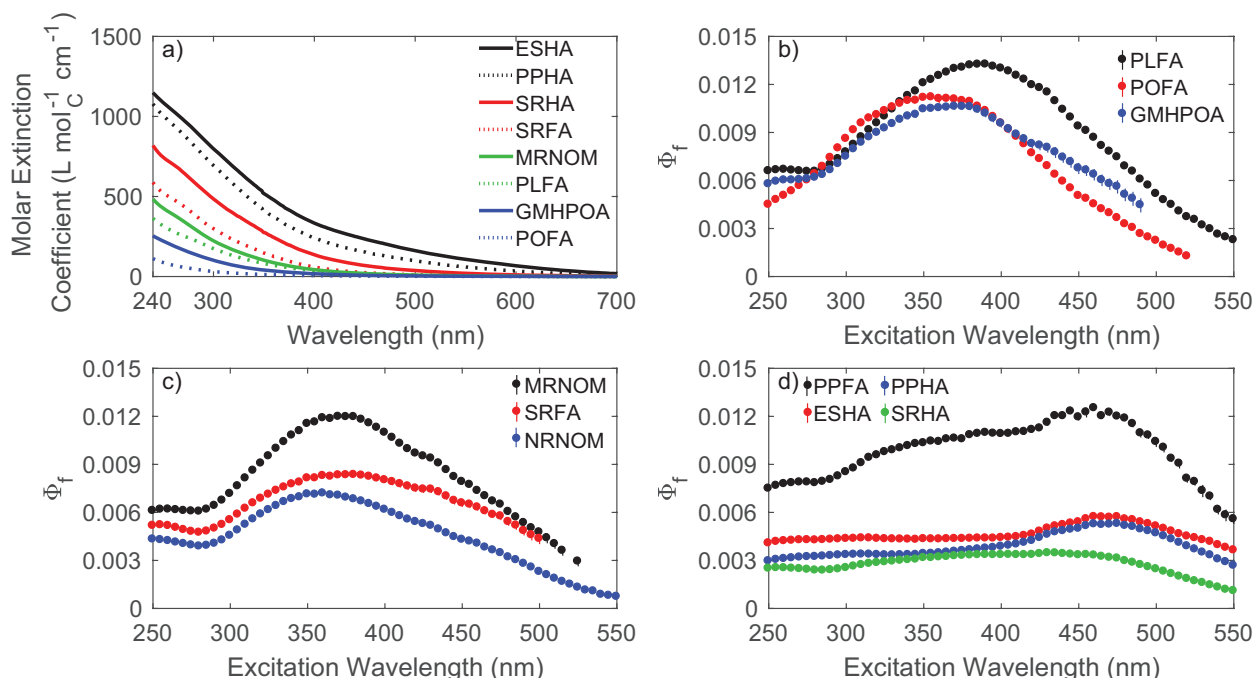
Figure 4.2. Optical properties of organic matter isolates in aqueous solution. a) Absorbance spectra normalized to carbon concentration and b) – d) fluorescence quantum yields for organic matter isolates for PLFA, POFA, GMHPOA (microbial/marine aquatic), SRHA, SRFA, MRNOM, NRNOM (terrestrial aquatic) and ESHA, PPHA, PPFA (soil).

4.5. Results and Discussion

4.5.1 Absorbance of CDOM

Figure 4.2a presents absorbance spectra of select organic matter isolates in aqueous solution. Spectra exhibited an exponential decrease in absorbance with increasing wavelength, as has been observed universally for CDOM (Ghassemi and Christman, 1968). Marine and microbial-derived isolates (i.e., GMHPOA, POFA and PLFA) had lower molar extinction coefficients than terrestrial aquatic and soil isolates. Table 4.1 summarizes compositional metrics that have been used as surrogates of organic matter molecular weight, aromaticity and genesis. Specific ultraviolet absorbance at 254 nm (SUVA$_{254}$), a widely used parameter correlated to aromatic carbon content, spanned a large range for aquatic samples (0.7 to 4.8 L mg$_C^{-1}$ m^{-1}) (Weishaar et al., 2003). Spectral slope (S$_{300-600}$) and the E2/E3 ratio, two surrogates inversely proportional to

organic matter molecular weight, were greater for marine- and microbial-derived isolates compared to soil and terrestrial aquatic isolates (Twardowski et al., 2004). YHPOA, a terrestrial isolate, was an exception and exhibited high E2/E3 and $S_{300-600}$, and low $SUVA_{254}$ values. This sample was isolated from the Yukon River (Alaska, USA) during winter and was reported to be enriched in carboxyl-rich aliphatic moieties, depleted in lignin phenols, and more indicative of microbial-derived organic matter (Cao et al., 2016). As a whole, this data set represents the wide range of properties in the studied organic matter isolates.

Table 4.1. Optical properties for samples in aqueous solution[a].

Isolate	Origin	$SUVA_{254}$[a] $(L\ mg_C^{-1}\ m^{-1})$	E2/E3[b]	$S_{300-600}$[c] (nm^{-1})	FI[d]	$\Phi_f \times 100$ at $\lambda_{ex} = 370$ nm	Max $\Phi_f \times 100$	λ_{ex} at max Φ_f
GMHPOA	Marine/ Microbial	1.7	7.0	0.0173	1.43	1.00	1.00	370
POFA		0.7	8.7	0.0161	1.54	1.00	1.00	355
PLFA		2.5	4.9	0.0155	1.58	1.20	1.20	390
MRNOM	Terrestrial Aquatic	3.4	5.4	0.0161	1.45	1.10	1.10	370
NRNOM		4.2	4.7	0.0149	1.44	0.70	0.70	360
SRNOM		3.0	4.7	0.0147	1.42	0.90	0.90	380
NRFA		4.9	4.2	0.0151	1.23	0.60	0.60	435
SRFA		4.2	4.5	0.0152	1.29	0.80	0.80	380
YHPOA		2.6	7.1	0.0186	1.53	2.00	2.10	380
SRHA		3.8	3.5	0.0130	1.09	0.30	0.30	430
ESHA	Soil	8.9[e]	2.4	0.0075	0.65	0.40	0.50	460
PPFA		6.3[e]	4.3	0.0134	1.06	1.00	1.20	460
PPHA		8.3[e]	2.9	0.0098	0.74	0.30	0.50	475

[a]Measurement uncertainty not shown for clarity. Coefficient of variations for all parameters were less than 5%, and values are included in Table B.4. [a]$SUVA_{254}$ is calculated as $Abs_{254}/[DOC]*100$; [b]E2/E3 is calculated as Abs_{250}/Abs_{365}; [c]$S_{300-600}$ (nm^{-1}) is calculated by a non-linear least squares fit to $Abs(\lambda) = Abs_0 \times \exp(-S(\lambda - \lambda_0))$; [d]FI is the ratio of emission intensity at 470 to 520 nm at an excitation of 370 nm; [e]$SUVA_{254}$ values > 6 L mg_C^{-1} m^{-1} should be interpreted with care due to the known interference of iron (Poulin et al., 2014)

The CT model posits that DA complex excitation begins to dominate at $\lambda_{ex} \approx 375$ nm, resulting in the formation of an excited CT state, $[D^+A^-]^*$, of lower energy than $^1D^*A$ (Boyle et al., 2009). The exponential decrease in absorbance with increasing wavelength would thus suggest that potential DA complexes that are excited to lower energy CT excited states have lower molar extinction coefficients than species absorbing at shorter wavelengths. The exact nature of potential DA complexes has not been firmly defined, but previous studies suggest that

covalently tethered D and A moieties (Figure 4.1b) are most likely (Del Vecchio and Blough, 2004).

In this study, no changes in absorbance spectral shape or intensity were observed at different temperatures (10-40 °C) or solvent viscosities (0.38-1.31 cP), while minor changes (primarily at λ_{ex} < 375 nm) were observed between spectra in H_2O, ACN, and THF (Figure B.2, Figure B.6, Figure B.8, and Figure B.9), indicating that the dynamics of potential DA complexes are unchanged over these conditions.

These results are striking in that the concentration of DA complexes giving rise to CT absorbance (Abs_{DA}), formed either from independent D and A molecules or covalently tethered D and A moieties (Figure 4.1a and Figure 4.1b, respectively), is determined by an equilibrium constant (D + A $\rightleftharpoons$ DA, K_{DA}), which is expected to be temperature-dependent as described by the van't Hoff equation. For example, an approximately 25% increase in Abs_{DA} is expected for a complex with a formation enthalpy (ΔH_{DA}) of -2 kcal mol^{-1} for a temperature decrease from 35 to 10 °C (see Appendix B) (Foster, 1969). This example ΔH_{DA} value is similar to the value for p-benzoquinone and benzene measured in heptane (-1.8 kcal mol^{-1}) (Kuboyama and Nagakura, 1955). Thus, the lack of temperature-dependence in absorbance spectra at long wavelengths suggests that DA complexes are not significant contributors to CDOM absorbance. Conjugated DA chromophores remain a possibility (Figure 4.1c) but are also unlikely due to the lack of significant solvatochromism observed in CDOM absorbance spectra. Solvatochromic shifts occur widely in CT absorbance spectra of well-defined organic DA complexes due to the large change in molecular dipole moment between ground and excited states (Foster, 1969). If the dipole decreases upon excitation, a blue shift is expected with increasing solvent polarity (hypsochromic), whereas a red shift is expected if the dipole increases upon excitation

(bathochromic). In effect, these absorbance data suggest that the DA complexes shown in Figure 4.1a-c are not major contributors to long wavelength absorbance. There is another explanation, in which all of the hypsochromic shifts are exactly balanced by bathochromic shifts of the same intensity. We reject this latter possibility as it seems unlikely to occur across all three solvents and thirteen organic matter isolates investigated.

4.5.2   Fluorescence of CDOM.

Maximum Φ_f values spanned almost an order of magnitude for the different isolates (Figure 4.2b-d, $\Phi_f = 0.0030\text{-}0.021$ at $\lambda_{ex} = 370$ nm). All aquatic isolates exhibited an increase in Φ_f with increasing λ_{ex} up to a maximum value of ~370 nm, followed by a decrease with increasing λ_{ex}. This behavior has been used as evidence in favor of the CT model (Del Vecchio and Blough, 2004). Φ_f values for soil isolates (ESHA, PPHA) and one aquatic isolate (SRHA) were largely independent of λ_{ex} up to ~480 nm, followed by a monotonic decrease with increasing λ_{ex}, notably distinct from aquatic samples. The characteristic dependence of Φ_f on excitation wavelength commonly observed in aquatic organic matter isolates, which has been attributed to the relative contribution of LE state versus CT state fluorescence as λ_{ex} increases to 375 nm, does not apply to soil isolates. Yet, soil isolates exhibit the greatest abundance of long wavelength absorbance, which has also been used as evidence supporting the CT model. These results contradict models that ascribe CT transitions as a significant contributor to the optical properties of soil isolates. Thus, the same line of reasoning used to support the CT model for aquatic samples cannot be applied to soil isolates.

CDOM exhibits large apparent Stokes shifts that decrease with increasing excitation wavelength (Boyle et al., 2009; Del Vecchio and Blough, 2004). In most cases, emission spectra exhibit a behavior in which spectra at longer excitation wavelengths are lower in intensity and

narrower in width, as if fitting inside emission spectra at shorter excitation wavelengths (Figure B.14 and Figure B.15). The CT model rationalizes this observation by suggesting that CDOM fluorescence occurring at emission wavelengths (λ_{em}) > 470 nm results from the charge-recombination-induced luminescence of $[D^+A^-]^*$ and that these states are highly coupled, resulting in a near continuous energy distribution. Reduction of carbonyl moieties in DOM with sodium borohydride has been shown to increase Φ_f values (Ma et al., 2010; McKay et al., 2016), and it has been argued that this is due to either a decrease in excited-state electron transfer or direct excitation into CT states. The relative importance of fluorescence and CT deactivation pathways should be affected by temperature, solvent viscosity, and solvent polarity for independent and covalently tethered DA complexes shown in Figure 4.1d-f. Emission from CT states formed from conjugated DA moieties (Figure 4.1f) would only be affected by solvent polarity. The underlying physics are that the rate of solvent reorientation about the excited state dipole is slower at lower temperatures, which leads to increased emission from the LE state and would manifest as a blue shift in the emission spectrum (Lakowicz, 1999). Solvent polarity similarly influences the energy of the emitting state relative to the ground state. This solvent dependence can be due to general solvent polarizability or fluorophore-specific effects such as the presence of red-emitting CT states (Lakowicz, 1999).

Increasing temperature consistently decreased fluorescence intensity and Φ_f at all λ_{ex} (Figure 4.3), with notable exceptions being soil humic acids (Figure B.3 and Figure B.5). Emission spectral shape did not change as a function of temperature (Figure 4.3), which indicates that the energy distribution of fluorophores is unchanged over the temperature range studied. Fluorescence spectra of select samples were measured at -10 °C and 70 °C in approximately 70% v/v glycerol in water solution and exhibited no difference in spectral shape (Figure B.25).

62

These results call into question the significance of fluorescence from CT excited states. A temperature-dependence would be expected since the rates of DA exciplex formation from LE states and subsequent conversion to lower-lying CT states are temperature-dependent, each with presumably different activation energies. These rates, in part, determine the contribution of each excited state to observed fluorescence at a given emission wavelength. Thus, for emission spectral shape to be invariant with temperature, thermodynamic parameters for these processes would need to be approximately equal, which seems highly improbable given the chemical diversity within a given organic matter isolate.
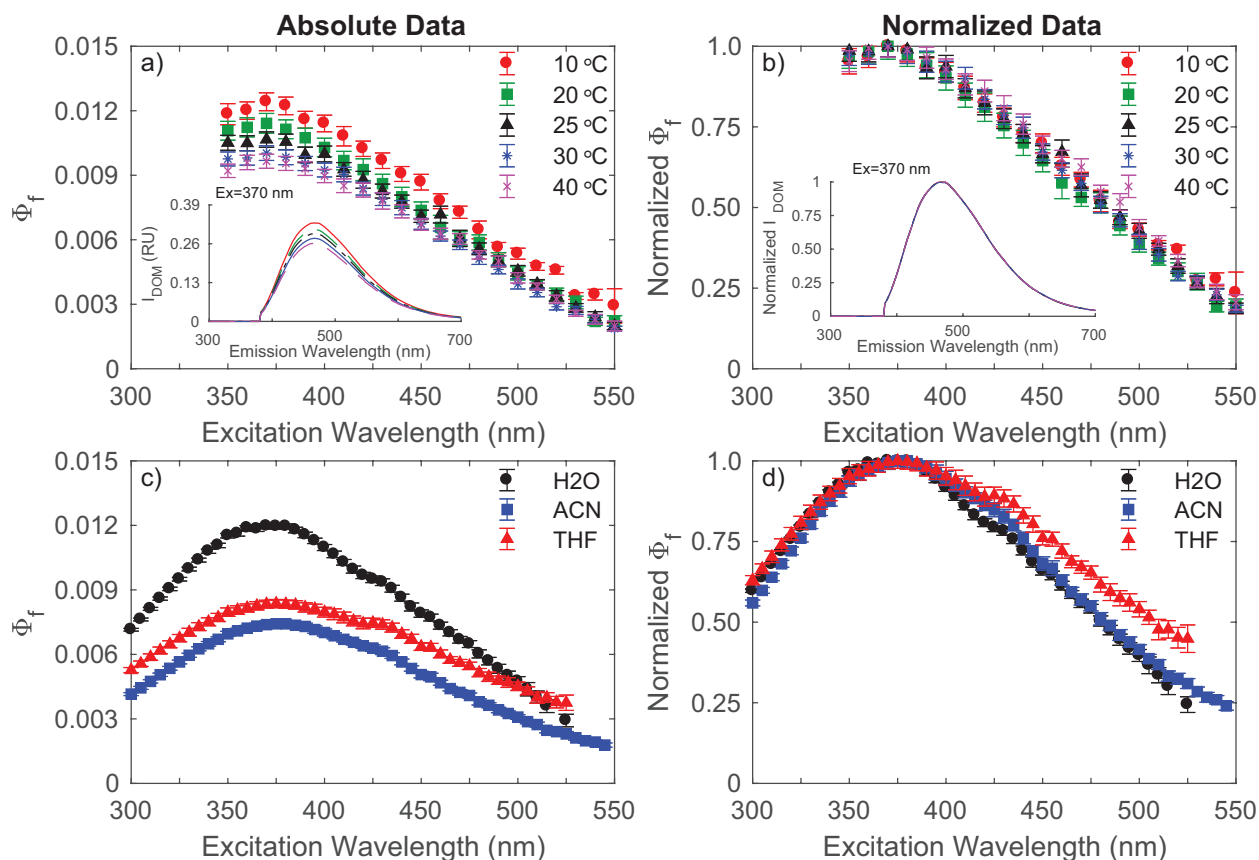
Figure 4.3. Temperature and solvent effects for MRNOM by comparing fluorescence quantum yields as a function of temperature and solvent polarity. a) Φ_f as a function of excitation wavelength over 10-40 °C. Inset: emission spectra at an excitation wavelength of 370 nm. b) Data from a) normalized to maximum value. c) Φ_f as a function of excitation wavelength in H_2O, ACN, and THF. d) Normalized Φ_f data from c).

A change in temperature affects the rate of multiple photophysical processes, including the rate of excited singlet state decay, and in the case of DA complex photophysics, the rate of CT excited state formation from a LE state (Lakowicz, 1999). Temperature also affects the viscosity of the solvent, and thus the rate of solvent reorientation about the excited state dipole. To separate the effects of changing temperature and viscosity, absorbance and fluorescence spectra were measured for a subset of samples at varying water:glycerol ratios and temperatures (Table B.5). There were no significant changes in absorbance spectra over the temperature-solvent combinations studied (Figure B.6). However, we observed a significant decrease in Φ_f

(Table B.6 and Figure B.7) with increasing temperature (10-40 °C; corresponding to a viscosity range of 0.83-1.31 cP) at a constant solvent composition, except for ESHA (Figure B.7). Increased viscosity due to increasing glycerol content (10-30% v/v; corresponding to a viscosity range of 0.83-1.46 cP) at constant temperature did not affect Φ_f (Table B.6). This observation suggests that decreased fluorescence intensity with increasing temperature is due specifically to the effect of temperature on the rate of radiationless decay mechanisms (Birks, 1970) and not the indirect effect of temperature on solvent viscosity.
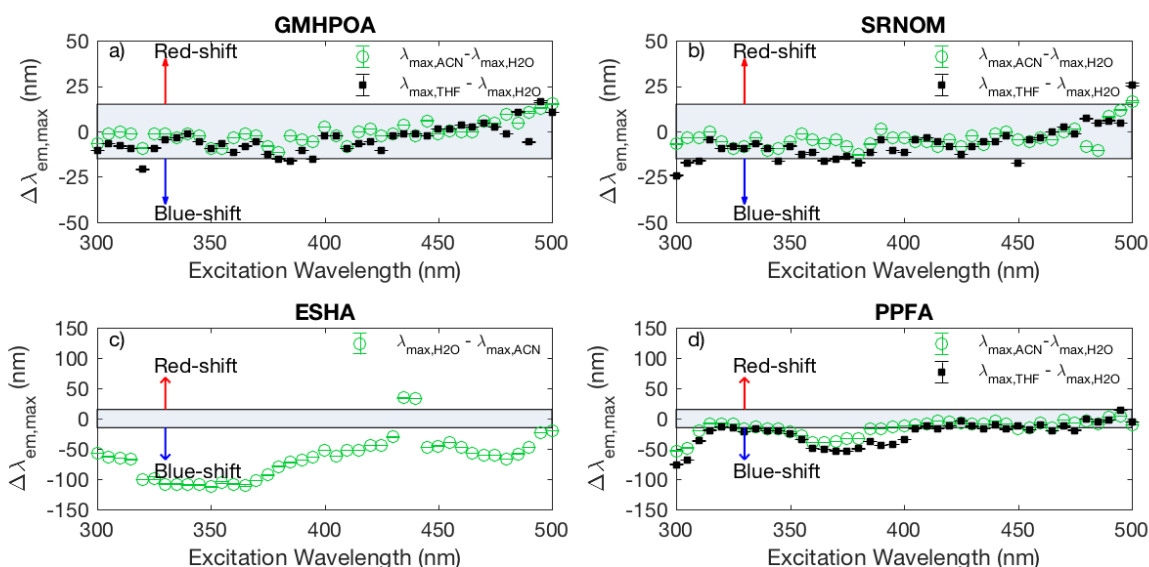
Figure 4.4. Solvatochromic shifts in peak emission wavelength in ACN and THF relative to water fora) GMHPOA, b) SRNOM, c) ESHA, and d) PPFA. ESHA in THF were not evaluated. Data within the gray region (± 15 nm) indicates no significant shift in peak emission wavelength.

To further test the importance of CT excited state emission, fluorescence spectra were measured in ACN and THF. Fluorescence spectra containing contributions from CT emission are expected to be red-shifted (increase in λ_{em}) due to the greater stabilization of the excited state species by high polarity solvents in CT excited states relative to LE states. In contrast to this hypothesis, few samples showed red-shifted emission spectra in H_2O relative to ACN or THF

(Figure 4.4). While low concentrations (5% v/v) of water in an organic solvent can impact fluorescence spectra (Lakowicz, 1999), the lack of change in emission maximum was also evident for SRFA when dissolved directly in THF (Figure B.26), corroborating the results obtained at 95:5% v/v organic solvent to water. Changes in emission maxima were only observed for PPFA, PPHA, and ESHA (all soil isolates) in ACN (Figure 4.4 and Figure B.24). Importantly, SRFA, a terrestrial organic matter isolate that has been used as an exemplar for the CT model (Boyle et al., 2009; Del Vecchio and Blough, 2004; Ma et al., 2010), exhibited no spectral shift at any excitation wavelength across the tested solvents. In the CT model, it is thought that excitation at $\lambda_{ex} > 375$ nm leads to $[D^+A^-]^*$ states, however, the absence of solvatochromism in fluorescence spectra calls into question the presence of these states. It is also noteworthy that soil isolates exhibited solvatochromism at $\lambda_{ex} < 375$ nm, whereas aquatic isolates did not (Figure 4.4c,d vs. a,b). Assuming that these excitations lead to LE states, this result indicates that polar solvents stabilize these states more for soil isolates compared to aquatic organic matter. The only sample that showed systematic solvatochromism in fluorescence spectra at $\lambda_{ex} > 375$ nm was ESHA.

Φ_f for all samples decreased in THF and ACN relative to H_2O (Figure 4.3) at all excitation wavelengths. Although viscosity varies widely between the solvents, this decrease in Φ_f is attributed to solvent polarity based on the minimal change in Φ_f observed by changing solvent viscosity using glycerol. Spectra for the soil isolates PPHA and ESHA in THF showed evidence of light scattering due to particles and were not considered in the analysis. The wavelength-dependence of Φ_f is largely the same in different solvents (Figure 4.3 and Figure B.16 through Figure B.19). The decrease in fluorescence intensity and Φ_f with decreasing solvent polarity is opposite the behavior observed of *intermolecular* CT complexes of organic molecules

(e.g. trimethylbenzene + pyromellitic dianhydride, or 4-(*N,N*)-(dimethylamino)benzonitrile) (Prochorow, 1974; 1973; Prochorow and Bernard, 1974; Prochorow and Siegoczynski, 1969), but consistent with observations of *intramolecular* CT fluorescence (Graff et al., 2016). Regardless, solvatochromism is observed in these inter- and intramolecular CT model systems, which is generally not observed for the organic matter isolates examined in this study.

4.6. Implications for CDOM photophysics

This study questions the validity and wide applicability of the CT model to explain the photophysical properties of CDOM. The presence of CT-derived transitions is not supported in the examined isolates due to the absence of expected changes in absorbance and fluorescence responses as a function of temperature, solvent polarity and viscosity that are characteristic of DA complexes of organic molecules. Although we cannot categorically reject the presence of CT transitions within CDOM, our results suggest that these transitions are not prominent photophysical mechanisms. Rather, this work suggests that organic matter contains unidentified chromophores that absorb and emit at long wavelengths. Identification and characterization of the photophysics and photochemistry of these long wavelength-absorbing chromophores remains a challenge for the years ahead and is necessary if we are to correctly understand how organic matter is photochemically degraded, how it sensitizes the degradation of pollutants, and how the optical properties of natural waters will be altered by changing climate and land use.

5. Temperature-Dependence of Dissolved Organic Matter Fluorescence: Implications for DOM Photophysics

5.1. Abstract

The temperature-dependence of organic matter fluorescence quantum yields (Φ_f) was measured for a diverse set of organic matter isolates (microbial and terrestrial aquatic, soil, and lignite-derived) in aqueous solution in order to determine activation energies (E_a) for radiationless decay processes of the excited singlet state. E_a was calculated from the temperature-dependent Φ_f data measured between 10-40 °C using a simplified photophysical model and the Arrhenius equation All aquatically-derived isolates and one soil-derived fulvic acid isolate exhibited temperature-dependent Φ_f values consistent with a single radiationless decay process dominating over this temperature range, with E_a ranging from 6.02 to 8.35 kJ mol^{-1}. Conversely, soil and lignite-derived humic acid isolates exhibited no temperature-dependence in Φ_f. There was a significant relationship between Φ_f and the rate of radiationless decay derived from the photophysical model, implying a structural basis underpinning the measured E_a values. The narrow range of E_a values observed for these samples when compared to literature E_a values for model fluorophores (~ 5-30 kJ mol^{-1}) points to a consistent group of fluorophores across organic matter isolates of diverse character. In addition, the fundamental approach to temperature-dependent fluorescence analysis complements existing empirical relationships for the correction of online fluorescence sensors for temperature effects.

5.2. Introduction

Fluorescence (the emission of light from an electronically excited singlet state) is a widely used tool to characterize dissolved organic matter (DOM) due to the relative ease of use, minimal sample preparation and volume requirements, and multitude of quantitative tools that have been developed for interpretation of spectra (Korak et al., 2014; Rosario-Ortiz and Korak, 2017). DOM fluorescence spectra are often presented as three-dimensional excitation-emission matrices (EEMs) and are characterized by large apparent Stoke's shifts, low quantum yields, and regions of intensity often assigned to specific classes of fluorophores (e.g. tryptophan-like Peak B) (Boyle et al., 2009; Korak et al., 2014). Despite its ubiquitous use, there is still a lack of understanding of the specific fluorophores present in DOM and their photophysical properties.

Multiple photophyscal models have been developed for describing DOM fluorescence. One model is that electron-rich polyphenols or alkoxy phenols and electron-poor aromatic ketones or quinones form intramolecular donor-acceptor complexes (DA) that can absorb light to form charge-transfer (CT) excited states (Boyle et al., 2009; Dalrymple et al., 2010; Del Vecchio and Blough, 2004; Ma et al., 2010; Power and Langford, 1988; Sharpless, 2012; Sharpless and Blough, 2014; Z.-D. Wang et al., 1990). This CT model postulates that these DA complexes are tresponsible for the long wavelength absorbance and fluorescence of DOM. In contrast, it could be argued that DOM optical properties are due to a superposition of non-interacting chromophores in which a given optical signal is simply the sum of contributions of individual chromophores.

A typical chromophore in DOM will undergo the following processes. Absorption of a photon excites the ground electronic state (S_0) to an excited singlet state (S_n), which quickly relaxes to the ground vibrational level of the first electronic excited state (S_1). The S_1 state

decays by fluorescence ($S_1 \to S_0 + h\nu$, k_f), internal conversion ($S_1 \to S_0$, k_{ic}), a radiationless process, or intersystem crossing ($S_1 \to T_n$, k_{isc}), another radiationless process. Fluorescence of single-fluorophore solutions of organic compounds can be characterized by the temperature-dependence of the fluorescence quantum yield (Φ_f). Fluorescence intensity tends to decrease with increasing temperature due to the temperature-dependence of non-radiative decay processes ($k_{ic} + k_{isc}$). Thus, the apparent activation energies (E_a) derived from these data can yield information about important non-radiative decay pathway of S_1.

In this study, we measured the temperature-dependence of DOM fluorescence and calculated E_a values from the data using the Arrhenius equation. A broad range of organic matter isolates were examined including aquatic, soil, and lignite-derived humic substance isolates between 10 and 40 °C. The resulting temperature-dependent data were compared to physicochemical properties of the examined isolates in an attempt to correlate photophysical observations to organic matter structure. The results in this study provide both a new way to gain information about organic matter fluorescence by measuring E_a as well as fundamental insight into the photophysical processes controlling organic matter fluorescence.

5.3. Materials and Methods

5.3.1 Samples

Organic matter isolates were obtained from the International Humic Substances Society (see Table C.1). For temperature-dependent fluorescence measurements, isolates were dissolved in pH 7.2, 10 mM phosphate buffer at a concentration of ~ 4 mgC L^{-1}. Non-buffered aqueous solutions were also prepared from ~100 mgC L^{-1} stock solutions adjusted to pH 7.0 with sodium hydroxide. pH was monitored after dilution and adjusted to 7.0 if necessary. These concentrated stocks were also used to prepare a 30% v/v solution of MRNOM in glycerol (spectrophotometric

grade) and 0-48 % v/v solutions of SRFA in D_2O. One sample (SRNOM) was fractionated to obtain a < 5K and > 5K molecular weight fraction. The fractionation was performed using Millipore ultrafiltration membranes (Millipore, USA) constructed from regenerated cellulose with a nominal molecular weight cutoff of 5 kDa (Dong et al., 2010).

5.3.2 Analytical methods

A Sievers M5310 C (GE, USA) TOC analyzer was used to measure DOC concentrations of diluted aqueous stock solutions utilizing a persulfate oxidation method. pH was measured with an Accumet pH meter (Fischer Scientific, USA). Absorbance was measured in triplicate with a Cary-100 Bio (Agilent, USA) spectrophotometer from 800 to 200 nm in 1 nm increments with a 1, 5, or 10 cm path length quartz cuvette.

Fluorescence measurements were performed using a Fluoromax-4 spectrofluorometer (Horiba, USA) in triplicate or an Aqualog (Horiba, USA) in duplicate. With the Fluoromax-4, emission intensity was measured between 300-800 nm (2 nm increments) with an integration time of 0.25 s at excitation wavelengths (λ_{ex}) between 240-550 nm (10 nm increments). All bandpass settings were 5 nm. With the Aqualog, emission intensity was measured using a charge-coupled device at 4.64 nm/pixel, resulting in an emission range of 254 to 824 nm. Excitation was measured between 240-600 nm with a 5 nm bandpass. Integration times were varied but did not exceed 10 s. Fluorescence intensity for both instruments was collected in signal divided by reference (S/R) mode and was corrected incorporating blank subtraction, instrument specific factors, inner filter corrections, and Raman normalization as described previously (Murphy et al., 2010). E2/E3, spectral slope (S300-600), SUVA at 254 nm ($SUVA_{254}$), and FI were calculated as previously described (Peuravuori and Pihlaja, 1997; Twardowski et al., 2004; Weishaar et al., 2003).

71

Fluorescence quantum yields were calculated using quinine sulfate as a reference standard ($\Phi_{f,\,QS}$ = 0.51 in 0.1 N H2SO4) according to Equation 5.1 with additional details provided in Appendix C. Note that Equation 5.1 is valid only at Abs < 0.05-0.1, a condition met for majority of the isolates examined.

$$\frac{\Phi_f(\lambda_{ex})}{\Phi_{f,QS}(350\text{ nm})} = \frac{\int_0^\infty I_{DOM}(\lambda_{ex},\lambda_{em})d\lambda_{em}}{Abs_{ex}(\lambda_{ex})} \frac{Abs_{ref}(350\text{ nm})}{\int_0^\infty I_{ref}(350\text{ nm},\lambda_{em})d\lambda_{em}} \quad \text{Equation} \quad 5.1$$

Φ_f obtained with the Fluoromax-4 were found to be systematically larger than those with the Aqualog at λ_{ex} less than 350 nm, which is attributed to the poorer grating quality of the Fluoromax-4. For this reason, Φ_f values obtained using the Fluoromax-4 are reported only at λ_{ex} greater than 350 nm.

5.4. Results and Discussion

5.4.1 Temperature-dependence of DOM fluorescence

Figure 5.1 shows typical data for fluorescence quenching as a function of increasing temperature. Fluorescence intensity (I_{DOM}) decreased with increasing temperature (Figure 5.1a). This result is consistent with fluorescence of single-fluorophore solutions of organic compounds, including benzene and substituted benzenes (Birks, 1970), polycylic aromatic hydrocarbons such as naphthalene (Birks, 1970), tryptophan and tyrosine (Y. Chen and Barkley, 1998; Eisinger and Navon, 1969; Gally and Edelman, 1962), flavones (Oncul and Demchenko, 2006), and coumarins (Giri, 1992). Each of these moieties, besides perhaps polycyclic aromatic hydrocarbons, have been identified as plausible chromophores and fluorophores within DOM. This decrease in I_{DOM} was observed for all aquatically-derived isolates as well as a soil-derived fulvic acid isolate (PPFA), but not for soil and lignite-derived humic acid isolates (PPHA,

ESHA, and LHA, see Figure C.2). Importantly, although I_{DOM} decreased, spectral shape remained unchanged (i.e. see dashed line in Figure 5.1a), indicating that maximum emission wavelength ($\lambda_{em,max}$) is constant). Constant $\lambda_{em,max}$ with changing temperature was observed at all λ_{ex} examined. Constant $\lambda_{em,max}$ is also observed for single-fluorophore solutions of organic compounds in which fluorescence occurs from a local excited (LE) state (e.g. tryptophan, tyrosine, and flavones) (Gally and Edelman, 1962; Oncul and Demchenko, 2006). Thus, the constancy of $\lambda_{em,max}$ for DOM suggests that fluorescence is occuring mainly from LE states and not from CT excited states.
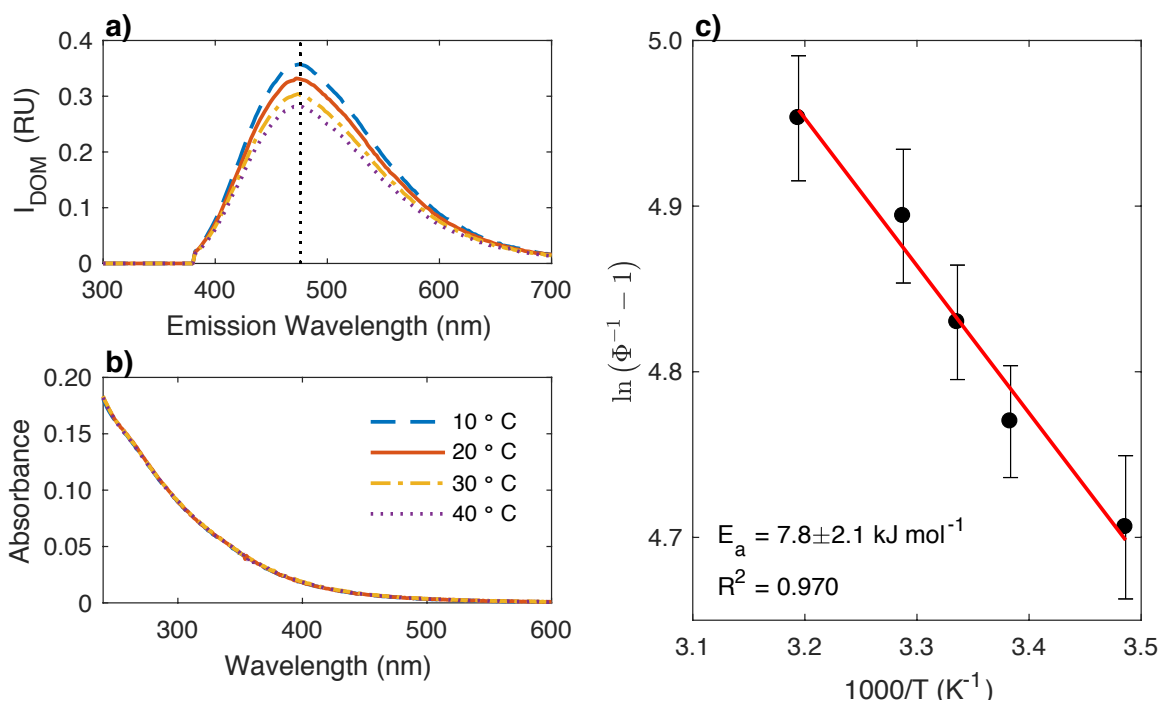
Figure 5.1. Temperature-dependent fluorescence (a) and absorbance (b) spectra measured between 10 and 40 °C for Suwannee River Fulvic Acid (SRFA, 1S101F). Fluorescence spectra in a) are at an excitation wavelength of 370 nm. Subplot c) shows a plot of the Φ_f plotted according to Equation 5.9 at an excitation wavelength of 370 nm. The activation energy, E_a, is obtained from multiplication of the slope of the linear regression (red line) by the gas constant, 8.314 J mol^{-1} K^{-1}. Error bars in c) represent propagated error from triplicate absorbance and fluorescence measurements on the sample and quinine sulfate reference standard. Error bars represent the 95% confidence interval.

5.4.2 Photophysical model

The relative importance of fluorescence compared to radiationless transitions can be described by the fluorescence quantum yield,

$$\Phi_f = k_f / (k_f + k_{nr})$$

Equation 5.2

where $k_{nr} = k_{ic} + k_{isc}$ represents the overall non-radiative decay. Φ_f values for DOM are in the range of 0.005 to 0.020 indicating that fluorescing moieties make up only a small subset of the total chromophoric DOM pool (Boyle et al., 2009; McKay et al., 2016; Mostafa and Rosario-Ortiz, 2013; Wünsch et al., 2015). Identification of the fluorophores present in DOM and the photophysical mechanisms responsible for the magnitude of Φ_f has remained a challenge, due in part to the complex nature of DOM. Although past work has suggested that a significant portion of DOM photophysics is due to DA complexes (Sharpless and Blough, 2014), which could lead to excitation into CT states, recent work suggests that this may not be the primary photophysical mechanism (McKay et al., n.d.).

Quantitative information regarding the temperature-dependence of fluorescence can be gained by measuring fluorescence lifetimes or quantum yields at various temperatures and using the simplified kinetic scheme,

$$\text{DOM} + h\nu_a \rightarrow {}^1\text{DOM*} \qquad \text{(absorption, } k_a\text{)} \qquad \text{Equation 5.3}$$

$$^1\text{DOM*} \rightarrow \text{DOM} + h\nu_f \qquad \text{(fluorescence, } k_f\text{)} \qquad \text{Equation 5.4}$$

$$^1\text{DOM*} \rightarrow \text{DOM} \qquad \text{(non-radiative decay, } k_{nr} = k_{ic} + k_{isc}\text{)} \qquad \text{Equation 5.5}$$
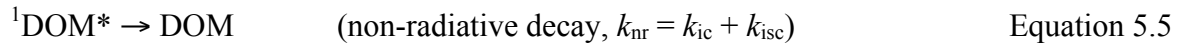
Assuming that k_{nr} is the only temperature-dependent process (k_f is not generally temperature-dependent) (Birks, 1970), we can write for k_{nr}

$$k_{nr} = k_{nr}^0 e^{-E_a/RT}$$

Equation 5.6

which when substituted into Equation 5.2 gives,

$$\Phi_f = \frac{k_f}{k_f + k_{nr}^0 e^{-E_a/RT}}$$

Equation 5.7

Taking the inverse of both sides and rearranging yields,

$$\frac{1}{\Phi_f} - 1 = \frac{k_{nr}^0}{k_f} e^{-E_a/RT}$$

Equation 5.8

and taking the natural logarithm results in the expression,

$$\ln\left(\frac{1}{\Phi_f} - 1\right) = \ln\left(\frac{k_{nr}^0}{k_f}\right) - \frac{E_a}{RT}$$

Equation 5.9

Based on Equation 5.9, a plot of the natural logarithm of ($\Phi_f^{-1} - 1$) versus T^{-1} should give a straight line with a slope of $-E_a/R$ and intercept of $\ln(k_{nr}^0/k_f)$ (Birks, 1970). E_a represents the activation energy for the temperature-dependent, non-radiative decay pathways of the first excited singlet state, S_1. If there is more than one temperature-dependent inactivation pathway from S_1, then E_a will represent a combination of activation energies for these different processes. Non-linearity is sometimes observed when data are plotted according to Equation 5.9, which is often taken as evidence of multiple inactivation processes occurring simultaneously (Bowen and Sahu, 1959; Eastman, 1968; Gally and Edelman, 1962; Matsumoto et al., 1972). In addition, sometimes one inactivation process will dominate over another in a certain temperature regime.

5.4.3   Activation energies

Figure 5.1c shows Φ_f values obtained using plotted according to Equation 5.9 for SRFA. The linearity of the data in Figure 5.1c indicates that the temperature-dependent inactivation

processes for ^{1}DOM* over the temperature range of 10 to 40 °C have a narrow range of energies. Temperature-dependent Φ_f values were treated in an analogous way for the other isolates that exhibited a temperature-dependence (i.e. not PPHA, ESHA, or LHA) and the resulting E_a values are shown in Table 5.1. There was a surprisingly narrow range of E_a values (5.9 to 8.6 kJ mol^{-1}), with no discernable statistical difference at a 95% confidence level.

Table 5.1. Arrhenius parameters for the fluorescence of organic matter

Isolate	Solvent	$E_a \pm 95\%$ CI (kJ mol^{-1})	$\ln(k_{nr}^0/k_f) \pm 95\%$ CI
MRNOM	30% glyc	7.72 ± 0.71	7.52 ± 0.88
MRNOM	H_2O	7.62 ± 2.18	7.61 ± 0.87
PLFA	H_2O	8.35 ± 1.16	7.85 ± 0.46
PPFA	H_2O	6.02 ± 0.27	6.82 ± 0.11
SRFA	H_2O	7.40 ± 2.05	7.80 ± 0.82
SRHA	H_2O	6.94 ± 0.55	8.65 ± 0.22
SRNOM	H_2O	7.05 ± 2.17	7.66 ± 0.87
SRNOM > 5K	H_2O	6.71 ± 4.16	8.05 ± 1.67
average ± 1 standard deviation[a]		7.22 ± 0.66	7.75 ± 0.48

[a]Does not include MRNOM in 30% glycerol

The temperature range used in this study is most relevant to natural waters, but does not cover the typically much larger range explored in studies of single-fluorophore solutions of organic compounds. This is important because changes in the temperature-dependence of Φ_f could be due to the relative importance of different radiationless decay pathways under different temperature regimes (Bowen and Sahu, 1959; Eastman, 1968; Gally and Edelman, 1962; Matsumoto et al., 1972). In addition, studies on the temperature-dependence of Φ_f for macromolecules indicate that non-linearity in Equation 5.9 is sometimes observed when changing temperature modifies the tertiary or quaternary structure (e.g. coil versus helical for collagen) (Menter, 2006).

In order to assess the adequacy of the model depicted in Equation 5.9, we measured Φ_f at 9 temperatures between 10 and 55 °C for a select isolate (MRNOM) in 30% glycerol solution. These data were treated according to Equation 5.9 and are compared to data obtained using only

5 temperature points in Figure C.2a and Figure C.2b, respectively. The E_a values obtained using these analyses are statistically the same (7.7 ± 1.8 kJ mol^{-1} for 5 point regression vs. 7.4 ± 0.7 kJ mol^{-1} for 9 point regression). These results support the use of Equation 5.9 and the implied photophysical model in analyzing these data. Furthermore, the linearity in Figure C.2a and Figure C.2b provide evidence against a supramolecular DOM structure in which intermolecular interactions occur for aquatic organic matter (Sutton and Sposito, 2005). The range in temperatures investigated would likely affect the structure of such a supramolecular assembly, and consequently its fluorescence spectra.

A question that arises given the complex nature of DOM fluorescence is whether E_a depends on λ_{ex}. Figure C.2c shows E_a values as a function of λ_{ex} for MRNOM (see Figure C.3). There is a statistically significant decrease in E_a when λ_{ex} is increased from 350 to 440 nm (slope p-values of 0.0017 and 1.52 × 10^{-10} for the 5- and 9-temperature regression, respectively). However, future work should be done to verify this observation and determine potential causes given the large 95% confidence intervals in E_a.

5.4.4   Comparison with model compounds

What is the interpretation of the E_a values observed for DOM in terms of the relevant photophysical processes? Table C.2 shows E_a values obtained from the literature for model organic compounds, including some aromatics, aminoacids, and coumarins, as well as the E_a for the viscosity of water (~18 kJ mol^{-1}) (J. H. Wang et al., 1953). The measured E_a values for DOM are most similar in magnitude to analogous values for polycyclic aromatic hydrocarbons (~5-9 kJ mol^{-1}), the latter being attributable to the temperature-dependence of intersystem crossing (Birks, 1970). Interestingly, the E_a values for DOM are less than the E_a for the viscosity of water (J. H. Wang et al., 1953), indicating that the values represent intrinsic photophysical processes

occurring in DOM and not just changes in solvent environment. Viscosity affects fluorescence intensity because solvent viscosity influences its ability to reorient around and stabilize the new dipole of the ^{1}DOM* state (Lakowicz, 1999). The measured E_a values are lower than analogous values for alkoxy substituted 4-methyl coumarins (16-30 kJ mol^{-1}) (Giri, 1992), which are potential fluorophores within DOM. The E_a for tryptophan fluorescence quenching (~ 30 kJ mol-1) is also greater than the values observed from DOM. Although also speculative, another process that could be occurring is excited state proton transfer of excited phenolic moieties to the solvent (H_2O) (Kaneko et al., 2009; Robinson et al., 1986) or other DOM moieties (i.e. intramolecular processes). For example, this process for 2-napthol (a weak photoacid) has an activation energy of ~ 11 kJ mol^{-1} in aqueous solution (Robinson et al., 1986), comparable in magnitude to the E_a values observed here for DOM fluorescence.

Physical quenching of ^{1}DOM* by solvent molecules could be an important deactivation process. For example, when D_2O is used as a solvent for tryptophan, a decrease in Φ_f by a factor of ~2.5 is observed; however, the E_a for this process remains unchanged (Eisinger and Navon, 1969). To investigate the possibility of solvent quenching of ^{1}DOM*, Φ_f was measured for SRFA in varying volume percentages of D_2O (10-48 % v/v). We observed minimal changes in Φ_f with increasing concentration of D_2O (Φ_f increased from 0.00205 to 0.00213 between 0 and 48% v/v D_2O, respectively), unlike the trend observed for tryptophan (Eisinger and Navon, 1969) and other proton donating or accepting aromatic compounds in previous studies (Stryer, 1966). That Φ_f did not decrease with increasing D_2O concentration indicates that solvent quenching of ^{1}DOM* is a non-existent or relatively unimportant pathway.

5.4.5   Correlations with DOM physicochemical properties

We examined correlations between measured E_a values for DOM isolates and relevant optical and physicochemical properties of DOM. Two of these relationships are shown in Figure 5.2 while the rest are presented in Figure C.4 through Figure C.6. Although some of the correlations between E_a and DOM physicochemical properties exhibited significant p-values, most of the correlations were heavily weighted by PLFA and PPFA, end-member isolates with E_a values of 8.6 and 5.9 kJ mol^{-1}, respectively. More work is needed to establish whether these relationships are significant.
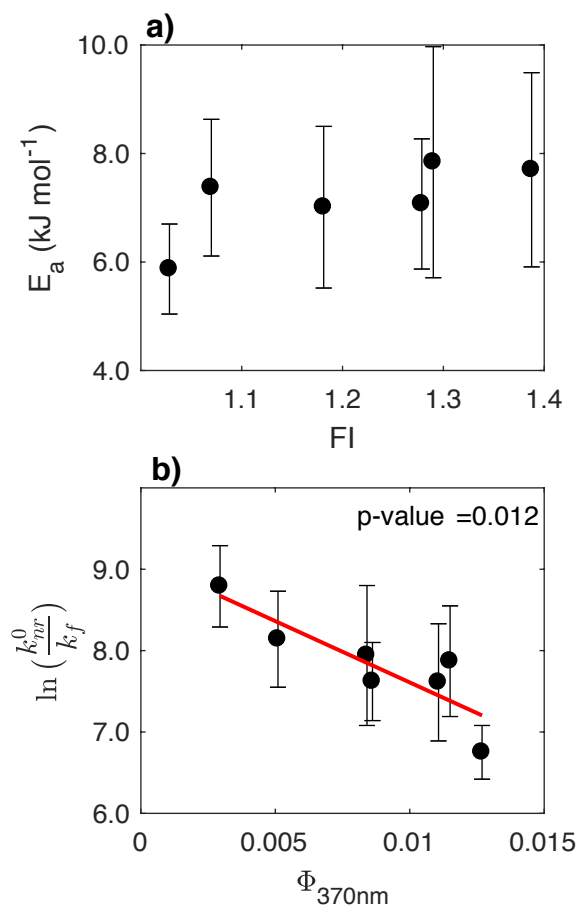
Figure 5.2. Correlations between Arrhenius parameters and physicochemical properties for organic matter isolates. a) Relationship between activation energy, E_a, obtained via Equation 5.9 and the specific ultraviolet absorbance at 254 nm, $SUVA_{254}$. b) Relationship between intercept term in Equation 5.9 and the fluorescence quantum yield, Φ_f, at an excitation wavelength of 250 nm. Errorbars represent 95% confidence intervals based on a linear fit of Equation 5.9 to the transformed data.

This would certainly be of value in expanding the field of DOM photophysics. For example, a positive between E_a and FI could indicate that E_a tends to be lower for DOM isolates with greater aromatic character (Weishaar et al., 2003). Furthermore, many physicochemical parameters, including FI, have been related to DOM molecular weight (Korak et al., 2014; Maizel and Remucal, 2017; McKay et al., 2016; Shimabuku et al., 2014). Thus, additional temperature-dependent studies of DOM fluorescence could gain insight into the relationship between DOM molecular weight and E_a.

Figure 5.2b shows the relationship between $\ln(k_{nr}^0/k_f)$ obtained from the intercept of the linear regression using Equation 5.9 and the fluorescence quantum yield at $\lambda_{ex} = 370$ nm. This correlation was less heavily weighted by PLFA and PPFA and held true at multiple λ_{ex} (Figure C.6). Figure 5.2b also corroborates use of the photophysical model in Equation 5.9, because k_{nr}^0/k_f is inversely proportional to Φ_f based on Equation 5.2. In addition, it has been shown that Φ_f is inversely related to DOM molecular weight. From this we can infer that DOM of higher molecular weight has a faster rate of radiationless decay (greater k_{nr}^0). It has been observed previously that DOM of lower molecular weight has increased reactive intermediate (e.g. $^1O_2$, $^3DOM^*$, and $^{\bullet}OH$) quantum yields (E. Lee et al., 2013; Maizel and Remucal, 2017; McKay et al., 2016; Mostafa and Rosario-Ortiz, 2013; Richard et al., 2004). The results of this present study support the interpretation that differences in photochemical reactivity of DOM as a function of molecular weight is due to differences in radiationless decay.

5.4.6 Environmental Implications

A significant conclusion from this study is that E_a values measured for DOM fluorescence fell within a narrow range (5.9 to 8.6 kJ mol^{-1}), especially when comparing the larger differences observed for model fluorophores in Table C.2. Although $\ln(k_{nr}^0/k_f)$, but not E_a, correlated with DOM physicochemical properties, indicating a structural basis for the measured values, the lack of variation points to a consistent group of fluorophores in organic matter. In addition, these results have an immediate practical use in the correction of fluorescence spectra for temperature-effects. Taking the average value of E_a and $\ln(k_{nr}^0/k_f)$ results in an increase in Φ_f of ~10% with a change in temperature from 20 to 10 °C. For online sensors that measure fluorescence intensity, the decrease in signal would be identical, both because DOM absorbance is unaffected by temperature (McKay et al., n.d.) and because fluorescence intensity is directly proportional to Φ_f.

These results derived from a fundamental perspective complement proposed empirical relationships (Ryder et al., 2012; Watras et al., 2011) developed for correcting online fluorescence sensors.

6. Temperature Dependence of the Photochemical Formation of Hydroxyl Radical from Dissolved Organic Matter

6.1. Abstract

In this paper, the temperature dependence of the photochemical production of the hydroxyl radical ($^\bullet$OH) from dissolved organic matter (DOM) was investigated by measuring the apparent temperature dependence of the quantum yield (Φ_a) for this process. Temperature dependent Φ_a values were analyzed using the Arrhenius equation. Apparent activation energies obtained for DOM isolates purchased from the International Humic Substances Society ranged from 16 to 32 kJ mol^{-1}. Addition of 40 units mL^{-1} catalase, used to hinder the hydrogen peroxide (H_2O_2)-dependent pathway to •OH, did not impact the observed activation energy. However, an increase in activation energy was observed in lower molecular weight DOM obtained by size fractionation. We also measured the temperature dependence of p-benzoquinone photolysis as a model compound for DOM and observed no temperature dependence (slope p = 0.41) for the formation of phenol from oxidation of benzene (the $^\bullet$OH probe used), but a value of about 10 kJ mol^{-1} for p-benzoquinone loss, which is consistent with formation of a water-quinone exciplex. These data provide insight into DOM photochemistry as well as provide parameters useful for modeling steady state •OH concentrations in natural systems.

6.2. Introduction

Reactive oxygen species (ROS) play an important role in the photochemistry of natural aquatic systems. These ROS include the hydroxyl radical ($^\bullet$OH), singlet oxygen ($^1O_2$), superoxide ($O_2^{\bullet-}$), hydrogen peroxide (H_2O_2) and triplet excited states. From an engineering standpoint, degradation of many organic contaminants is increased by ROS (Legrini et al., 1993;

Xu et al., 2011). Ecologically, ROS are involved in the mineralization of organic carbon (Vione et al., 2006), contributing to the global carbon cycle. The presence of H_2O_2 was first detected in marine waters in 1966 and was shown later to result from photochemical reactions (Cooper et al., 1988). Since then, other ROS such as •OH and $^1O_2$ have been shown to be produced photochemically in natural waters (Vaughan and Blough, 1998; Vione et al., 2006; Zepp et al., 1977).

Multiple chemical species undergo photochemical reactions to produce ROS, such as nitrate, nitrite, and dissolved organic matter (DOM) (Vaughan and Blough, 1998; Vione et al., 2014; 2006). In particular, DOM photolysis produces $^•OH$ and $^1O_2$, as well as H_2O_2, triplet states (here abbreviated as $^3DOM*$), and $O_2^{•-}$. The generally accepted model is that $^1DOM*$ is formed following absorption of a photon by ground state DOM, which can subsequently undergo internal conversion, vibrational relaxation, or intersystem crossing to $^3DOM*$. Early work by Zepp et al. established an average energy of around 250 kJ mol^{-1} for $^3DOM*$ molecules (Zepp et al., 1985), sufficiently high to form $^1O_2$ from reaction with dissolved oxygen. H_2O_2 results from the disproportionation of $O_2^{•-}$, which is formed by reaction of dissolved oxygen with some photo-produced reductant (Zepp et al., 1987). The $^•OH$ radical is believed to be formed by multiple pathways, however, steady state concentrations are limited to around 10^{-18} to 10^{-16} M in natural waters due to its high reactivity (Mopper and Zhou, 1990; Vione et al., 2006). $^1O_2$ is a weaker and more selective oxidant than $^•OH$ and thus reaches steady state concentrations a few orders of magnitude higher (Vione et al., 2014). Additionally, steady state concentrations of $^•OH$ and $^1O_2$ are generally higher for effluent organic matter compared to DOM isolates (Dong and Rosario-Ortiz, 2012; Mostafa and Rosario-Ortiz, 2013). Reported apparent quantum yields (Φ_a)

84

for $^{\bullet}$OH radical are on the order of 10^{-4} to 10^{-5}, again being generally higher for wastewater samples (Dong and Rosario-Ortiz, 2012).

$$\text{DOM} + \text{h}\nu \left\{ \begin{array}{l} \text{Photo-Fenton} \\ \text{H}_2\text{O}_2 \text{ photolysis} \\ \text{Low energy hydroxylator} \\ {}^3\text{DOM*, } {}^1\text{DOM*, DOM}^{\bullet+/\bullet-} \end{array} \right. \longrightarrow \bullet\text{OH}$$
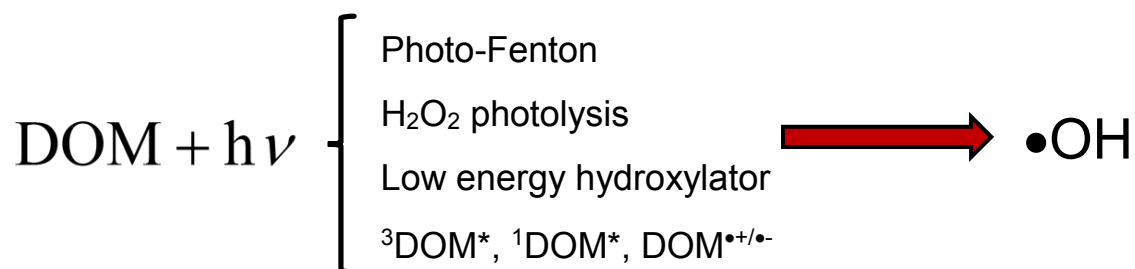
Figure 6.1. Reaction pathways leading to •OH from DOM photolysis.

While it is clear that DOM is a photochemical source of $^{\bullet}$OH, the underlying mechanisms are not completely understood. Some of the formation pathways are summarized in Figure 6.1. There likely exist two pathways to $^{\bullet}$OH: an H_2O_2-dependent and H_2O_2-independent pathway (Dong and Rosario-Ortiz, 2012; Vaughan and Blough, 1998; Vione et al., 2014). The H_2O_2-dependent pathway involves the photo-Fenton reaction (Southworth and Voelker, 2003; Zepp et al., 1992) and possibly direct photolysis of photochemically produced H_2O_2 (Mostofa and Sakugawa, 2003). The importance of this pathway has been demonstrated by using catalase to decompose H_2O_2, which decreases $^{\bullet}$OH production by up to 50 % for some samples (Page et al., 2011; White et al., 2003). Super-oxidized iron species (e.g. ferryl, FeO^{2+}), which are operational at neutral pH (Hug and Leupin, 2003), may also account for some $^{\bullet}$OH-like activity by reacting with various organic compounds (Jacobsen et al., 1998). The H_2O_2-independent pathway involves species that lead to free $^{\bullet}$OH as well as so-called low energy hydroxylating species (Gan et al., 2008; Page et al., 2011; Pochon et al., 2002). H-atom abstraction from water by some DOM excited state (^{3}DOM*, ^{1}DOM*, or charge transfer species-DOM$^{\bullet+/\bullet-}$) is one mechanism suggested to produce free $^{\bullet}$OH, but this has not been confirmed (Glover and Rosario-Ortiz, 2013; Vione et al., 2014). Generation of low energy hydroxylators has been argued largely on the

85

quenching of •OH-like activity with addition of methane. For example, Page et al. (2011) showed that some DOM isolates exhibited less than calculated decreases in photochemical •OH production with addition of known concentrations of methane (Page et al., 2011). Though uncertain, these species could be modeled by the quinone-water exciplex formed during irradiation of 2-methyl-p-benzoquinone. For example, Pochon et al. (2002) (Pochon et al., 2002) and Gan et al. (2008) (Gan et al., 2008) demonstrated no methyl radical production upon irradiation of methyl-p-benzoquinone containing methane as an •OH probe.

This paper presents data on the apparent temperature dependence of Φ_a for bulk DOM isolates, with and without catalase present, as well as apparent molecular weight fractions. The temperature dependence of the photolysis of p-benzoquinone was also investigated as a model compound for comparison. These data provide insight into DOM characterization and photochemistry by comparing the temperature dependence of different DOM samples to a model compound. In addition, the measured activation energies can be used for kinetic modeling of steady state •OH concentrations in natural and engineered systems exhibiting temperature fluctuations or large deviations from room temperature.

6.3. Materials and Methods

DOM isolates including Suwannee River Fulvic Acid I (SRFA, 1S101F), Suwannee River Humic Acid II (SRHA, 2S101H), Suwannee River NOM (SRNOM, 2R101N) Pony Lake Fulvic Acid (PLFA, 1R109F), and Elliot Soil Humic Acid (ESHA, 1S102H) were purchased from the International Humic Substance Society. All other chemicals were obtained from commercial sources. The solution conditions, irradiation conditions, and analytical methods used in this study are presented in detail elsewhere (Dong and Rosario-Ortiz, 2012). Briefly, solutions used in irradiation experiments were buffered at pH 7.2 in equimolar KH_2PO_4/K_2HPO_4 (total

[phosphate] = 10 mM). Samples were irradiated in clear, glass vials free of headspace. Irradiations were ran in duplicate for 2.5 to 8 hours (depending on sample to achieve measurable •OH concentrations) with an Oriel 1429A Solar Simulator equipped with a 1000 W Xenon lamp (see Figure D.1 for lamp spectrum). Over the irradiation period, samples were collected at 5 time intervals. Temperature control within ± 2 °C was accomplished by laying the vials flat in a water-jacketed petri dish. Benzene was used as an •OH probe by following the formation of phenol through the Dorfman reaction (Dorfman et al., 1964). Though not described in detail here, this mechanism involves reaction of the cyclohexadienyl radical with dissolved oxygen, which facilitates the formation of phenol. Based on the experimental conditions used in this study (gas tight vials, ~ μM phenol formation) no oxygen depletion due either to temperature changes or phenol formation during the course of experiments was expected. A benzene concentration of 3 mM was used to quantitatively scavenge •OH radicals. Phenol concentrations were measured by HPLC utilizing a gradient mobile phase of pH 2.8, 10 mM H_3PO_4 and methanol with a flow rate of 1.0 mL min^{-1}. The retention time of phenol under these conditions was around 4.7 minutes. Using the same HPLC method, p-benzoquinone eluted at 2.2 minutes (column dead time ~ 1.6 minutes). The column used was a Zorbax Eclipse XBD (4.6 x 150 mm) C18 column. Bovine liver catalase was used in some experiments to quench H_2O_2.

Apparent molecular weight fractions were collected using < 5 kDa and < 1 kDa ultrafiltration membranes (Millipore, USA). Membranes were soaked three times in fresh 1 L batches of Milli-Q water before use. To remove any remaining organic material, 200 mL of Milli-Q water was passed through the membrane before fractionating DOM samples. Approximately 200 mL of DOM solution was added to the ultrafiltration cell. The first 100 mL of permeate was collected.

The apparent quantum yield of $^\bullet$OH from DOM photolysis is given by

$$\Phi_a = \frac{R_{\bullet OH}}{k_{DOM-a}[\text{DOM}]}$$

Equation 6.1

where $R_{\bullet OH}$ is the rate of $^\bullet$OH radical formation in M s^{-1} and k_{DOM-a} is the specific rate of light absorption by DOM in s^{-1}. The specific rate of light absorption was calculated by the following equation

$$k_{DOM-a} = \sum_{\lambda=290nm}^{400nm} \frac{E_p^0(\lambda)\varepsilon_{DOM}(\lambda)(1-10^{-\varepsilon_{DOM}(\lambda)[\text{DOM}]z})}{\varepsilon_{DOM}(\lambda)[\text{DOM}]z}$$

Equation 6.2

where $E_p^0(\lambda)$ is the photon irradiance of the solar simulator in Einstein^{-1} cm^{-2}, $\varepsilon_{DOM}(\lambda)$ is the molar absorptivity of DOM in M_C^{-1} cm^{-1}, [DOM] is the DOM concentration in M_C, and z is the cell depth in cm. Absolute irradiance was measured with a spectroradiometer. Absorbance was measured with a Cary 100 UV/Vis spectrophotometer. Molar absorptivity data for p-benzoquinone were taken from the National Institute of Standards and Technology Chemistry WebBook.

The rate of phenol formation in this system is given by

$$\frac{d[\text{C}_6\text{H}_5\text{OH}]}{dt} = k_{\text{C6H6-OH}}[\bullet\text{OH}][\text{C}_6\text{H}_5] = Y_{phenol}R_{\bullet OH}$$

Equation 6.3

where $k_{\text{C6H6-OH}}$ is the second-order rate constant between benzene and $^\bullet$OH radical and Y_{phenol} is the yield of phenol from this reaction. Making the steady state assumption for $^\bullet$OH radical gives

$$\frac{d[\bullet\text{OH}]}{dt} = k_{DOM-a}\Phi_a[\text{DOM}] - \sum k_s[\text{S}][\bullet\text{OH}] \approx 0$$

Equation 6.4

$$[\bullet\text{OH}]_{ss} = \frac{k_{DOM-a}\Phi_a[\text{DOM}]}{\sum k_s[\text{S}]}$$

Equation 6.5

where k_S is the second order rate constant between $^\bullet$OH and scavenger S. Since the experimental

conditions are such that $\Sigma k_s[\text{S}][^{\bullet}\text{OH}] \approx k_{\text{C6H6-OH}}[\text{C}_6\text{H}_6][^{\bullet}\text{OH}]$, that is, benzene is the dominant $^{\bullet}\text{OH}$ scavenger Equation 6.3 becomes

$$\frac{d[\text{C}_6\text{H}_5\text{OH}]}{dt} = k_{DOM-a}\Phi_a[\text{DOM}] \qquad \text{Equation} \quad 6.6$$

and solving for Φ_a gives

$$\Phi_a = R_{\bullet OH}\frac{Y_{phenol}}{k_{DOM-a}[\text{DOM}]} \qquad \text{Equation} \quad 6.7$$

Clearly, Φ_a depends on the yield of phenol from hydroxylation of benzene. We discuss below the temperature dependence of Y_{phenol}.

Activation energies were determined by plotting the measured temperature dependent Φ_a according to the Arrhenius equation:

$$\ln(\Phi_a) = -\frac{E_a}{R}\frac{1}{T} + \ln(A) \qquad \text{Equation} \quad 6.8$$

Quantum yields were measured at 4 or 5 temperatures over a range of around 10 to 40 °C. Temperature dependent quantum yields have been analyzed in this way before (Chu and Anastasio, 2003; Kieber et al., 2014; Zellner et al., 1990) and the present data generally fit the Arrhenius model, with the average relative error (based on a linear fit of the Arrhenius plots) in activation energies being 15 %.

6.4. Results and Discussion

6.4.1   Temperature Dependence of Phenol Yield from Benzene

In order to use Equation 6.8 at different temperatures, the temperature dependence of Y_{phenol} needed to be assessed. Work by Chu and Anastasio (2003) has demonstrated that the $^{\bullet}\text{OH}$ probe

benzoic acid is not sensitive to temperature (Chu and Anastasio, 2003), suggesting that this may be the case for benzene.

Measuring Y_{phenol} involves knowing the actual rate of phenol produced (R_{phenol}) and the theoretical or calculated amount of $\cdot$OH resulting from photolysis of H_2O_2 ($R_{\cdot OH,calc}$) – i.e. Y_{phenol} = R_{phenol} / $R_{\cdot OH,calc}$. $R_{\cdot OH,calc}$ depends on the rate constant k for the photochemical transformation, which is calculated in general by

$$R_{\cdot OH,calc} = k[H_2O_2]$$ Equation 6.9

$$k = 2.303 \int_{\lambda=290nm}^{400nm} (\Phi_\lambda \varepsilon_\lambda I_\lambda l) d\lambda$$ Equation 6.10

where Φ_λ, ε_λ, and I_λ represent the quantum yield of $\cdot$OH from H_2O_2, molar absorptivity, and irradiance at a given wavelength and l is the pathlength. Note that the (small) temperature dependence of Φ_λ and ε_λ measured by Chu and Anastasio was used in Equation 6.9 (Chu and Anastasio, 2005). Solutions of 90 to 100 μM H_2O_2 were spiked with 3 mM benzene and irradiated for periods of 100 to 220 min. R_{phenol} was found from linear fits of the resulting data (not shown). Experiments were conducted at temperatures ranging from 11.6 to 38.4 °C and resulted in Y_{phenol} values of 0.63 ± 0.07 (Figure D.2) with no apparent temperature dependence (slope p = 0.14). In addition, an activation energy of 16.6 ± 5.0 kJ mol^{-1} for the production of •OH from nitrate photolysis was measured using benzene as the $\cdot$OH probe. This value is in good agreement with that measured by Chu and Anastasio (2003) (Chu and Anastasio, 2003) of 19 ± 4 kJ mol^{-1} and Zellner et al. (1990) (Zellner et al., 1990) of 16 ± 4 kJ mol^{-1}.

The Y_{phenol} determined here is within the range of values in the literature (0.43 to 0.95 depending on pH) (Arakaki and Faust, 1998; Balakrishnan and Reddy, 1972; Deister et al., 1990) and agrees well with the recently determined value of 0.69 measured by Sun et al. (2014) (Sun et

al., 2014). In previous publications by our group (Dong and Rosario-Ortiz, 2012; Glover and Rosario-Ortiz, 2013) and others (Vermilyea and Voelker, 2009), a yield of 0.85 was used. In this work, the determined yield was 26 % lower. This highlights the importance authors reporting $^{\bullet}$OH formation rates should report the value of Y_{phenol} to allow for comparison to other studies.

One limitation to this study is that irradiations were performed using a solar simulator (opposed to a monochromatic source) as the quantum yield for $^{\bullet}$OH radical are strongly wavelength-dependent (Lester et al., 2013; Vaughan and Blough, 1998). Subsequently, the quantum yields reported here should be interpreted as an average over the spectral output of the solar simulator ($\lambda > 290$ nm). Nevertheless, this paper provides the first temperature dependent measurements of Φ_a for $^{\bullet}$OH; also, previous studies have used polychromatic irradiation to investigate DOM photochemistry.
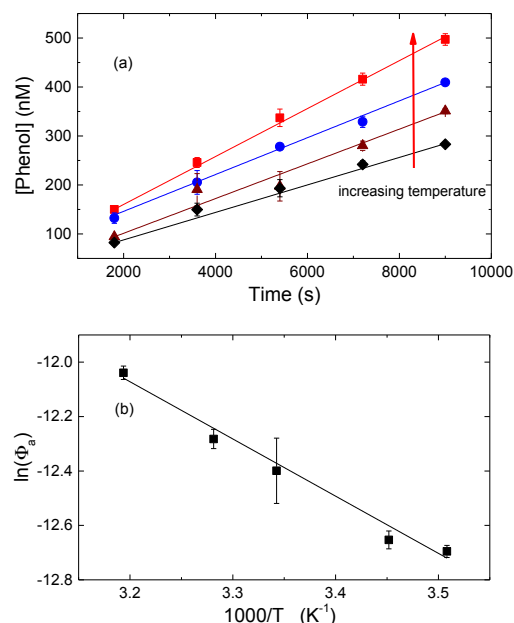
Figure 6.2. Temperature dependence of photochemical hydroxyl radical production by ESHA. (a) Increase in phenol concentration with solar simulator exposure time from 11.9-40.0 °C. Error bars in (a) represent one standard deviation of duplicate experiments (b) Arrhenius plot of the data in (a). Error bars in (b) correspond to the propagated error from the quantum yield measurements. Line in (b) corresponds to a linear fit of the data with an apparent E_a of 17.6 ± 1.3 kJ mol^{-1}. Rate data for 11.9 °C removed from (a) for clarity.

6.4.2   Temperature Dependence for Bulk DOM Isolates

DOM isolates were chosen to give a range of bulk chemical functionalities, type (e.g. humic acid vs. fulvic acid), and source (e.g. Pony Lake vs. Suwannee River). A typical data set is shown in Figure 6.2 for ESHA. Apparent quantum yields were plotted according to the Arrhenius equation in order to obtain the apparent activation energy (hereafter called activation energy). The term *apparent* activation energy is used to acknowledge the complexity of the system in that DOM is a heterogeneous, complex material and that the activation energies are obtained using a polychromatic source. Activation energies for all samples are summarized in Table 6.1. There is surprisingly little variation in the values for bulk DOM isolates, besides

SRFA (34.3 ± 7.2 kJ mol^{-1}), which suggests a consistent mechanism for $^{\bullet}$OH production. In addition, data are plotted according to the Eyring equation (see Table D.1) and some discussion is provided in Appendix D.

Table 6.1. Thermodynamic parameters of activation measured for DOM samples. Errors represent one standard deviation based on the linear fit of the data plotted according to Equation 5.8.

Sample	E_a (kJ mol^{-1})
PLFA	21.6 ± 3.1
Nitrate	16.6 ± 5.0
SRFA	34.3 ± 7.2
ESHA	17.6 ± 1.3
SRHA	16.0 ± 2.0
SRNOM	17.8 ± 2.3
SRNOM < 5 kDa	26.6 ± 4.6
SRNOM < 1 kDa	33.3 ± 1.4

Values for bulk samples are in the range of reported activation energies for other photochemical processes (Table 6.2), though there is some variation depending on the reaction. For example, aqueous photolysis of H_2O_2 and NO_3^- results in primary photochemical processes characterized by different photofragments as shown below.

$$H_2O_2 \xrightarrow{h\nu} {^{\bullet}OH} \qquad\qquad \text{Equation 6.11}$$

$$[NO_3^-]^* \rightarrow NO_2^- + O(^3P) \qquad\qquad \text{Equation 6.12}$$

$$[NO_3^-]^* \rightarrow NO_2^{\bullet} + O^{\bullet -} \xrightarrow{H_2O} NO_2^{\bullet} + {^{\bullet}OH} + OH^- \qquad\qquad \text{Equation 6.13}$$
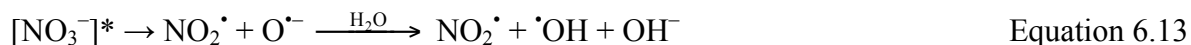
The lower activation energies of $\approx$ 16 to 18 kJ mol^{-1} for ESHA, SRHA, and SRNOM are closer to values characterizing diffusion-controlled reactions ($\approx$15 kJ mol^{-1}) (Buxton et al., 1988), while those for PLFA and SRFA, greater than 20 kJ mol^{-1}, are slightly higher. An explanation for the higher activation energy for nitrate photolysis (relative to H_2O_2) is that the primary photoproduct of H_2O_2 photolysis ($^{\bullet}$OH radical) diffuses more easily from the solvent cage than that of nitrate photolysis ($O^{\bullet -}$) (Chu and Anastasio, 2005; Zellner et al., 1990) (Mack and Bolton,

93

1999; Vione et al., 2011). Therefore the activation energies for Φ_a from DOM could reflect either secondary thermal chemistry or diffusion of different photoproducts from the solvent cage.

Table 6.2. Activation energies for different types of reactions. Primary photochemical process are those in which absorption of a photon results in direct chemical change (e.g. heterolytic bond cleavage) while secondary processes involve multiple reactions leading to the final product. The last entry gives the activation energy for a typical S_N2 reaction to provide context.

Reaction	Process	Activation energy (kJ mol^{-1})	Reference
$H_2O_2 + h\nu \rightarrow {}^{\bullet}OH$	primary	5-7	(Chu and Anastasio, 2005)
$NO_3^- + h\nu \rightarrow NO_2^{\bullet} + O^{\bullet-}$ $O^{\bullet-} + H_2O \rightarrow {}^{\bullet}OH + OH^-$	primary	19	(Chu and Anastasio, 2003)
Double bond isomerization	primary	20-26	(Canonica et al., 1997)
DOM + hν → → H_2O_2	probably secondary	8-57	(Kieber et al., 2014)
Ceterizene + hν → products	unknown	10.3	(Mead et al., 2014)
$C_6H_5COCH_2Cl + I^- \rightarrow$ $C_6H_5COCH_2I + Cl^-$	S_N2 reaction	71[a]	(Bordwell and Brannen, 1964)

[a]In acetone

Considering the activation energies for photochemical reactions of organic molecules, values for H-atom abstraction by ketones can vary from 9.2 to 29.3 kJ mol^{-1} depending on the reaction conditions and organic substrate (Turro et al., 2012). These Norrish Type reactions involve H-atom abstraction from the triplet state, subsequently producing a carbon-centered diradical. It is interesting that the activation energies in Table 6.1 match these values. However, the above activation energies are for production of a carbon-centered radical in organic solvents, while H-atom abstraction from water by ${}^3DOM^*$ would lead to ${}^{\bullet}OH$ in aqueous solution.

6.4.3   Catalase Experiments

The activation energies shown in Table 6.1 are for DOM samples not containing catalase, which is used to quench photochemically produced H_2O_2 in order to minimize the contribution of

direct photolysis and photo-Fenton reactions to •OH production (Page et al., 2011; White et al., 2003). Activation energies for the photochemical production of H_2O_2 from DOM have recently been reported by Kieber et al. (2014) for seawater samples, ranging from about 8 to 53 kJ mol^{-1} depending on the irradiation wavelength (Kieber et al., 2014). Their analysis revealed that when taken as an average across all samples, activation energies ranged from 15 to 30 kJ mol^{-1} over 290 to 400 nm.

To examine the H_2O_2-independent pathway, Φ_a values were measured for ESHA solutions containing increasing concentrations of catalase. A similar experiment including the same DOM sample is described by Page et al. for the terephthalate probe (Page et al., 2011). These data for ESHA are shown in Figure D.3 and demonstrate an almost identical quenching of $^{•}OH$ production for the same sample (ESHA) determined by Page et al. (2011) - about 50 %, at similar concentrations of catalase ($\approx$ 40 units mL^{-1}) (Page et al., 2011). Using a catalase concentration of 40 unit mL^{-1}, an activation energy of 16.6 ± 3.4 kJ mol^{-1} was measured for ESHA, which matches well with the non-catalase value of 17.6 ± 1.3. This result indicates that the H_2O_2-independent pathway to $^{•}OH$ (H-atom abstraction by $^{3}DOM^*$ and/or low-energy hydroxylator) has an activation energy of about 17 kJ mol^{-1} for ESHA. The addition of catalase also limits photo-Fenton reactions from occurring. Again the similarity in activation energies with addition of catalase, which essentially shuts down any Fenton chemistry, suggests that the H_2O_2-dependent pathway has a similar or lower activation energy than the H_2O_2-independent pathway.

6.4.4 Temperature dependence of p-Benzoquinone photolysis

To gain further insight into the H_2O_2-independent pathway, the temperature dependent photolysis of p-benzoquinone was investigated using benzene as an $^{•}OH$ probe. Others have

investigated this system at room temperature using dimethylsulfoxide (DMSO) to trap $^\bullet$OH, leading to the mechanism proposed in Figure 6.4 (Gan et al., 2008; Pochon et al., 2002).

In our experiments, solutions of 92.5 μM p-benzoquinone produced about 500 nM phenol over 12 minute irradiations (Figure D.4). The fact that phenol was produced from irradiation of p-benzoquinone shows that benzene may be susceptible to hydroxylation by species other than free $^\bullet$OH, e.g. low energy hydroxylators. Though there is some debate as to whether irradiation of quinones produces free $^\bullet$OH, there is evidence that hydroxylation occurs through a quinone-water exciplex (Gan et al., 2008; Pochon et al., 2002). As quinone moieties are believed to be present in DOM, this may explain the presence of low energy hydroxylators in irradiated DOM observed previously (Page et al., 2011; Pochon et al., 2002).
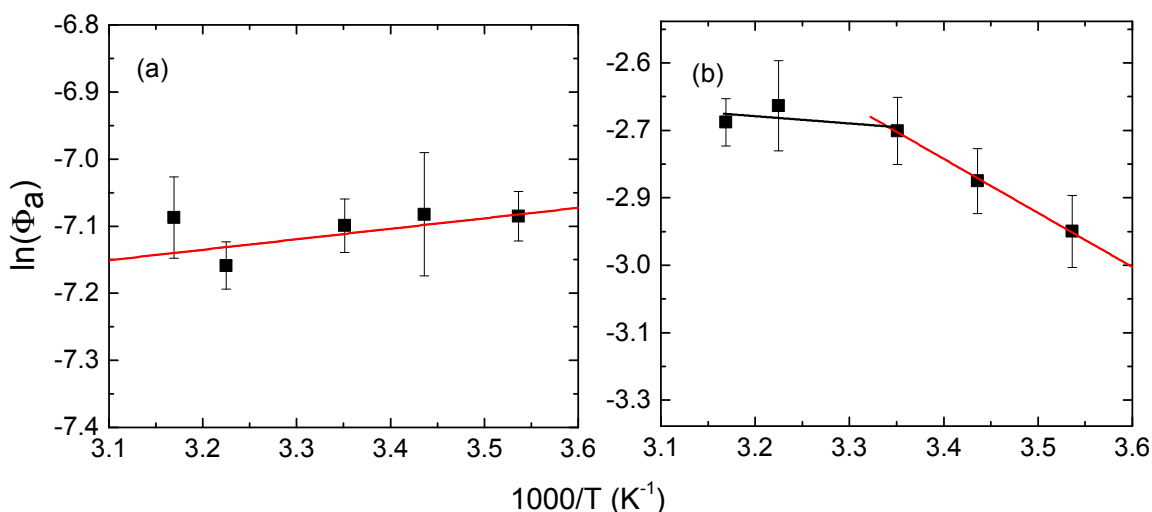
Figure 6.3. Apparent temperature dependence of the photolysis of p-BQ. (a) Φ_a for phenol production. (b) Φ_a for loss of p-BQ. Error bars in correspond to the propagated error from the quantum yield measurements.

As seen in Figure 6.3a, the Φ_a of phenol from p-benzoquinone irradiation was essentially temperature independent with an activation energy of $\approx$ 0 kJ mol^{-1} (slope p = 0.41). The loss of p-benzoquinone, however, shows more complex behavior (Figure 6.3b). At temperatures lower than $\approx$ 23 °C, p-benzoquinone loss is temperature dependent (9.7 kJ mol^{-1}), while above 23 °C,

there is almost no temperature dependence. These data are consistent with formation of a water-quinone exciplex that can hydroxylate benzene or proceed by other reactions to form hydroxy-p-benzoquinone or hydroquinone. The loss of p-benzoquinone, and production of hydroxy-p-benzoquinone and hydroquinone was confirmed in separate experiments by measuring the spectral changes in irradiated solutions containing 75 μM p-benzoquinone with and without 3 mM benzene (with benzene experiment shown in Figure D.5). The presence of 3 mM benzene did not eliminate the production of hydroxy-p-benzoquinone, suggesting that the intermediate species formed is not quantitatively quenched by benzene at a concentration of 3 mM. Conversely, others have reported quenching of this intermediate by DMSO at concentrations of 100 mM (Gan et al., 2008).
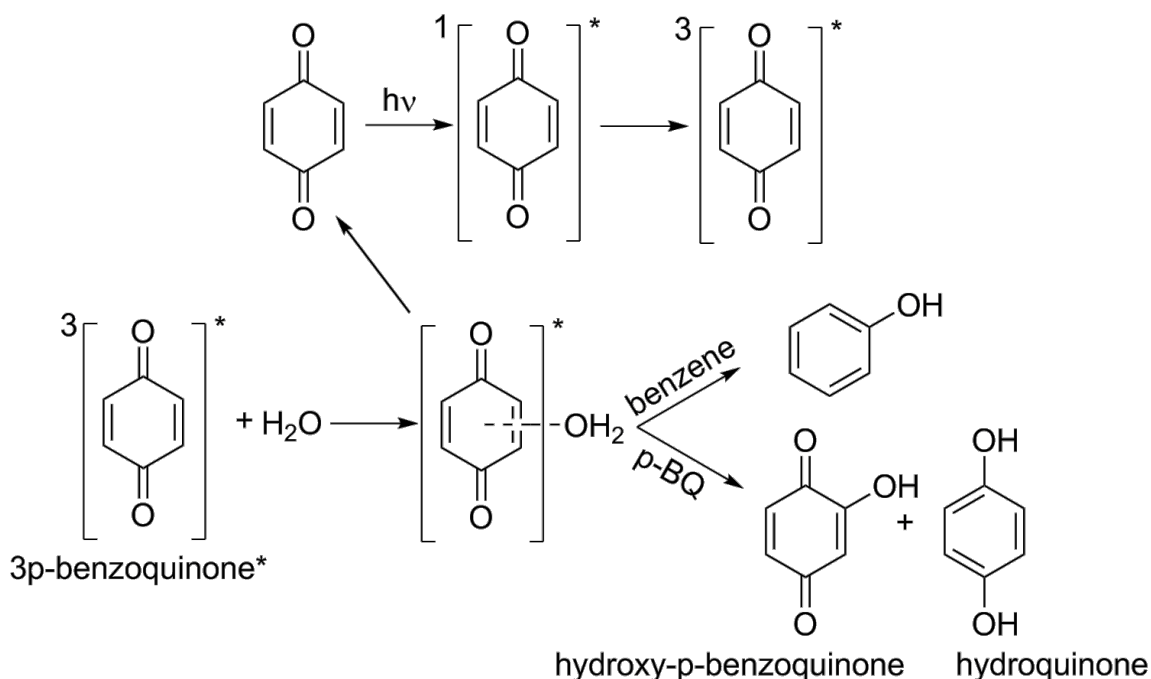
Figure 6.4. Reaction mechanism for photochemistry of p-benzoquinone.

The reactions shown in Figure 6.4 are likely affected by temperature in two ways. First, forward reactions to form phenol, hydroxy-p-benzoquinone, and the hydroquinone are expected

to increase with increasing temperature. Additionally, an increase in temperature likely encourages dissociation of the exciplex to re-form ground state p-benzoquinone. Based on these data, it seems that an increase in temperature favors production of hydroxy-p-benzoquinone and the hydroquinone up to a certain point (around 23 °C), while at higher temperatures, dissociation of the exciplex dominates. This explanation also accounts for the net zero temperature dependence of Φ_a for phenol. Negative and near zero activation energies have been taken as evidence for exciplex formation in other chemical systems (Gorman et al., 1982; Man Him Hui and Ware, 1976; O'Connor and Ware, 1976), albeit better characterized systems than DOM. Taken as a whole, these experiments demonstrate that the activation energies observed for $^{\bullet}$OH production from DOM cannot be attributed solely to a simple quinone model, even though the experimental approach depended on the measurement of the formation of phenol from the hydroxylation of benzene.

6.4.5 Effect of Molecular Size

Additional observation of Table 6.1 reveals differences in activation energies between humic (average of 17.1 ± 0.9 kJ mol^{-1}) and fulvic (average of 27.9 ± 9.0 kJ mol^{-1}) acids. It is difficult to specify what could account for this phenomenon because there are many differences between these samples. For example, although SRFA and PLFA are both fulvic acids, they differ widely in geographic source (Antarctica vs. Georgia, USA) and type (microbial vs. terrestrial influence). However, fulvic acids in general have lower average molecular weights (Chin et al., 1994).

To further discern the effect of molecular size on the temperature dependence of Φ_a, SRNOM was size-fractionated with <5 kDa and <1 kDa ultrafiltration membranes. Activation energies for $^{\bullet}$OH radical production from these samples, shown in Table 6.1, exhibited a

consistent increase with decreasing molecular size. There is precedent for considering two causes: the obvious change in molecular size and configuration, and any differences in chemical composition between different size fractions (Dong et al., 2010; Mostafa and Rosario-Ortiz, 2013). For the sake of argument, consider the H_2O_2-independent pathway to •OH radical (e.g. H-atom abstraction by ^{3}DOM* or a low energy hydroxylator) (Latch and McNeill, 2006). Considering the first cause, if DOM chromophores that ultimately lead to •OH radicals are localized in the hydrophobic interior of DOM (as has been observed for the formation of $^1O_2$ from DOM), then a larger temperature dependence for bulk samples would be expected (contrary to the present data). In other words, increasing temperature for bulk samples may allow more •OH radicals to diffuse away from the DOM interior, due to changes in three-dimensional configuration with temperature, and react with benzene. A second explanation is found by considering the lack of temperature dependence of Φ_a for phenol production from p-benzoquinone photolysis. If one assumes a greater concentration of low energy hydroxylators (quinones) in bulk relative to fractionated DOM, than the observed activation energy, which is due to a combination of these species and other (temperature-dependent) pathways, would be lowered. Sharpless has suggested, based on studies of DOM redox properties (Aeschbacher et al., 2010; Wenk et al., 2011), that higher molecular weight DOM may contain a higher amount of donor and acceptor moieties than lower molecular weight DOM (quinones are often thought of as electron acceptors in DOM) (Sharpless, 2012), providing some evidence for this speculation. This issue should further be explored in future studies.

The observed results are counterintuitive when considering the charge-transfer model for DOM (Sharpless and Blough, 2014). Higher molecular weight DOM with more charge transfer interactions would be expected to have lower energy excited states, with the converse being true

for low molecular weight DOM. Making the assumption that charge transfer states are one pathway to $^\bullet$OH and that the transition state energy is similar for the high and low molecular weight DOM reactions (see discussion of this assumption in next paragraph), a higher activation energy for the higher molecular weight sample would be expected. Clearly the photochemistry and photophysics of this system are complex. One explanation, though speculative, can be derived from fluorescence measurements of DOM as a function of temperature. Previous work by Baker has shown that fluorescence intensity decreases with increasing temperature (Baker, 2005), probably due to increases in quenching of ^{1}DOM* or intersystem crossing. An increase in temperature is expected to increase the rate of internal conversion, vibrational relaxation, intersystem crossing, and, though unexplored for DOM, the rate of dynamic quenching of the excited singlet state. For higher molecular weight DOM where both intra- and intermolecular quenching likely occur, increases in dynamic quenching with temperature may be greater than in lower molecular weight DOM. Thus, decreases in ^{1}DOM* and ^{3}DOM* concentrations would ultimately decrease the concentration of charge-transfer states in high molecular weight DOM more significantly relative to lower molecular weight DOM.

Alternatively, if one assumes that different molecular weight fractions vary in chemical composition, then it would follow that their excited or transition states would also have different energies. This is an alternative, and perhaps more straightforward explanation than the one given in the previous paragraph. However, we wanted to put forth an interpretation of these results considering charge-transfer interactions, which has become a popular explanation for the photophysics and photochemistry of organic carbon (Sharpless and Blough, 2014).

6.5. Environmental Implications

The results from this work can be used to assess the temperature dependence of the steady state concentrations of $^{\bullet}$OH in surface waters, by considering DOM as the main source (photochemical) and sink (scavenging of $^{\bullet}$OH by DOM). The temperature dependence of the bimolecular rate constant between $^{\bullet}$OH and DOM has been previously measured for three of the DOM isolates examined in this study, with values ranging from about 12 to 30 kJ mol^{-1} (McKay et al., 2011). Assessing the effect of temperature on steady state •OH concentrations in natural systems involves taking into account both the (photochemical) production and scavenging due to DOM. Given that the magnitude of the activation energies for both processes are the same within a factor of two, the change in steady state concentrations over the range of environmentally relevant temperatures is expected to be minimal. Using temperature dependent data for PLFA, SRFA, and ESHA for both production and scavenging, steady state concentrations were calculated as a function of temperature from 10 to 40 °C and are plotted in Figure D.6. Thought changes are minimal, it is interesting to note that the direction of the change (i.e. increasing or decreasing steady state concentrations) are not the same for each isolate, which is ultimately determined by the difference in activation energies for the two processes.

7. Predicting Reactive Intermediate Quantum Yields from Dissolved Organic Matter Photolysis Using Optical Properties and Antioxidant Capacity

7.1. Abstract

The antioxidant capacity and formation of photochemically produced reactive intermediates (RI) was studied for water samples collected from the Florida Everglades with different spatial (marsh versus estuarine) and temporal (wet versus dry season) characteristics. Measured RI included triplet excited states of dissolved organic matter (^{3}DOM*), singlet oxygen (^{1}O$_2$), and the hydroxyl radical ($^{\bullet}$OH). Single and multiple linear regression modeling was performed using a broad range of extrinsic (to predict RI formation rates, R_{RI}) and intrinsic (to predict RI quantum yields, Φ_{RI}) parameters. Multiple linear regression models consistently led to better predictions of R_{RI} and Φ_{RI} for our data set, but poor prediction of Φ_{RI} for a previously published data set (McCabe and Arnold, 2016), probably because the predictors are intercorrelated (Pearson's $r >$ 0.5). Single linear regression models were built with data compiled from previously published studies ($n \approx 120$) in which E2:E3, S, and Φ_{RI} values were also measured. This study reveals that $^{\bullet}$OH formation is, in general, decoupled from ^{3}DOM* and ^{1}O$_2$ formation, providing supporting evidence that ^{3}DOM* is not a $^{\bullet}$OH precursor. Additionally, Φ_{RI} for ^{1}O$_2$ and ^{3}DOM* correlated negatively with antioxidant activity (a surrogate for electron donating capacity) for the collected samples.

7.2. Introduction

Dissolved organic matter (DOM) plays an important biogeochemical role in aquatic ecosystems [2]. The structure of DOM is highly dependent on its source (e.g., terrestrial vs.

aquatic) and history (e.g. microbial, photochemical processing) (Helms et al., 2008; McKnight et al., 2001; Sharpless et al., 2014). DOM that absorbs ultraviolet and visible light is classified as chromophoric dissolved organic matter (CDOM) (Ghassemi and Christman, 1968; Shapiro, 1964). This fraction determines the depth of the photic zone in natural waters and is a source and sink of reactive intermediates (RI) (Cory et al., 2009; Leifer, 1988; McCabe and Arnold, 2016; Page et al., 2014), which likewise influence several biogeochemical processes such as carbon mineralization, pathogen inactivation, and trace metal speciation and cycling (Blough and Zepp, 1995; Gao and Zepp, 1998; Kadir and Nelson, 2014; McCabe and Arnold, 2016). In addition, previous research has shown that light absorption by DOM can lead to photobleaching, production of carbon monoxide and carbon dioxide, and formation of lower molecular weight organic compounds (Gao and Zepp, 1998; Helms et al., 2008; Sharpless et al., 2014).

Absorption of light by DOM in aquatic environments ($\lambda > 290$ nm) produces RI including hydrogen peroxide (H_2O_2), singlet oxygen ($^1O_2$), excited triplet states ($^3DOM^*$), superoxide radical anion ($O_2^{\cdot-}$), and the hydroxyl radical ($^\cdot OH$) (Canonica and Freiburghaus, 2001; Cooper et al., 1988; Haag et al., 1984; Helms et al., 2008; McKnight et al., 2001; Sharpless et al., 2014; Vaughan and Blough, 1998; Zepp et al., 1981a; Zhang et al., 2012). The formation pathways, measurement, and importance of these RI has been discussed in detail in several recent reviews (Rosario-Ortiz and Canonica, 2016; Sharpless and Blough, 2014; Vione et al., 2014). The redox properties of DOM have also recently received significant interest, as this may be a controlling factor of DOM's ability to scavenge free radicals, interact with metals, and inhibit photosensitized contaminant degradation (Aeschbacher et al., 2012b; Canonica and Laubscher, 2008; Wenk et al., 2011; Wenk and Canonica, 2012). As such, electron accepting capacity (EAC) and electron donating capacity (EDC) have been quantified for freshwater and soil humic

substances using direct and mediated electrochemical methods (Aeschbacher et al., 2012b; 2010). Similarly, the antioxidant capacities of DOM (a surrogate for EDC), have been reported for DOM of various origins (Romera-Castillo and Jaffé, 2015).

Although it has been known for some time that RI are formed from DOM photolysis, there is still limited information on how DOM quantity and quality determine RI formation rates (R_{RI}) and apparent quantum yields (Φ_{RI}), respectively. In terms of DOM quantity, Peterson et al. (2012) demonstrated that DOC concentration and the absorption coefficient at 300 nm (a_{300}) were good predictors of $^1O_2$ steady state concentrations ($[^1O_2]_{ss}$) for a notably large dataset collected from Lake Superior (USA) and inflowing rivers (Peterson et al., 2012). More recently, Timko et al. (2014) measured $^3DOM^*$, $^1O_2$, and $^{\bullet}OH$ formation rates and steady state concentrations from surface water samples from the Florida Everglades, and also observed that RI formation rates positively correlated with light absorption, specifically the absorption coefficient at 254 nm (a_{254}) (Timko et al., 2014), particularly for samples enriched in terrestrial DOM in contrast to microbial DOM. Similar results observed by Haag and Hoigné (1986) (Haag and Höigne, 1986), strongly suggest that the rate of RI formation is a function of the amount of DOM:

$$R_{RI} = \sum_{all\ \lambda} R_{a-DOM,\lambda} \Phi_{RI,\lambda} = [DOM] \sum_{all\ \lambda} k_{a-DOM,\lambda} \Phi_{RI,\lambda}$$

Equation 7.1

In Equation 7.1, $R_{a\text{-DOM},\lambda}$ and $k_{a\text{-DOM},\lambda}$ are the rate of light absorption and the specific rate of light absorption by DOM, respectively.

In terms of DOM quality, several reports have examined links between RI quantum yields and DOM optical and physicochemical properties (Boyle et al., 2009; Dalrymple et al., 2010; Haag and Höigne, 1986; Helms et al., 2008; Mostafa and Rosario-Ortiz, 2013; Sharpless, 2012). It has been consistently shown that Φ_{RI} ($^3DOM^*$, $^1O_2$, H_2O_2, and more recently $^{\bullet}OH$) positively

correlate with both spectral slope (S) and absorbance ratios (e.g., Abs_{250}/Abs_{365} = E2:E3) (Coelho et al., 2010; Dalrymple et al., 2010; Halladja et al., 2007; McCabe and Arnold, 2016; McKay et al., 2016; Sharpless and Blough, 2014) and fluorescence quantum yields (E. Lee et al., 2013; McKay et al., 2016; Mostafa et al., 2014a), all of which are indicators of DOM molecular weight (McKay et al., 2016; Peuravuori and Pihlaja, 1997). Most research has focused on S or E2:E3 to model RI quantum yields using linear regression (Dalrymple et al., 2010; McCabe and Arnold, 2016; Page et al., 2014; Sharpless, 2012). These models lead to similar results (i.e. regression coefficients) for these relationships, the most commonly explored being the relationship between Φ_{1O2} and E2:E3. These optical properties vary with DOM molecular weight and inverse correlations between Φ_{RI} and DOM molecular weight have been consistently demonstrated (Boyle et al., 2009; McKay et al., 2016; Peuravuori and Pihlaja, 1997).

Besides S and E2:E3, few intrinsic variables have been explored in regression analysis of RI data. Timko et al., reported a strong coupling between RI formation rates and the abundance of terrestrial humic substances for a similar set of Everglades DOM samples using excitation emission matrix (EEM) fluorescence measurements and parallel factor analysis (PARAFAC) (Timko et al., 2014). These authors also reported linear relationships between RI formation rates and steady state concentrations and DOM optical properties, but for a rather small dataset. To our knowledge, most regression modeling of RI data thus far have used a single regressor as opposed to a multivariate approach. An issue that further hinders complete understanding of this topic is that many reports do not provide complete datasets in tabular form, which would facilitate broader modeling applications. Our study aims are to address this knowledge gap by building regression models for a diverse set of DOM physicochemical properties, incorporating previous studies' data into these regression models, and by investigating DOM antioxidant

capacity as a predictor of photoreactivity. To this end, R_{RI} and Φ_{RI} were measured for whole water DOM samples (n=21) from the Florida Everglades [Everglades National Park (ENP), Florida, USA]. The samples were comprised of DOM of diverse sources and environments (see below). A diverse set of DOM physicochemical properties were explored in linear regression analysis with measured R_{RI} and Φ_{RI}. Additional regression analysis was done by incorporating data from previous studies in an attempt to compare and consolidate existing models. In an effort to better predict Φ_{RI} based on DOM chemical properties, antioxidant capacity was measured for each sample using a recently developed assay (Romera-Castillo and Jaffé, 2015). As well as contributing to the steadily growing knowledge base of the relationships between DOM optical properties and RI production, this study provides one of the first analyses of relationships between Φ_{RI} and DOM antioxidant capacity.

7.3. Experimental methods

7.3.1 Chemicals.

Furfuryl alcohol (FFA, 97+%, TCI America), phenol (99+%, Sigma Aldrich), 2,4,6-trimethylphenol (TMP, 99+% Alfa Aesar), benzene (99+%, Alfa Aesar), methanol (HPLC grade, VWR), and phosphoric acid (85%, JT Baker) were used as received. Varian Bond Elut PPL cartridges were purchased from Agilent Technologies. Suwanee River NOM (1R101N) was purchased from the International Humic Substances Society, dissolved at either ~5 or ~10 mg$_C$ L^{-1} in 10 mM pH 7.2 phosphate buffer, and filtered through 0.7 μm muffled glass fiber filters (GF/F) prior to use.

7.3.2 Sampling.

As the largest subtropical wetland in the United States, the Everglades not only exhibits diverse vegetation, but is unique in its low concentrations of iron, phosphate, nitrate, and nitrite (Chambers and Pederson, 2006), and exhibits high variability in DOM character (M. Chen et al., 2013; Maie et al., 2005).
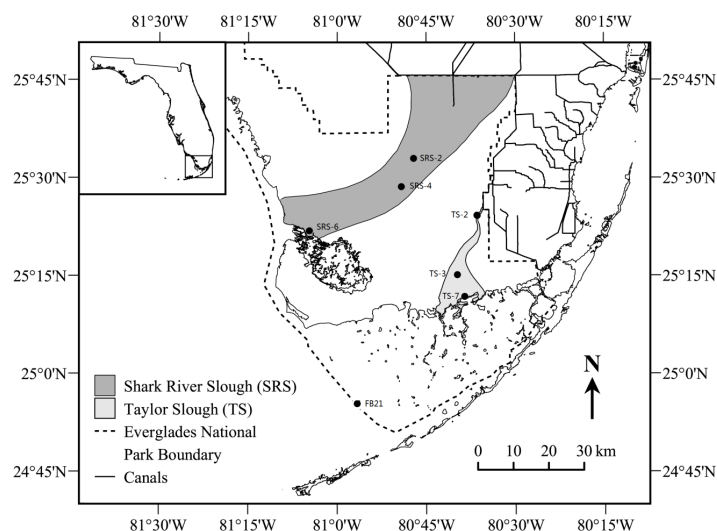
Figure 7.1. Sampling sites along Shark River Slough (SRS-2/4/6), Taylor Slough (TS-2/3/7) and Florida Bay (FB21). Sub-environments: freshwater marsh (peat; SRS-2/3), freshwater marsh (marl; TS-2), mangrove estuarine (peat; SRS-4/6), mangrove estuarine (TS-7), and Florida Bay (FB) estuary (FB-21).

Two main hydrological systems were sampled in ENP (Figure 7.1): Shark River Slough (SRS) and the Taylor Slough (TS), which drain freshwater marshes through mangrove estuaries into the Florida Shelf and Florida Bay (FB) respectively, creating a salinity gradient along SRS and TS transects. The seasonal climate variations in the Everglades represent clear wet (between June and November) and dry seasons (December to May) with about 80% of total annual precipitation occurring in the wet season. In the dry season, freshwater flows are reduced and estuarine residence time and salinity intrusions increase. These altering processes are responsible

for nutrient availability and water quality (Childers et al., 2006) which includes changes in DOM sources and residence times, with potential effects on its reactivity. The Shark River Slough estuary is strongly connected to the Gulf of Mexico and receives significant tidal influence.

Samples were collected from long-term monitored FCE-LTER sites located in the Shark River Slough (SR2, SR4, and SR6), Taylor Slough (TS2, TS3, and TS7) and Florida Bay (FB21) in September, October, and November of 2014. Samples were collected as surface water (maximum depth of 1 ft) in pre-rinsed (trace metal grade nitric acid, base, then deionized water) polyethylene bottles and transported back to the lab on ice. Samples were then filtered through muffled 0.7 µm filters (Gelman GF/F) and stored in polyethylene bottles at 4 °C.

DOM composition varies on spatial scales in the Everglades, in part due to source material changes (M. Chen et al., 2013; Maie et al., 2005). Upstream SRS and TS, both freshwater marshes, are dominated by sawgrass (*Cladium*), spikerush (*Eleocharis*) and periphyton. TS sites dry more frequently and for a longer duration (short hydroperiod) compared to SRS sites (long hydroperiod) and are thus characterized as marl soils rather than peat soils. Biomass in downstream TS and SRS sites is dominated by mangroves, however, TS sites have significantly smaller trees, and lower rates of litterfall and root production. FB biomass is dominated by seagrass. Overall, these vegetation and hydrological patterns result in highly variable DOM character on spatial and temporal scales.

7.3.3 Antioxidant activity measurement.

DOM antioxidant activity was assessed by reacting 2,2-diphenyl-1-picrylhydrazyl (DPPH$^\bullet$) with DOM in methanol solution (Brand-Williams et al., 1995; Romera-Castillo and Jaffé, 2015; Wei et al., 2010). DPPH$^\bullet$ has a characteristic absorbance at 515 nm that is reduced by reaction with an antioxidant (AH) or a radical species (R$^\bullet$). This assay has been described in detail

previously (Brand-Williams et al., 1995; Wei et al., 2010) and recently adapted to DOM (Romera-Castillo and Jaffé, 2015). Briefly, a volume of 1 L of sample was extracted using PPL cartridges with methanol as the eluent. The resulting methanolic extracts were mixed with DPPH$^{\bullet}$ reagent (70.9 µM), shaken, and left to react in the dark at room temperature for 15 minutes. The loss in absorbance at 515 nm was measured using a Varian Cary 50 spectrophotometer. The antioxidant activity or redox potential is expressed as

$$A_{\times}A = \left(1 - \frac{A_A - A_C}{A_B}\right) \times 100$$ Equation 7.2

where A_A is the absorbance of the antioxidant sample at the end of the reaction time, A_C is the absorbance of the sample blank at the beginning of the reaction time (t=0), and A_B is the absorbance of the methanol blank at the beginning of the reaction time (t=0). The antioxidant activity of a sample is reported as the $A_{\times}A_{50}$ value that is the antioxidant activity for a 50 mg L^{-1} of dissolved organic carbon (DOC) of the methanol extracted sample based on the calibration curve (see (Romera-Castillo and Jaffé, 2015)). A greater $A_{\times}A_{50}$ value corresponds to a greater DOM antioxidant capacity.

It is important to note at this point that these values were measured on PPL extracts, whereas Φ_{RI} values were measured on whole water samples. Control experiments performed to assess the validity of this approach showed that the comparison is valid within the scope of this work (see Appendix E for detailed discussion).

7.3.4 DOC and optical property measurements.

DOC concentrations were measured after filtration (0.7 µm GF/F) with a Shimadzu TOC-5000 analyzer using high temperature combustion. DOC concentrations of the PPL extracts were determined by drying an aliquot (200 µL) of each methanol DOM extract with N_2 gas and freeze

drying under vacuum for 2 hr to insure complete dryness of the samples. Once dried, all the samples were re-dissolved with 10 mL Milli-Q water for DOC measurement.

DOM absorbance was measured at both labs participating in this study. Absorbance and fluorescence spectra were measured at FIU for whole water samples using an Aqualog spectrofluorometer (Horiba) with a 1 cm quartz cuvette. The excitation wavelength was scanned from 240 nm to 621 nm with an increment of 3 nm. The emission wavelength was scanned from 241 nm to 622 nm in 1.5 nm steps. UV-Vis spectra were collected from 240 nm to 621 nm with an increment of 3 nm simultaneously. The optical parameters used in this study that derived from these measurements include HIX (humification index) (Huguet et al., 2009; Senesi et al., 1991; Zsolnay et al., 1999); absorption coefficient at 255 nm [a_{255} (cm^{-1})], and the Slope Ratio (S_R) (Helms et al., 2008). Absorbance spectra at CU Boulder were measured in triplicate using a Cary 100-Bio in a 1 cm quartz cuvette, scanned from 800 to 200 nm, and baseline corrected to deionized water. The optical parameters used in this study that derived from these measurements included absorption coefficients (Naperian, m^{-1}) at 254 and 300 nm (a_{254} and a_{300}), E2:E3 (Abs_{250}/Abs_{365}), spectral slope ($S_{300-600}$), and specific ultraviolet absorbance at 254 nm (SUVA$_{254}$) and 300 nm (SUVA$_{300}$). $S_{300-600}$ was calculated by nonlinear regression over 300 to 600 nm using a single exponential model with $\lambda = 350$ nm as the reference wavelength. S is used to denote spectral slope in general and (when provided) subscripts denote the wavelength range over which the regression was performed.

7.3.5 Photochemical methods and regression modeling.

The methods used here to measure RI formation rates and calculate Φ_{RI} values have been discussed in detail previously and more information is provided in Appendix E (Bodhipaksha et al., 2015; Dong and Rosario-Ortiz, 2012; Mostafa and Rosario-Ortiz, 2013). We note that no

effort was made to distinguish between free ·OH and low energy hydroxylators in ·OH measurements (McKay and Rosario-Ortiz, 2015; Page et al., 2011). Linear regression modeling was performed using the Statistics Toolbox in Matlab (R2015a). Model terms and prediction intervals were evaluated at α=5%. The 95% prediction interval (PI) and R^2 predicted (R^2_{pred}) values were calculated to assess uncertainty in predicting future observations. R^2_{pred} was chosen as a model diagnostic over R^2 because it penalizes for model over fitting (especially important for multiple linear regression). The Kolmogrov-Smirnov test was used to assess residual distribution (studentized residuals were used). Normal probability plots of studentized residuals and plots of studentized residuals versus effects were further evaluated for normalcy.

7.4. Results and Discussion

7.4.1 General observations and cluster analysis.

Selected water quality data (DOC values, absorption coefficients, and salinities) and RI data (formation rates and quantum yields) are provided in Appendix E. Samples could generally be divided into three groups based DOC concentrations and absorption coefficients. Low absorbing waters with lower DOC concentrations were from the seagrass-dominated, marine, Florida Bay site (FB21). Freshwater marsh samples (TS2, TS3, SRS2) and the upper estuary samples (SRS4) comprised the second group, having intermediate to high absorption coefficients and DOC values. SRS4 is at the interface of freshwatwer marshes and estuarine, mangrove-influenced waters (Figure 7.1) and thus this sample's DOM character is a function of season (i.e. freshwater marsh and estuarine influenced in wet and dry season, respectively). The third group consisted of two estuarine samples (SRS6 and TS7), which are associated with mangrove forests and significant tidal action (SRS6) and saltwater intrusion (TS7 during dry season).

To further identify relationships based on optical character and reactivity between samples, hierarchical cluster analysis was performed using Φ_{RI} values, antioxidant activity ($A_{\times}A_{50}$) values, and optical properties (E2:E3, a_{255}, HIX). The results from these analyses are shown in Figure E.1, and as previously reported for molecular composition and optical properties only (M. Chen et al., 2013; Maie et al., 2005), a clear spatial cluster was evident, likely driven by DOM source based on the sites' soil type and plant cover characteristics. The cluster clearly separated the dataset (using monthly samples; Figure E.1a) into sub-environment types as follows: Taylor River mangrove estuary site (TS7; long inundation), Shark River mangrove estuary site (SRS6; tide influenced), Shark River mangrove ecotone (SRS4), Taylor River freshwater marsh sites (TS2, TS3; short hydroperiod), Shark River freshwater marsh site (SRS2; long hydroperiod) and marine the marine Florida Bay site (FB21; seagrass dominated). Cluster analysis using averaged monthly data was also performed (Figure E.1b) with similar results, with the samples grouping into similar sub-environments such as Florida Bay, fresh water marshes, and mangrove-influenced sites. This suggests that Everglades DOM can be categorized based on a combination of compositional features (optical properties) and photoreactivity (RI data). A notable exception in the general cluster distribution however, was that the November TS7 sample fell out from the general mangrove group (Figure E.1a). The salinity value for this sample was 25.3 practical salinity units (PSU), which is about three times higher than the other two months at this site (average = 9.6 PSU) indicating that the TS7 site was strongly influenced by Florida Bay water intrusions at that time. November is the beginning of dry season in the Everglades, when reduced freshwater discharge at this site has previously shown to lead to a shift from estuary DOM to marine DOM (M. Chen et al., 2013), explaining why the TS7 November sample had a low a_{255} and DOC concentration, more similar to Florida Bay samples.

These observations are consistent with previous results, in which the fringe mangrove environment in ENP has been reported to have higher DOC concentrations and highly aromatic DOM (M. Chen et al., 2013), leading to higher absorption coefficients for TS7 as compared to TS2 and TS3 which are overlaying marl soils. Mangrove-influenced sites (SRS6 and TS7) had consistently greater $SUVA_{254}$ values than sites further upstream, whose DOM input was dominated by peat soils and vegetative leaching, including significant periphyton-derived inputs (M. Chen et al., 2013). In addition, mangrove-influenced samples exhibited the greatest antioxidant capacity, likely a result of an increased proportion of polyphenols such as tannins (Romera-Castillo and Jaffé, 2015). It is interesting to see such a clear agreement between this cluster analysis (including RI data) and previously reported clusters (M. Chen et al., 2013; Maie et al., 2005), (based on molecular or optical properties only) for DOM in diverse Everglades sub-environments, suggesting that this sample set is well suited to investigate the relationships between DOM source and reactivity as reflected through RI production and antioxidant activity.

7.4.2 Regression models between RI formation rates and DOM quantity.

R_{RI} and Φ_{RI} are shown in Appendix E and fall within the range of previously measured values for each species (Vione et al., 2014) (0.0249 to 0.104 for Φ_{1O2}, 1.30×10^{-5} to 4.76×10^{-5} for Φ_{OH}, and 35.0 to 318 M^{-1} for f_{TMP}). Figure E.3 shows regression models for R_{RI} with DOC concentration, a_{254}, and a_{300} as potential predictors. Significant positive correlations were observed between all R_{RI} and these predictors, although R^2_{pred} varied greatly (0.1 to 0.91). The positive correlations observed between R_{RI} and DOC concentration, a_{254}, and a_{300}, all of which describe the quantity of DOM or CDOM, supports the hypothesis that DOM is the photosensitizer producing these species. The linear relationship between R_{OH} and DOC

concentration suggests that DOM (and not nitrite or nitrate) is the source of $^{\bullet}$OH in this system, particularly when considering that nitrate and nitrite concentrations are known be low in the Everglades (Davis et al., 2003). This fact was confirmed for these samples using ion chromatography (Laboratory for Environmental and Geological Studies, CU Boulder). All samples were below the detection limit for nitrite (0.01 mg$_{NO2^-}$ L^{-1}) and the highest nitrate concentration was 3.5 mg$_{NO3^-}$ L^{-1} (~0.056 mM). These levels are too low to be a competitive source of $^{\bullet}$OH at the elevated DOC concentrations in these samples (see Appendix E) (Dong and Rosario-Ortiz, 2012; Vione et al., 2006).

7.4.3 Relationships between RI quantum yields and DOM optical properties.

Because the rate of RI formation is proportional to the quantum yield ($R_{RI} = R_{a\text{-}DOM}\Phi_{RI}$), it is desirable to have a predictive model for Φ_{RI} based on easily measurable DOM properties. Optical properties based parameters such as SUVA, E2:E3 and S have historically been used to model RI formation rates and Φ_{RI} (Dalrymple et al., 2010; McCabe and Arnold, 2016; Sharpless, 2012), and as discussed above there is a need to examine additional predictors and consolidate previous models. Regression models are presented in this section and potential interpretations of the data based on DOM character are given in the following section.

In this work, several DOM optical properties were examined to identify potential predictors of Φ_{RI} including E2:E3, $S_{300-600}$, S_R, SUVA$_{254}$, SUVA$_{300}$ and HIX (Table 7.1). Figure E.4 shows regression models for Φ_{RI} with E2:E3, S, and S_R as potential predictors. Significant positive correlations were observed between all Φ_{RI} and E2:E3 and $S_{300-600}$. Only Φ_{1O2} was significantly correlated to S_R (although poorly, $R^2_{pred} = 0.09$). R^2_{pred} was consistently higher for Φ_{1O2} and f_{TMP} than for Φ_{OH} when E2:E3 or $S_{300-600}$ was the predictor. This difference in the behavior for Φ_{OH}

has been observed for water samples of natural and anthropogenic origins undergoing different treatments (size fractionation and chemical reduction) as well as for prairie pothole waters (McCabe and Arnold, 2016; McKay et al., 2016). While in the former study there was no significant correlation reported between Φ_{OH} and E2:E3 (McKay et al., 2016), in the later study (McCabe and Arnold, 2016), the Φ_{OH}-E2:E3 relationship was weaker than the f_{TMP}- and Φ_{1O2}-relationships (based on reported R^2 values of 0.34, 0.87, and 0.82, respectively). For our dataset, $S_{300-600}$ was a better predictor of Φ_{1O2} and f_{TMP} (R^2_{pred} = 0.80 and 0.89, respectively) than E2:E3 (R^2_{pred} = 0.69 and 0.69, respectively).

With regards to other optical parameters, Φ_{RI} correlated negatively to HIX, SUVA$_{254}$, and SUVA$_{300}$ (Figure E.5). HIX is a metric that is intended to describe the degree of DOM humification and is a measure of how red-shifted the fluorescence spectrum is (Huguet et al., 2009; Senesi et al., 1991; Zsolnay et al., 1999). In addition, higher HIX values have been linked to higher DOM aromaticity (Senesi et al., 1991). Although this relationship has not been reported previously, it is consistent with the negative correlations observed between Φ_{RI} and SUVA$_{254}$, which specifically describes DOM aromaticity (Weishaar et al., 2003).

The correlations between Φ_{RI} and DOM optical properties observed here have been attributed in part to the effects of intramolecular (charge transfer, CT) interactions, which influence the steady state concentration of DOM excited states that are precursors to RI (Boyle et al., 2009; Ma et al., 2010; Sharpless and Blough, 2014). In contrast, differences in molecular character due to DOM source and degree of degradation could play an important role in determining optical properties and Φ_{RI} (this has previously been referred to as an individual chromophore model). The trends and patterns observed in the current dataset, which exhibits a

large range of optical property values, can be explained by a combination of these two models, as discussed below.

7.4.4 Effects of seasonal and temporal variations on DOM character and Φ_{RI}.

DOM character in the Everglades is a function of source (spatial scale) and season (temporal scale; wet/dry) (M. Chen et al., 2013; Maie et al., 2005; Yamashita et al., 2010), which in turn influenced observed optical and photochemical properties.

Taylor Slough and Shark River sites exhibited a general increase in E2:E3 and $S_{300-600}$, decrease in A_xA_{50} and $SUVA_{254}$, with a concomitant increase in Φ_{1O2} and f_{TMP} going from wet (September and October) to early dry (November) season. There is little variation in Φ_{OH} between sites and sampling times; most of the values are $\sim 1.5 - 2 \times 10^{-5}$ (FB21 sites are a factor of about three greater). This temporal trend is consistent with enhanced dry season condition (November) driven estuarine inputs, in which the primary DOM source is seagrass-derived and is characterized by low molecular weight and low aromaticity (M. Chen et al., 2013). From a physicochemical standpoint, this observation can be attributed to a lessened ability of low molecular weight DOM molecules to form intramolecular CT interactions, increasing the steady state concentration of DOM excited states leading to RI (Boyle et al., 2009; McKay et al., 2016). However, the presence of chromophores more reactive towards forming RI cannot be excluded without further molecular-level characterization (e.g. NMR or FTICR-MS). The importance of sample-specific characteristics in RI formation was indicated by Timko et al., who demonstrated stronger correlations to specific PARAFAC components derived from fluorescent measurements than to optical properties from absorbance measurements (Timko et al., 2014). In addition, these authors reported a stronger correlation between $^{\bullet}$OH formation rates and $SUVA_{254}$ for their TS transect (compared to SRS), suggesting differences in the molecular composition of the

aromatics involved in the generation of $^\bullet$OH. Indeed, the abundance of microbial-like humic and protein-like PARAFAC components and non-lignin phenols (particularly at TS7 and FB21) might support this hypothesis (M. Chen et al., 2013; Maie et al., 2005).

Conversely, there is a general decrease (north to south) in E2:E3 and $S_{300-600}$, increase in SUVA$_{254}$ (excluding FB21) and A$_x$A$_{50}$with a concomitant decrease in Φ_{1O2} and f_{TMP} spatially along the Taylor Slough and Shark River Slough. This spatial trend is potentially attributable to two competing processes: varied DOM input [freshwater marshes (high molecular weight and low/intermediate aromaticity) to mangrove forest (high molecular weight and high aromaticity)] (M. Chen et al., 2013), and photo-bleaching of DOM from north to south (which would be expected to form lower molecular weight, less aromatic molecules) (Helms et al., 2008; Sharpless et al., 2014). Due to a high level of shading as a consequence of the presence of aquatic vegetation and elevated CDOM, it is unlikely that the latter hypothesis is the dominant process. In contrast, DOM source changes along these transects have been clearly established as explained above. In addition, mangrove-derived DOM contains a high amount of tannins, which have a greater proportion of polyphenols than aromatic ketones/aldehydes (Maie et al., 2008) (typical ^{3}DOM* and ^{1}O$_2$ precursors) (Canonica et al., 1995). Thus, a reasonable hypothesis is that a decreased amount of ^{3}DOM* precursors (and thus ^{1}O$_2$ sensitizers) are present in the SRS6 and TS7 sites, leading to decreased f_{TMP} and Φ_{1O2}, indicating that mangrove forest inputs to the DOM pool are critical in controlling DOM photoreactivity in southern ENP. Although mangroves are known to contain significant amounts of tannins (Maie et al., 2008), the observed effect of mangrove-derived DOM on Φ_{RI} might be related to the antioxidant capacity of these compounds (see 7.4.8).

7.4.5   Effect of salinity on R_{RI} and Φ_{RI}.

Because of the large salinity gradient in ENP (increasing salinity north to south) the potential exists for probe compound reactions to be influenced by general and specific ion effects, thus affecting R_{RI} and Φ_{RI}. Although this topic is mostly unexplored, Parker et al. have examined the effects of high ionic strength and halides on $^3DOM*$ photochemistry (Parker et al., 2013). These authors showed that high ionic strength decreases the rate constant for $^3DOM*$ loss, increases $[^3DOM*]_{ss}$, but does not affect the apparent quantum yield for $^3DOM*$ formation. Our dataset was examined for general and specific ion effects by comparing R_{RI} and Φ_{RI} to total salinity, $[Cl^-]$, and $[Br^-]$ (Figure E.13 and Figure E.14). There were significant decreases in R_{RI} with increasing salinity, but this trend was likely influenced by the concomitant decrease in DOC for these samples. Only four of nine relationships between Φ_{RI} and salinity, $[Cl^-]$, or $[Br^-]$ were significant, and the highest degree of correlation was between f_{TMP} and total salinity (R^2_{pred}=0.39). These data, along with Figure E.12 suggests that general and specific ionic strength effects are likely not playing a significant role in determining Φ_{RI} for this study site.

7.4.6   Multiple linear regression models and consolidation of single linear regression models.

While there are clearly many physicochemical factors controlling Φ_{RI} for these samples, correlations with E2:E3 and $S_{300\text{-}600}$ are consistent with previous reports (Dalrymple et al., 2010; McCabe and Arnold, 2016; Sharpless, 2012). E2:E3, $S_{300\text{-}600}$, HIX, SUVA$_{254}$, and SUVA$_{300}$ are all thought to be surrogates for DOM molecular weight, structure, and history (source and transformations) (Helms et al., 2008; McKay et al., 2016; Peuravuori and Pihlaja, 1997). However, there has yet to be a compilation and comparison of published correlations between

Φ_{RI} and these physicochemical parameters. In addition, no attempts at using multiple linear regression to predict R_{RI} or Φ_{RI} have been published. We discuss these two points below.
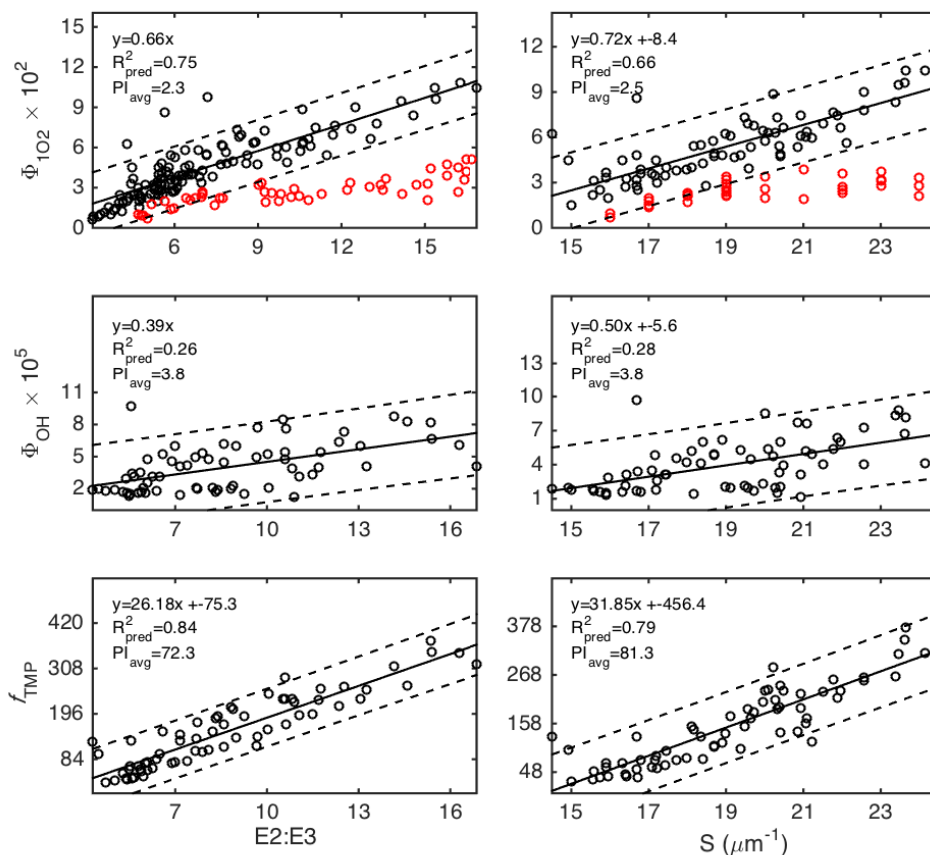
Figure 7.2. Regression models for absorbance predictors used in estimating RI quantum yields. Solid line indicates the model prediction and dashed lines indicate the 95% prediction interval. The fitted model equation, R^2_{pred} , and average prediction interval are shown for each prediction-regressor pair. Data in red are from Peterson et al. (2012) and are not included in regression models. Data used in the model included that from this study, Dalrymple et al., Mostafa and Rosario-Ortiz (un-treated samples; i.e., not oxidized), Bodhipaksha et al., and McCabe and Arnold.

Although multiple linear regression resulted in better predictability (i.e. R^2_{pred}) for the ENP samples, all regressors were intercorrelated, even when standardized (i.e. $\bar{x} = 0; \sigma = 1$) ; see Table E.2 through Table E.6). Additional analysis demonstrated that these models are probably

not applicable in general. Further details are provided in Appendix E. Thus, previously published relationships between Φ_{RI} and optical properties were compiled (Bodhipaksha et al., 2015; Dalrymple et al., 2010; McCabe and Arnold, 2016; Mostafa and Rosario-Ortiz, 2013; Peterson et al., 2012), focusing on correlations between Φ_{RI} and E2:E3 and S because these data were the most widely available, and were shown above to be significant predictors of Φ_{RI}. Inclusion of additional physicochemical properties described herein would reduce the amount of published data that could be used in the modeling effort. Regression models for the compiled dataset are shown in Figure 7.2 and exhibit good predictability for Φ_{1O2} and f_{TMP} using either E2:E3 or S ($0.66 < R^2_{pred} < 0.84$). However, as observed for the ENP samples (Figure E.4 and Figure E.5), these models poorly predict Φ_{OH} ($R^2_{pred} \approx 0.3$). It is worth noting that Φ_{1O2} data from the study of Peterson et al. (Peterson et al., 2012) (data shown in red in Figure 7.2) were not included in either the Φ_{1O2}-E2:E3 or Φ_{1O2}-S regression models because of their obvious deviation from the trend exhibited by the other studies. This deviation is surprising and its reasons remain undetermined.

As suggested by the data shown in Figure 7.2, the slope of the linear relationship between Φ_{1O2} and E2:E3 may depend on the range of E2:E3 values used in the regression. To test this hypothesis, we determined slope parameters using subsets of the data presented in Figure 7.2. These results are shown in Table E.7 and demonstrate that indeed the slope is dependent on the range of E2:E3 (and corresponding Φ_{1O2}) values used in the linear regression. For example, analysis of samples with E2:E3 values ranging from 3.1-6.0 (includes 50% of data) compared to 3.1-16.9 (includes 100% data) results in linear regression slopes of 1.16 ± 0.18 (mean $\pm$ standard error) compared to 0.66 ± 0.035, respectively. Whether this "two regions" result is general

should be a topic of future research. However, it is notable that there does not seem to be a similar partitioning of the data if S is used as the regressor. The model presented here is robust in that it has good predictability for the majority of previously published studies examined (four out of six). This potentially suggests that Φ_{RI}-optical property relationships may be more similar than previously thought (McKay et al., 2016; Peterson et al., 2012). Further research is needed to clarify this issue, and future efforts should focus on measurements of Φ_{RI} for DOM samples with high E2:E3 values.
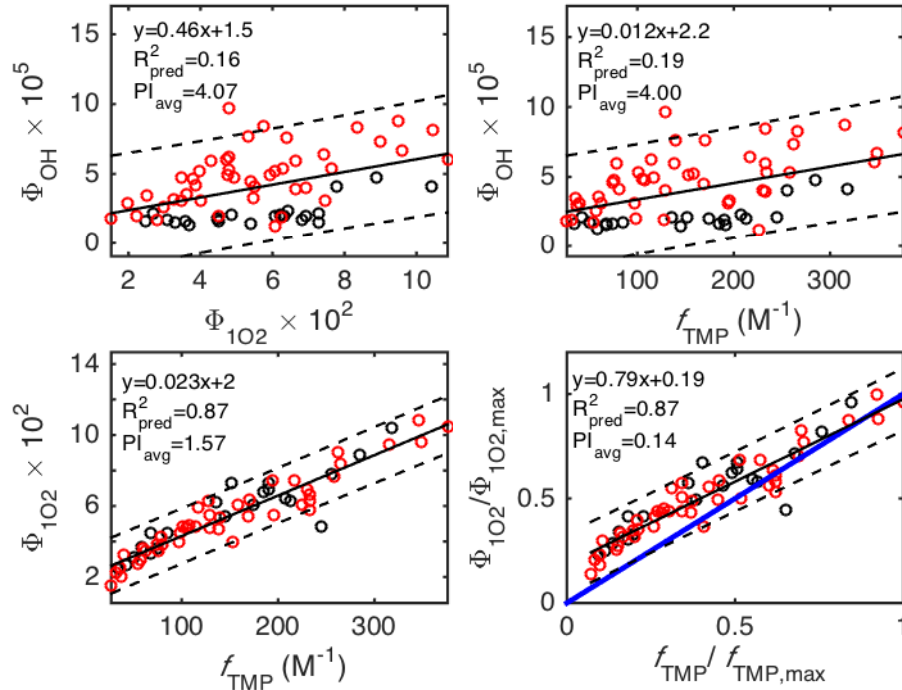
Figure 7.3. Inter-correlations between measured RI quantum yields. Data from McCabe and Arnold are shown in red and data from this study are shown in black. One to one line shown in blue for comparison.

7.4.7 Comparison of Φ_{RI} and poor predictability of Φ_{OH}.

Intercorrelations between different Φ_{RI} values measured in this study are shown in Figure 7.3. The lack of correlation between Φ_{OH} and Φ_{1O2} or f_{TMP} indicates that ^{3}DOM* is not a

significant precursor to $^{\bullet}$OH, which is consistent with previous studies (Gan et al., 2008; McKay et al., 2016; McKay and Rosario-Ortiz, 2015; Pochon et al., 2002). The correlation between f_{TMP} and Φ_{1O2} is expected given $^1O_2$'s formation pathway: $^3DOM^* + O_2 \rightarrow DOM + {}^1O_2$ (Haag and Höigne, 1986; Zepp et al., 1981b), and previous authors have suggested that O_2 could be used as a probe for $^3DOM^*$ (McNeill and Canonica, 2016; Sharpless and Blough, 2014). Surprisingly, this correlation has not been explored quantitatively in the literature and further studies are warranted. Combining this knowledge with a better understanding of the relationship between f_{TMP} and actual (but difficult to accurately determine) $^3DOM^*$ quantum yields would facilitate use of Φ_{1O2} as an assessment of $^3DOM^*$ reactivity. The strong linear relation ($R^2_{pred} \approx 0.9$) observed here between Φ_{1O2} and f_{TMP} indicates that this is probable.

All regression models built for Φ_{OH} exhibited weaker predictability than for Φ_{1O2} and f_{TMP}. Figure 7.2 shows that Φ_{1O2} and f_{TMP} values span an order of magnitude, whereas Φ_{OH} varies by approximately a factor of three. The highest Φ_{OH} values were for the three FB21 samples ($\sim 4.5 \times 10^{-5}$), whereas all others clustered around $1.5\text{-}2 \times 10^{-5}$. Thus, it is possible that the weaker correlations between DOM physicochemical properties and Φ_{OH} are due to the smaller range of Φ_{OH} values (as compared to Φ_{1O2} and f_{TMP}). In terms of predicting (DOM-derived) $^{\bullet}$OH steady state concentrations in natural waters a more effective strategy may be to use linear regression models for R_{OH}, which exhibited excellent predictability for ENP samples ($R^2_{pred} \approx 0.9$). The full application of this strategy would require characterizing the irradiance for the system of interest.

7.4.8 RI and redox potential ($A_{\times}A_{50}$).

Previous studies using electrochemical methods have reported EDC and EAC for a number of DOM isolates (Aeschbacher et al., 2012b; 2010). It was recently shown that the antioxidant

capacity of DOM as measured by free radical scavengers correlated well with EDC (Romera-Castillo and Jaffé, 2015). This observation is expected given that DOM components such as polyphenols are known for their antioxidant capacity (Halliwell, 1990; Rice-Evans et al., 1996) and are thought to be the main electron donating moieties within DOM (Aeschbacher et al., 2012b).
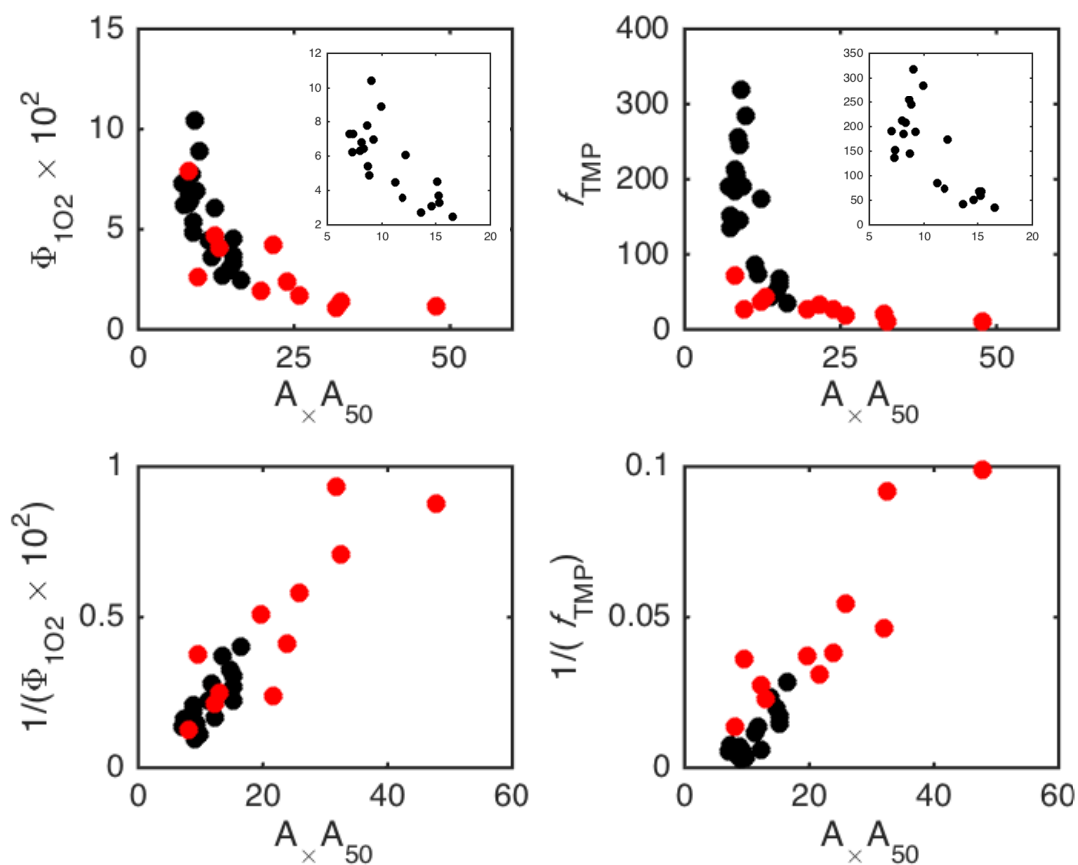
Figure 7.4. Relationships between Φ_{1O2}, f_{TMP} and $A_{\times}A_{50}$. EDC values from Bodhipaksha et al.(Bodhipaksha et al., 2015) were converted to $A_{\times}A_{50}$ using the relationship determined by Romera-Castillo and Jaffé (2015) - $A_{\times}A_{50} = 17.48 \times EDC - 0.12$ - and are shown in red with the corresponding Φ_{1O2} and f_{TMP} values. Data from this study are shown in black. Insets correspond to first row with a narrower $A_{\times}A_{50}$ range.

In this study, antioxidant activity was measured for each DOM sample using the abovementioned methodology (Romera-Castillo and Jaffé, 2015), and significant negative

correlations were observed between $A_{\times}A_{50}$ with Φ_{1O2} and f_{TMP}, but not with Φ_{OH} (Figure 7.4 inset and Figure E.17). It is important to note that degradation of the $^3DOM^*$ probe TMP is not inhibited by DOM (i.e. $TMP^{\bullet+} + DOM \rightarrow TMP + DOM^{\bullet+}$) (Canonica and Laubscher, 2008), and therefore, the above observation for f_{TMP} is attributable to changes in DOM character and not inhibition of TMP degradation. This result is consistent with a previous study that measured f_{TMP}, Φ_{1O2}, and EDC for samples of varying origins (combination of wastewater organic matter isolates and IHSS-purchased isolates) (Bodhipaksha et al., 2015). EDC values from this study were used to calculate $A_{\times}A_{50}$ based on the linear relationship reported by Romera-Castillo and Jaffé (Romera-Castillo and Jaffé, 2015), $A_{\times}A_{50} = 17.48 \times EDC - 0.12$, and these data are plotted in Figure 4 for comparison. Taken together, Figure 4 indicates that Φ_{1O2} and f_{TMP} have some type of non-linear dependence on $A_{\times}A_{50}$. This trend agrees with suggestions in the literature that electron rich DOM (larger $A_{\times}A_{50}$ or EDC values) is more capable of forming intramolecular interactions (charge transfer complexes) that would decrease $[^3DOM^*]_{ss}$ via excited state electron transfer, a possibility that cannot be excluded or verified based on the present data (Sharpless and Blough, 2014). In other words, $^3DOM^*$ could be acting as an (intramolecular) oxidant, in which electron donating moieties such as polyphenols reduce $^3DOM^*$ (Wenk et al., 2015). The potential of this reaction would increase with more electron rich DOM as measured by the $A_{\times}A_{50}$ assay, explaining the observed correlation. The relationship is conceivable considering that moieties responsible for high $A_{\times}A_{50}$ (polyphenols) may not sensitize $^1O_2$ production when in polymeric form (such as tannins) [79], whereas chromophores that do (i.e. aromatic ketones/aldehydes and quinones) have comparatively lower electron donating capacities. This is especially likely for mangrove-influenced samples from the ENP (which had the highest $A_{\times}A_{50}$ values in our dataset (Romera-Castillo and Jaffé, 2015)). Thus, it seems that

DOM with greater EDC is expected to have a lower propensity to form ^{3}DOM* and ^{1}O$_2$. We propose that the relationship observed in Figure 7.4 is due to a combination of these two processes. Finally, it is significant that these correlations were observed using an easily measurable proxy for EDC (i.e. A$_x$A$_{50}$), which is less cumbersome to quantify compared to electrochemical methods.

7.5. Environmental Implications

Linear regression models built with ENP data showed that many DOM physicochemical properties are accurate predictors of RI formation rates and quantum yields. The relationships observed for E2:E3 and $S_{300\text{-}600}$ were consistent with previous studies, whereas predictors not previously examined that proved significant in this work included HIX, SUVA$_{254}$, and SUVA$_{300}$. The correlations between Φ_{RI} and E2:E3, HIX, and SUVA indicate that aromaticity is a significant driver of photoreactivity, and suggests that waters with more terrestrially-derived DOM will produce RI less efficiently. However, because the rate of RI formation also depends on the rate of light absorption, which is faster for high SUVA waters, steady state concentrations of RI in these systems will be high. Another significant finding is that multiple linear regression models developed using our data were not successful at predicting RI quantum yields from previously published studies. Although more research is needed to verify this finding, the high amount of intercorrelation observed between regressors presents a challenge that is not easily overcome and highlights the need for additional metrics to describe DOM character.

The correlation between ^{1}O$_2$ and ^{3}DOM* formation and antioxidant capacity observed here is in agreement with previously reported relationships between these RI and EDC (Bodhipaksha et al., 2015; Wenk et al., 2015), and suggests that DOM with more phenolic groups (electron donors) will have a lower than expected ^{1}O$_2$ and ^{3}DOM* photoproduction. It has recently been

proposed that reduction of ^{3}DOM*, followed by reduction of O_2, is a mechanism of H_2O_2 formation (Zhang et al., 2014). Although not measured in this study, this suggests that samples with high antioxidant capacities may exhibit enhanced H_2O_2 production. It is thought that the abovementioned reduction of ^{3}DOM* is facilitated by oxidation of phenolic moieties to phenoxy radicals (Canonica et al., 1995; Zhang et al., 2014), which can be further oxidized (Canonica et al., 1995). Thus, one implication is that DOM samples with higher polyphenol content will have faster rates of photooxidation (Sharpless et al., 2014). Recent work has also shown that hydroxy benzoic acids (also electron donors) may be sources of $^\bullet$OH. The lack of correlation between Φ_{OH} and $A_\times A_{50}$ does not support this conclusion; however, as mentioned before, this may be due to the relatively narrow variation range in Φ_{OH} values as compared to Φ_{1O2} and f_{TMP}.

The results shown in this study have significant implications for aquatic environmental photochemistry in terms of modeling RI formation and understanding the physicochemical properties of DOM driving RI formation in these systems. In addition, this work provides potential insight into the complex roles of DOM character, including aromatic composition, molecular size and antioxidant capacity on RI formation in aquatic ecosystems.

Table 7.1. Single linear regression parameters ($\Phi_{RI} = a\bullet$Predictor $+ b$) for Φ_{RI} measured in this study.

Regression Parameter	a			b			R^2_{pred}			PI_{avg}		
Predictor/Φ_{RI}	Φ_{1O2}[a]	Φ_{OH}[b]	f_{TMP}	Φ_{1O2}	Φ_{OH}	f_{TMP}	Φ_{1O2}	Φ_{OH}	f_{TMP}	Φ_{1O2}	Φ_{OH}	f_{TMP}
E2:E3	0.64	0.26	27.09	n.s.	n.s.	-69.5	0.69	0.54	0.69	2.4	1.3	82.7
$S_{300-600}$	0.82	0.28	34.64	-9.8	-3.0	-496.6	0.80	0.37	0.89	2.0	1.6	57.3
S_R	n.s.[c]	6.69	427.93	n.s.	-5.1	-316.5	n.s.	0.64	0.26	n.s.	1.1	153.4
HIX	-0.37	-0.16	-17.69	9.4	3.8	328.3	0.52	0.47	0.82	3.0	1.3	75.8
SUVA$_{254}$	-2.27	-0.85	-92.92	11.2	4.3	379.7	0.82	0.49	0.87	1.8	1.3	63.7
SUVA$_{300}$	-3.79	-1.38	-158.29	10.1	3.8	337.1	0.81	0.44	0.90	1.8	1.4	54.9

[a]Model yields Φ_{1O2} multiplied by 1×10^2, so to determine actual Φ_{1O2} values, calculated values should be multiplied by 0.01. [b]Model yields Φ_{OH} multiplied by 1×10^5, so to determine actual Φ_{OH} values, calculated values should be multiplied by 1×10^{-5}. [c]- indicates that parameter was not significant at $\alpha = 5\%$.

8. References

Aeschbacher, M., Graf, C., Schwarzenbach, R.P., Sander, M., 2012a. Antioxidant Properties of Humic Substances. Environmental Science & Technology 46, 4916–4925. doi:10.1021/es300039h

Aeschbacher, M., Graf, C., Schwarzenbach, R.P., Sander, M., 2012b. Antioxidant Properties of Humic Substances 46, 4916–4925. doi:10.1021/es300039h

Aeschbacher, M., Sander, M., Schwarzenbach, R.P., 2010. Novel Electrochemical Approach to Assess the Redox Properties of Humic Substances. Environmental Science & Technology 44, 87–93. doi:10.1021/es902627p

Aiken, G., 2014. Fluorescence and Dissolved Organic Matter, Aquatic Organic Matter Fluorescence. Cambridge University Press, Cambridge. doi:10.1017/cbo9781139045452.005

Aiken, G.R., Malcolm, R.L., 1987. Molecular weight of aquatic fulvic acids by vapor pressure osmometry. Geochimica et Cosmochimica Acta 51, 2177–2184.

Aiken, G.R., McKnight, D.M., Thorn, K.A., Thurman, E.M., 1992. Isolation of hydrophilic organic acids from water using nonionic macroporous resins. Organic Geochemistry 18, 567–573. doi:10.1016/0146-6380(92)90119-i

Andrew, A.A., Del Vecchio, R., Zhang, Y., Subramaniam, A., Blough, N.V., 2016. Are Extracted Materials Truly Representative of Original Samples? Impact of C18 Extraction on CDOM Optical and Chemical Properties. Front. Chem. 4, 1. doi:10.1021/es3029582

Arakaki, T., Faust, B.C., 1998. Sources, sinks, and mechanisms of hydroxyl radical (•OH) photoproduction and consumption in authentic acidic continental cloud waters from Whiteface Mountain, New York: The role of the Fe(r) (r = II, III) photochemical cycle. J. Geophys. Res. 103, 3487–3504. doi:10.1029/97JD02795

Ariese, F., van Assema, S., Gooijer, C., Bruccoleri, A.G., Langford, C.H., 2004. Comparison of Laurentian Fulvic Acid luminescence with that of the hydroquinone/quinone model system: Evidence from low temperature fluorescence studies and EPR spectroscopy. Aquatic Sciences - Research Across Boundaries 66, 86–94. doi:10.1007/s00027-003-0647-8

Baker, A., 2005. Thermal fluorescence quenching properties of dissolved organic matter. Water Research 39, 4405–4412. doi:10.1016/j.watres.2005.08.023

Balakrishnan, I., Reddy, M.P., 1972. Effect of temperature on the .gamma. radiolysis of aqueous solutions. J. Phys. Chem. 76, 1273–1279. doi:10.1021/j100653a008

Barker, D.J., Stuckey, D.C., 1999. A review of soluble microbial products (SMP) in wastewater treatment systems. Water Research. doi:10.1016/0043-1354(85)90320-3

Birks, J.B., 1970. Photophysics of aromatic molecules. John Wiley & Sons Ltd.

Blough, N.V., Zepp, R.G., 1995. Reactive oxygen species in natural waters. Active Oxygen in Chemistry 2, 280–333.

Bodhipaksha, L.C., Sharpless, C.M., Chin, Y.-P., Sander, M., Langston, W.K., MacKay, A.A., 2015. Triplet Photochemistry of Effluent and Natural Organic Matter in Whole Water and Isolates from Effluent-Receiving Rivers. Environmental Science & Technology 49, 3453–3463. doi:10.1021/es505081w

Bordwell, F.G., Brannen, W.T., 1964. The Effect of the Carbonyl and Related Groups on the Reactivity of Halides in SN2 Reactions. J. Am. Chem. Soc. 86, 4645–4650. doi:10.1021/ja01075a025

Bowen, E.J., Sahu, J., 1959. The Effect of Temperature on Fluorescence of Solutions. J. Phys. Chem. 63, 4–7. doi:10.1021/j150571a003

Boyle, E.S., Guerriero, N., Thiallet, A., Vecchio, R.D., Blough, N.V., 2009. Optical Properties of Humic Substances and CDOM: Relation to Structure. Environmental Science & Technology 43, 2262–2268. doi:10.1021/es803264g

Brand-Williams, W., Cuvelier, M.E., Berset, C., 1995. Use of a free radical method to evaluate antioxidant activity. LWT - Food Science and Technology 28, 25–30. doi:10.1016/S0023-6438(95)80008-5

Brezonik, P.L., Olmanson, L.G., Finlay, J.C., Bauer, M.E., 2015. Factors affecting the measurement of CDOM by remote sensing of optically complex inland waters. Remote Sensing of Environment 157, 199–215. doi:10.1016/j.rse.2014.04.033

Bricaud, A., Morel, A., Prieur, L., 1981. Absorption by dissolved organic matter of the sea (yellow substance) in the UV and visible domains. Limnol. Oceanogr. 26, 43–53.

Bruccoleri, A., Langford, C., Arbour, C., 1990. Pulsed photo acoustic evaluation of intersystem crossing quantum yields in fulvic acid. Env. Tech. 11, 169–172. doi:10.1080/09593339009384852

Buxton, G.V., Greenstock, C.L., Helman, W.P., Ross, A.B., Tsang, W., 1988. Critical Review of rate constants for reactions of hydrated electrons, hydorgen atoms, and hydroxyl radicals in Squeous Solution. J. Phys. Chem. Ref. Data 17, 513–886. doi:10.1063/1.555805

Canonica, S., 2007. Oxidation of Aquatic Organic Contaminants Induced by Excited Triplet States. CHIMIA 61, 641–644. doi:10.2533/chimia.2007.641

Canonica, S., Freiburghaus, M., 2001. Electron-rich phenols for probing the photochemical reactivity of freshwaters. Environmental Science & Technology 35, 690–695.

Canonica, S., Hellrung, B., Müller, P., Wirz, J., 2006. Aqueous Oxidation of Phenylurea Herbicides by Triplet Aromatic Ketones. Environmental Science & Technology 40, 6636–6641. doi:10.1021/es0611238

Canonica, S., Hellrung, B., Wirz, J., 2000. Oxidation of Phenols by Triplet Aromatic Ketones in Aqueous Solution. J. Phys. Chem. A 104, 1226–1232. doi:10.1021/jp9930550

Canonica, S., Jans, U., Stemmler, K., Höigne, J., 1995. Transformation kinetics of phenols in water: photosensitization by dissolved natural organic material and aromatic ketones. Environmental Science & Technology 29, 1822–1831. doi:10.1021/es00007a020

Canonica, S., Kramer, J.B., Reiss, D., Gygax, H., 1997. Photoisomerization kinetics of stilbene-type fluorescent whitening agents. Environmental Science & Technology 31, 1754–1760.

Canonica, S., Laubscher, H.-U., 2008. Inhibitory effect of dissolved organic matter on triplet-induced oxidation of aquatic contaminants. Photochem. Photobiol. Sci. 7, 547. doi:10.1039/b719982a

Cao, X., Aiken, G.R., Spencer, R.G.M., Butler, K., Mao, J., Schmidt-Rohr, K., 2016. Novel insights from NMR spectroscopy into seasonal changes in the composition of dissolved organic matter exported to the Bering Sea by the Yukon River. Geochimica et Cosmochimica Acta 181, 72–88. doi:10.1016/j.gca.2016.02.029

Cawley, K.M., Korak, J.A., Rosario-Ortiz, F.L., 2015. Quantum Yields for the Formation of Reactive Intermediates from Dissolved Organic Matter Samples from the Suwannee River. Environmental Engineering Science 32, 31–37. doi:10.1089/ees.2014.0280

Chambers, R.M., Pederson, K.A., 2006. Variation in soil phosphorus, sulfur, and iron pools among south Florida wetlands. Hydrobiologia 569, 63–70. doi:10.1007/s10750-006-0122-3

Chen, M., Maie, N., Parish, K., Jaffé, R., 2013. Spatial and temporal variability of dissolved organic matter quantity and composition in an oligotrophic subtropical coastal wetland. Biogeochemistry 115, 167–183. doi:10.1007/s10533-013-9826-4

Chen, Y., Barkley, M.D., 1998. Toward understanding tryptophan fluorescence in proteins. Biochemistry 37, 9976–9982. doi:10.1021/bi980274n

Childers, D.L., Boyer, J.N., Davis, S.E., Madden, C.J., Rudnick, D.T., Sklar, F.H., 2006. Relating precipitation and water management to nutrient concentrations in the oligotrophic "upside-down" estuaries of the Florida Everglades. Limnol. Oceanogr. 51, 602–616. doi:10.4319/lo.2006.51.1_part_2.0602

Chin, Y.-P., Aiken, G., O'Loughlin, E., 1994. Molecular weight, polydispersity, and spectroscopic properties of aquatic humic substances. Environmental Science & Technology 26, 1853–1858.

Chu, L., Anastasio, C., 2005. Formation of Hydroxyl Radical from the Photolysis of Frozen Hydrogen Peroxide. J. Phys. Chem. A 109, 6264–6271. doi:10.1021/jp051415f

Chu, L., Anastasio, C., 2003. Quantum Yields of Hydroxyl Radical and Nitrogen Dioxide from the Photolysis of Nitrate on Ice. J. Phys. Chem. A 107, 9594–9602. doi:10.1021/jp0349132

Coble, P.G., Green, S.A., Blough, N.V., Gagosian, R.B., 1990. Characterization of dissolved organic matter in the Black Sea by fluorescence spectroscopy. Nature 348, 432–435. doi:10.1038/348432a0

Coelho, C., Guyot, G., Halle, ter, A., Cavani, L., Ciavatta, C., Richard, C., 2010. Photoreactivity of humic substances: relationship between fluorescence and singlet oxygen production. Environ Chem Lett 9, 447–451. doi:10.1007/s10311-010-0301-3

Cooper, W.J., Zika, R.G., Petasne, R.G., Plane, J.M., 1988. Photochemical formation of hydrogen peroxide in natural waters exposed to sunlight. Environmental Science & Technology 22, 1156–1160.

Cory, R.M., Cotner, J.B., McNeill, K., 2009. Quantifying Interactions between Singlet Oxygen and Aquatic Fulvic Acids. Environmental Science & Technology 43, 718–723. doi:10.1021/es801847g

Cory, R.M., Ward, C.P., Crump, B.C., Kling, G.W., 2014. Sunlight controls water column processing of carbon in arctic fresh waters. Science 345, 925–928. doi:10.1126/science.1253119

Cottrell, B.A., Timko, S.A., Devera, L., Robinson, A.K., Gonsior, M., Vizenor, A.E., Simpson, A.J., Cooper, W.J., 2013. Photochemistry of excited-state species in natural waters: A role for particulate organic matter. Water Research 47, 5189–5199. doi:10.1016/j.watres.2013.05.059

Cronan, C.S., Aiken, G.R., 1985. Chemistry and Transport of Soluble Humic Substances in Forested Watersheds of the Adirondack Park, New-York. Geochimica et Cosmochimica Acta 49, 1697–1705.

Dalrymple, R.M., Carfagno, A.K., Sharpless, C.M., 2010. Correlations between Dissolved Organic Matter Optical Properties and Quantum Yields of Singlet Oxygen and Hydrogen Peroxide. Environmental Science & Technology 44, 5824–5829. doi:10.1021/es101005u

Davis, S.E., III, Childers, D.L., Day, J.W., Jr, Rucnick, D.T., Sklar, F.H., 2003. Factors affecting the concentration and flux of materials in two southern Everglades mangrove wetlands. Mar. Ecol.: Prog. Ser. 253, 85–96. doi:10.3354/meps253085

Deister, U., Warneck, P., Wurzinger, C., 1990. OH Radicals Generated by NO 3− Photolysis in Aqueous Solution: Competition Kinetics and a Study of the Reaction OH+ CH2 (OH) SO 3−. Ber. Bunsen-Ges. Phys. Chem. 94, 594–599.

Del Vecchio, R., Blough, N.V., 2004. On the Origin of the Optical Properties of Humic Substances. Environmental Science & Technology 38, 3885–3891. doi:10.1021/es049912h

Dong, M.M., Mezyk, S.P., Rosario-Ortiz, F.L., 2010. Reactivity of effluent organic matter (EfOM) with hydroxyl radical as a function of molecular weight. Environmental Science & Technology 44, 5714–5720. doi:10.1021/es1004736

Dong, M.M., Rosario-Ortiz, F.L., 2012. Photochemical Formation of Hydroxyl Radical from Effluent Organic Matter. Environmental Science & Technology 46, 3788–3794. doi:10.1021/es2043454

Dong, M.M., Trenholm, R., Rosario-Ortiz, F.L., 2015. Photochemical degradation of atenolol, carbamazepine, meprobamate, phenytoin and primidone in wastewater effluents. Journal of Hazardous Materials 282, 216–223. doi:10.1016/j.jhazmat.2014.04.028

Dorfman, L.M., Taub, I.A., Harter, D.A., 1964. Rate Constants for the Reaction of the Hydroxyl Radical with Aromatic Molecules. J. Chem. Phys. 41, 2954–2955. doi:10.1063/1.1726387

Driver, S.J., Perdue, E.M., 2015. Acid-Base Chemistry of Natural Organic Matter, Hydrophobic Acids, and Transphilic Acids from the Suwannee River, Georgia, as Determined by Direct Potentiometric Titration. Environmental Engineering Science 32, 66–70. doi:10.1089/ees.2014.0356

Eastman, J.W., 1968. Fluorescence of Benzene. The Effects of Solvent and Temperature on the Quantum Yield. J. Chem. Phys. 49, 4617–4621. doi:10.1063/1.1669920

Eisinger, J., Navon, G., 1969. Fluorescence Quenching and Isotope Effect of Tryptophan. J. Chem. Phys. 50, 2069–2077. doi:10.1063/1.1671335

Filella, M., Hummel, W., 2010. Trace element complexation by humic substances: issues related to quality assurance. Accred Qual Assur 16, 215–223. doi:10.1007/s00769-010-0716-3

Fimmen, R.L., Cory, R.M., Chin, Y.-P., Trouts, T.D., McKnight, D.M., 2007. Probing the oxidation–reduction properties of terrestrially and microbially derived dissolved organic matter. Geochimica et Cosmochimica Acta 71, 3003–3015. doi:10.1016/j.gca.2007.04.009

Fischer, A.M., Kliger, D.S., Winterle, J.S., Mill, T., 1985. Direct observation of phototransients in natural waters. Chemosphere 14, 1299–1306. doi:10.1016/0045-6535(85)90150-X

Foster, R., 1969. Organic charge-transfer complexes. Academic Press, New York.

Frimmel, F.H., Bauer, H., Putzlen, J., Murasecco, P., Braun, A.M., 1987. Laser Flash Photolysis of Dissolved Aquatic Humic Material and the Sensitized Production of Singlet Oxygen. Environmental Science & Technology 21, 541–545.

Furman, G.S., Lonsky, W.F., 1988. Charge-transfer complexes in kraft lignin Part 1: Occurrence. Journal of Wood Chemistry and Technology 8, 165–189.

Gally, J.A., Edelman, G.M., 1962. The effect of temperature on the fluorescence of some aromatic amino acids and proteins. Biochimica et Biophysica Acta 60, 499–509. doi:10.1016/0006-3002(62)90869-7

Gan, D., Jia, M., Vaughan, P.P., Falvey, D.E., Blough, N.V., 2008. Aqueous Photochemistry of Methyl-Benzoquinone. J. Phys. Chem. A 112, 2803–2812. doi:10.1021/jp710724e

Gao, H., Zepp, R.G., 1998. Factors influencing photoreactions of dissolved organic matter in a coastal river of the southeastern United States. Environmental Science & Technology 32, 2940–2946.

Ghassemi, M., Christman, R.F., 1968. Properties of the yellow organic acids of natural waters. Limnol. Oceanogr. 13, 583–597.

Giri, R., 1992. Temperature effect study upon the fluorescence emission of substituted coumarins. Spectrochimica Acta Part A: Molecular Spectroscopy 48, 843–848. doi:10.1016/0584-8539(92)80080-g

Glover, C.M., Rosario-Ortiz, F.L., 2013. Impact of Halides on the Photoproduction of Reactive

Intermediates from Organic Matter. Environmental Science & Technology 47, 13949–13956. doi:10.1021/es4026886

Golanoski, K.S., Fang, S., Del Vecchio, R., Blough, N.V., 2012. Investigating the Mechanism of Phenol Photooxidation by Humic Substances. Environmental Science & Technology 46, 3912–3920. doi:10.1021/es300142y

Gorman, A.A., Gould, I.R., Hamblett, I., 1982. Time-Resolved Study of the Solvent and Temperature Dependence of Singlet Oxygen (1Δ g) Reactivity toward Enol Ethers: Reactivity Parameters Typical of Rapid Reversible Exciplex Formation. J. Am. Chem. Soc. 104, 7098–7104. doi:10.1021/ja00389a036

Grabowski, Z.R., Rotkiewicz, K., Rettig, W., 2003. Structural Changes Accompanying Intramolecular Electron Transfer: Focus on Twisted Intramolecular Charge-Transfer States and Structures. Chem. Rev. 103, 3899–4032. doi:10.1021/cr940745l

Graff, B.M., Lamont, D.N., Parker, M.F.L., Bloom, B.P., Schafmeister, C.E., Waldeck, D.H., 2016. Through-Solvent Tunneling in Donor–Bridge–Acceptor Molecules Containing a Molecular Cleft. J. Phys. Chem. A 120, 6004–6013. doi:10.1021/acs.jpca.6b05624

Grannas, A.M., Martin, C.B., Chin, Y.-P., Platz, M., 2006. Hydroxyl Radical Production from Irradiated Arctic Dissolved Organic Matter. Biogeochemistry 78, 51–66. doi:10.1007/s10533-005-2342-4

Grebel, J.E., Pignatello, J.J., Mitch, W.A., 2010. Effect of Halide Ions and Carbonates on Organic Contaminant Degradation by Hydroxyl Radical-Based Advanced Oxidation Processes in Saline Waters. Environmental Science & Technology 44, 6822–6828. doi:10.1021/es1010225

Green, S.A., Blough, N.V., 2003. Optical absorption and fluorescence properties of chromophoric dissolved organic matter in natural waters. Limnol. Oceanogr. 39, 1903–1916. doi:10.4319/lo.1994.39.8.1903

Haag, W.R., Hoigne, J.R., Gassman, E., Braun, A.M., 1984. Singlet oxygen in surface waters — Part II: Quantum yields of its production by some natural humic materials as a function of wavelength. Chemosphere 13, 641–650.

Haag, W.R., Höigne, J., 1986. Singlet Oxygen in Surface Waters .3. Photochemical Formation and Steady-State Concentrations in Various Types of Waters. Environmental Science & Technology 20, 341–348.

Haag, W.R., Höigne, J., 1985. Photo-sensitized oxidation in natural water via. OH radicals. Chemosphere 14, 1659–1671.

Halladja, S., Halle, ter, A., Aguer, J.-P., Boulkamh, A., Richard, C., 2007. Inhibition of Humic Substances Mediated Photooxygenation of Furfuryl Alcohol by 2,4,6-Trimethylphenol. Evidence for Reactivity of the Phenol with Humic Triplet Excited States. Environmental Science & Technology 41, 6066–6073. doi:10.1021/es070656t

Halliwell, B., 1990. How to characterize a biological antioxidant. Free Radic. Res. Commun. 9, 1–32.

Hayes, M.H.B., MacCarthy, P., Malcolm, R.L., Swift, R.S., 1989. Humic substances II. In search of structure. John Wiley & Sons Ltd.

Hedges, J.I., Keil, R.G., Benner, R., 1997. What happens to terrestrial organic matter in the ocean? Organic Geochemistry 27, 195–212.

Helms, J.R., Stubbins, A., Ritchie, J.D., Minor, E.C., Kieber, D.J., Mopper, K., 2008. Absorption spectral slopes and slope ratios as indicators of molecular weight, source, and photobleaching of chromophoric dissolved organic matter. Limnology and Oceanography

53, 955–969. doi:10.4319/lo.2008.53.3.0955

Henderson, R.K., Baker, A., Murphy, K.R., Hambly, A., Stuetz, R.M., Khan, S.J., 2009. Fluorescence as a potential monitoring tool for recycled water systems: A review. Water Research 43, 863–881. doi:10.1016/j.watres.2008.11.027

Hug, S.J., Leupin, O., 2003. Iron-Catalyzed Oxidation of Arsenic(III) by Oxygen and by Hydrogen Peroxide: pH-Dependent Formation of Oxidants in the Fenton Reaction. Environmental Science & Technology 37, 2734–2742. doi:10.1021/es026208x

Huguet, A., Vacher, L., Relexans, S., Saubusse, S., Froidefond, J.M., Parlanti, E., 2009. Properties of fluorescent dissolved organic matter in the Gironde Estuary. Organic Geochemistry 40, 706–719. doi:10.1016/j.orggeochem.2009.03.002

Jacobsen, F., Holcman, J., Sehested, K., 1998. Reactions of the Ferryl Ion with Some Compounds Found in Cloud Water. International Journal of Chemical Kinetics 30, 215–221.

Jasper, J.T., Nguyen, M.T., Jones, Z.L., Ismail, N.S., Sedlak, D.L., Sharp, J.O., Luthy, R.G., Horne, A.J., Nelson, K.L., 2013. Unit Process Wetlands for Removal of Trace Organic Contaminants and Pathogens from Municipal Wastewater Effluents. Environmental Engineering Science 30, 421–436. doi:10.1089/ees.2012.0239

Kadir, K., Nelson, K.L., 2014. Sunlight mediated inactivation mechanisms of Enterococcus faecalis and Escherichia coli in clear water versus waste stabilization pond water. Water Research 50, 307–317. doi:10.1016/j.watres.2013.10.046

Kaneko, S., Yotoriyama, S., Koda, H., Tobita, S., 2009. Excited-State Proton Transfer to Solvent from Phenol and Cyanophenols in Water. J. Phys. Chem. A 113, 3021–3028. doi:10.1021/jp8086489

Keen, O.S., McKay, G., Mezyk, S.P., Linden, K.G., Rosario-Ortiz, F.L., 2014. Identifying the factors that influence the reactivity of effluent organic matter with hydroxyl radicals. Water Research 50, 408–419. doi:10.1016/j.watres.2013.10.049

Kieber, D.J., Miller, G.W., Neale, P.J., Mopper, K., 2014. Wavelength and temperature-dependent apparent quantum yields for photochemical formation of hydrogen peroxide in seawater. Environ. Sci.: Processes Impacts 16, 777. doi:10.1039/c4em00036f

Korak, J.A., 2014. Use of Fluorescence Spectroscopy to Characterize Dissolved Organic Matter.

Korak, J.A., Dotson, A.D., Summers, R.S., Rosario-Ortiz, F.L., 2014. Critical analysis of commonly used fluorescence metrics to characterize dissolved organic matter. Water Research 49, 327–338. doi:10.1016/j.watres.2013.11.025

Korshin, G., Chow, C.W.K., Fabris, R., Drikas, M., 2009. Absorbance spectroscopy-based examination of effects of coagulation on the reactivity of fractions of natural organic matter with varying apparent molecular weights. Water Research 43, 1541–1548. doi:10.1016/j.watres.2008.12.041

Kotzias, D., Herrmann, M., Zsolnay, A., Beyerle-Pfnür, R., Parlar, H., Korte, F., 1987a. Photochemical aging of humic substances. Chemosphere 16, 1463–1468. doi:10.1016/0045-6535(87)90086-5

Kotzias, D., Hustert, K., Wieser, A., 1987b. Formation of oxygen species and their reactions with organic chemicals in aqueous solution. Chemosphere.

Krogh, A., Keys, A., 1934. Methods for the determination of dissolved organic carbon and nitrogen in sea water. The Biological Bulletin.

Kuboyama, A., Nagakura, S., 1955. On the binding energies of some molecular compounds between p-benzoquinone and various aromatic substances. J. Am. Chem. Soc. 77, 2644–2646. doi:10.1021/ja01614a092

Lakowicz, J.R., 1999. Principles of Fluorescence Spectroscopy. Kluwer, New York.

Lamola, A.A., Hammond, G.S., 1965. Mechanisms of Photochemical Reactions in Solution. XXXIII. Intersystem Crossing Efficiencies. J. Chem. Phys. 43, 2129. doi:10.1063/1.1697084

Laskin, A., Laskin, J., Nizkorodov, S.A., 2015. Chemistry of Atmospheric Brown Carbon. Chem. Rev. 115, 4335–4382. doi:10.1021/cr5006167

Latch, D.E., McNeill, K., 2006. Microheterogeneity of singlet oxygen distributions in irradiated humic acid solutions. Science 311, 1743–1747. doi:10.1126/science.1121636

Le, T.P., Rogers, J.E., Kelly, L.A., 2000. Photoinduced Electron Transfer in Covalently Linked 1,8-Naphthalimide/Viologen Systems. J. Phys. Chem. A 104, 6778–6785. doi:10.1021/jp000855y

Lee, E., Glover, C.M., Rosario-Ortiz, F.L., 2013. Photochemical Formation of Hydroxyl Radical from Effluent Organic Matter: Role of Composition. Environmental Science & Technology 47, 12073–12080. doi:10.1021/es402491t

Lee, M.-H., Hur, J., 2013. Photodegradation-Induced Changes in the Characteristics of Dissolved Organic Matter with Different Sources and Their Effects on Disinfection By-Product Formation Potential. Clean Soil Air Water 42, 552–560. doi:10.1002/clen.201200685

Leenheer, J.A., Croue, J.P., 2003. Characterizing aquatic dissolved organic matter. Environmental Science & Technology 37, 18A–26A.

Legrini, O., Oliveros, E., Braun, A.M., 1993. Photochemical processes for water treatment. Chem. Rev. 93, 671–698.

Leifer, A., 1988. The kinetics of environmental aquatic photochemistry: theory and practice. American Chemical Society.

Lester, Y., Sharpless, C.M., Mamane, H., Linden, K.G., 2013. Production of Photo-oxidants by Dissolved Organic Matter During UV Water Treatment. Environmental Science & Technology 47, 11726–11733. doi:10.1021/es402879x

Lin, P., Aiona, P.K., Li, Y., Shiraiwa, M., Laskin, J., Nizkorodov, S.A., Laskin, A., 2016. Molecular Characterization of Brown Carbon in Biomass Burning Aerosol Particles. Environmental Science & Technology 50, 11815–11824. doi:10.1021/acs.est.6b03024

Ma, J., Del Vecchio, R., Golanoski, K.S., Boyle, E.S., Blough, N.V., 2010. Optical Properties of Humic Substances and CDOM: Effects of Borohydride Reduction. Environmental Science & Technology 44, 5395–5402. doi:10.1021/es100880q

Machado, V.G., Stock, R.I., Reichardt, C., 2014. PyridiniumN-Phenolate Betaine Dyes. Chem. Rev. 114, 10429–10475. doi:10.1021/cr5001157

Mack, J., Bolton, J.R., 1999. Photochemistry of nitrite and nitrate in aqueous solution: a review. Journal of Photochemistry and Photobiology A: Chemistry 128, 1–13. doi:10.1039/b510796m

Maie, N., Parish, K.J., Watanabe, A., Knicker, H., Benner, R., Abe, T., Kaiser, K., Jaffé, R., 2006. Chemical characteristics of dissolved organic nitrogen in an oligotrophic subtropical coastal ecosystem. Geochimica et Cosmochimica Acta 70, 4491–4506. doi:10.1016/j.gca.2006.06.1554

Maie, N., Pisani, O., Jaffé, R., 2008. Mangrove tannins in aquatic ecosystems: Their fate and possible influence on dissolved organic carbon and nitrogen cycling. Limnol. Oceanogr. 53, 160–171. doi:10.4319/lo.2008.53.1.0160

Maie, N., Yang, C., Miyoshi, T., Parish, K., Jaffé, R., 2005. Chemical characteristics of dissolved organic matter in an oligotrophic subtropical wetland/estuarine. Limnol. Oceanogr. 50, 23–35. doi:10.4319/lo.2005.50.1.0023

Maizel, A.C., Remucal, C.K., 2017. Molecular Composition and Photochemical Reactivity of Size-Fractionated Dissolved Organic Matter. Environmental Science & Technology 51, 2113–2123. doi:10.1021/acs.est.6b05140

Man Him Hui, Ware, W.R., 1976. Exciplex photophysics. V. The kinetics of fluorescence quenching of anthracene by N,N-dimethylaniline in cyclohexane. J. Am. Chem. Soc. 98, 4718–4727. doi:10.1021/ja00432a005

Matsumoto, T., Sato, M., Hirayama, S., 1972. Intersystem crossing in 9-carbonyl derivatives of anthracene. Chemical Physics Letters 13, 13–15. doi:10.1016/0009-2614(72)80031-9

McCabe, A.J., Arnold, W.A., 2016. Chemosphere. Chemosphere 155, 640–647. doi:10.1016/j.chemosphere.2016.04.078

McKay, G., Couch, K.D., Mezyk, S.P., Rosario-Ortiz, F.L., 2016. Investigation of the Coupled Effects of Molecular Weight and Charge-Transfer Interactions on the Optical and Photochemical Properties of Dissolved Organic Matter. Environmental Science & Technology 50, 8093–8102. doi:10.1021/acs.est.6b02109

McKay, G., Dong, M.M., Kleinman, J.L., Mezyk, S.P., Rosario-Ortiz, F.L., 2011. Temperature Dependence of the Reaction between the Hydroxyl Radical and Organic Matter. Environmental Science & Technology 45, 6932–6937. doi:10.1021/es201363j

McKay, G., Korak, J.A., Erickson, P.R., Latch, D.E., McNeill, K., Rosario-Ortiz, F.L., n.d. The Case Against Charge Transfer Interactions in Dissolved Organic Matter Photphysics. Environmental Science & Technology.

McKay, G., Rosario-Ortiz, F.L., 2015. Temperature Dependence of the Photochemical Formation of Hydroxyl Radical from Dissolved Organic Matter. Environmental Science & Technology 49, 4147–4154. doi:10.1021/acs.est.5b00102

McKnight, D.M., Boyer, E.W., Westerhoff, P.K., Doran, P.T., Kulbe, T., Andersen, D.T., 2001. Spectrofluorometric characterization of dissolved organic matter for indication of precursor organic material and aromaticity. Limnology and Oceanography 46, 38–48.

McNeill, K., Canonica, S., 2016. Triplet state dissolved organic matter in aquatic photochemistry: reaction mechanisms, substrate scope, and photophysical properties. Environ. Sci.: Processes Impacts 18, 1381–1399. doi:10.1039/c6em00408c

Mead, R.N., Barefoot, S., Helms, J.R., Morgan, J.B., Kieber, R.J., 2014. Photodegradation of the antihistamine cetirizine in natural waters. Environ Toxicol Chem 33, 2240–2245. doi:10.1002/etc.2691

Menter, J.M., 2006. Temperature dependence of collagen fluorescence. Photochem. Photobiol. Sci. 5, 403–410. doi:10.1039/b516429j

Menzel, D.W., Vaccaro, R.F., 1964. The measurement of dissolved organic and particulate carbon in seawater. Limnology and Oceanography 9, 138–142.

Mopper, K., Zhou, X., 1990. Hydroxyl Radical Photoproduction in the Sea and Its Potential Impact on Marine Processes. Science 250, 661–664.

Mori, T., Inoue, Y., 2005. Circular Dichroism of a Chiral Tethered Donor–Acceptor System: Enhanced Anisotropy Factors in Charge-Transfer Transitions by Dimer Formation and by Confinement. Angew. Chem. Int. Ed. 44, 2582–2585. doi:10.1002/anie.200462071

Mostafa, S., Korak, J.A., Shimabuku, K., Glover, C.M., Rosario-Ortiz, F.L., 2014a. Relation between Optical Properties and Formation of Reactive Intermediates from Different Size Fractions of Organic Matter, in: Advances in the Physicochemical Characterization of Dissolved Organic Matter: Impact on Natural and Engineered Systems, ACS Symposium Series. American Chemical Society, Washington, DC, pp. 159–179. doi:10.1021/bk-2014-

1160.ch008

Mostafa, S., Korak, J.A., Shimabuku, K., Glover, C.M., Rosario-Ortiz, F.L., 2014b. Relation between Optical Properties and Formation of Reactive Intermediates from Different Size Fractions of Organic Matter, in: Advances in the Physicochemical Characterization of Dissolved Organic Matter: Impact on Natural and Engineered Systems, ACS Symposium Series. American Chemical Society, Washington, DC, pp. 159–179. doi:10.1021/bk-2014-1160.ch008

Mostafa, S., Rosario-Ortiz, F.L., 2013. Singlet oxygen formation from wastewater organic matter. Environmental Science & Technology 47, 8179–8186. doi:10.1021/es401814s

Mostofa, K.M., Sakugawa, H., 2003. Spatial and temporal variation of hydrogen peroxide in stream and river waters: Effect of photo-bio-physio-chemical processes of aquatic matters. Geochim Cosmochim Acta 67, A309.

Mulder, G.J., 1840. Untersuchungen über die Humussubstanzen. J. Prakt. Chem. 21, 321–370. doi:10.1002/prac.18400210139

Mulliken, R.S., 1952. Molecular compounds and their spectra. II. J. Am. Chem. Soc. 74, 811–824. doi:10.1021/ja01123a067

Murphy, K.R., Butler, K.D., Spencer, R.G.M., Stedmon, C.A., Boehme, J.R., Aiken, G.R., 2010. Measurement of Dissolved Organic Matter Fluorescence in Aquatic Environments: An Interlaboratory Comparison. Environmental Science & Technology 44, 9405–9412. doi:10.1021/es102362t

Namkung, E., Rittmann, B.E., 1986. Soluble microbial products (SMP) formation kinetics by biofilms. Water Research.

O'Connor, D.V., Ware, W.R., 1976. Exciplex photophysics. III. Kinetics of fluorescence quenching of .alpha.-cyanonaphthalene by dimethylcyclopentene-1,2 in hexane. J. Am. Chem. Soc. 98, 4706–4711. doi:10.1021/ja00432a003

Oncul, S., Demchenko, A.P., 2006. The effects of thermal quenching on the excited-state intramolecular proton transfer reaction in 3-hydroxyflavones. Spectrochimica Acta Part A: Molecular and Biomolecular Spectroscopy 65, 179–183. doi:10.1016/j.saa.2005.10.002

Opsahl, S., Benner, R., 1997. Distribution and cycling of terrigenous dissolved organic matter in the ocean. Nature 386, 480–482. doi:10.1038/386480a0

Orgel, L.E., Mulliken, R.S., 1957. Molecular Complexes and Their Spectra. VII. The Spectrophotometric Study of Molecular Complexes in Solution; Contact Charge-transfer Spectra1. J. Am. Chem. Soc. 79, 4839–4846. doi:10.1021/ja01575a006

Page, S.E., Arnold, W.A., McNeill, K., 2011. Assessing the Contribution of Free Hydroxyl Radical in Organic Matter-Sensitized Photohydroxylation Reactions. Environmental Science & Technology 45, 2818–2825. doi:10.1021/es2000694

Page, S.E., Logan, J.R., Cory, R.M., McNeill, K., 2014. Evidence for dissolved organic matter as the primary source and sink of photochemically produced hydroxyl radical in arctic surface waters. Environ. Sci.: Processes Impacts 16, 807. doi:10.1039/c3em00596h

Parker, K.M., Pignatello, J.J., Mitch, W.A., 2013. Influence of Ionic Strength on Triplet-State Natural Organic Matter Loss by Energy Transfer and Electron Transfer Pathways. Environmental Science & Technology 47, 10987–10994. doi:10.1021/es401900j

Perdue, E.M., Ritchie, J.D., 2003. Dissolved organic matter in freshwaters. Elsevier Amsterdam, Netherlands.

Peterson, B.M., McNally, A.M., Cory, R.M., Thoemke, J.D., Cotner, J.B., McNeill, K., 2012. Spatial and Temporal Distribution of Singlet Oxygen in Lake Superior. Environmental

Science & Technology 46, 7222–7229. doi:10.1021/es301105e

Peuravuori, J., Pihlaja, K., 1997. Molecular size distribution and spectroscopic properties of aquatic humic substances. Analytica Chimica Acta 337, 133–149.

Phillips, S.M., Bellcross, A.D., Smith, G.D., 2017. Light Absorption by Brown Carbon in the Southeastern United States is pH-dependent. Environmental Science & Technology 51, 6782–6790. doi:10.1021/acs.est.7b01116

Phillips, S.M., Smith, G.D., 2015. Further Evidence for Charge Transfer Complexes in Brown Carbon Aerosols from Excitation–Emission Matrix Fluorescence Spectroscopy. J. Phys. Chem. A 119, 4545–4551. doi:10.1021/jp510709e

Phillips, S.M., Smith, G.D., 2014. Light Absorption by Charge Transfer Complexes in Brown Carbon Aerosols. Environ. Sci. Technol. Lett. 1, 382–386. doi:10.1021/ez500263j

Piccolo, A., 2001. The supramolecular structure of humic substances. Soil Sci. 166, 1–23.

Pochon, A., Vaughan, P.P., Gan, D., Vath, P., Blough, N.V., Falvey, D.E., 2002. Photochemical Oxidation of Water by 2-Methyl-1,4-benzoquinone: Evidence against the Formation of Free Hydroxyl Radical. J. Phys. Chem. A 106, 2889–2894. doi:10.1021/jp012856b

Poulin, B.A., Ryan, J.N., Aiken, G.R., 2014. Effects of iron on optical properties of dissolved organic matter. Environmental Science & Technology 48, 10098–10106. doi:10.1021/es502670r

Power, J.F., Langford, C.H., 1988. Optical absorbance of dissolved organic matter in natural water studies using the thermal lens effect. Anal. Chem. 60, 842–846. doi:10.1021/ac00160a004

Power, J.F., Sharma, D.K., Langford, C.H., 1986. Photophysics of a well characterized humic substance. Photochemistry and ….

Prochorow, J., 1974. Deactivation of an excited charge-transfer complex II. Influence of rigidity of medium on radiative and radiationless transitions. Journal of Luminescence 9, 131–142. doi:10.1016/0022-2313(74)90027-1

Prochorow, J., 1973. Change of the luminescence properties of charge-transfer complexes in liquid solutions. Chemical Physics Letters 19, 596–600. doi:10.1016/0009-2614(73)85156-5

Prochorow, J., Bernard, E., 1974. Deactivation of an excited charge-transfer complex I. Influence of solvent polarity on radiative and radiationless transitions. Journal of Luminescence 8, 471–487. doi:10.1016/0022-2313(74)90013-1

Prochorow, J., Siegoczynski, R., 1969. Radiative and radiationless processes in charge-transfer complexes. Chemical Physics Letters 3, 635–639.

Rathore, R., Lindeman, S.V., Kochi, J.K., 1997. Charge-transfer probes for molecular recognition via steric hindrance in donor-acceptor pairs. J. Am. Chem. Soc. 119, 9393–9404.

Reuter, J.H., Perdue, E.M., 1977. Importance of heavy metal-organic matter interactions in natural waters. Geochimica et Cosmochimica Acta 41, 325–334.

Rice-Evans, C.A., Miller, N.J., Paganga, G., 1996. Structure-antioxidant activity relationships of flavonoids and phenolic acids. Free Radical Biology & Medicine 20, 933–56.

Richard, C., Trubetskaya, O., Trubetskoj, O., Reznikova, O., Afanas'eva, G., Aguer, J.P., Guyot, G., 2004. Key Role of the Low Molecular Size Fraction of Soil Humic Acids for Fluorescence and Photoinductive Activity. Environmental Science & Technology 38, 2052–2057. doi:10.1021/es030049f

Ritchie, J.D., Perdue, E.M., 2003. Proton-binding study of standard and reference fulvic acids, humic acids, and natural organic matter. Geochimica et Cosmochimica Acta 67, 85–96. doi:10.1016/S0016-7037(02)01044-X

Robinson, G.W., Thistlethwaite, P.J., Lee, J., 1986. Molecular aspects of ionic hydration reactions. J. Phys. Chem. 90, 4224–4233. doi:10.1021/j100409a003

Romera-Castillo, C., Jaffé, R., 2015. Marine Chemistry. Marine Chemistry 177, 668–676. doi:10.1016/j.marchem.2015.10.008

Rook, J.J., 1977. Chlorination reactions of fulvic acids in natural waters. Environmental Science & Technology 11, 478–482. doi:10.1021/es60128a014

Rosario-Ortiz, F.L., Canonica, S., 2016. Probe Compounds to Assess the Photochemical Activity of Dissolved Organic Matter. Environmental Science & Technology 50, 12532–12547. doi:10.1021/acs.est.6b02776

Rosario-Ortiz, F.L., Korak, J.A., 2017. Oversimplification of Dissolved Organic Matter Fluorescence Analysis: Potential Pitfalls of Current Methods. Environmental Science & Technology 51, 759–761. doi:10.1021/acs.est.6b06133

Rosario-Ortiz, F.L., Mezyk, S.P., Doud, D.F.R., Snyder, S.A., 2008. Quantitative correlation of absolute hydroxyl radical rate constants with non-isolated effluent organic matter bulk properties in water. Environmental Science & Technology 42, 5924–5930.

Ryder, E., Jennings, E., de Eyto, E., Dillane, M., NicAonghusa, C., Pierson, D.C., Moore, K., Rouen, M., Poole, R., 2012. Temperature quenching of CDOM fluorescence sensors: temporal and spatial variability in the temperature response and a recommended temperature correction equation. Limnol. Oceanogr. Methods 10, 1004–1010. doi:10.4319/lom.2012.10.1004

Senesi, N., Miano, T.M., Provenzano, M.R., Brunetti, G., 1991. CHARACTERIZATION, DIFFERENTIATION, AND CLASSIFICATION OF HUMIC SUBSTANCES BY FLUORESCENCE SPECTROSCOPY. Soil Sci. 152, 259–271. doi:10.1097/00010694-199110000-00004

Shapiro, J., 1964. Effect of yellow organic acids on iron and other metals in water. J. - Am. Water Works Assoc. 56, 1062–82.

Sharpless, C.M., 2012. Lifetimes of Triplet Dissolved Natural Organic Matter (DOM) and the Effect of NaBH 4Reduction on Singlet Oxygen Quantum Yields: Implications for DOM Photophysics. Environmental Science & Technology 46, 4466–4473. doi:10.1021/es300217h

Sharpless, C.M., Aeschbacher, M., Page, S.E., Wenk, J., Sander, M., McNeill, K., 2014. Photooxidation-Induced Changes in Optical, Electrochemical, and Photochemical Properties of Humic Substances. Environmental Science & Technology 48, 2688–2696. doi:10.1021/es403925g

Sharpless, C.M., Blough, N.V., 2014. The importance of charge-transfer interactions in determining chromophoric dissolved organic matter (CDOM) optical and photochemical properties. Environ. Sci.: Processes Impacts 16, 654–671. doi:10.1039/c3em00573a

Shimabuku, K.K., Cho, H., Townsend, E.B., Rosario-Ortiz, F.L., Summers, R.S., 2014. Modeling Nonequilibrium Adsorption of MIB and Sulfamethoxazole by Powdered Activated Carbon and the Role of Dissolved Organic Matter Competition. Environmental Science & Technology 48, 13735–13742. doi:10.1021/es503512v

Shon, H.K., Vigneswaran, S., Snyder, S.A., 2006. Effluent organic matter (EfOM) in wastewater: constituents, effects, and treatment. Critical Reviews in Environmental Science and Technology 36, 327–374. doi:10.1080/10643380600580011

Siemiarczuk, A., McIntosh, A.R., Ho, T.F., Stillman, M.J., Roach, K.J., Weedon, A.C., Bolton, J.R., Connolly, J.S., 1983. Intramolecular Photochemical Electron-Transfer .2. Fluorescence

Studies of Linked Porphyrin-Quinone Compounds. J. Am. Chem. Soc. 105, 7224–7230.

Southworth, B.A., Voelker, B.M., 2003. Hydroxyl radical production via the photo-Fenton reaction in the presence of fulvic acid. Environmental Science & Technology 37, 1130–1136.

Steinberg, C., 2008. 7 Regulatory Impacts of Humic Substances in Lakes. The Lakes Handbook: Limnology and Limnetic ….

Stenson, A.C., Marshall, A.G., Cooper, W.T., 2003. Exact Masses and Chemical Formulas of Individual Suwannee River Fulvic Acids from Ultrahigh Resolution Electrospray Ionization Fourier Transform Ion Cyclotron Resonance Mass Spectra. Anal. Chem. 75, 1275–1284. doi:10.1021/ac026106p

Stryer, L., 1966. Excited-State Proton-Transfer Reactions. A Deuterium Isotope Effect on Fluorescence. J. Am. Chem. Soc. 88, 5708–5712. doi:10.1021/ja00976a004

Stubbins, A., Hood, E., Raymond, P.A., Aiken, G.R., Sleighter, R.L., Hernes, P.J., Butman, D., Hatcher, P.G., Striegl, R.G., Schuster, P., Abdulla, H.A.N., Vermilyea, A.W., Scott, D.T., Spencer, R.G.M., 2012. Anthropogenic aerosols as a source of ancient dissolved organic matter in glaciers. Nature Geosci 5, 198–201. doi:10.1038/ngeo1403

Summers, R.S., Cornel, P.K., Roberts, P.V., 1987. Molecular size distribution and spectroscopic characterization of humic substances 62, 27–37.

Sun, L., Chen, H., Abdulla, H.A., Mopper, K., 2014. Estimating hydroxyl radical photochemical formation rates in natural waters during long-term laboratory irradiation experiments. Environ. Sci.: Processes Impacts 16, 757–763. doi:10.1039/C3EM00587A

Sun, L., Perdue, E.M., McCarthy, J.F., 1995. Using reverse osmosis to obtain organic matter from surface and ground waters. Water Research 29, 1471–1477. doi:10.1016/0043-1354(94)00295-I

Sun, L., Qian, J., Blough, N.V., Mopper, K., 2015. Insights into the Photoproduction Sites of Hydroxyl Radicals by Dissolved Organic Matter in Natural Waters. Environ. Sci. Technol. Lett. 2, 352–356. doi:10.1021/acs.estlett.5b00294

Sutton, R., Sposito, G., 2005. Molecular Structure in Soil Humic Substances: The New View. Environmental Science & Technology 39, 9009–9015. doi:10.1021/es050778q

Tang, S., Wang, Z., Wu, Z., Zhou, Q., 2010. Role of dissolved organic matters (DOM) in membrane fouling of membrane bioreactors for municipal wastewater treatment. Journal of Hazardous Materials 178, 377–384.

Thormählen, I., Straub, J., Grigull, U., 2009. Refractive Index of Water and Its Dependence on Wavelength, Temperature, and Density. J. Phys. Chem. Ref. Data 14, 933–945. doi:10.1063/1.555743

Thurman, E.M., 1985. Organic geochemistry of natural waters. Kluwer.

Thurman, E.M., Malcolm, R.L., 1981. Preparative isolation of aquatic humic substances. Environmental Science & Technology 15, 463–466. doi:10.1021/es00086a012

Thurman, E.M., Wershaw, R.L., Malcolm, R.L., 1982. Molecular size of aquatic humic substances. Organic Geochemistry 4, 27–35.

Timko, S.A., Romera-Castillo, C., Jaffé, R., Cooper, W.J., 2014. Photo-reactivity of natural dissolved organic matter from fresh to marine waters in the Florida Everglades, USA. Environ. Sci.: Processes Impacts 16, 866–878. doi:10.1039/C3EM00591G

Tinnacher, R.M., Honeyman, B.D., 2007. A New Method to Radiolabel Natural Organic Matter by Chemical Reduction with Tritiated Sodium Borohydride. Environmental Science & Technology 41, 6776–6782. doi:10.1021/es070563b

Tseng, L.Y., Gonsior, M., Schmitt-Kopplin, P., Cooper, W.J., Pitt, P., Rosso, D., 2013. Molecular Characteristics and Differences of Effluent Organic Matter from Parallel Activated Sludge and Integrated Fixed-Film Activated Sludge (IFAS) Processes. Environmental Science & Technology 130827102639005. doi:10.1021/es4002482

Turro, N.J., Ramamurthy, V., Scaiano, J.C., 2012. Modern Molecular Photochemistry of Organic Molecules. University Science Books, Sausalito, California.

Twardowski, M.S., Boss, E., Sullivan, J.M., Donaghay, P.L., 2004. Modeling the spectral shape of absorption by chromophoric dissolved organic matter. Marine Chemistry 89, 69–88. doi:10.1016/j.marchem.2004.02.008

Valeur, B., Berberan-Santos, M.N., 2012. Molecular Fluorescence: Principles and Applications. Wiley-VCH.

Vaughan, P.P., Blough, N.V., 1998. Photochemical formation of hydroxyl radical by constituents of natural waters. Environmental Science & Technology 32, 2947–2953.

Velapoldi, R.A., Mielenz, K.D., 1980. A Fluorescence Standard Reference Material (No. 260-64), National Bureau Standards Special Publication.

Vermilyea, A.W., Voelker, B.M., 2009. Photo-Fenton Reaction at Near Neutral pH. Environmental Science & Technology 43, 6927–6933. doi:10.1021/es900721x

Vione, D., Falletti, G., Maurino, V., Minero, C., Pelizzetti, E., Malandrino, M., Ajassa, R., Olariu, R.-I., Arsene, C., 2006. Sources and Sinks of Hydroxyl Radicals upon Irradiation of Natural Water Samples. Environmental Science & Technology 40, 3775–3781. doi:10.1021/es052206b

Vione, D., Minella, M., Maurino, V., Minero, C., 2014. Indirect Photochemistry in Sunlit Surface Waters: Photoinduced Production of Reactive Transient Species. Chemistry - A European Journal 20, 10590–10606. doi:10.1002/chem.201400413

Vione, D., Ponzo, M., Bagnus, D., Maurino, V., Minero, C., Carlotti, M.E., 2010. Comparison of different probe molecules for the quantification of hydroxyl radicals in aqueous solution. Environ Chem Lett 8, 95–100. doi:10.1007/s10311-008-0197-3

Vione, D., Sur, B., Dutta, B.K., Maurino, V., Minero, C., 2011. On the effect of 2-propanol on phenol photonitration upon nitrate photolysis. Journal of Photochemistry and Photobiology A: Chemistry 224, 68–70. doi:10.1016/j.jphotochem.2011.09.008

Visser, S.A., 1985. Viscosimetric studies on molecular weight fractions of fulvic and humic acids of aquatic, terrestrial and microbial origin. Plant Soil 87, 209–221.

Wang, J.H., Robinson, C.V., Edelman, I.S., 1953. Self-diffusion and Structure of Liquid Water. III. Measurement of the Self-diffusion of Liquid Water with H 2, H 3and O 18as Tracers 1. J. Am. Chem. Soc. 75, 466–470. doi:10.1021/ja01098a061

Wang, Z.-D., C Pant, B., H Langford, C., 1990. Spectroscopic and structural characterization of a Laurentian fulvic acid: notes on the origin of the color. Analytica Chimica Acta 232, 43–49.

Ward, C.P., Cory, R.M., 2016. Complete and Partial Photo-oxidation of Dissolved Organic Matter Draining Permafrost Soils. Environmental Science & Technology 50, 3545–3553. doi:10.1021/acs.est.5b05354

Watras, C.J., Hanson, P.C., Stacy, T.L., Morrison, K.M., Mather, J., Hu, Y.H., Milewski, P., 2011. A temperature compensation method for CDOM fluorescence sensors in freshwater. Limnol. Oceanogr. Methods 9, 296–301. doi:10.4319/lom.2011.9.296

Wei, S.-D., Zhou, H.-C., Lin, Y.-M., 2010. Antioxidant Activities of Extract and Fractions from the Hypocotyls of the Mangrove Plant Kandelia candel. Int J Mol Sci 11, 4080–4093.

doi:10.3390/ijms11104080

Weishaar, J.L., Aiken, G.R., Bergamaschi, B.A., Fram, M.S., Fujii, R., Mopper, K., 2003. Evaluation of Specific Ultraviolet Absorbance as an Indicator of the Chemical Composition and Reactivity of Dissolved Organic Carbon. Environmental Science & Technology 37, 4702–4708. doi:10.1021/es030360x

Wenk, J., Aeschbacher, M., Sander, M., Gunten, U.V., Canonica, S., 2015. Photosensitizing and Inhibitory Effects of Ozonated Dissolved Organic Matter on Triplet-Induced Contaminant Transformation. Environmental Science & Technology 49, 8541–8549. doi:10.1021/acs.est.5b02221

Wenk, J., Canonica, S., 2012. Phenolic antioxidants inhibit the triplet-induced transformation of anilines and sulfonamide antibiotics in aqueous solution. Environmental Science & Technology 46, 5455–5462. doi:10.1021/es300485u

Wenk, J., Eustis, S.N., McNeill, K., Canonica, S., 2013. Quenching of Excited Triplet States by Dissolved Natural Organic Matter. Environmental Science & Technology 47, 12802–12810. doi:10.1021/es402668h

Wenk, J., Gunten, von, U., Canonica, S., 2011. Effect of Dissolved Organic Matter on the Transformation of Contaminants Induced by Excited Triplet States and the Hydroxyl Radical. Environmental Science & Technology 45, 1334–1340. doi:10.1021/es102212t

Westerhoff, P., Mezyk, S.P., Cooper, W.J., Minakata, D., 2007. Electron Pulse Radiolysis Determination of Hydroxyl Radical Rate Constants with Suwannee River Fulvic Acid and Other Dissolved Organic Matter Isolates. Environmental Science & Technology 41, 4640–4646. doi:10.1021/es062529n

White, E., Vaughan, P., Zepp, R., 2003. Role of the photo-Fenton reaction in the production of hydroxyl radicals and photobleaching of colored dissolved organic matter in a coastal river of the southeastern United States. Aquat Sci 65, 402–414. doi:10.1007/s00027-003-0675-4

Wünsch, U.J., Murphy, K.R., Stedmon, C.A., 2015. Fluorescence Quantum Yields of Natural Organic Matter and Organic Compounds: Implications for the Fluorescence-based Interpretation of Organic Matter Composition. Front. Mar. Sci. 2, 35. doi:10.1016/j.marchem.2004.02.006

Xu, H., Cooper, W.J., Jung, J., Song, W., 2011. Photosensitized degradation of amoxicillin in natural organic matter isolate solutions. Water Research 45, 632–638. doi:10.1016/j.watres.2010.08.024

Yacobi, Y.Z., Alberts, J.J., Takacs, M., McElvaine, M., 2003. Absorption spectroscopy of colored dissolved organic carbon in Georgia (USA) rivers: the impact of molecular size distribution. Journal of Limnology 62, 41–46.

Yamashita, Y., Jaffé, R., Male, N., Tanoue, E., 2008. Assessing the dynamics of dissolved organic matter (DOM) in coastal environments by excitation emission matrix fluorescence and parallel factor analysis (EEM-PARAFAC). Limnology and Oceanography 53, 1900.

Yamashita, Y., Scinto, L.J., Maie, N., Jaffé, R., 2010. Dissolved Organic Matter Characteristics Across a Subtropical Wetland's Landscape: Application of Optical Properties in the Assessment of Environmental Dynamics. Ecosystems 13, 1006–1019. doi:10.1007/s10021-010-9370-1

Zellner, R., Exner, M., Herrmann, H., 1990. Absolute OH quantum yields in the laser photolysis of nitrate, nitrite and dissolved H_2O_2 at 308 and 351 nm in the temperature range 278–353 K. J. Atmos. Chem. 10, 411–425.

Zepp, R.G., Baughman, G.L., Schlotzhauer, P.F., 1981a. Comparison of photochemical behavior

of various humic substances in water: I. Sunlight induced reactions of aquatic pollutants photosensitized by humic substances. Chemosphere 10, 109–117.

Zepp, R.G., Baughman, G.L., Schlotzhauer, P.F., 1981b. Comparison of photochemical behavior of various humic substances in water: II. Photosensitized oxygenations. Chemosphere 10, 119–126.

Zepp, R.G., Braun, A.M., Hoigné, J., Leenheer, J.A., 1987. Photoproduction of Hydrated Electrons from Natural Organic Solutes in Aquatic Environments. Environmental Science & Technology 21, 485–490.

Zepp, R.G., Cline, D.M., 1977. Rates of direct photolysis in aquatic environment. Environmental Science & Technology 11, 359–366. doi:10.1021/es60127a013

Zepp, R.G., Faust, B.C., Hoigne, J., 1992. Hydroxyl radical formation in aqueous reactions (pH 3-8) of iron (II) with hydrogen peroxide: the photo-Fenton reaction. Environmental Science & Technology 26, 313–319.

Zepp, R.G., Schlotzhauer, P.F., 1981. Comparison of photochemical behavior of various humic substances in water: III. Spectroscopic properties of humic substances. Chemosphere 10, 479–486.

Zepp, R.G., Schlotzhauer, P.F., Sink, R.M., 1985. Photosensitized transformations involving electronic energy transfer in natural waters: role of humic substances. Environmental Science & Technology 19, 74–81. doi:10.1021/es00131a008

Zepp, R.G., Wolfe, N.L., Baughman, G.L., Hollis, R.C., 1977. Singlet oxygen in natural waters. Nature 267, 421–423. doi:10.1038/267421a0

Zhang, Y., Del Vecchio, R., Blough, N.V., 2012. Investigating the Mechanism of Hydrogen Peroxide Photoproduction by Humic Substances. Environmental Science & Technology 46, 11836–11843. doi:10.1021/es3029582

Zhang, Y., Simon, K.A., Andrew, A.A., Del Vecchio, R., Blough, N.V., 2014. Enhanced Photoproduction of Hydrogen Peroxide by Humic Substances in the Presence of Phenol Electron Donors. Environmental Science & Technology 48, 12679–12688. doi:10.1021/es5035798

Ziechmann, W., 1972. Über die elektronen-donator-und acceptoreigenschaften von huminstoffen. Geoderma 8, 111–131. doi:10.1016/0016-7061(72)90040-7

Zsolnay, A., Baigar, E., Jimenez, M., Steinweg, B., Saccomandi, F., 1999. Differentiating with fluorescence spectroscopy the sources of dissolved organic matter in soils subjected to drying. Chemosphere 38, 45–50. doi:10.1016/S0045-6535(98)00166-0

9. Conclusions and Outlook

The research chapters presented in this thesis represent an advance in the understanding of DOM photophysics and photochemistry in natural waters. Overall, this thesis provides evidence that the photophysical and photochemical properties of DOM can be explained by an individual chromophore approach as opposed to a charge-transfer (CT) model. Chapters 4 and 5 represent the first critical evaluation of the CT model as it has been presented in the literature, whereas Chapters 3, 6, and 7 represent advances in the understanding of $^\bullet$OH photochemistry. These studies are initial steps and more work is necessary in order to arrive at a complete understanding.

The results in Chapters 3-5 pose a number of questions about the nature of chromophores and fluorophores in DOM. Although Chapter 3 was supportive of the CT model based on experiments used previously to characterize CT interactions in DOM (e.g. borohydride reduction), Chapters 4 and 5 provide strong evidence against its prevalance based on experiments using techniques to characterize CT interactions in well-defined organic DA complexes (e.g. solvatochromism). The solvatochromism observed in these experiments in absorbance and fluorescence spectra was typically less than ~ 15 nm, consistent with excitation into, and emission from, local excited (LE) states as opposed to CT excited states. This minimal solvatochromism brings up the issue of the solvent accessibility of chromophores. Specifically, because known chromophores and fluorophores in DOM are expected to exhibit specific solvent effects (e.g. H-bonding in hydroxybenzoic acids), one could potentially infer that these chromophores are inaccessible, buried in a hydrophobit core or microenvironment. This microenvironment model has support from studies investigating the role of probe polarity on singlet oxygen formation (Latch and McNeill, 2006). However, there are many lines of evidence

142

that suggest DOM chromophores are generally solvent accessible. First, these chromophores are in general polar molecules with appreciable water solubility (e.g. phenols, quinones, and substituted aromatic ketone/aldehydes). Second, much of the photochemistry of DOM requires solvent accessibility, for example, triplet-induced degradation of contaminants. Finally, the formation of such a microenvironment is thermodynamically driven by the hydrophobic effect, which is expected to be influenced by solvents of varying polarity.

More work is necessary to verify the results of the studies in Chapters 4 and 5. Investigations into the photophysics of DOM could benefit from the use of model compounds, which, for example, have been useful in studies of ^{3}DOM* chemistry. This approach would entail building a realistic picture of chromophores and fluorophores present in DOM (e.g. based on high-resolution molecular weight data), preparing solutions containing these components, and performing optical property measurements. An alternative methodology that would allow a more systematic investigation of the effect of molecular size and composition on optical properties and photochemistry, would be to synthesize individual model DOM molecules containing these identified chromophores and fluorophores with varying molecular weights and spacing between D and A groups.

The temperature-dependence of $^\bullet$OH formation in Chapter 6 demonstrated that low-energy hydroxylation pathways (of model compounds) from DOM photolysis are characterized by a barrierless process, which is attributed to the formation of a quinone-water exciplex. Understanding of photochemical $^\bullet$OH formation from DOM photolyis will be improved in future studies if a method is developed that can differentiate free $^\bullet$OH from low-energy hydroxylators. Application of this method to a diverse collection of isolates is necessary in order to assess the

ubiquity of low-energy hydroxylators in DOM as a whole and the importance of these species on contaminant attenuation in aquatic environments.

The modeling work in Chapter 7 focuses on the ability to model $^{\bullet}$OH formation quantum yields from DOM photolysis and is the most applied of the research chapters. Chapter 7 demonstrates that $^{\bullet}$OH quantum yields were poorly modeled by all physicochemical properties explored as predictors, which demonstrates that $^{\bullet}$OH precursors are a small component of the overall DOM pool. Data from Chapter 3 suggests that fluorescence quantum yield may be a viable approach for modeling $^{\bullet}$OH formation.

With Chapters 3, 6 and 7 in mind, there are a few points worth making regarding the current state of knowledge of $^{\bullet}$OH formation from DOM. The activation energy for formation of $^{\bullet}$OH from the H_2O_2-dependent and H_2O_2-independent pathway were identical (Chapter 5), indicating that secondary thermal reactions (e.g. the reduction of H_2O_2 by Fe^{2+}) is not the source of this temperature-dependence. The activation energy for benzene oxidation by *p*-benzoquinone, a model sensitizer, was 0 kJ mol^{-1}, consistent with the photooxidant being an exciplex between a triplet excited state quinone and a water molecule. Although more work needs to be done to verify whether this chemistry is occuring in DOM, the fact that quinones are known to be present in DOM makes this likely.

Overall, many significant challenges remain in the field of $^{\bullet}$OH photochemistry. First, the nature, reactivity, and ubiquity of low-energy hdyroxylators formed from DOM photolysis needs to be established, which will be possible only if a quantitative method for differentiating $^{\bullet}$OH from these species is developed. Second, contribution of the H_2O_2-dependent pathway to $^{\bullet}$OH formation (in terms of a quantum yield) has yet to be linked to the amount of iron present in a given DOM isolate or whole water sample. This could be easily done and is important if we are

144

to fully understand the apportionment of these two pathways. In addition, as demonstrated in Chapter 7, there is a poor understanding of what DOM physicochemical properties describe $^{\bullet}$OH formation. This also indicates that the precursors of $^{\bullet}$OH formation are either very different than those of $^1O_2$ and ^{3}DOM* or that they are not well described by traditionally used parameters (e.g. E2/E3). Chapter 3 showed that fluorescence quantum yield may be a good metric for describing $^{\bullet}$OH formation, indicating that fluorescing moieties may be important $^{\bullet}$OH precursors.

Finally, additional work needs to be done in order to understand the photochemistry of DOM in light of the competing photophysical models. The CT model has also been used as a general framework to explain DOM photochemistry. Thus, future work should focus on explaining the photochemical properties of DOM under the individual chromophore model. I anticipate that debate between the CT and superposition model will continue for years to come. A correct understanding of molecular basis for the photophysical and photochemical properties of DOM if we are to accurately describe processes involving DOM in the future.

Appendix A Supporting Information for Chapter 3

A.1. Water Sample Information.

Wastewater samples included secondary treated wastewater effluent from Boulder Wastewater Treatment Facility (BWW), which uses UV disinfection prior to effluent release and secondary effluent (pre-chlorination) used by the Orange County Water District (OCWD) as influent to its advanced wastewater recycling facility. The latter sample is a blend of nitrified activated sludge and trickling filter effluents produced by the Orange County Sanitation District. Longmont Wastewater Treatment Facility (LM) samples were secondary treated and disinfected with UV light prior to collection. An additional sample was collected from Boulder Creek (BC) at 75th and Jay St. (Boulder, CO), which is ca. 100 yards downstream of wastewater effluent discharge. This sample was subjected to the same base-modification treatment described in the main text, but no visible precipitate formed. This sample was used as a control for assessing the effect of base modification on DOM when coagulation did not occur. Samples were collected in pre-combusted amber glass bottles, filtered with pre-combusted and rinsed 0.7 μm glass fiber filters, and stored at 4 °C. Samples were used over several months.

A.2. Analytical Methods.

A.3. HPLC.

An Agilent 1200 Series HPLC with a variable wavelength detector (VWD) was used for analyze concentrations of probe compounds used in photolysis experiments. Either an Eclipse XBD C-18 or Eclipse Plus C-18 column was used (1.5 x 250 mm dimensions, 5 μm particle size).

A.4. $^1O_2$ Measurement.

Degradation of 2-furanmethanol (furfuryl alcohol, FFA) was used to measure the rate of $^1O_2$ production, R_{1O2}, (e.g. see ref (Mostafa and Rosario-Ortiz, 2013)) at a concentration of ca. 22.5 µM. Pseudo-first order rate constants for furfuryl alcohol loss allowed for calculation of R_{1O2} using the known rate constant for this reaction as well as the rate constant for physical quenching of $^1O_2$ by water. HPLC detection was accomplished using VWD at 219 nm and a gradient of pH 2.3 phosphoric acid (ca. 10 mM) and methanol: 30/70 ramped to 50/50 from 0 to 5 minutes. Furfuryl alcohol eluted at 3.2 ± 0.2 minutes under these conditions. Measured concentrations were far above the detection limit for furfuryl alcohol.

A.5. $^3DOM^*$ Estimation.

$^3DOM^*$ quantum efficiencies were estimated using the electron transfer probe 2,4,6-trimethylphenol (TMP). This method has been explained in detail previously (Bodhipaksha et al., 2015). Briefly, because DOM has a spectrum of triplet states, all of which react at different rate constants with TMP, exact quantification of $^3DOM^*$ formation rates are not attainable. However, the pseudo-first order rate for TMP loss can be used (at a fixed TMP concentration) to calculate the quantum efficiency for TMP loss, f_{TMP} (M^{-1}), which is proportional to the quantum yield for $^3DOM^*$ (Bodhipaksha et al., 2015). This analysis works under the assumption that both k_{TMP} and Σk_{3DOM^*} are constant, which represent the second order rate constant between $^3DOM^*$ and TMP and the sum over all first- and pseudo-first order $^3DOM^*$ loss reactions, respectively. In this study, a TMP concentration of 5 µM was used. HPLC measurement of TMP loss was accomplished using VWD at 219 nm and an isocratic flow of pH 2.3 phosphoric acid and methanol (40/60). TMP eluted at 7.0 ± 0.2 minutes under these conditions. Measured concentrations were far above the detection limit for TMP.

A.6. $^\bullet$OH Measurement.

$^\bullet$OH was measured by following the formation of phenol from the oxidation of benzene (3 mM). The previously determined yield of 0.63 from this reaction was used to convert the rate of phenol formation into the rate of $^\bullet$OH formation (McKay and Rosario-Ortiz, 2015). While not all of the phenol produced is formed from free $^\bullet$OH, all reported values used this conversion for consistency with previous studies (McKay and Rosario-Ortiz, 2015).

For whole water samples, nitrate and nitrite concentrations (Table A.1) were used to calculate the formation rate of $^\bullet$OH from these species by using a calibration curve, similar to the procedure of Dong and Rosario-Ortiz (Dong and Rosario-Ortiz, 2012). The remaining $^\bullet$OH formation rate was then attributed to DOM photolysis. Phenol was detected using HPLC with VWD detection at 210 nm. An isocratic mobile phase of 60% pH 2.3 phosphoric acid (ca. 10 mM) 40% methanol was used. Under these conditions, phenol eluted at 4.8 ± 0.2 minutes. The limit of detection under these conditions (for phenol in deionized water) was around 20 nM while the limit of quantitation was around 55 nM. These limits were slightly greater in DOM-containing solutions due to background DOM absorbance.

A.7. Estimation of polychromatic quantum yields.

The quantum yield for ROS production can be defined as the rate of that process divided by the rate of light absorption

$$\Phi = \frac{R_{ROS}}{R_{a-DOM}}$$

Equation A.1

R_{ROS} (M s^{-1}) is measured as described above, while the rate of light absorption by DOM, $R_{a\text{-DOM}}$ (Es L^{-1} s^{-1}), is calculated. f_{TMP} is calculated by dividing the measured pseudo first order rate constant for TMP loss (at [TMP]$_0$ = 5 μM) by $R_{a\text{-DOM}}$. For the polychromatic system used here,

$R_{a\text{-DOM}}$ is equal to the total rate of light absorption, which is a sum over all wavelengths of interest (Leifer, 1988), times the DOM concentration:

$$R_{a-DOM} = k_{a-DOM}[\text{DOM}] =$$

$$= \sum_{\lambda=290}^{i} \frac{E_{p,\lambda}^0 \varepsilon_\lambda \left(1-10^{-\varepsilon_\lambda[\text{DOM}]z}\right)}{\varepsilon_\lambda[\text{DOM}]z}[\text{DOM}] =$$

$$= \sum_{\lambda=290}^{i} \frac{E_{p,\lambda}^0 \left(1-10^{-A_\lambda z}\right)}{A_\lambda z}A_\lambda =$$

$$= \sum_{\lambda=290}^{i} \frac{E_{p,\lambda}^0 \left(1-10^{-A_\lambda z}\right)}{z}$$

Equation A.2

with the terms above defined as: $k_{a\text{-DOM}}$ (specific rate of light absorption), [DOM] (concentration of carbon in molar), $E_{p,\lambda}^0$ (spectral photon flux at wavelength λ), ε_λ (molar absorptivity of DOM at wavelength λ defined on a molar carbon basis), z (optical pathlength). In Equation A.2, wavelengths are summed between 290 nm and i where i represents the upper wavelength limit. This is represented in Figure A.2 in which the lamp spectra, DOM absorbance spectra, and wavelength dependent rate of light absorption by the system are displayed. The AM 1.5 filter as shown cuts off wavelengths below ca. 290 nm and i was typically equal to 400 nm. Table A.4 shows results of calculations of quantum yields for fluorescence, $^1O_2$, $^\bullet$OH, and ^{3}DOM* in which the upper bound was varied.

A.8. Additional notes about CT states

The CT model attributes much of DOM photophysics to *intramolecular* CT interactions. For DOM, these states arise from either partial or complete transfer of an electron between electron-rich donors (hydroxy-/alkoxy-benzenes) and electron-poor acceptors (carbonyl-containing moieties like quinones or aromatic ketones). These groups can be denoted as D and A, respectively, and a CT state is typically written as $^1(D^+ / A^-)$ indicating transfer of an electron

149

from D to A. The superscript is meant to indicate that the excited state is a singlet state. Parentheses around D and A are meant to indicate the close association between D and A groups within a DOM molecule. This can also be denoted as $DOM^{\bullet+/\bullet-}$, which similarly describes transfer of an electron, although it is implicit here that the transfer is from a D to an A group. $^1(D^* + A)$ indicates a local singlet excited donor, $^1(D + A^*)$ indicates a local singlet excited acceptor, and $^3(D + A^*)$ indicates a local triplet excited acceptor.

In principle, these interactions are possible in either the ground or excited electronic state. Weak CT complexes have little to no CT character in the ground state, but significant CT character in an electronic excited state (Birks, 1970). Here, character is specified by the contribution of the dative-bond (in which complete electron transfer has occurred) wave function (ψ_1) to the ground state. For a given DA complex, the ground-state wave function can be written as (Equation A.3)(Birks, 1970; Mulliken, 1952)

$$\psi_N(D, A) = a\psi_0(D/A) + b\psi_1(D^+/A^-)$$
<div align="right">Equation A.3</div>

and the excited state wave function can be written as (Equation A.4)

$$\psi_E(D, A) = a^*\psi_1(D^+/A^-) + b^*\psi_0(D/A)$$
<div align="right">Equation A.4</div>

The coefficients a, b, a^*, b^* describe the contribution of each state (no bond (ψ_0) and dative-bond) to the total wave function of the ground and excited state, respectively. For weak CT complexes, $a \simeq a^* \simeq 1$ and $b \simeq b^* \simeq 0$. These coefficients have yet to be characterized for DOM and thus it is presently unknown if the CT interactions within DOM are primarily in the ground or an electronic excited state. Future research should explore this question.

Under this formalism, a CT excitation could be written as (Equations A.5, A.6)

$$^1(D + A) + h\nu \rightarrow {}^1(D^* + A)$$
<div align="right">Equation A.5</div>

$$(D^* + A) \rightarrow {}^1(D^+ / A^-) \hspace{4cm} \text{Equation A.6}$$

It is important to note that only excitation of a D group [i.e. to form ${}^1(D^* + A)$] could lead to a CT state because by definition an excited local *acceptor* would not donate electron density.

A.9. Calculations on the number of carbonyl groups in SRFA

Below we present an analysis on the statistical likelihood of intramolecular CT interactions for SRFA based on known physicochemical data for this isolate. Discussion is presented first and then the calculations are presented afterwards. Based on the (number average) molecular weight of SRFA (829 Da by vapor pressure osmometry) (Aiken and Malcolm, 1987) and reported carbonyl content (by ^{13}C-NMR, including shifts between 165 to 220 ppm),[219] the number of carbonyl groups in a SRFA molecule are estimated to be: 2 (aldehyde, ketone) and 7 (ester, carboxylic acid). Using the reported carboxylic acid content of SRFA (6 mmol g DOM^{-1}),[10] there are ca. 5 carboxylic acid groups, which leaves ca. 2 ester groups. The CT model states that A groups are primarily aromatic ketones/aldehydes and quinones (Sharpless and Blough, 2014). While esters and acids would not be as electron-deficient acceptors as ketones or aldehydes, it seems unlikely that the substantial intramolecular CT interactions attributed to this sample would be configurationally or statistically possible with only 2 A groups per molecule. Based on the below calculations, 4 to 5 A groups per SRFA molecule is a reasonable upper limit for this sample. This estimate assumes that not all of the ester and acid carbonyls act as acceptors. Lower molecular weight DOM likely has fewer than 4 A groups. In fact, two recent reports indicate that terrigeneous humic substances have greater antioxidant and electron donating capacities than aquatic humic substances (Aeschbacher et al., 2010; Bodhipaksha et al., 2015; McKay and Rosario-Ortiz, 2015; Wenk et al., 2011), suggesting a greater proportion of D and A groups within the higher molecular weight (terrigenous) humic material.

Detailed calculations are made on the number of carbonyl groups present in SRFA. Relevant carbonyl-containing functional groups in SRFA are aldehydes, ketones, esters, and carboxylic acids. Data for these calculations are derived from the International Humic Substances Society (IHSS) website (^{13}C-NMR estimations of C-content), Aiken and Malcolm (1987) for the molecular weight of SRFA (Aiken and Malcolm, 1987), and Thurman and Malcolm (1983) for the carboxylic acid content of SRFA. Reported estimates of carbon distribution in SRFA (1S101F) obtained from the IHSS website are (chemical shift range, mass % of total C mass): carbonyl (220-190 ppm, 7%) and ester (190-165 ppm, 20%). The reported molecular weight of SRFA by vapor pressure osmometry is 829 Da and the reported carboxylic acid content is 6 mmol g DOM^{-1}. The reported % C by mass for SRFA is 52.44 % (Filella and Hummel, 2010).

The number of carbonyl groups from aldehydes and ketones is calculated as

$$\frac{7 \text{ g } C=O \text{ carbon}}{100 \text{ g carbon}} \times \frac{0.5244 \text{ g carbon}}{1 \text{ g SRFA}} \times \frac{1 \text{ mol carbon}}{12 \text{ g carbon}} \times \frac{1 \text{ mol } C=O}{1 \text{ mol } C=O \text{ carbon}} \times \frac{829 \text{ g}}{1 \text{ mol SRFA}}$$

$$= \boldsymbol{2.54 \; C = O \; groups} \; per \; molecule \; of \; DOM \; from \; aldehydes/ketones$$

The number of carbonyl groups from esters and carboxylic acids is calculated as

$$\frac{20 \text{ g } C=O \text{ carbon}}{100 \text{ g carbon}} \times \frac{0.5244 \text{ g carbon}}{1 \text{ g SRFA}} \times \frac{1 \text{ mol carbon}}{12 \text{ g carbon}} \times \frac{1 \text{ mol } COO}{1 \text{ mol } COO \text{ carbon}}$$

The number of carboxylic acid groups is calculated as

$$\frac{6 \text{ mmol } COOH}{\text{g SRFA}} \times \frac{829 \text{ g}}{\text{mol SRFA}} \times \frac{1 \text{ mol}}{1000 \text{ mmol}} = 4.97 \text{ } COOH \text{ groups} = \boldsymbol{4.97} \qquad \boldsymbol{C}$$

$$= \boldsymbol{O \; groups} \; per \; molecule \; of \; DOM \; from \; carboxylic \; acids$$

Thus, the number of carbonyl groups from esters is $7.25 - 4.97 = 2.28 \approx 2$.

A.10. Additional discussion of the relationship between RI quantum yields and molecular weight using current models

The below text presents a more in depth explanation of the relationship between RI quantum yields and molecular weight than presented in the main text.

Increases for Φ_{1O2} with decreasing molecular weight are attributable to either (i) a greater bulk $^1O_2$ steady state concentration with decreasing molecular weight (Latch and McNeill, 2006; Mostafa and Rosario-Ortiz, 2013) and/or (ii) a greater concentration of or more reactive $^1O_2$ precursors. Latch and McNeill (2006) reported greater $^1[O_2]_{ss}$ in the DOM microenvironment as opposed to bulk, aqueous $[^1O_2]_{ss}$ due to decreased quenching by water in the hydrophobic DOM core (Latch and McNeill, 2006). Thus, for lower molecular weight DOM, $^1O_2$ would have less distance to diffuse before reaching the aqueous phase, resulting in greater aqueous $[^1O_2]_{ss}$. Secondly, the CT model says that DOM excited states can be deactivated to CT states; for example, $^3DOM^* \rightarrow DOM^{+\bullet/\bullet}$. Lower molecular weight DOM would have a decreased rate of such a deactivation pathway and Φ_{1O2} and f_{TMP} would increase. The rate of $^1DOM^*$ deactivation to $DOM^{+\bullet/\bullet}$ would decrease as well, explaining concomitant increase in Φ_f.

Finally, Figure 3.4 also demonstrates an increase in Φ_{OH} with decreasing molecular size, which has previously been observed for size-fractionated EfOM obtained by ultrafiltration (E. Lee et al., 2013; Mostafa et al., 2014a). The explanation for this is not simple. Although the same correlation is observed for f_{TMP}, it is unlikely that $^3DOM^*$ are precursors to free $^\bullet OH$. However, $^3DOM^*$ could be precursors to low energy hydroxylators. For example, benzene is oxidized to phenol upon irradiation of p-benzoquinone (McKay and Rosario-Ortiz, 2015), which likely occurs through a quinone-water exciplex (Gan et al., 2008) that results from triplet state p-benzoquinone. Figure 3.5 as well as Lee et al. (2013) reports a positive correlation between Φ_f

and Φ_{OH}, which suggests a greater population of excited state $^\bullet$OH precursors (E. Lee et al., 2013). The correlation holds for both DOM undergoing size-fractionation and chemical reduction (SRFA) as well as coagulation (LM wastewater).

A.11. Possible assignments of peak in SEC chromatograms at retention time of ~ 45 min

The peak observed at a retention time of ~ 45 min. in the borohydride reduced samples was also observed by Tinnacher and Honeyman (2007) (Tinnacher and Honeyman, 2007), who labeled the DOM with tritiated NaBH$_4$. In addition to TOC analysis, the Tinnacher and Honeyman study also measured tritium (^{3}H) activity after elution from the SEC column. This revealed that the DOM responsible for this peak was tritiated. Based on the consistent retention times between native and reduced samples, we feel that the overall effects of this new peak are minimal. However, based on the data of Tinnacher and Honeyman, it does seem likely that lower molecular weight compounds are being produced due to reduction of esters by borohydride.

For example, if an ester reacts with tritiated NaBH$_4$, the following reaction occurs

Equation A.7
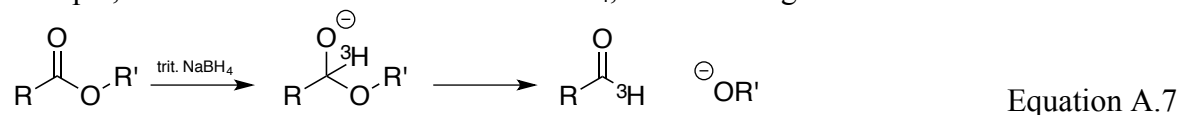
The tritiated aldehyde could be further reduced. Either of these products would account for the tritium signal detected by Tinnacher and Honeyman at longer SEC retention times. Based on the fact that the signal at this retention time exhibited tritium activity, it seems unlikely that it is due to ester hydrolysis. Tritiated NaBH$_4$ would not produce a significant amount of O^{3}H$^-$ (see calculations in Supplementary Information of ref. (Sharpless, 2012)) and so its incorporation into DOM is also expected to be minimal.

A.12. Analysis of whether preferential removal of long wavelength absorption by borohydride reduction increases the apparent quantum yield because of the RI wavelength dependence

To answer this question, consider the observation that Φ_{RI} formation are wavelength dependent (e.g. ref. (Sharpless and Blough, 2014)). In a polychromatic system, the rate of light absorption by DOM over all wavelengths of interest, $R_{a\text{-}DOM}$, is (Equation A.8)

$$R_{a\text{-}DOM} = 2.303 \int_{all\,\lambda} I_a(\lambda)A(\lambda)d\lambda \qquad\qquad \text{Equation A.8}$$

where I_a is the rate of light absorption by the system and A is the solution absorbance in a 1 cm pathlength, both at wavelength λ. With these parameters known, the rate of RI formation is (Equation A.9)

$$R_{ROS} = \int_{all\,\lambda} I_{a\text{-}DOM}(\lambda)\Phi(\lambda)d\lambda \qquad\qquad \text{Equation A.9}$$

where $I_{a\text{-}DOM}$ is the rate of light absorption by DOM at wavelength λ. For $^1O_2$, Φ seems an exponential function of λ (Sharpless and Blough, 2014). The dependence for $^{\bullet}OH$ is similar (Grannas et al., 2006; Vaughan and Blough, 1998; White et al., 2003). Regardless, $\Phi(\lambda)$ decays to zero quickly past ~ 350 nm and thus a substantial portion of the light being absorbed may not be inducing formation of RI, decreasing the calculated value of Φ. To examine this, Φ values were calculated using the discrete version of Equation A.9 with the upper bound of the sum as 350, 400, and 450 nm; results are shown in Table A.4. For $^1O_2$ and $^3DOM^*$, the difference between native and reduced SRFA diminishes as the upper wavelength bound increases. Interestingly, the difference is less pronounced for f_{TMP} than Φ_{1O2}. Conclusions presented in 3 regarding "environmental" $^1O_2$ and $^3DOM^*$ quantum yields should be investigated more thoroughly given the above analysis; however, there is good precedent in the literature for

choosing an upper wavelength bound of 400 nm (Dalrymple et al., 2010; Dong and Rosario-Ortiz, 2012; Glover and Rosario-Ortiz, 2013; Golanoski et al., 2012; E. Lee et al., 2013; Mostafa et al., 2014a; Mostafa and Rosario-Ortiz, 2013). The differences in Φ_{OH} are actually accentuated by increasing the upper wavelength bound.

Table A.1. Water quality of samples undergoing the base-modification and coagulation procedures.

Sample	Total Iron (ppm)	Total Aluminum (mg Al/L)	DOC (mgC/L)	Nitrate (mM)	Nitrite (mM)	Abs(254nm)
BCnBM	0.054	n.m.[b]	3.982	0.457	BDL[a]	0.126
BCBM	0.045	n.m.[b]	3.871	0.483	BDL[a]	0.127
BWWnBM	0.017	n.m.[b]	5.924	0.723	BDL[a]	0.112
BWWBM	BDL[a]	n.m.[b]	5.144	0.723	BDL[a]	0.093
BWW ppt	931	n.m.[b]	n.m.[b]	n.m.[b]	n.m.[b]	n.m.[b]
OCWDnBM	0.070	n.m.[b]	8.412	0.755	0.050	0.182
OCWDBM	BDL[a]	n.m.[b]	7.588	0.770	0.050	0.145
OCWD ppt	353	n.m.[b]	n.m.[b]	n.m.[b]	n.m.[b]	n.m.[b]
LMC 0ppm Alum	0.060	BDL[a]	8.210	0.968	BDL[a]	0.163
LM30ppm Alum	0.034	0.028	7.200	0.945	BDL[a]	0.137
LM60ppm Alum	0.032	0.018	6.530	1.004	BDL[a]	0.118
LM90ppm Alum	0.027	0.006	6.090	0.931	BDL[a]	0.108
LM 120ppm Alum	0.024	0.017	5.470	0.932	BDL[a]	0.098

[a]below detection limit, [b]not measured

Table A.2 Average SEC retention time (R_t) for all samples.

Sample	Average R_t (min)	Sample	Average R_t (min)	Sample	Average R_t (min)
BWW nBM	13.80	LM 0 mg Alum/L	38.13	SRFA <5K nat	31.04
BWW BM	13.67	LM 30 mg Alum/L	37.98	SRFA <5K red	31.40
OCWD nBM	13.61	LM 120 mgAlum/L	37.81	SRFA nat	29.90
OCWD BM	13.77	-	-	SRFA red	29.98
BC BM	11.81	-	-	SRFA >5K nat	29.56
BC nBM	12.03	-	-	SRFA >5K red	30.27

Table A.3. Data on various metrics for determining CT contributions to DOM absorbance and fluorescence.

Metric/Sample	SRFA<5K	SRFA bulk	SRFA>5K	Similar to $f_{a,min}$ result?
Absorbance				
$f_{a,min}$	0.620	0.485	0.364	-
Area under $\varepsilon_{red}/\varepsilon_{nat}$ (254nm<λ<480nm)	178	132	104	Yes, more area indicates less removal
Area under $\varepsilon_{red} - \varepsilon_{nat}$ (254nm<λ<480nm)	-1731	-11674	-19949	Yes, more negative value corresponds to more removal
Fluorescence				
($\Phi_{f,red} - \Phi_{f,nat}$)/$\Phi_{f,nat}$	0.82	1.15	1.25	-
($\Phi_{f,red} - \Phi_{f,nat}$)	0.0145	0.0109	0.00890	-

Table A.4. Polychromatic quantum yields calculated over different wavelength intervals.

	$^1O_2$ QY		$^{\bullet}OH$ QY		$f_{TMP}(M^{-1})$	
$290 \leq \lambda \leq 350$ nm	**Mean**	**2 s**	**Mean**	**2 s**	**Mean**	**2 s**
SRFA <5K nat	2.77E-01	4.13E-02	1.59E-04	4.60E-05	3.73E+02	4.26E+01
SRFA <5K red	2.00E-01	3.32E-03	2.22E-04	5.81E-05	2.32E+02	1.62E+00
SRFA nat	1.90E-01	5.43E-03	1.86E-04	7.76E-06	2.64E+02	6.88E+00
SRFA red	1.41E-01	1.28E-03	1.74E-04	3.72E-05	2.11E+02	1.03E+01
SRFA >5K nat	1.65E-01	1.05E-02	1.18E-04	4.03E-05	2.27E+02	2.62E+01
SRFA >5K red	1.33E-01	9.71E-03	1.68E-04	3.96E-05	1.47E+02	1.41E+01
$290 \leq \lambda \leq 400$ nm	**Mean**	**2 s**	**Mean**	**2 s**	**Mean**	**2 s**
SRFA <5K nat	3.52E-02	5.26E-03	2.03E-05	5.86E-06	4.82E+01	5.50E+00
SRFA <5K red	3.03E-02	5.04E-04	3.38E-05	8.82E-06	3.56E+01	2.49E-01
SRFA nat	2.13E-02	6.10E-04	2.09E-05	8.71E-07	3.03E+01	1.43E+00
SRFA red	1.94E-02	1.76E-04	2.38E-05	5.11E-06	2.96E+01	8.59E-01
SRFA >5K nat	1.80E-02	1.15E-03	1.28E-05	4.39E-06	2.52E+01	2.90E+00
SRFA >5K red	1.79E-02	1.30E-03	2.25E-05	5.31E-06	2.01E+01	1.93E+00
$290 \leq \lambda \leq 450$ nm	**Mean**	**2 s**	**Mean**	**2 s**	**Mean**	**2 s**
SRFA <5K nat	1.99E-02	2.97E-03	1.14E-05	3.31E-06	2.72E+01	3.11E+00
SRFA <5K red	1.85E-02	3.09E-04	2.07E-05	5.40E-06	2.19E+01	1.53E-01
SRFA nat	1.13E-02	3.23E-04	1.10E-05	4.61E-07	1.61E+01	8.63E-01
SRFA red	1.12E-02	1.02E-04	1.38E-05	2.96E-06	1.72E+01	3.94E-01
SRFA >5K nat	9.50E-03	6.05E-04	6.78E-06	2.32E-06	1.34E+01	1.54E+00
SRFA >5K red	1.06E-02	7.73E-04	1.34E-05	3.15E-06	1.20E+01	1.15E+00

Table A.5. Results of linear correlations between Φ_{1O2} and E2/E3 as measured in this study. Sample acronyms are BC (Boulder Creek), BWW (Boulder Wastewater), OCWD (Orange County Wastewater), LM (Longmont Wastewater), SRFA (Suwanee River Fulvic Acid).

Sample	Sample	Slope	Intercept	*n*
This study				
BC	creek water	-3.57	23.68	2
BWW	wastewater	1.50	-5.13	2
OCWD	wastewater	8.54	-40.17	2
LM	wastewater	1.38	-3.97	5
SRFA native	DOM isolate	1.61	-5.82	3
SRFA reduced	DOM isolate	0.95	-4.48	3
All data besides reduced SRFA	wastewater + DOM isolates	1.59[a]	-5.29[a]	14
Previous work				
Mostafa et al. (2013)(Mostafa and Rosario-Ortiz, 2013)	wastewater + DOM isolates	0.72	0.20	> 20
Peterson et al. (2012)(Peterson et al., 2012)	water from Lake Superior	0.61	0.20	> 45
Dalrymple et al. (2010)(Dalrymple et al., 2010)	DOM isolates of diverse origin	0.87	-1.53	18

[a]Found to be significant at α = 5% (slope *p* < 0.01)
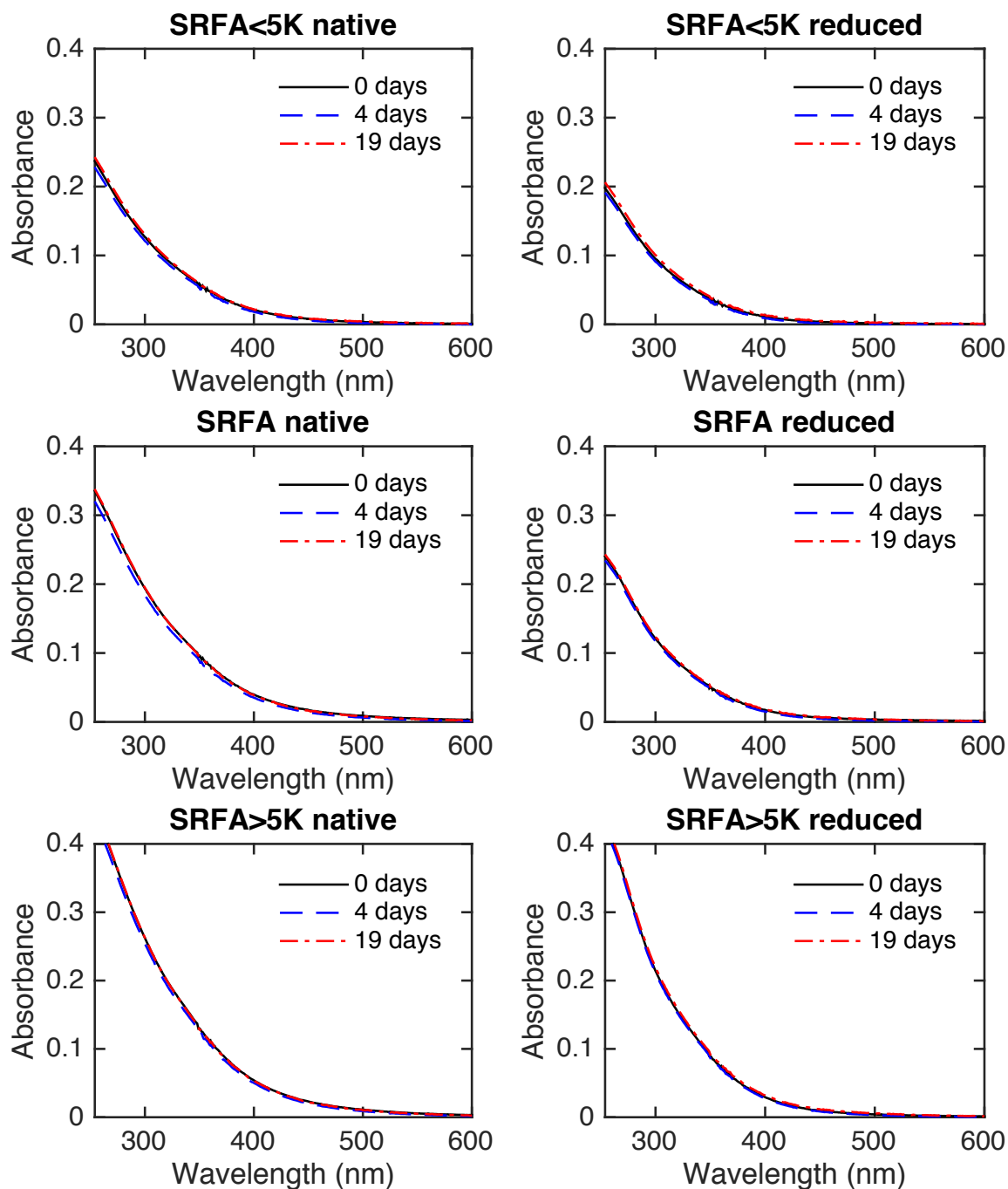
Figure A.1. Time course of absorbance spectra (1 cm pathlength) for SRFA plotted from 254 to 600 nm for SRFA <5K, unfractionated, and >5K before and after reduction with sodium borohydride over the time period of this study.
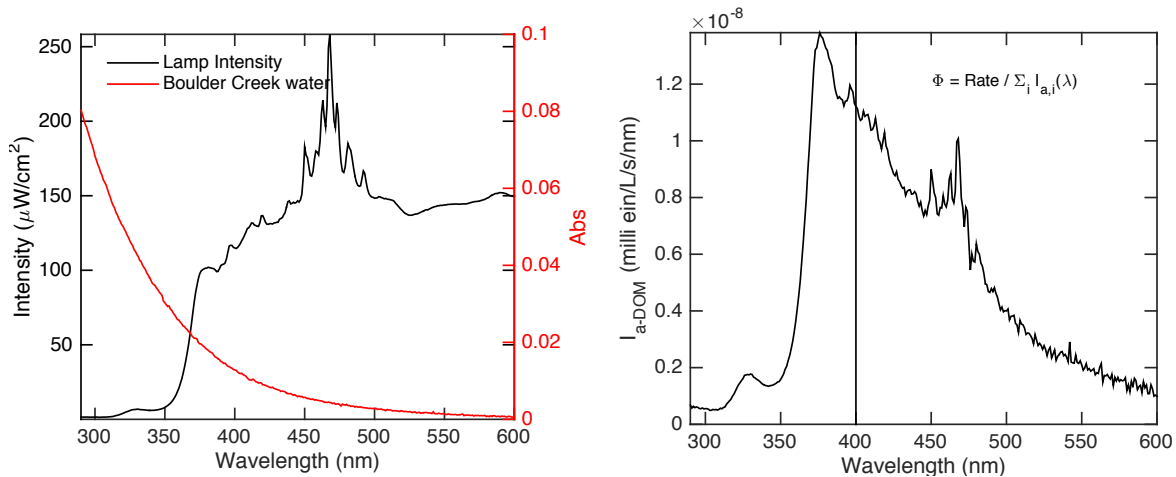
Figure A.2. (Left) Lamp spectra (black, left axis) for Oriel 94041 A solar simulator described in main text and absorbance spectra (red, right axis) for Boulder Creek non-base-modified. (Right) calculation of the rate of light absorption by DOM based on Equation A.2).
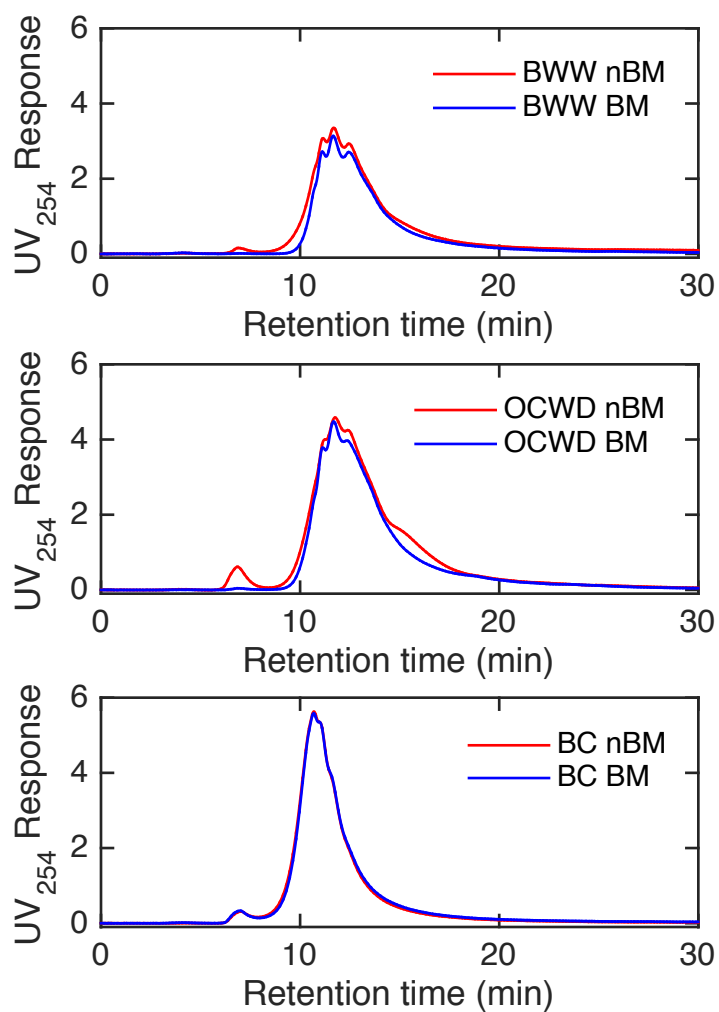
Figure A.3. Size exclusion chromatograms for pre-and post-base-modified samples. Solution and eluent conditions are given in (Dong et al., 2010) Detector was a VWD set at 254 nm.
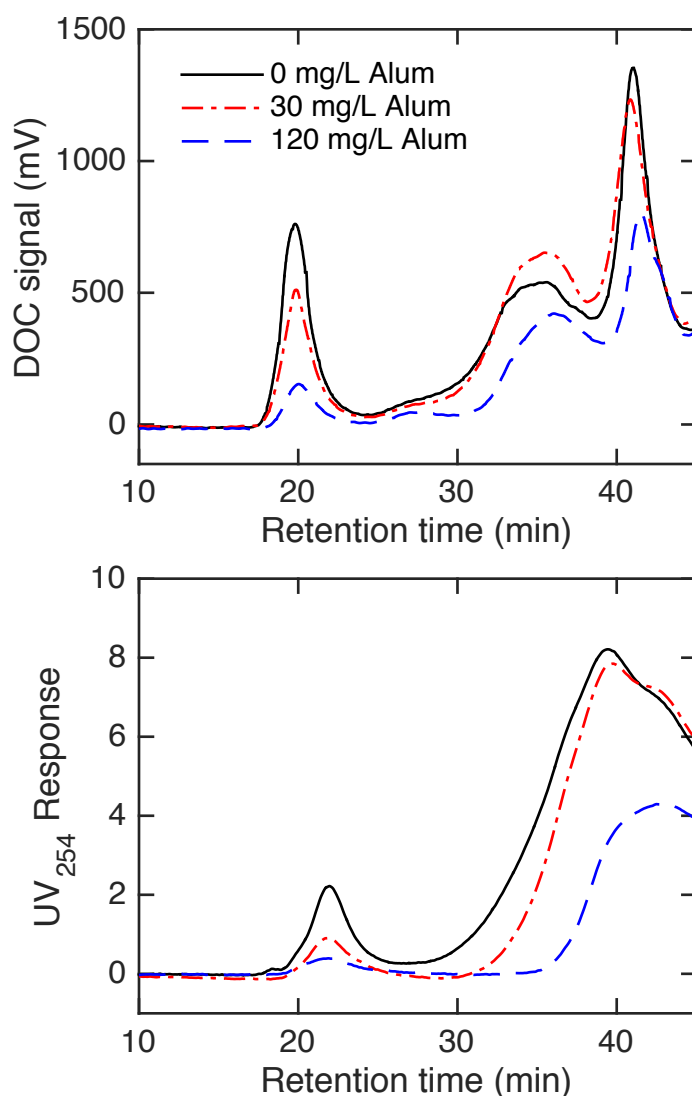
Figure A.4. Size exclusion chromatograms for LM wastewater pre- and post-coagulation with Alum. Solution and eluent conditions are given in ref.(Dong et al., 2010) Note that DOC signal in top plot has been baseline subtracted (actual baseline was around 800 mV).
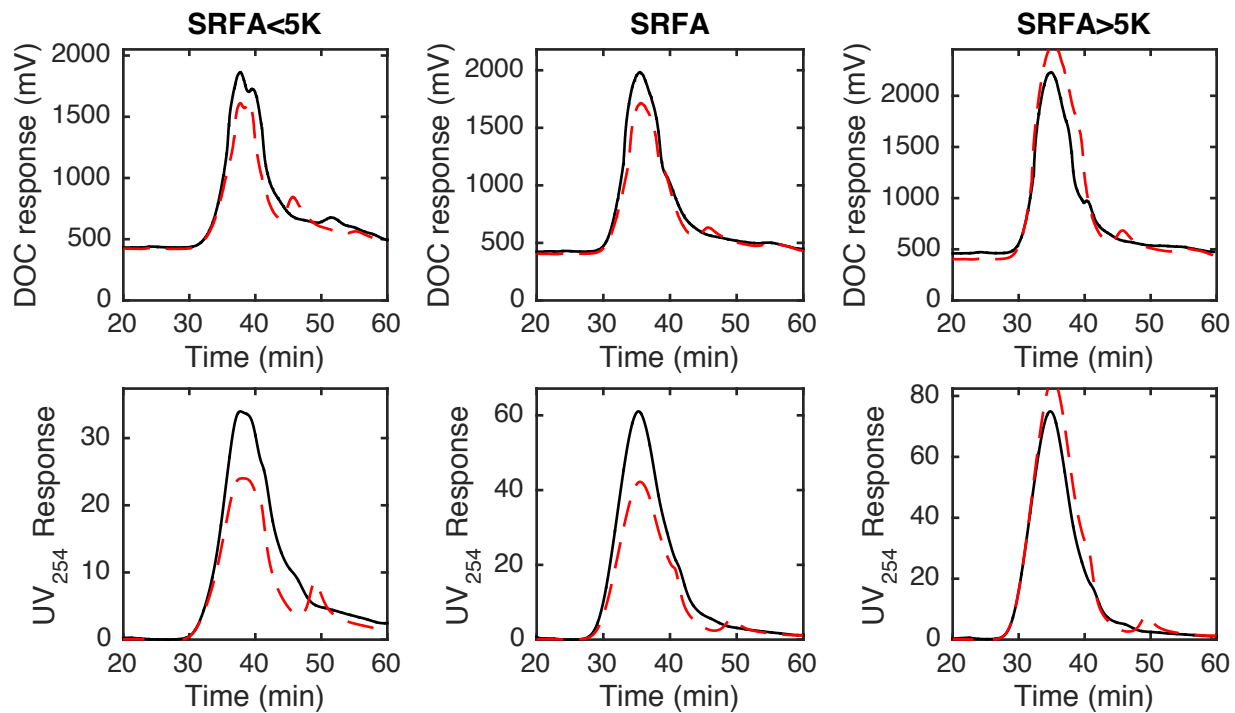
Figure A.5. Size exclusion chromatograms for SRFA <5K, unfractionated, and >5K before (solid, black line) and after reduction (dashed, red line) with sodium borohydride. Solution and eluent conditions are given in ref.(Dong et al., 2010) UV detection was at 254 nm.
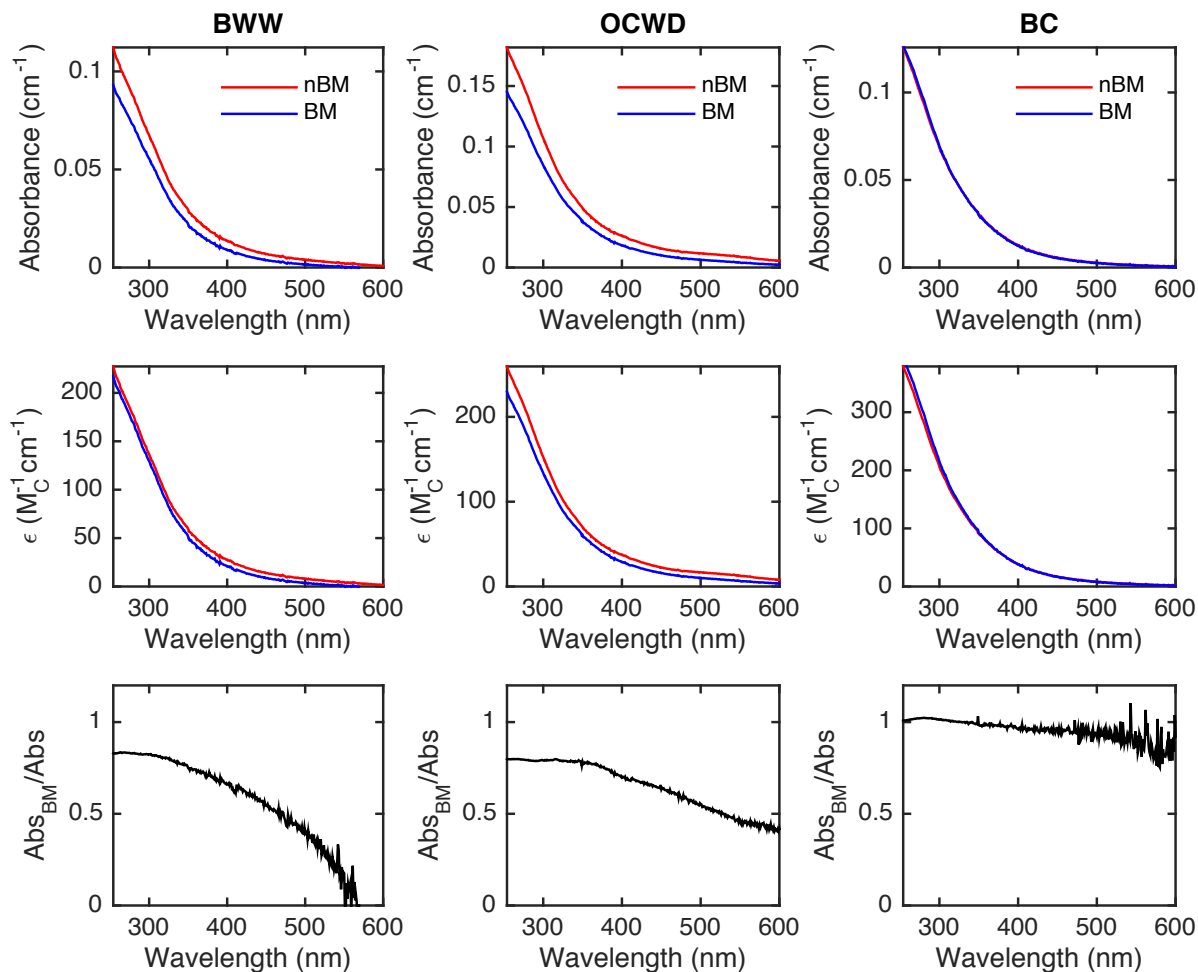
Figure A.6. (First row) Absorbance spectra (1 cm pathlength) plotted from 254 to 600 nm for BWW, OCWD, and BC. (Second row) Molar absorptivity on a per-carbon basis based on data in first row and DOC values in Table A.1. (Third row) Fractional absorbance based on data in first row. nBM and BM refer to non-base-modified and base modified, respectively.
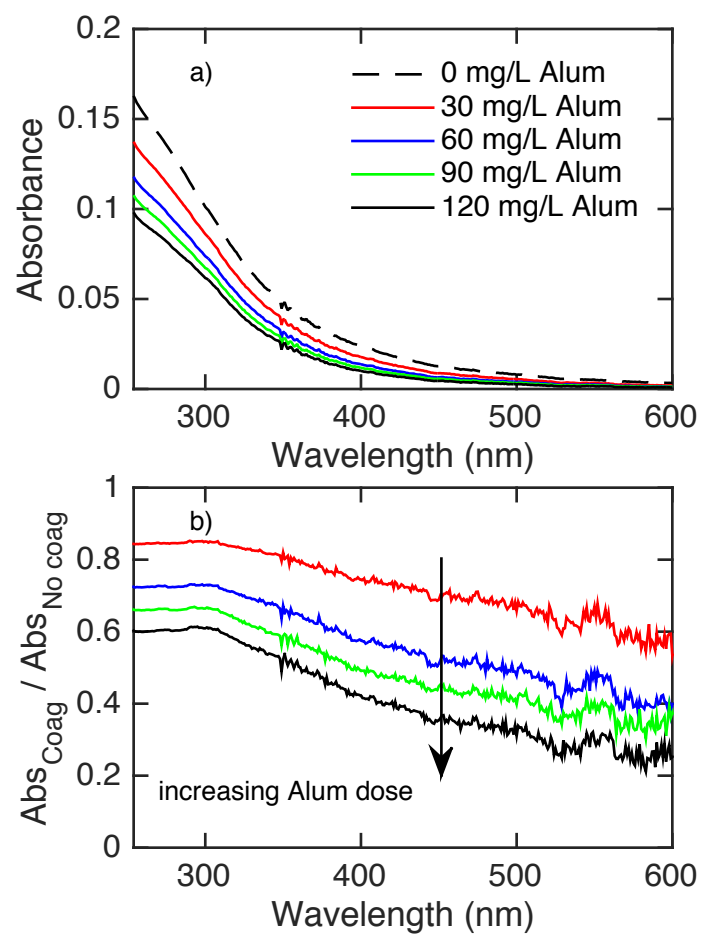
Figure A.7. Absorption spectra (1 cm pathlength) for LM wastewater plotted from 254 to 600 nm and fractional absorbance based on data in a).
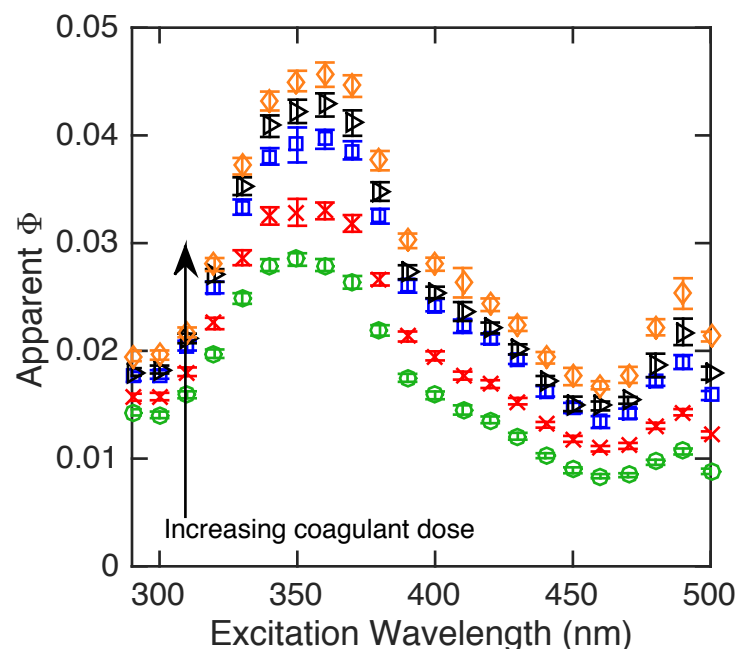
Figure A.8. Apparent fluorescence quantum yields for LM wastewater as a function of increasing alum dose.
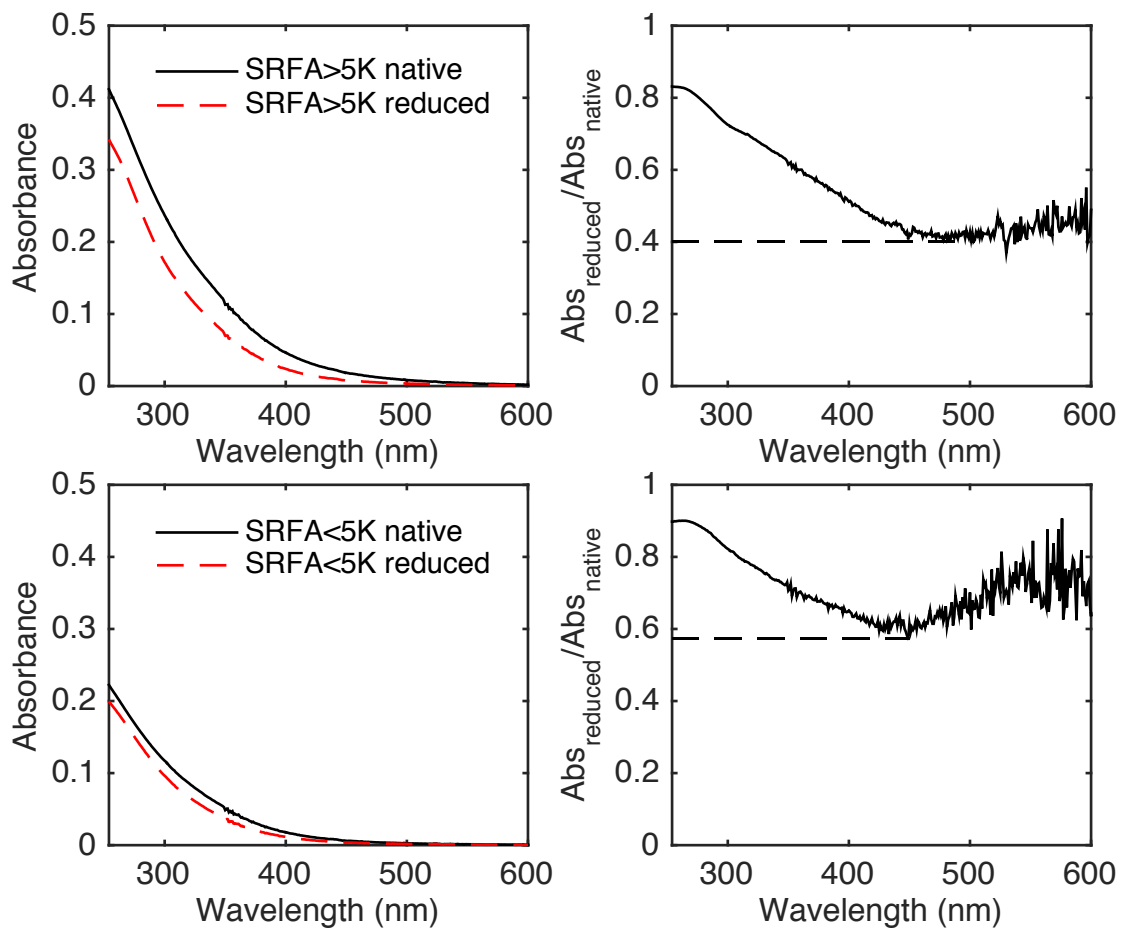
Figure A.9. Absorption spectra (1 cm pathlength) plotted from 254 to 600 nm for SRFA >5K and SRFA <5K fractions pre- and post-reduction. $f_{a,min}$ values for SRFA >5K and SRFA <5K are 0.401 and 0.573, respectively.
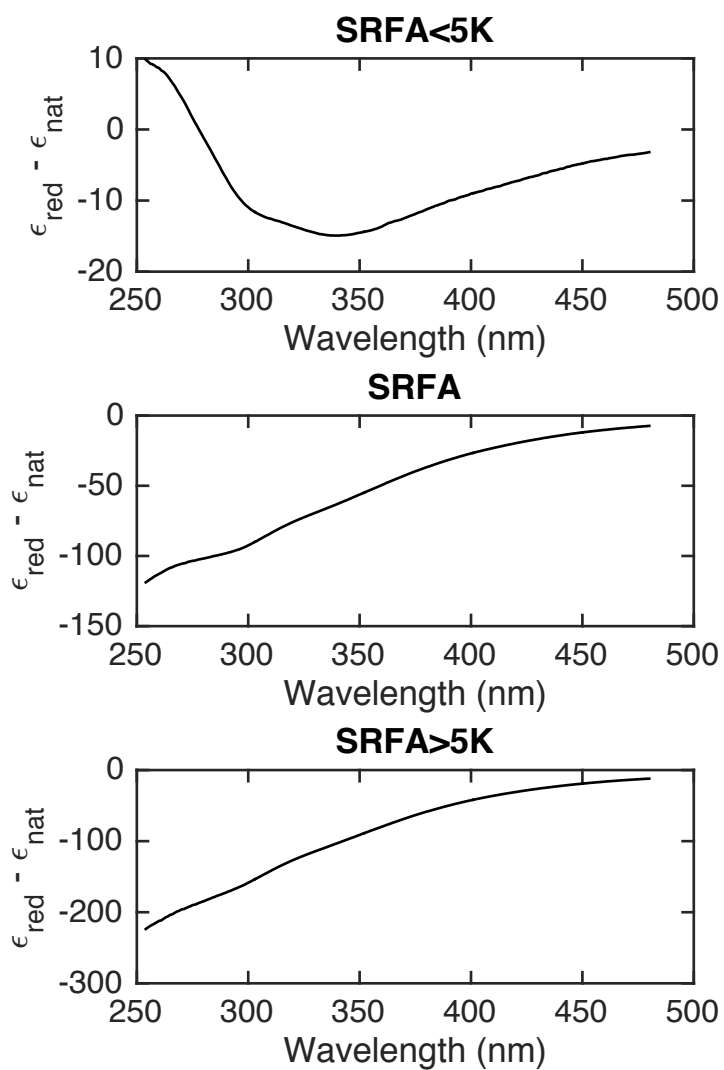
Figure A.10. Plot of ϵ_{red} - ϵ_{nat} for SRFA molecular weight fractions. Integration of the between the curve and ϵ_{red} - ϵ_{nat} = 0 gives the area for the metric provided in Table A.3 (row 3).
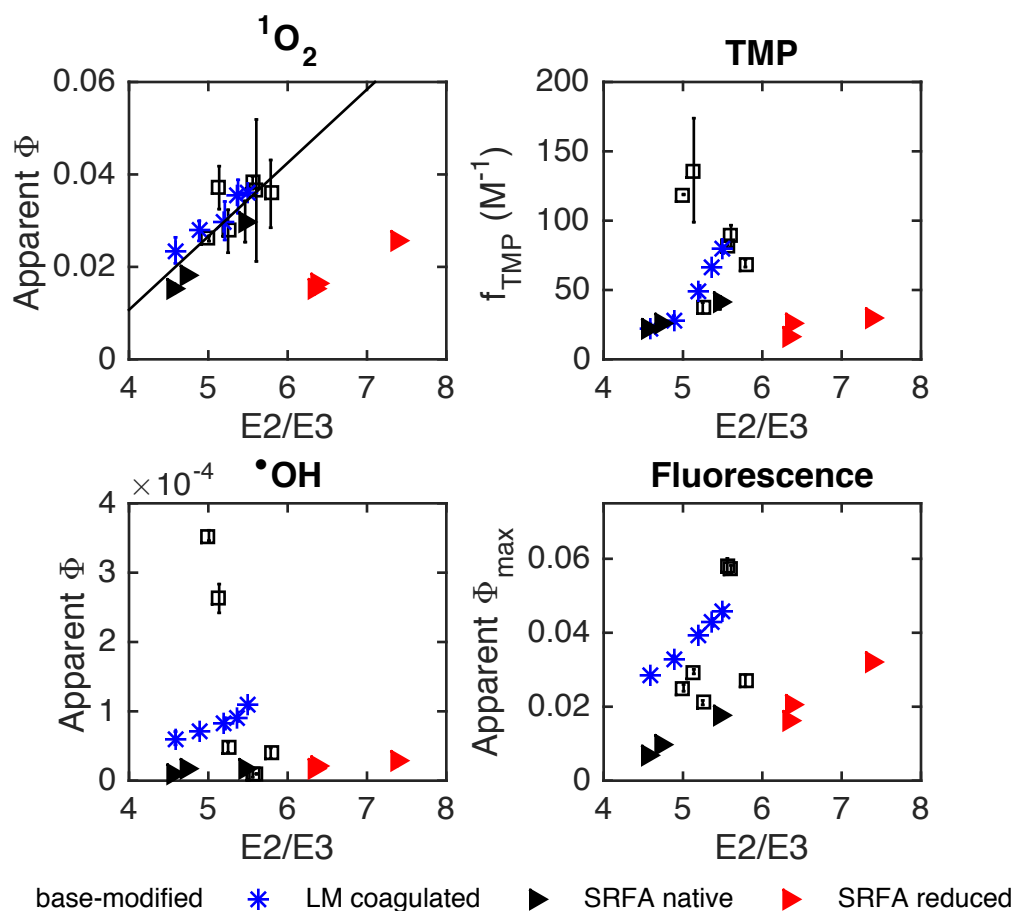
Figure A.11. Plots of apparent Φ versus E2/E3 for all samples in this study. See legend for sample identity. Solid line for $^{1}O_2$ represents linear regression of Φ_{1O2} and E2/E3 excluding SRFA reduced samples. Regression relation is Φ_{1O2} (%) = 1.59×E2/E3 − 5.29. Both the slope (p < 0.0001) and intercept ($p < 0.01$) are significant.
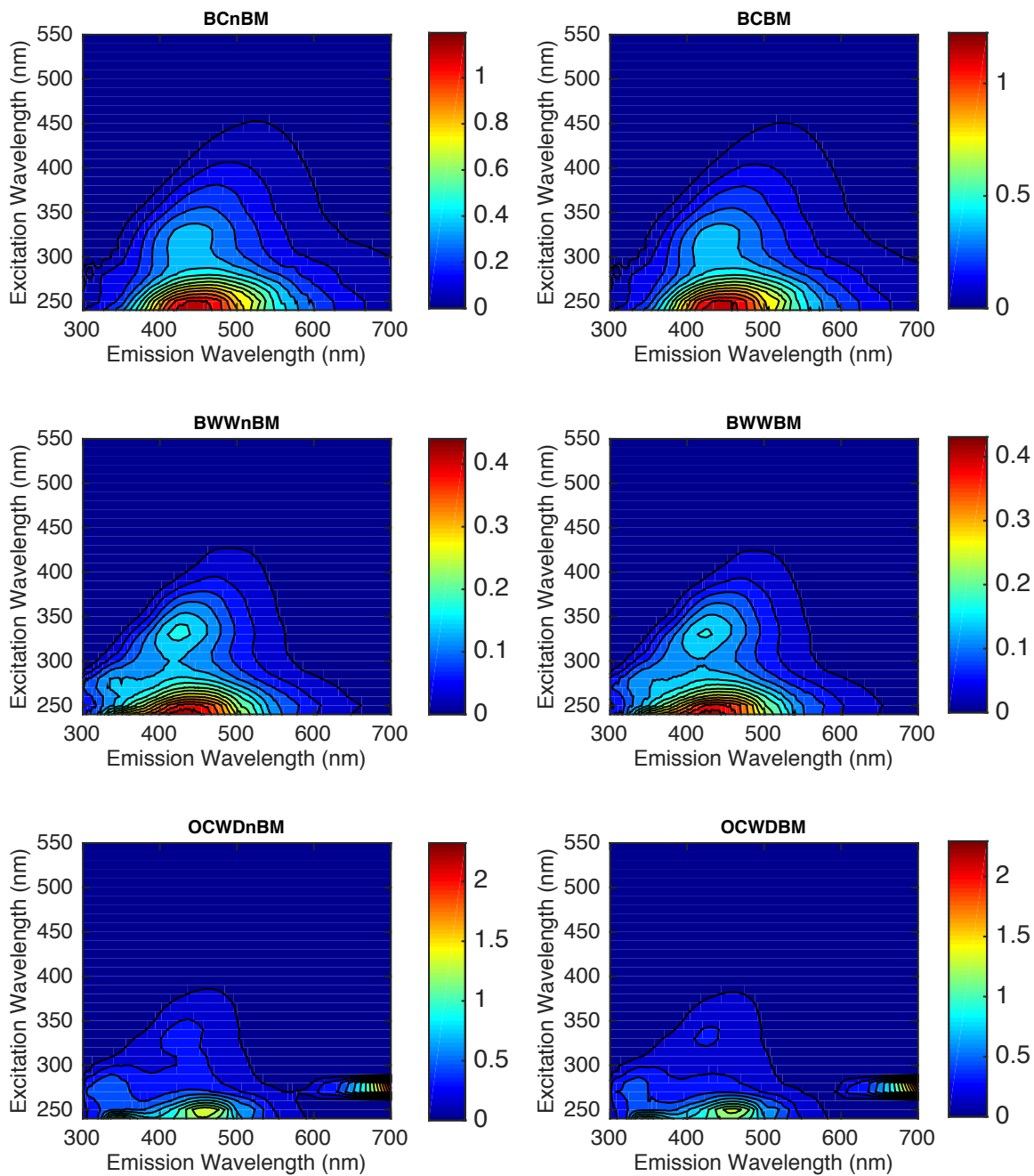
Figure A.12. Three dimensional excitation emission matrices for BC, BWW, and OCWD pre- and post-base-modification.
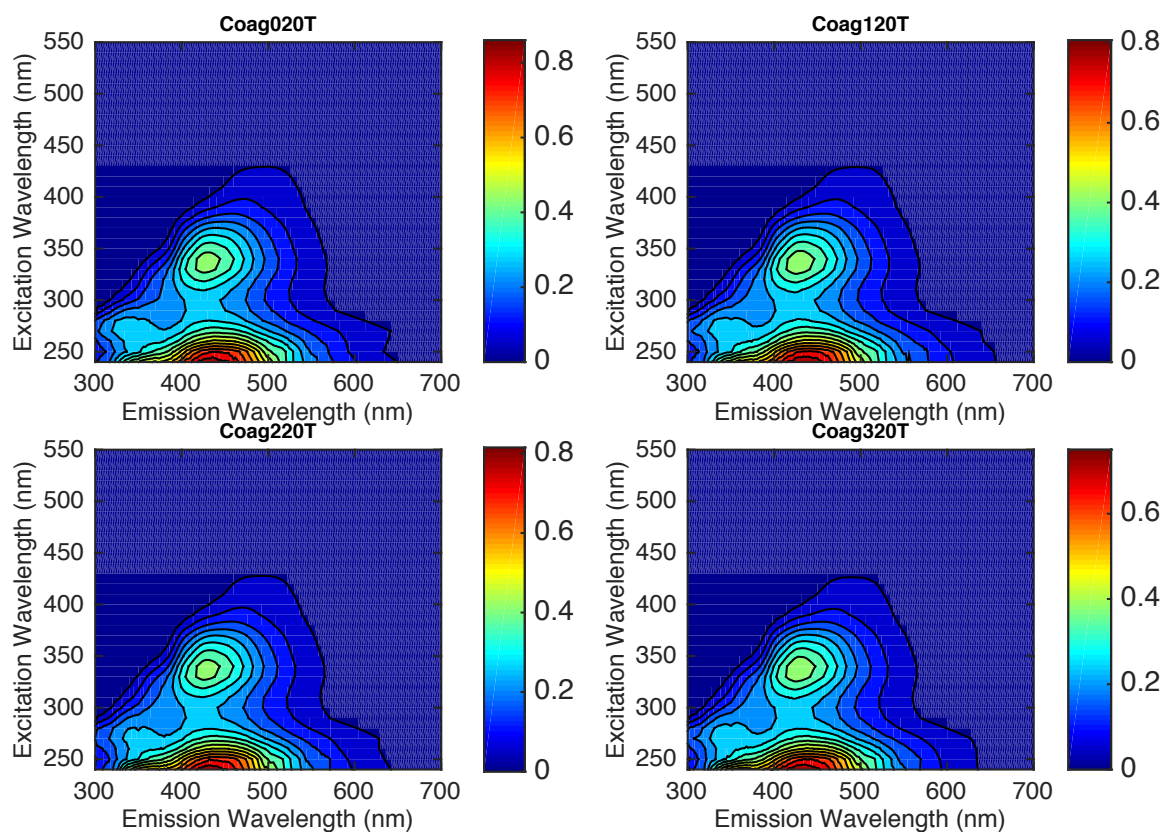
Figure A.13. Three dimensional excitation emission matrices for LM as a function of coagulation dose. From top left: Coag0 = 0 mg alum/L, Coag1 = 30 mg alum/L, Coag2 = 60 mg alum/L, Coag 3 = 90 mg alum/L.
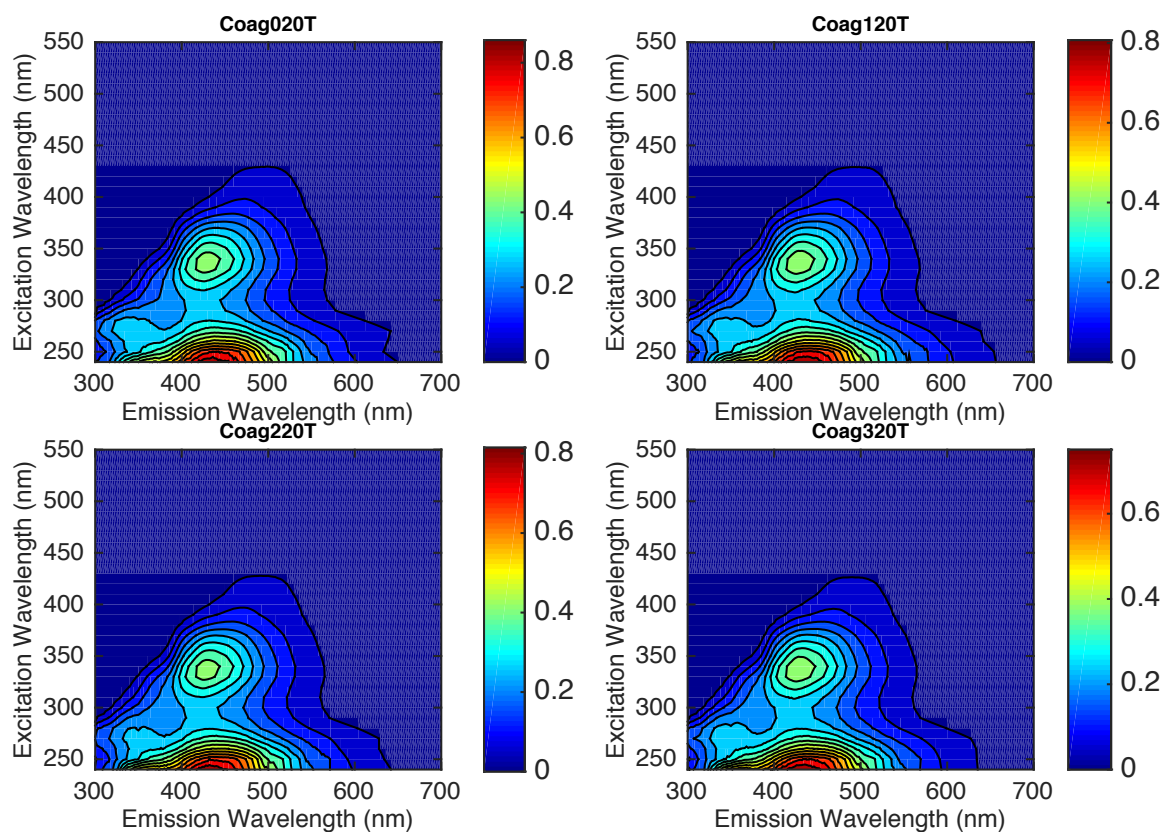
Figure A.14.Three dimensional excitation emission matrices for SRFA before and after reduction with sodium borohydride.

Appendix B Supporting Information for Chapter 4

B.1. Background

B.2. Charge Transfer

Mulliken developed charge transfer (CT) theory in a series of papers and used this model to calculate the intensity and position of previously observed CT absorption bands (Mulliken, 1952). We have provided below a brief outline of CT theory as described by Mulliken and a discussion of the application of this theory to dissolved organic matter (DOM).

Association of an electron-rich donor (D) with an electron-poor acceptor (A) forms a donor-acceptor complex (DA) that is described quantum mechanically by the states (Equation B.1)

$$\psi_N = a\psi_0(D,A) + b\psi_1(D^+A^-) \qquad \text{ground state}$$
$$\psi_E = a*\psi_1(D^+A^-) + b*\psi_0(D,A) \qquad \text{excited state}$$

Equation B.1

Here, ψ_0 represents the no-bond wave function of the complex DA and ψ_1 represents the dative wave function in which an electron is transferred completely from D to A. The contribution of ψ_1 to the ground (ψ_N) and excited state (ψ_E) describes the amount of CT character of the complex and is determined by the scalar product of Equation B.1. Assuming ψ_N is normalized (Equation B.2):

$$\langle \psi_N | \psi_N \rangle = \langle a\psi_0 + b\psi_1 | a\psi_0 + b\psi_1 \rangle =$$
$$= \bar{a}a\langle \psi_0 | \psi_0 \rangle + \bar{a}b\langle \psi_0 | \psi_1 \rangle + \bar{b}a\langle \psi_1 | \psi_0 \rangle + \bar{b}b\langle \psi_1 | \psi_1 \rangle =$$
$$= a^2 + 2abS + b_2 = 1 \quad \text{where } S = \langle \psi_0 | \psi_1 \rangle$$

Equation B.2

A bar is used above to denote the complex conjugate so as not to confuse, for example, *a* versus *a**. The coefficients a and b above can be determined, which yields the CT character as (Equation B.3)

$$\lambda = \frac{b^2}{a^2 + b^2} \qquad 0 \le \lambda \le 1$$

Equation B.3

So-called weak DA complexes have $\lambda \approx 0$ and thus have close to no D^+A^- character in their ground state. Strong DA complexes have $\lambda \approx 1$ and have substantial D^+A^- character in their ground state (i.e., substantial ionic character).

With this in mind, upon light absorption weak DA complexes undergo what is appropriately described as a CT transition (Equation B.4)

$$\psi_N \to \psi_E$$
$$\psi_0(DA) \to \psi_1(D^+A^-)$$

Equation B.4

Conversely, upon light absorption strong DA complexes undergo a transition in which the excited state ψE has little or no CT character (Equation B.5)

$$\psi_N \to \psi_E$$
$$\psi_1(D^+A^-) \to \psi_0(DA)$$

Equation B.5

The above discussion focuses on absorption of light by DA complexes. Concerning fluorescence, there is an important distinction between fluorescence of CT excited states (i.e. $\psi_E \approx \psi_1(D^+A^-)$ for weak DA complexes) and donor-acceptor exciplexes. The distinction is in the route by which the excited CT state complex, $[D^+A^-]^*$, is formed. This distinction is important because excited-state deactivation mechanisms differ between the two pathways. For the DA exciplex route, formation of the exciplex D*A or DA* is a pre-requisite for electron transfer to form D^+A^- and is in competition with local excited (LE) state fluorescence and formation of solvent separated charged species (D^+…..A^-). Furthermore, exciplex emission from D*A or DA* can occur prior to electron transfer. All of these mechanisms decrease the contribution of this pathway to D^+A^- fluorescence. For the CT absorption route, formation of the DA complex is a

prerequisite to CT absorption, which directly populates $[D^+A^-]^*$. Emission by $[D^+A^-]^*$ formed by this pathway is in competition with formation of a solvent separated charged species $(D^+…..A^-)$.
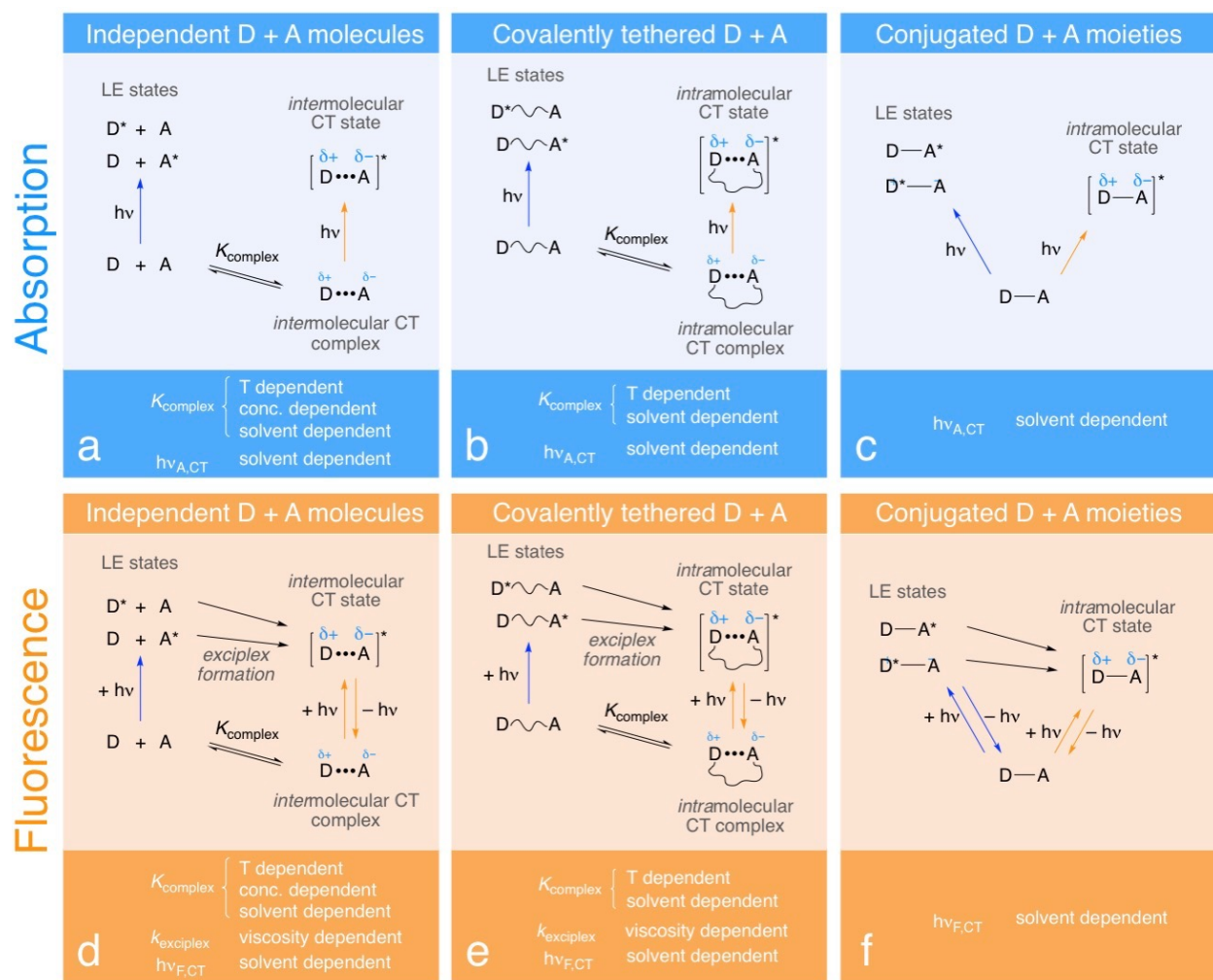
Figure B.1. Scheme depicting the possible photophysical processes of CDOM, including local excited (LE) states and charge-transfer (CT) interactions and expected effects of temperature, solvent polarity, and viscosity on CDOM absorption (a-c) and fluorescence (d-f) properties. Scenarios are depicted for independent D and A molecules (a, d), covalently tethered D and A (b, e) and conjugated D and A moieties (c, f). Only some of the critical dependencies are indicated. For example, the wavelength of fluorescence (hvF,CT) has been shown to be dependent on solvent viscosity due to dipole reorientation effects (Lakowicz, 1999). Note also that temperature also perturbs solvent viscosity and solvent polarity and is thus expected to have effects beyond DA complex equilibrium position.

B.3. Application of CT theory to DOM

CT theory was first used to explain DOM optical properties by Ziechman in the 1970s, who investigated humic substances and model compounds (Ziechmann, 1972). This work suggested an enthalpic component to DA complex formation in humic substances and that this could be

177

investigated by UV-Vis spectrophotometry. Subsequent work by Langford and coworkers developed these ideas further, wherein it was proposed that intramolecular complexation of chromophores resulted in long wavelength absorbance. Work by Blough and Sharpless has led to the CT model for DOM photophysics, which is summarized in Table B.1 (Sharpless and Blough, 2014). Other optical property models are used by the DOM community, mainly one in which chromophores are assumed to act independently of one another (i.e. a superposition). An application of this model is parallel factor analysis (PARAFAC), which decomposes DOM fluorescence spectra into components, which researchers often interpret as specific groups of fluorophores.

Table B.1 outlines the major photophysical and photochemical observations that have lent support for the CT model. Readers are referred to references listed in Table B.1 for details. Figure B.1 shows schematically the possible arrangements of D and A moieties under this model.

Table B.1.Photophysical and photochemical properties of DOM and their proposed explanation by the CT model.

Observation	Reference	Superposition of chromophores explanation	CT Explanation
Absorption in visible region of spectrum	Shapiro (1964),(Shapiro, 1964) Ghassemi and Christman (1968)(Ghassemi and Christman, 1968)	Absorption due to chromophores containing extended π systems, or electron rich aromatics (polyphenols)	Absorption due to the lower energy excitation of a weak DA complex into a CT excited state, $[D^+A^-]^*$
Preferential decrease in visible absorbance as a result of photobleaching and lower molecular weight	Boyle (2009),(Boyle et al., 2009) Helms (2008),(Helms et al., 2008) Sharpless (2014),(Sharpless et al., 2014) McKay (2016)(McKay et al., 2016)	Lower abundance of conjugated DOM molecules, polyphenols, quinones in lower molecular weight DOM	Formation of lower molecular weight compounds upon photobleaching, which have a decreased likelihood of forming DA complexes due to size constraints
Shape of Φ_f versus excitation wavelength plot	Del Vecchio and Blough (2004),(Del Vecchio and Blough, 2004) Boyle (2009)(Boyle et al., 2009)	This shape is not universal for organic matter isolates (vide infra and main manuscript)	Emission at wavelengths > 475 nm is due to a coupled manifold of CT states that are increasingly lower in energy
Preferential loss of visible absorption, blue-shifted fluorescence emission, and increased fluorescence quantum yields following DOM reduction with borohydride	Ma (2010),(Ma et al., 2010) McKay (2016)(McKay et al., 2016)	Formation of lower molecular weight molecules due to ester hydrolysis during borohydride reduction	Reduction of aromatic ketones/aldehydes (D groups) decreases DA complex (i.e. visible) absorption, and also decreases LE decay into CT states
Decrease of reactive intermediate quantum yields with increasing wavelength	Vaughan et al. (1998),(Vaughan and Blough, 1998) Sharpless (2012),(Sharpless, 2012) refs within Sharpless and Blough (2014)(Sharpless and Blough, 2014)	Formation of lower energy excited states that preempt reactive intermediate formation	Excitation into CT states does not lead to formation of reactive intermediates

B.4. Materials and methods

Additional sample sources and details are given in Table B.2.

Table B.2. Names, classifications, and sources for samples used in this study.

Sample	Classification	Source	Acronym	Identification #	Isolation method
Suwannee River Fulvic Acid	Terrestrial, aquatic	IHSS	SRFA	2S101F	Thurman and Malcolm (1981, EST)(Thurman and Malcolm, 1981)
Suwannee River Humic Acid	Terrestrial, aquatic	IHSS	SRHA	2S101H	Thurman and Malcolm (1981, EST)
Nordic Lake Fulvic Acid	Terrestrial, aquatic	IHSS	NRFA	1R105F	Thurman and Malcolm (1981, EST)
Pony Lake Fulvic Acid	Microbial, aquatic	IHSS	PLFA	1R109F	Thurman and Malcolm (1981, EST)
Suwannee River Natural Organic Matter	Terrestrial, aquatic	IHSS	SRNOM	2R101N	Sun, Perdue and McCarthy (1995, Water Res)(Sun et al., 1995)
Nordic Lake Natural Organic Matter	Terrestrial, aquatic	IHSS	NRNOM	1R108N	Sun, Perdue and McCarthy (1995, Water Res)
Upper Mississippi River Natural Organic Matter	Terrestrial, aquatic	IHSS	MRNOM	1R110N	Sun, Perdue and McCarthy (1995, Water Res)
Elliot Soil Humic Acid	Soil	IHSS	ESHA	1S102H	base extracted from solid material, XAD-8
Pahokee Peat Humic Acid	Soil	IHSS	PPHA	1S103H	base extracted from solid material, XAD-8
Pahokee Peat Fulvic Acid	Soil	IHSS	PPFA	2S103F	base extracted from solid material, XAD-8
Yukon HPOA	Terrestrial, aquatic	USGS	YHPOA	AK09-0044 HPOA	Aiken et al. (1992, Org Geoc)(Aiken et al., 1992)
Gulf of Maine HPOA	Estuarine	USGS	GMHPOA	MEG08-0029 HPOA	Aiken et al. (1992, Org Geoc)
Pacific Ocean FA	Marine	USGS	POFA	O-1 FA	Aiken et al. (1992, Org Geoc)

Table B.3 compares Fluoromax-4 and Aqualog spectrofluorometer specifications.

Table B.3. Comparison of Fluoromax-4 and Aqualog spectrofluorometers

Instrument	Source	Excitation rangea (nm)	Emission rangea (nm)	Monochromators	Detectors	S/N Ratiob
Fluoromax-4	150 W xenon, continuous output, ozone-free lamp	240-600	290-800	Czerny-Turner, Ruled gratings, 1200 grooves/mm Excitation: 330 nm blaze Emission: 500 nm blaze	Excitation: Photodiode PMT Emission: R928P PMT	3,000:1
Aqualog	150 W xenon, continuous output, ozone-free lamp	230-800	250-800	Excitation: Double-grating. Aberration-corrected with holographic gratings. Excitation grating: 1,200 gr/mm, 250 nm blaze Emission grating: 285 gr/mm, 350 nm blaze	Excitation: Photodiode PMT Emission: CCD	20,000:1
a Range with manufacturer determined instrument correction factors b Manufacturer specification, test conditions and method specified in instrument manual.						

B.5. Quantum yield calculation

The fluorescence quantum yield (Φ_f) was determined using steady state fluorescence data and quinine sulfate in 0.1 N H2SO4 as a reference (Φ_f of 0.51) (Velapoldi and Mielenz, 1980). Equation B.6 is the most general expression for fluorescence quantum yield (Birks, 1970). This method calculates the ratio of the integrated DOM sample fluorescence intensity (I_{DOM}) across all emission wavelengths (λ_{em}) at a given excitation wavelength (λ_{ex}) divided by the DOM absorbance at this excitation wavelength (Abs_{ex}). This ratio is divided by the same ratio for the quantum yield standard (I_{ref} and Abs_{ref}), in this case quinine sulfate. The first term corrects for differences in refractive index between the sample and quantum yield reference.

$$\frac{\Phi_{DOM}(\lambda_{ex})}{\Phi_{ref}(\lambda_{ex})} = \frac{n^2}{n_{ref}^2} \frac{\int_0^\infty I_{DOM}(\lambda_{ex},\lambda_{em})d\lambda_{em}}{Abs_{ex}(\lambda_{ex})} \frac{Abs_{ref}(\lambda_{ex})}{\int_0^\infty I_{ref}(\lambda_{ex},\lambda_{em})d\lambda_{em}}$$

Equation B.6

Quinine sulfate does not absorb at wavelengths > 400 nm, which are of interest to DOM fluorescence. Thus, the reference term in the above equation was fixed to an excitation wavelength of 350 nm. This approach has been used before and is justified by the fact that instrument-specific correction factors are applied to the fluorescence data (Valeur and Berberan-Santos, 2012). Finally, the dependence of refractive index on wavelength and solvent was assumed to be negligible. In aqueous samples, the wavelength dependence is due to the fixed quinine sulfate standard excitation wavelength compared to sample excitation wavelength. For aqueous samples, the maximum refractive index range between all excitation and temperature combinations tested is 1.33 to 1.36 (Thormählen et al., 2009). For the glycerol-water solutions, the refractive index at 20°C ranges from 1.33-1.37. In ACN and THF, the refractive index across excitation wavelengths ranges from 1.35-1.35 and 1.41-1.42 for ACN and THF, respectively from 600-400 nm (http://wtt-pro.nist.gov/wtt-pro/). Based on Equation 6, the maximum systematic error due to neglecting the refractive index term is 10%. With these assumptions, the Equation B.6 simplifies to Equation B.7.

$$\frac{\Phi_{DOM}(\lambda_{ex})}{\Phi_{ref}(350\,\text{nm})} = \frac{\int_0^\infty I_{DOM}(\lambda_{ex},\lambda_{em})d\lambda_{em}}{Abs_{ex}(\lambda_{ex})} \frac{Abs_{ref}(350\,\text{nm})}{\int_0^\infty I_{ref}(350\,\text{nm},\lambda_{em})d\lambda_{em}}$$

Equation B.7

The upper bound of the integral in Equation B.7 is given by the maximum emission wavelength for which the sample emits. For measurements performed on the Fluoromax-4, the maximum emission wavelength measured was 700 or 800 nm, depending on the sample (red-

shifted samples such as soil HA and SRHA were analyzed out to 800 nm). For measurements performed on the Aqualog, all samples were analyzed with a maximum emission wavelength of 800 nm.

Some additional details need to be mentioned regarding quantum yield determined with the Fluoromax-4 instrument. First, due to second order diffraction of fluorescence signal by the emission gratings, it was necessary to extrapolate (first order) fluorescence to zero using a single exponential function at excitation wavelengths less than 400 nm before integrating the signal. The difference in area between this method and simply stopping the integration when second order diffraction appeared was typically < 10% at excitation wavelengths > 300 nm. Second, comparison of quantum yield profiles determined on both instruments showed systematically higher values for the Fluoromax-4 as compared to the Aqualog at excitation wavelengths < 350 nm. This difference is due to the poorer quality excitation gratings in the Fluoromax-4 (plane ruled gratings) that lets more stray light pass than the gratings in the Aqualog excitation system (concave holographic). For these reasons, quantum yields determined on the Fluoromax-4 are only reported at excitation wavelengths greater than 350 nm, which did not exhibit this systematic bias. At excitation wavelengths greater than 350 nm, there was good agreement in quantum yields measured on both instruments.

B.6. Results and discussion

B.7. DOM optical properties in aqueous solution

The samples investigated in this study were diverse in origin, ranging from marine and microbial-derived isolates, to terrestrial aquatic isolates, to soil-derived isolates. This can be seen by looking at the wide range of $SUVA_{254}$ values measured (0.7 – 8.9 L mgC-1 m-1), which

indicates an approximate percent aromatic carbon ranging from about 7 % to 50 % (Weishaar et al., 2003). We note, however, that $SUVA_{254}$ values for soil samples are higher than what is typically observed for aquatic samples and should be interpreted with caution. Absorbance spectra for all aqueous samples are shown in Figure B.8 and Figure B.9. Fluorescence spectra for all aqueous samples are shown in Figure B.10 through Figure B.13.

Table B.4. Optical properties for all samples in aqueous solution. Uncertainty may be less than significant figures shown.

Isolate	ID Number	DOC (mg/L)	$SUVA_{254}$ (L/mgC/m)	E2:E3	Spectral Slope (nm^{-1})	FI	Max Em at λ_{Ex} = 370 nm	Φ_f at λ_{Ex} = 370 nm	Max Φ_f	λ_{Ex}
GMHPOA	MEG08-0029 HPOA	5.63±0.09	1.74±0.02	6.96±0.01	0.01725±0.00009	1.430±0.003	462±0	0.0099±0.0002	0.0099±0.0002	370
POFA	O-1 FA	10.55±0.07	0.67±0.01	8.69±0.00	0.01613±0.00009	1.540±0.029	457±0	0.0103±0.0001	0.0104±0.0001	355
PLFA	1R109F	4.77±0.13	2.52±0.03	4.89±0.00	0.01547±0.00009	1.575±0.016	456±0	0.0121±0.0001	0.0123±0.0000	390
MRNOM	1R110N	4.58±0.04	3.44±0.01	5.39±0.00	0.01609±0.00005	1.452±0.008	462±3	0.0111±0.0001	0.0111±0.0001	370
NRNOM	1R108N	4.17±0.13	4.20±0.03	4.68±0.00	0.01488±0.00005	1.437±0.003	463±3	0.0066±0.0001	0.0067±0.0001	360
SRNOM	2R101N	4.62±0.01	3.03±0.00	4.74±0.01	0.01469±0.00005	1.422±0.005	465±0	0.0087±0.0002	0.0087±0.0002	380
NRFA	1R105F	5.18±0.05	4.85±0.01	4.20±0.00	0.01506±0.00005	1.231±0.003	479±5	0.0058±0.0000	0.0062±0.0001	435
SRFA	1S101F	3.25±0.04	4.22±0.01	4.53±0.01	0.01519±0.00000	1.293±0.009	472±2	0.0077±0.0001	0.0078±0.0001	380
YHPOA	AK09-0044 HPOA	2.71±0.06	2.61±0.02	7.06±0.01	0.01863±0.00014	1.529±0.008	459±0	0.0201±0.0002	0.0206±0.0003	380
SRHA	2S101H	7.60±0.10	3.77±0.01	3.45±0.00	0.01303±0.00005	1.095±0.002	490±3	0.0030±0.0000	0.0032±0.0001	430
ESHA	1S102H	3.50±0.03	8.88±0.01	2.39±0.00	0.00750±0.00000	0.653±0.001	553±0	0.0040±0.0000	0.0053±0.0000	460
PPFA	2S103F	2.46±0.04	6.34±0.02	4.27±0.01	0.01344±0.00005	1.065±0.003	491±2	0.0099±0.0001	0.0116±0.0001	460
PPHA	1S103H	3.66±0.16	8.29±0.04	2.87±0.00	0.00978±0.00005	0.741±0.001	541±3	0.0033±0.0000	0.0049±0.0000	475

B.8. Temperature dependence of DOM absorbance and fluorescence.

Association of an electron donor D with an electron acceptor A can form a one to one complex, DA, with an equilibrium written as K_{DA} = [DA]/([D][A]). Typical K_{DA} values for intermolecular DA complexes between iodine and benzene derivatives range from 0.1 to 10, increasing with increasing substitution of electron-rich substituents on benzene. By measuring the temperature-dependence of K_{DA}, enthalpies of formation for these complexes have been reported, and it is expected that potential intramolecular DA complexes within DOM would have similar values. Importantly, absorbance by DA complexes depends on the concentration of DA in solution ($Abs_{DA} = \varepsilon_{CT}[DA]l$), which in turn is a function of temperature due to K_{DA}'s temperature-dependence (Foster, 1969; Orgel and Mulliken, 1957). As an example, the relative

184

change in Abs_{DA} for a complex having a ΔH_{form} = -1.8 kcal mol^{-1} (benzene + p-benzoquinone) (Kuboyama and Nagakura, 1955), is

$$\frac{Abs_{DA,T=10C}}{Abs_{DA,T=35C}} = \frac{(K[D][A])_{T=10C}}{(K[D][A])_{T=35C}} \simeq \frac{K_{T=10C}}{K_{T=35C}} = \frac{\exp(-\Delta H/(R\times 283\ \mathrm{K})}{\exp(-\Delta H/(R\times 308\ \mathrm{K})}$$

$$= \frac{\exp(7500\ \mathrm{J\ mol}^{-1}/(8.314\ \mathrm{J\ mol^{-1}K^{-1}}\times 283\ \mathrm{K})}{\exp(7500\ \mathrm{J\ mol}^{-1}/(8.314\ \mathrm{J\ mol^{-1}K^{-1}}\times 308\ \mathrm{K})} = \frac{24.2}{18.7} = 1.28$$

Equation B.8

corresponding to a 28% increase in absorbance in the CT band upon decreasing the temperature from 35 to 10 °C. Note that this calculation assumes that equilibrium concentrations of [D] and [A] are approximately equal at these two temperatures. Contrary to this hypothesis, no change in absorbance is observed at any excitation wavelength between 10 and 40 °C for any sample studied (Figure B.2).

The lack of change in DOM absorbance over the measured temperature range indicates either:

- – DA complexes are not as responsible for the optical properties of DOM as previously stated

- – DA complexes are of the rigid type as specified in Figure B.1

- – ΔH_{form} values for DA complexes are much smaller than -2.0 kcal mol^{-1} (as ΔH_{form} → 0 kcal mol.$_{-1}$, $Abs_{CT},T=10C/Abs_{CT},T=35C$ → 1)

It is difficult to specify which of (i) – (iii) is most correct, although it seems reasonable to disregard (iii) because of the abundance of measured ΔHform for π-π DA complexes similar to those hypothesized to be present in DOM.

Temperature is also expected to influence the fluorescence emission maximum and intensity. Decreasing temperature increases the viscosity of solvent molecules, decreasing the solvent reorientation rate around the excited state dipole, which in turn increases the proportion of fluorescence from the unrelaxed state and results in a blue shift. This spectral shift can be observed for LE states in addition to fluorescence from CT excited states, however, the change in emission maximum is much more prominent in the latter (Lakowicz, 1999). Although we observe a decrease in fluorescence intensity with increasing temperature, similar to a previous study (Baker, 2005), the spectral shape remained unchanged, which indicates that the proportion of fluorescing species is unchanged over this temperature range. The lack of change in emission maximum indicates that the solvent relaxation rate is still faster at 10 °C than the fluorescence emission rate. The same result was observed for fluorescence spectra collected for MRNOM and ESHA at -10 and 70 °C in ≈70% v/v glycerol in water.

In addition, the CT model for DOM postulates that charge-recombination-induced luminescence by $[D^+A^-]^*$ is responsible for fluorescence at longer emission wavelengths (i.e. at or greater than ~470 nm) due to a near continuous, coupled manifold of these states. Thus, for excitation wavelengths < 375 nm, emission is potentially due to both LE fluorescence and charge-recombination, while at wavelengths > 375 nm, emission is due solely to charge-recombination. The lack of change in emission spectra at wavelengths > 375 nm is inconsistent with this idea because these emitting states would be coupled by temperature-dependent processes, necessitating extremely fortuitous circumstances for each process to have the exact same (or similar) activation energy.
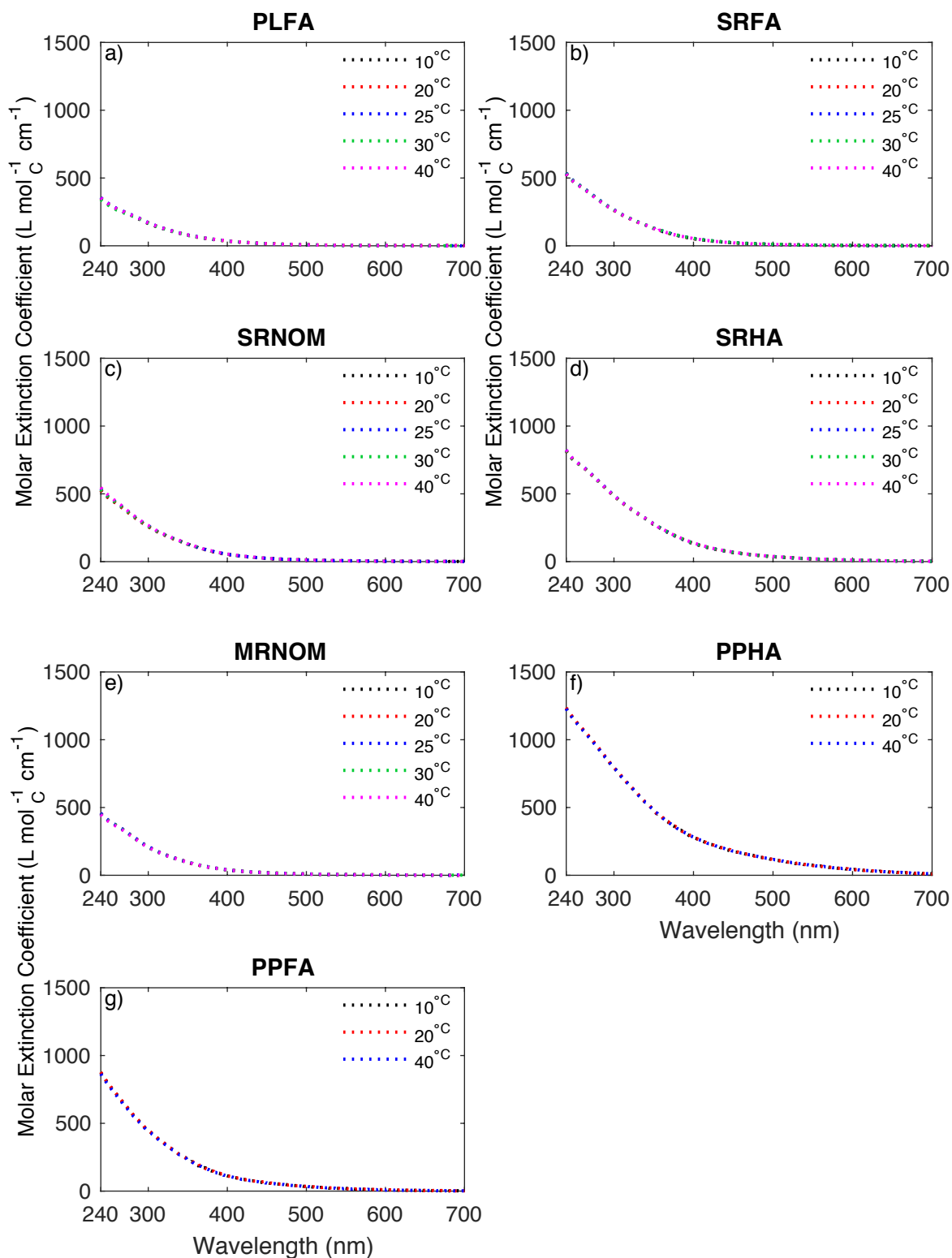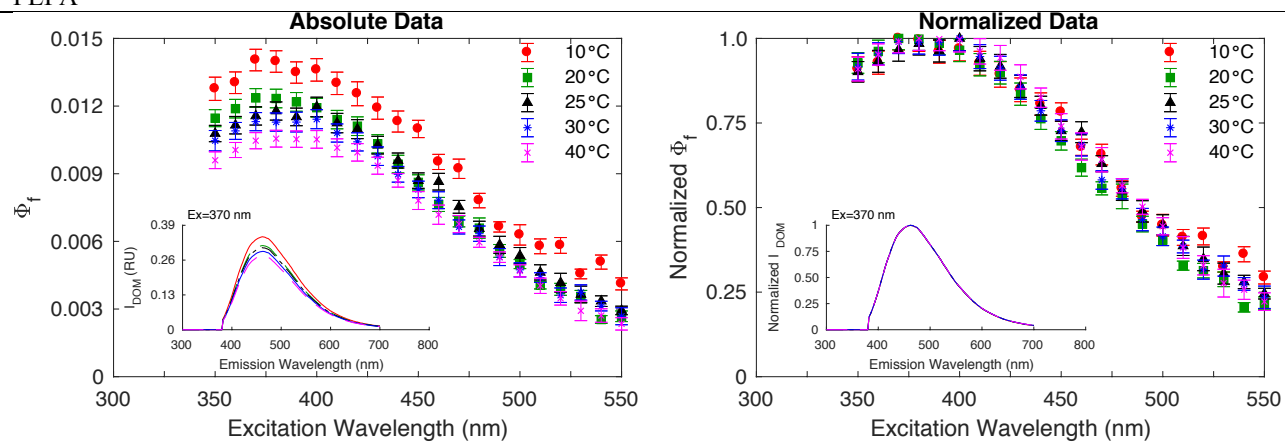
Figure B.2. Absorbance spectra for isolates at temperatures ranging from 10 to 40 °C.
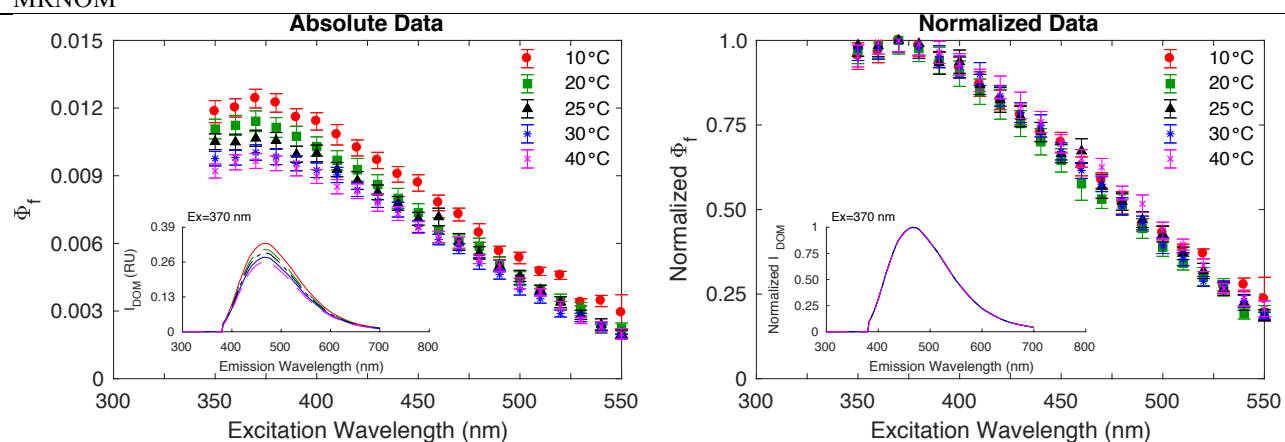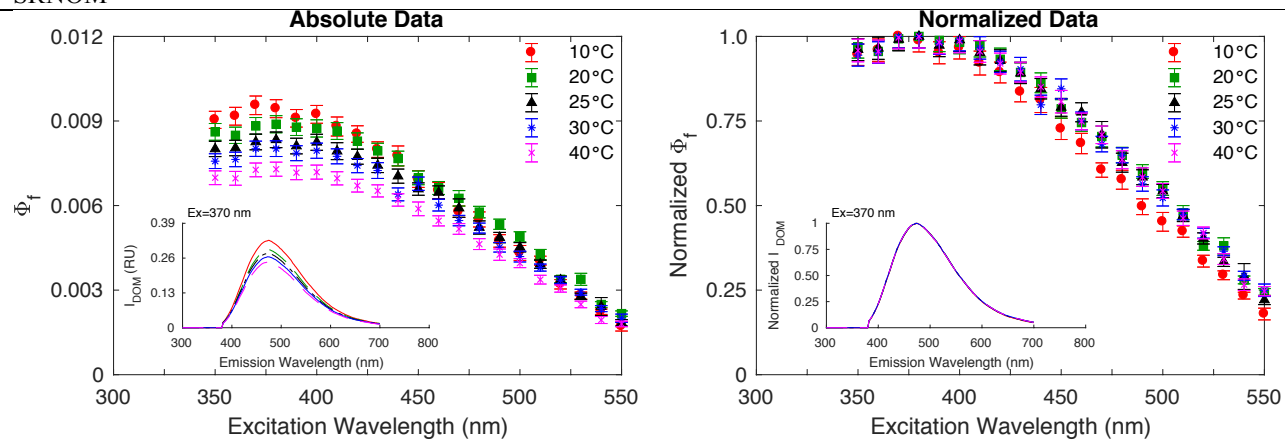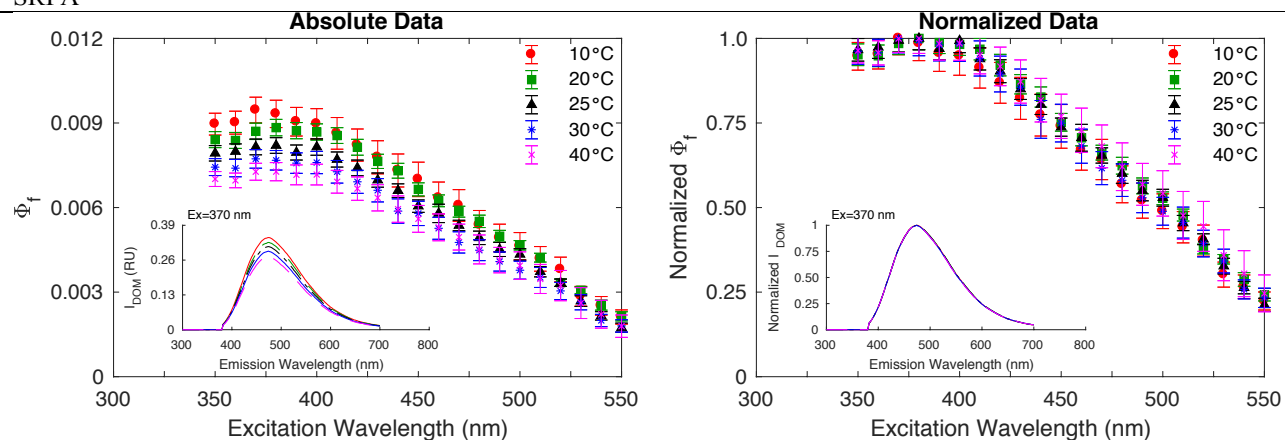
PLFA

MRNOM

Figure B.3. Effect of temperature on fluorescence quantum yields for PLFA and MRNOM presented as both a) measured quantum yields and b) quantum yields normalized to the maximum value at each temperature. Inset: emission spectra at an excitation wavelength of 370 nm.

Figure B.4. Effect of temperature on fluorescence quantum yields for SRNOM, SRFA and SRHA presented as both a) measured quantum yields and b) quantum yields normalized to the maximum at each temperature. Inset: emission spectra at an excitation wavelength of 370 nm.

189

Figure B.5. Effect of temperature on fluorescence quantum yields for PPFA and PPHA presented as both a) measured quantum yields and b) quantum yields normalized to the maximum at each temperature. Inset: emission spectra at an excitation wavelength of 370 nm.
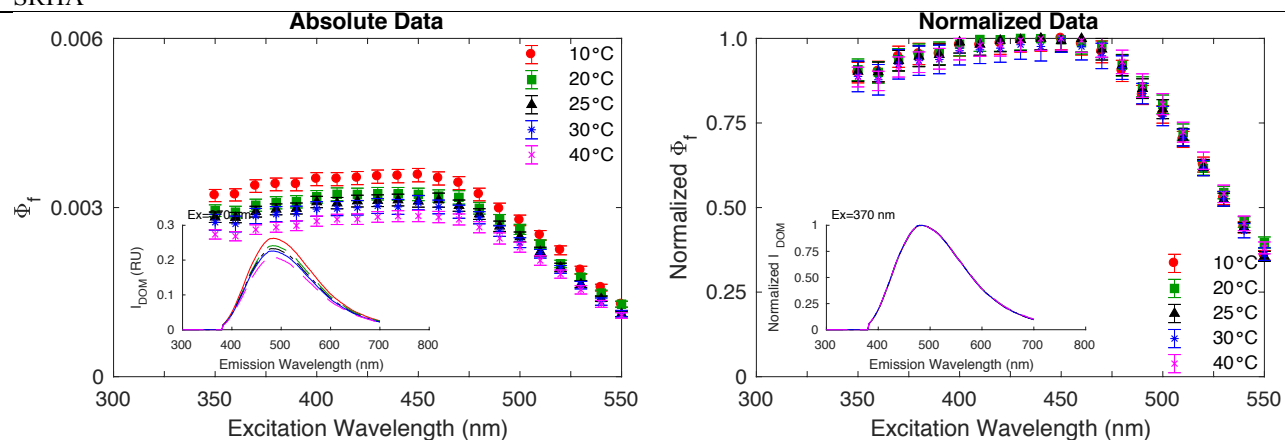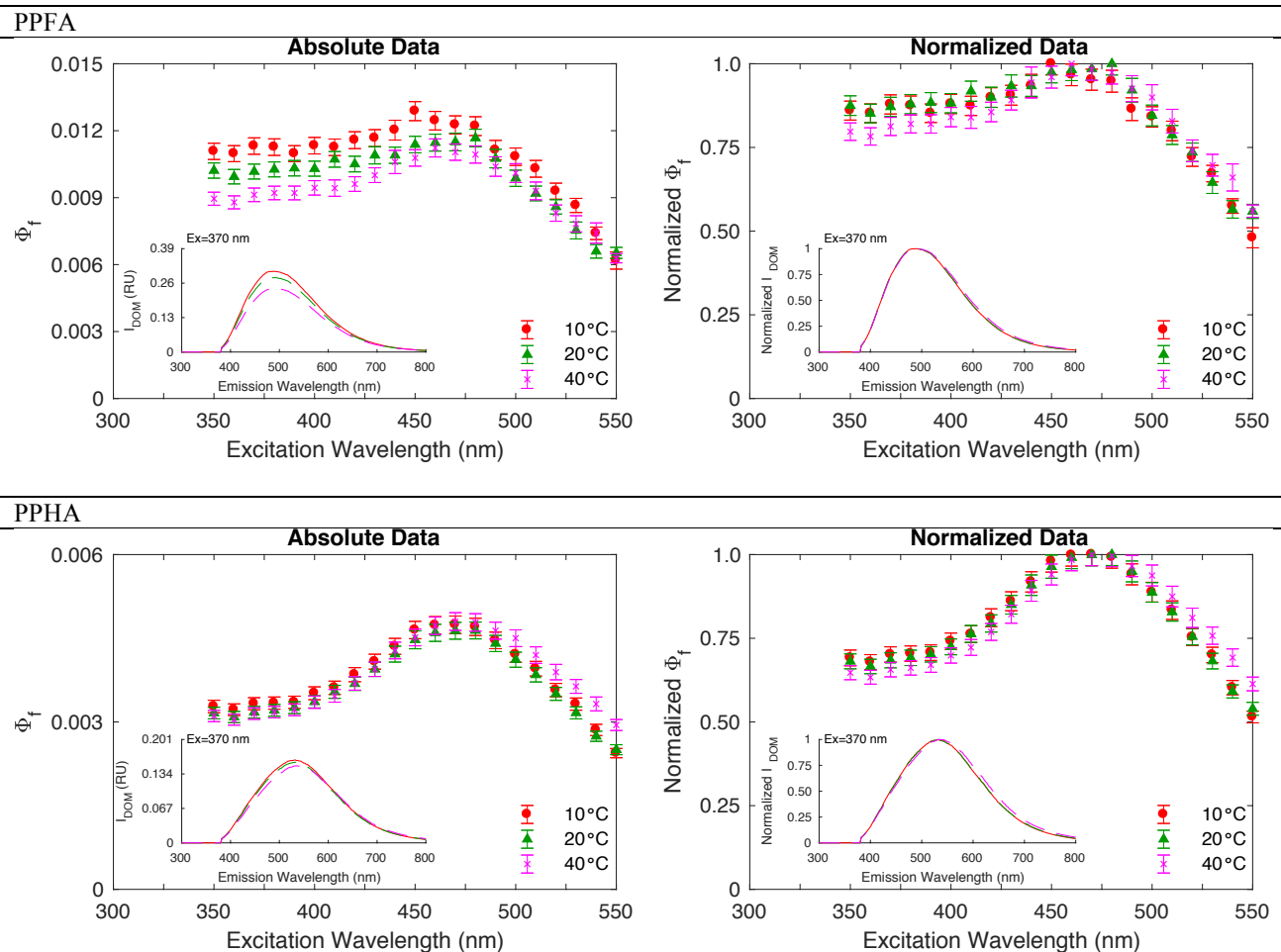
B.9. Differentiation of temperature and viscosity effects on fluorescence spectra and quantum yields

A change in temperature affects both the rate of fluorescence decay and the viscosity of the solvent, and thereby the rate of solvent relaxation. To separate the effects of changing temperature and viscosity, we measured absorbance and fluorescence spectra of a subset of

samples at varying volume percentages of glycerol at different temperatures chosen to keep

either viscosity or temperature constant (Table B.5 and Table B.6).

Table B.5. Experimental matrix for glycerol and water at different temperatures

Solvent	Temp (°C)	Dielectric Constant	Viscosity (cP)
Water	10	83.8	1.31
Water	20	80.1	1.01
Water	25	78.3	0.903
Water	30	76.5	0.801
Water	40	73.2	0.656
10% Glycerol	40	70.4	0.826
20% Glycerol	40	67.7	1.07
30% Glycerol	40	64.9	1.46
10% Glycerol	20	77.6	1.31
20% Glycerol	30	71.2	1.35

Table B.6. Quantum yields for glycerol-water experiments for ESHA, MRNOM, PLFA, and SRFA.

| Isolate	Glycerol (v/v %)	Temperature (°C)	Φ_f at Ex=370nm	
			Average	Error
ESHA	10	20	6.108E-03	8.946E-05
ESHA	10	40	5.984E-03	8.219E-05
ESHA	20	30	6.519E-03	9.666E-05
ESHA	20	40	6.397E-03	9.161E-05
ESHA	30	40	6.646E-03	8.842E-05
MRNOM	10	20	1.503E-02	2.015E-04
MRNOM	10	40	1.271E-02	1.728E-04
MRNOM	20	30	1.405E-02	2.092E-04
MRNOM	20	40	1.297E-02	1.863E-04
MRNOM	30	40	1.337E-02	1.881E-04
PLFA	10	20	1.691E-02	2.643E-04
PLFA	10	40	1.445E-02	2.224E-04
PLFA	20	30	1.626E-02	2.523E-04
PLFA	20	40	1.508E-02	2.351E-04
PLFA	30	40	1.522E-02	2.397E-04
SRFA	10	20	7.163E-03	1.856E-04
SRFA	10	40	6.138E-03	8.949E-05
SRFA	20	30	3.791E-03	5.888E-05
SRFA	20	40	3.520E-03	4.846E-05
SRFA	30	40	6.737E-03	1.124E-04
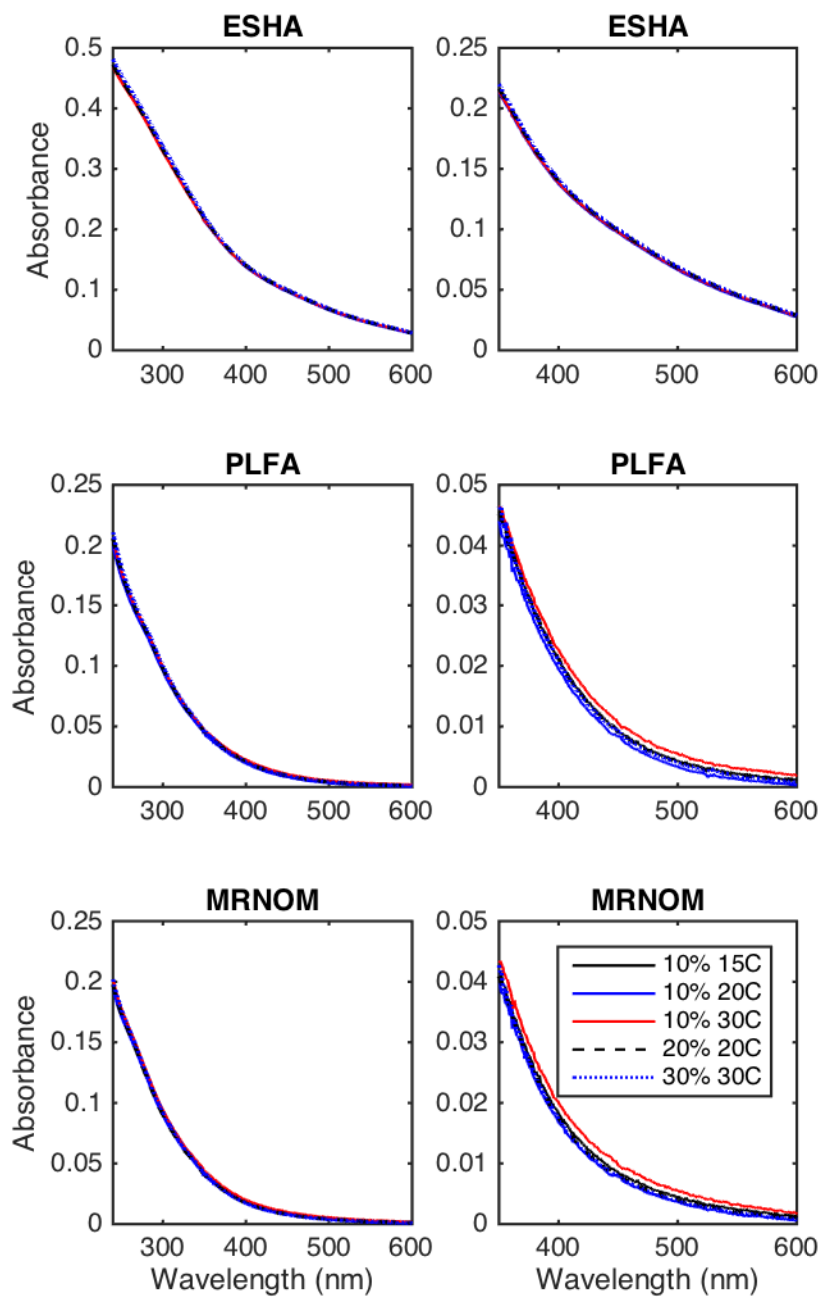
Figure B.6. Absorbance spectra for various temperature-glycerol combinations demonstrating no significant change in spectral shape. Note that the combinations shown here do not exactly match those in Table B.5.
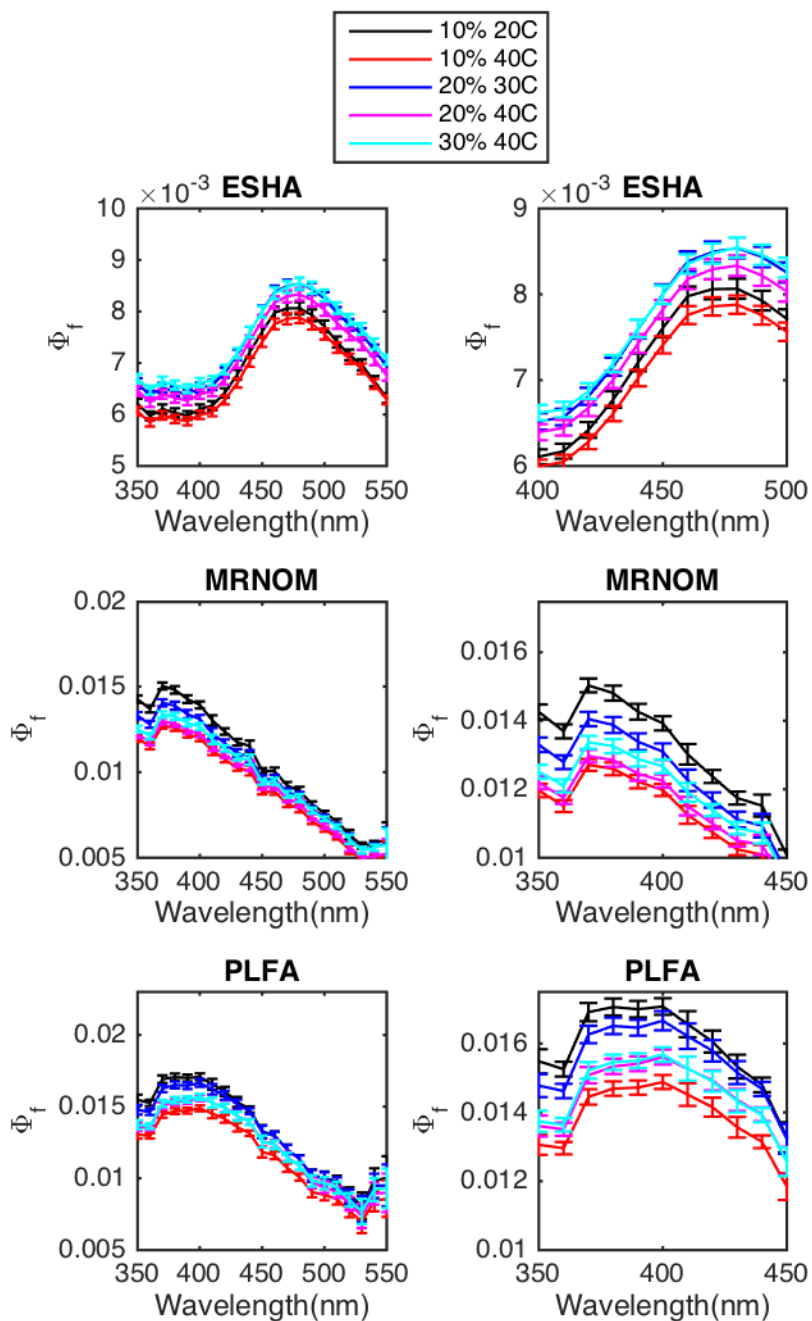
Figure B.7. Fluorescence quantum yield versus excitation wavelength for various temperature-glycerol combinations. Right column duplicates data in left column but focused on excitation wavelengths around the peak Φ_f.

B.10. Effect of solvent on DOM absorbance and fluorescence

Physicochemical properties of the solvents in which DOM absorbance and fluorescence spectra were measured are shown in Table B.7. It was hypothesized that solvatochromism would be observed in these spectra, which is typical for DA complexes of known organic compounds (e.g. dye compounds) due to CT character in either the ground or excited state. Absorbance spectra in ACN and THF are shown in Figure B.8 and Figure B.9. Fluorescence spectra for samples in ACN and THF are shown in Figure B.10 through Figure B.13.

Table B.7. Solvent properties at room temperature.

Solvent	Dielectric Constant (ε_r)	Refractive index (n)	Viscosity (cP)
Water (H_2O)	80.1	1.3330	1.00
Acetonitrile (ACN)	37.5	1.3441	0.38
Tetrahydrofuran (THF)	7.58	1.4072	0.55

Figure B.8 and Figure B.9 show all molar extinction coefficients for samples measured in H_2O, ACN, and THF. These spectra are largely the same in all three solvents, indicating no solvatochromism, and the small differences that are seen are not consistent between samples and primarily at excitation wavelengths < 350 nm. Note that we were unable to obtain reliable absorbance spectra for ESHA and PPHA in THF due to evidence of light scattering and particle formation. Although the samples diluted from aqueous stock initially dissolved in THF and spectra were recorded, spectra were markedly different after 24 and 72 hr, which were accompanied by the presence of observable particulates in solution. The exact mechanism behind this observation is undetermined, but we did not observe this for other sample spectra. We also note that an early study measuring fulvic acid molecular weights by vapor pressumer osmometry utilized THF as a solvent and no precipitate was observed (Aiken and Malcolm, 1987). Hence,

195

we do not suspect that the phenomena observed for ESHA and PPHA can be generalized to the other isolates.

The CT model predicts a blue shift in DOM emission spectra with decreasing solvent polarity due to destabilization of CT excited states relative to LE states, the latter of which then become the primary emitting fluorophores. Solvatochromism in fluorescence spectra is expected for LE states, but to a much lesser degree (Lakowicz, 1999). We assessed for solvatochromism in fluorescence spectra by calculating the change in maximum emission wavelength at a given excitation wavelength in ACN and THF relative to H_2O (Figure B.21 through Figure B.26). Most samples exhibited no statistically significant change in emission wavelength ($\pm$ 15 nm based on number of replicates and bandpass). Note that the $\pm$ 15 nm over which statistical significance was assessed falls within the region of solvatochromic shifts that could be expected for LE states, but is less than what would be expected for fluorescence from CT excited states. Conversely, all soil-derived isolates (ESHA, PPHA, PPFA) exhibited blue-shifted emission in organic solvents. This blue shift was significant at most excitation wavelengths for ESHA, while for PPHA and PPFA it occurred over a more selected wavelength range. In general, the largest changes in emission wavelength were observed at excitation wavelengths < 375 nm, which under the CT model, correspond to excitations into LE states.

Overall, the lack of solvatochromism in DOM fluorescence spectra is supporting evidence for a minor contribution of DA complexes to DOM photophysics.
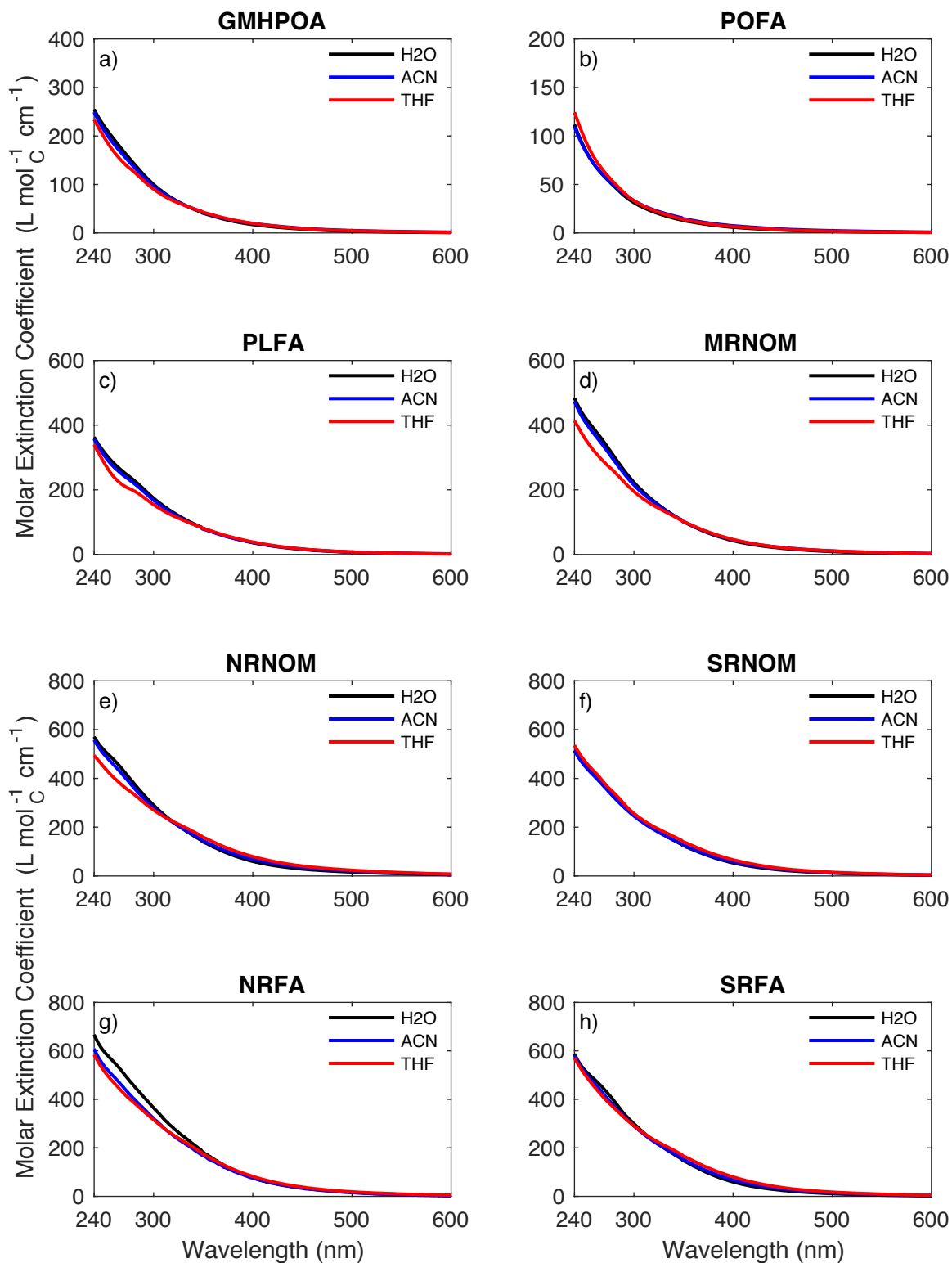
Figure B.8. Effect of solvent on absorbance for eight isolates in H_2O, ACN, and THF.
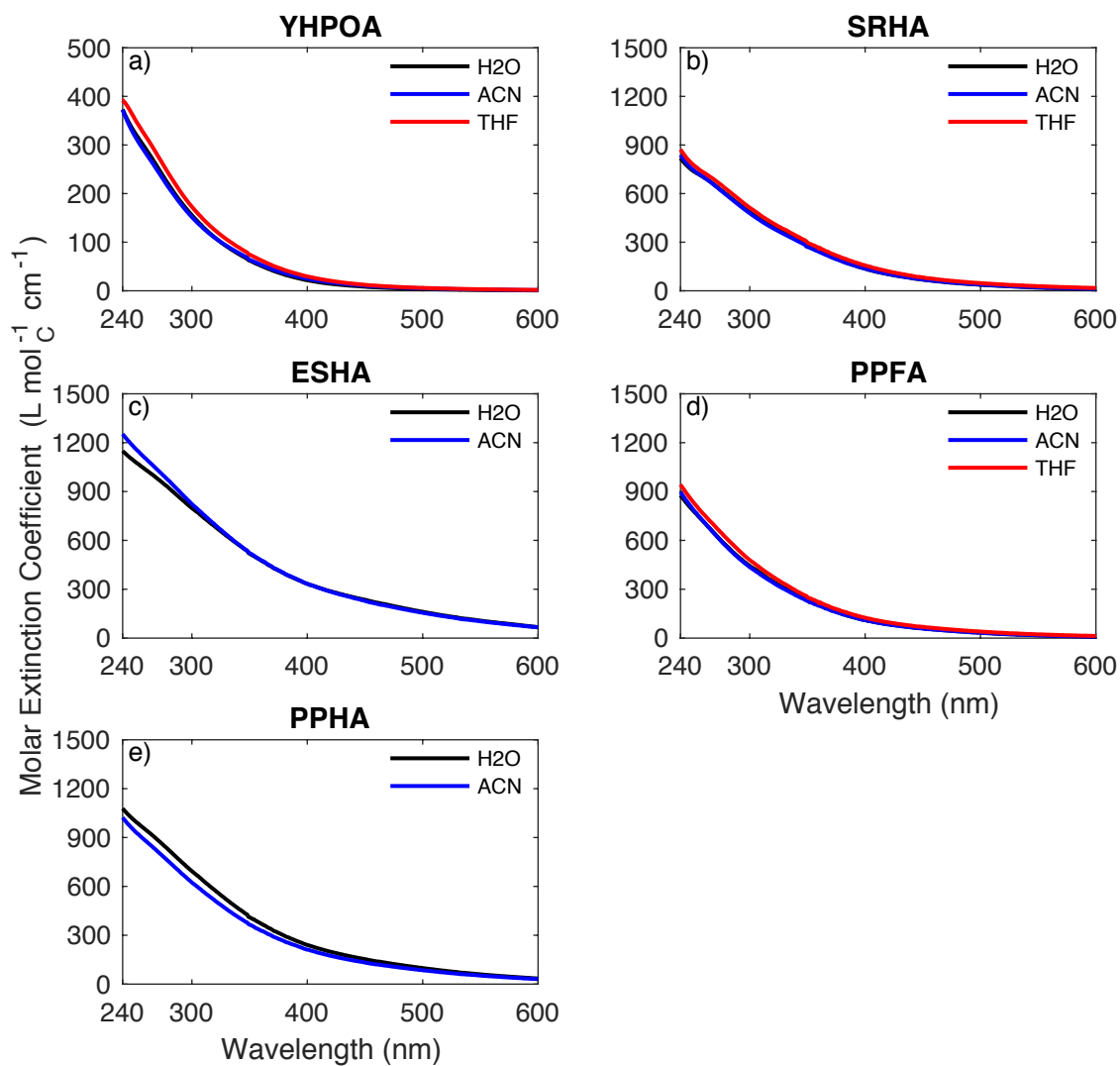
Figure B.9. Effect of solvent on absorbance for five isolates in H$_2$O, ACN, and THF (if applicable).
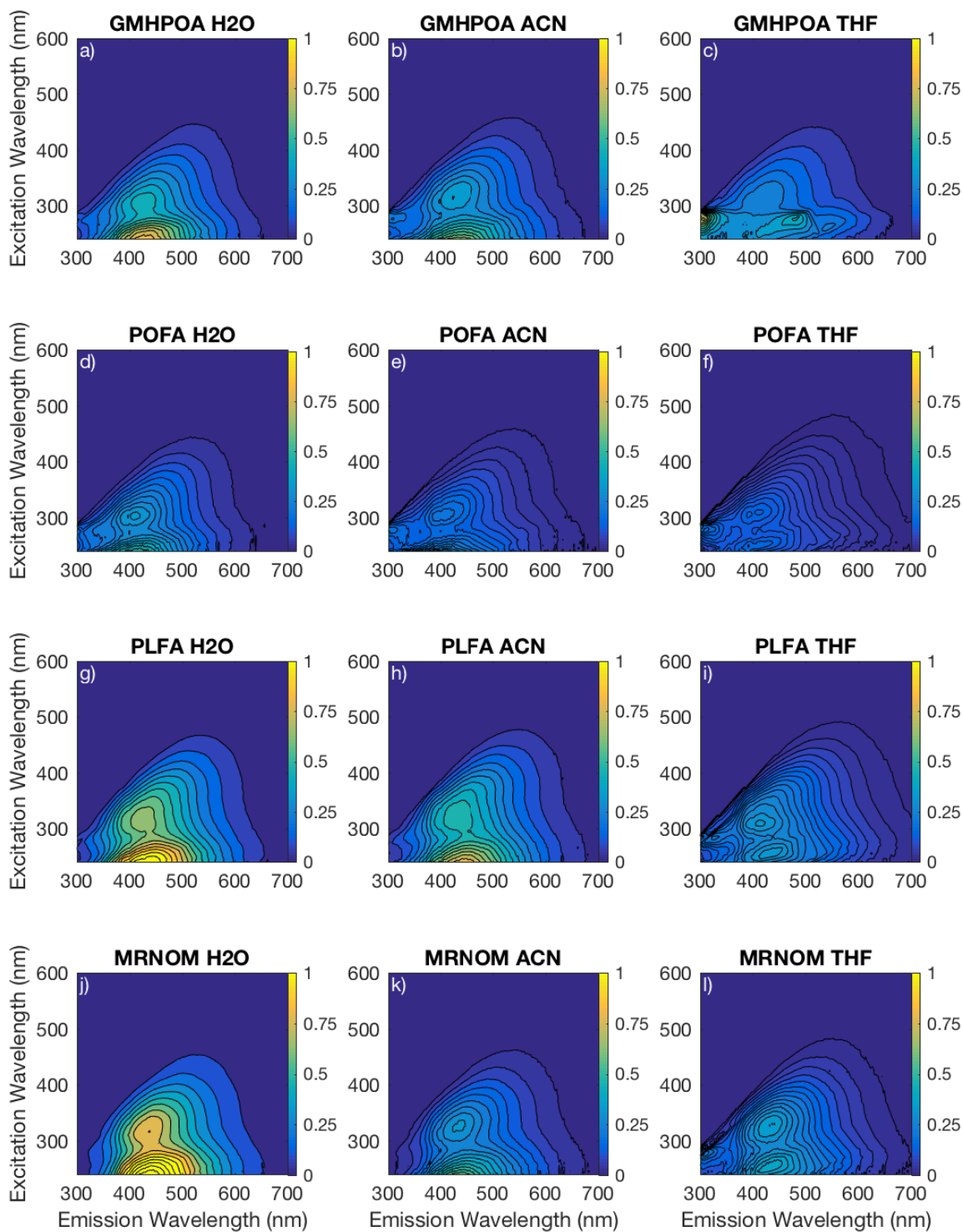
Figure B.10. Fluorescence EEM spectra for GMHPOA, POFA, PLFA, and MRNOM in H_2O (a, d, g, j), ACN (b, e, h, k), and THF (c, f, i, l).
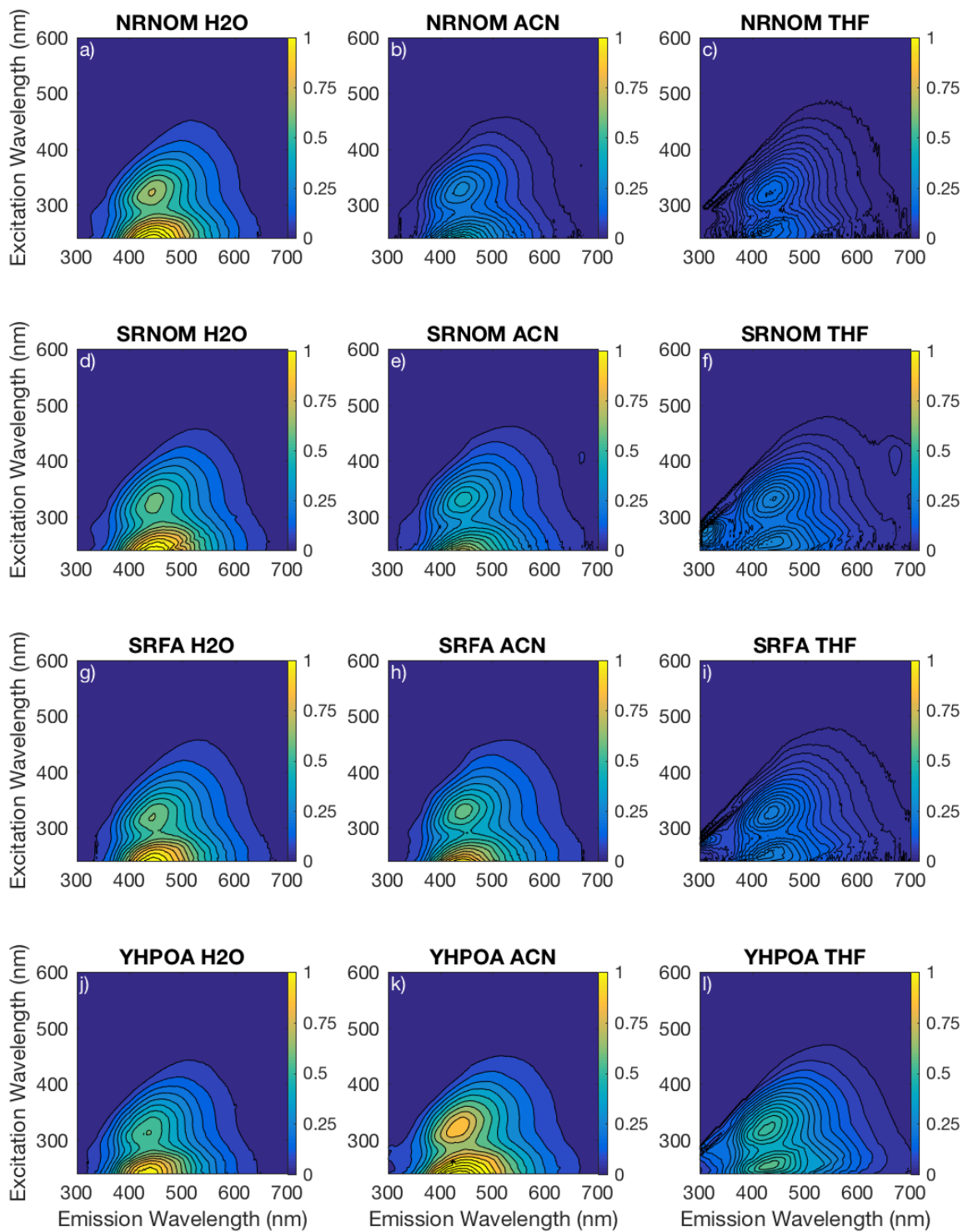
Figure B.11. Fluorescence EEM spectra for NRNOM, SRNOM, SRFA, and YHPOA in H_2O (a, d, g, j), ACN (b, e, h, k), and THF (c, f, i, l).
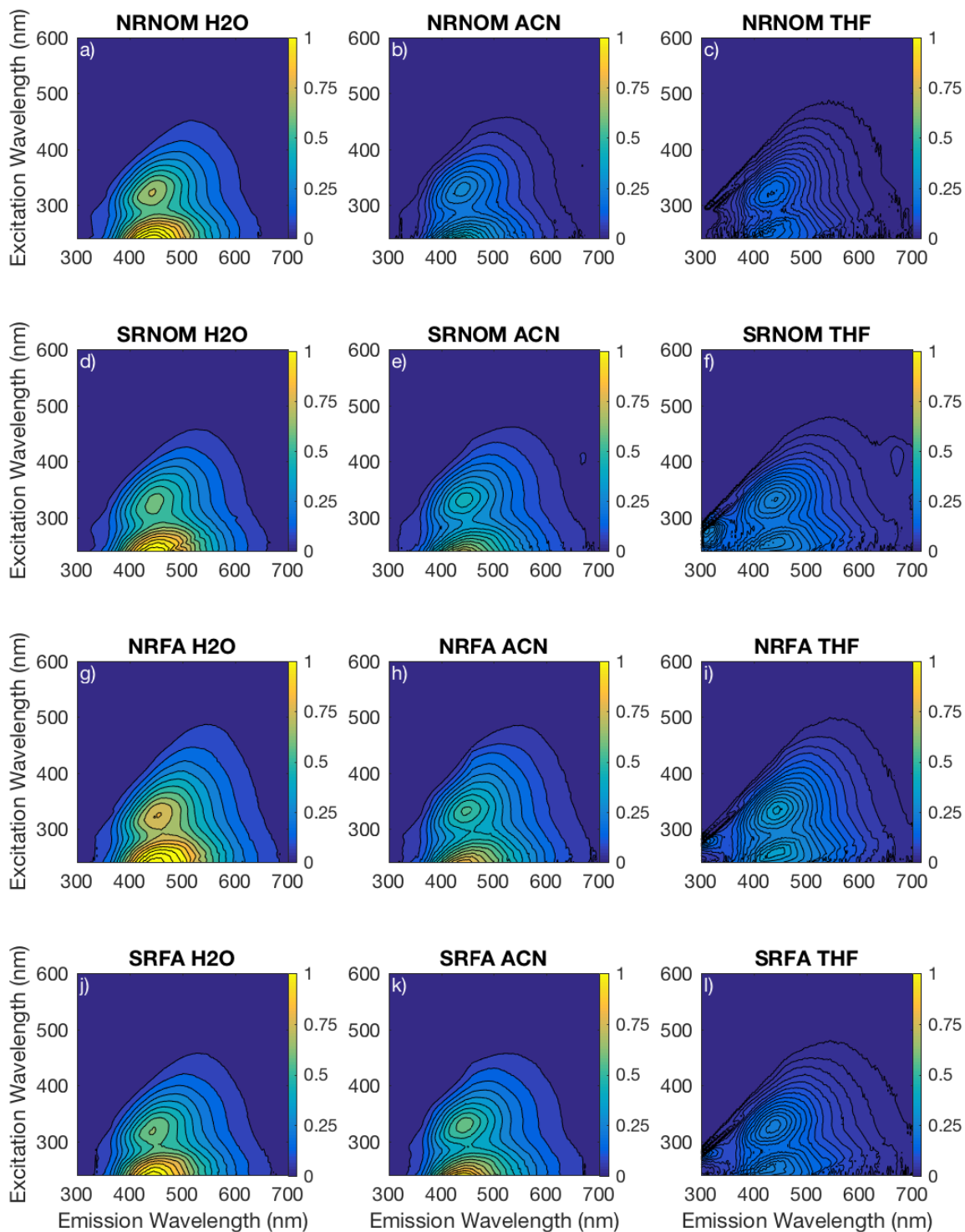
Figure B.12. Fluorescence EEM spectra for NRNOM, SRNOM, NRFA, and SRFA in H$_2$O (a, d, g, j), ACN (b, e, h, k), and THF (c, f, i, l).
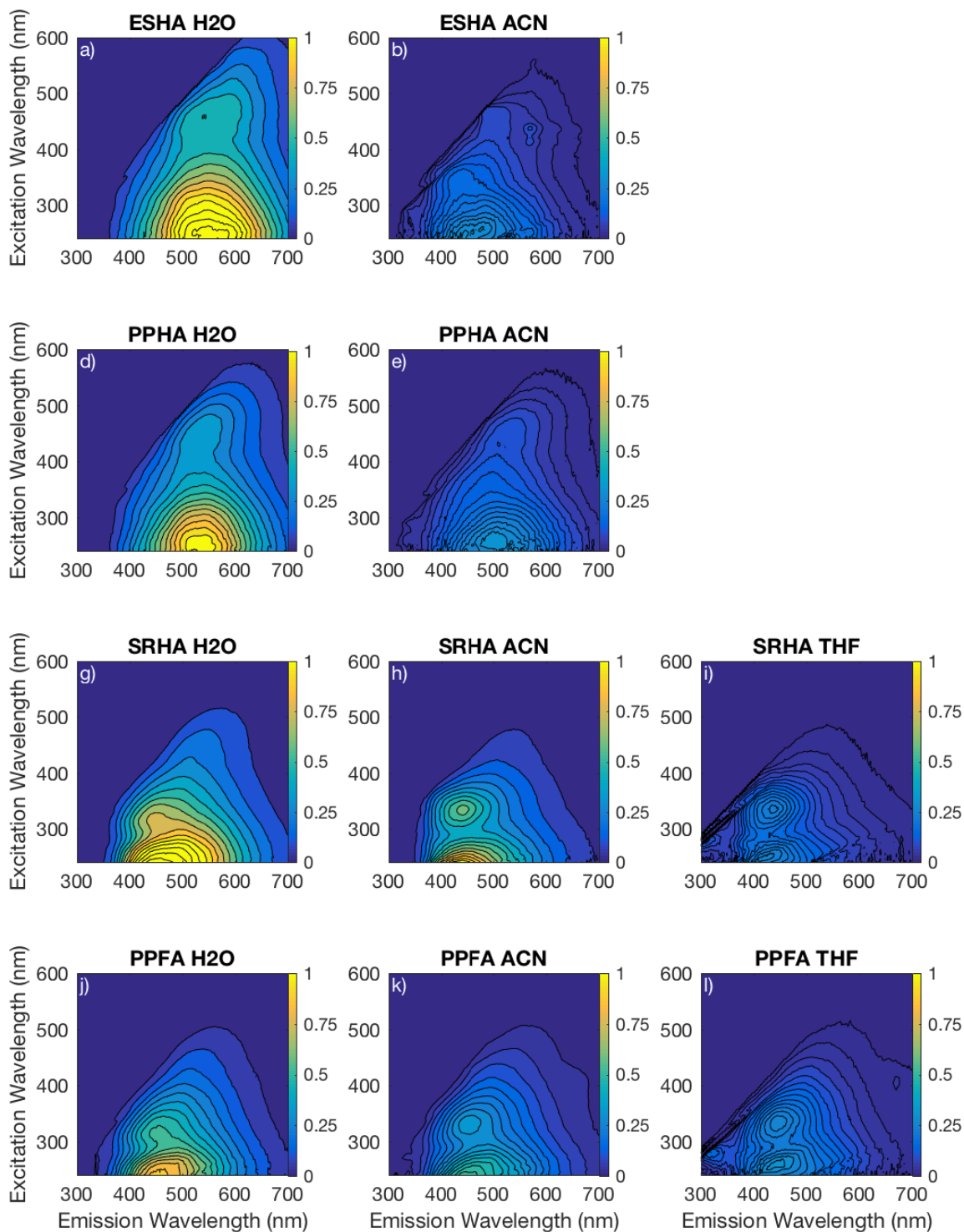
Figure B.13. Fluorescence EEM spectra for ESHA, PPHA, SRHA, and PPFA in H$_2$O (a, d, g, j), ACN (b, e, h, k), and THF (i, l). Note that spectra for ESHA and PPHA were not collected in THF.
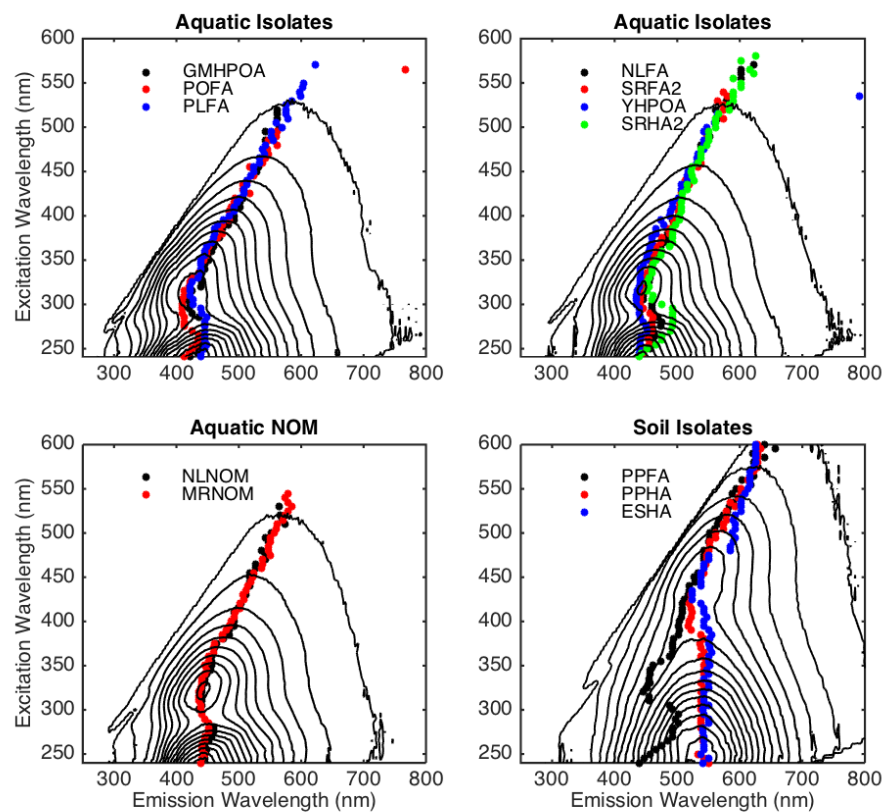
Figure B.14. Representative fluorescence EEMs for four isolates overlaid with markers to indicate the maximum emission wavelength as a function of excitation wavelength. Markers for other isolates exhibiting similar behaviors are plotted together.

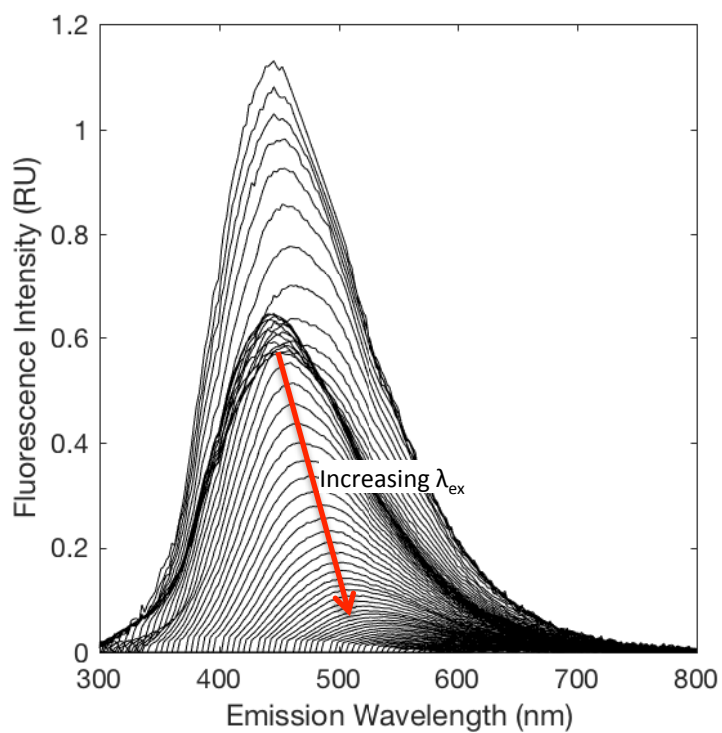Figure B.15. Two-dimensional plot of SRFA excitation-emission matrix illustrating the progressively narrower and lower intensity emission peaks at increasing excitation wavelength.

Figure B.16. Effect of solvent on fluorescence quantum yields for POFA, GMHPOA and PLFA presented as both measured quantum yields (left pane) and quantum yields normalized to the maximum in each solvent (right pane).

Figure B.17. Effect of solvent on fluorescence quantum yields for SRNOM, NRNOM and MRNOM presented as both measured quantum yields (left pane) and quantum yields normalized to the maximum in each solvent (right pane).
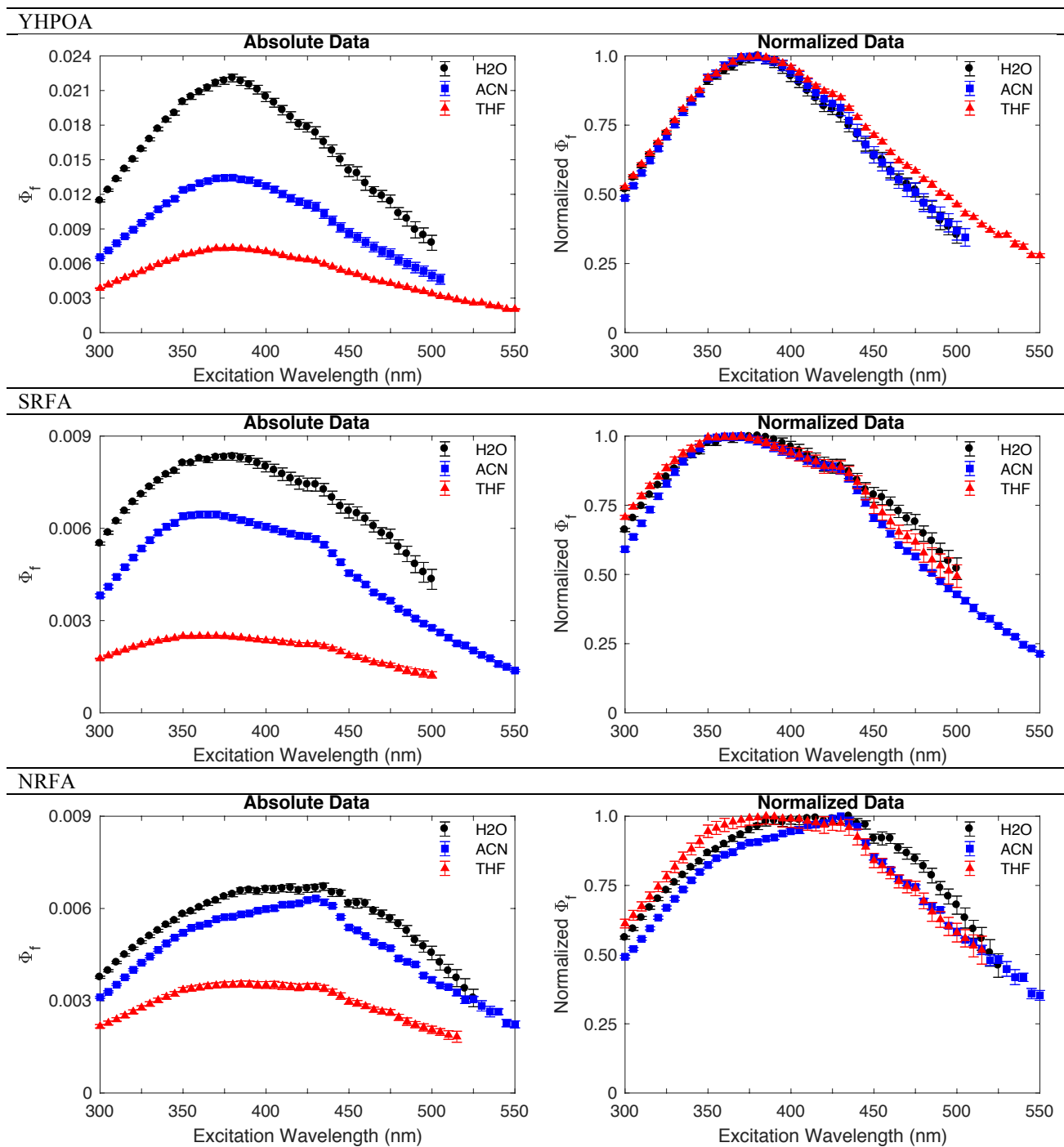
Figure B.18. Effect of solvent on fluorescence quantum yields for YHPOA, SRFA and NRFA presented as both measured quantum yields (left pane) and quantum yields normalized to the maximum in each solvent (right pane).
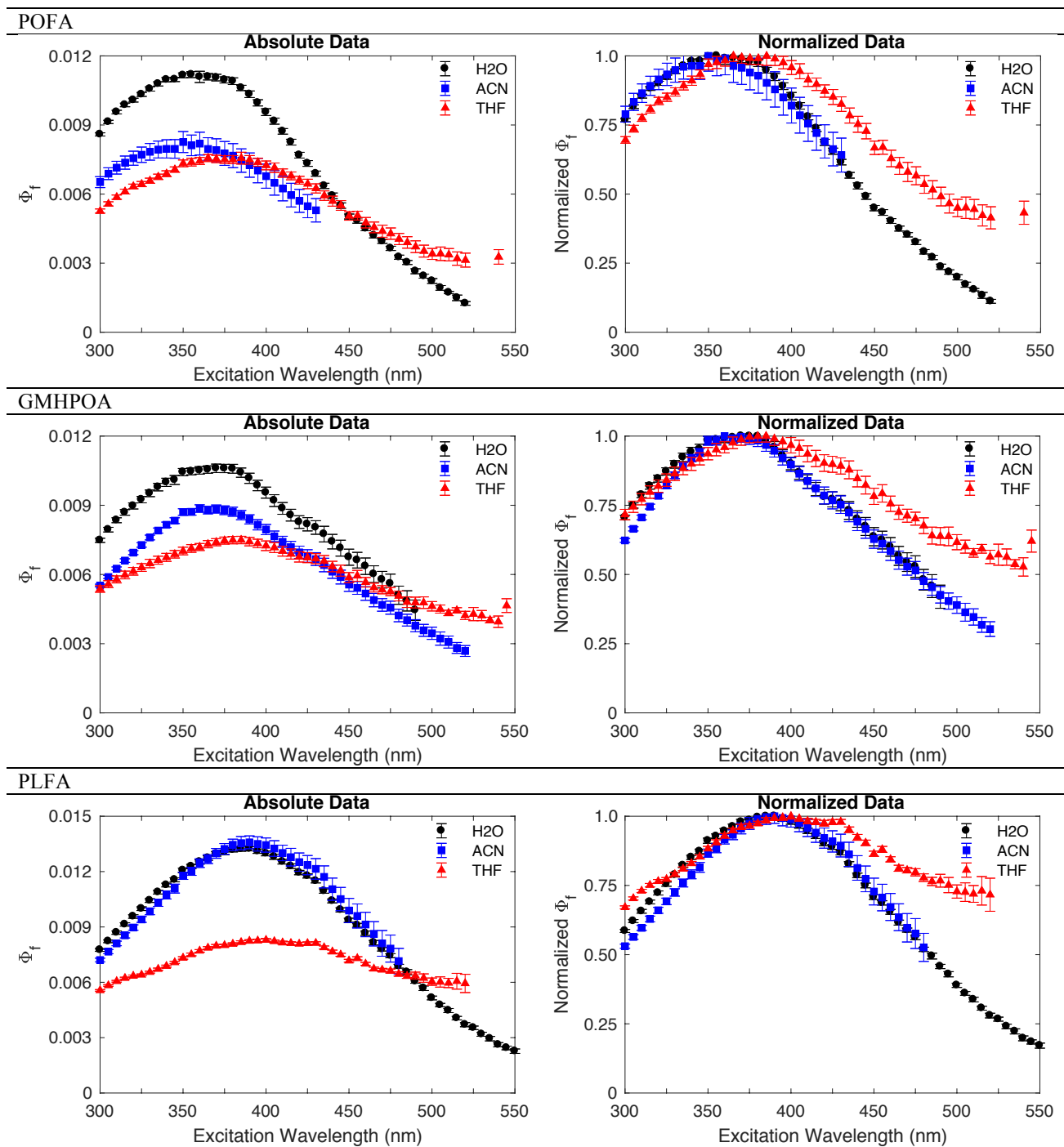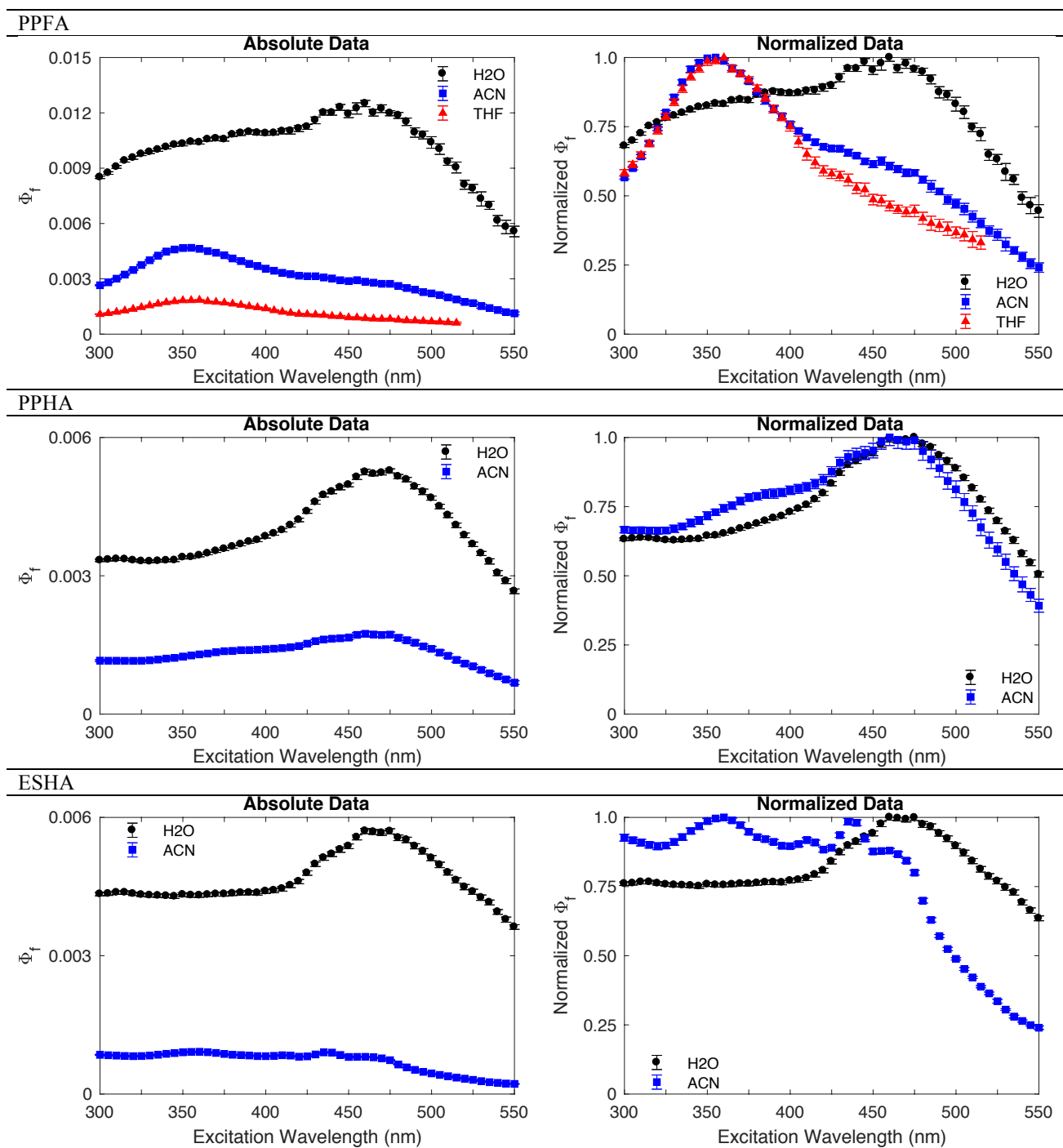
PPFA

PPHA

ESHA

Figure B.19. Effect of solvent on fluorescence quantum yields for PPFA, PPHA and ESHA presented as both measured quantum yields (left pane) and quantum yields normalized to the maximum in each solvent (right pane).
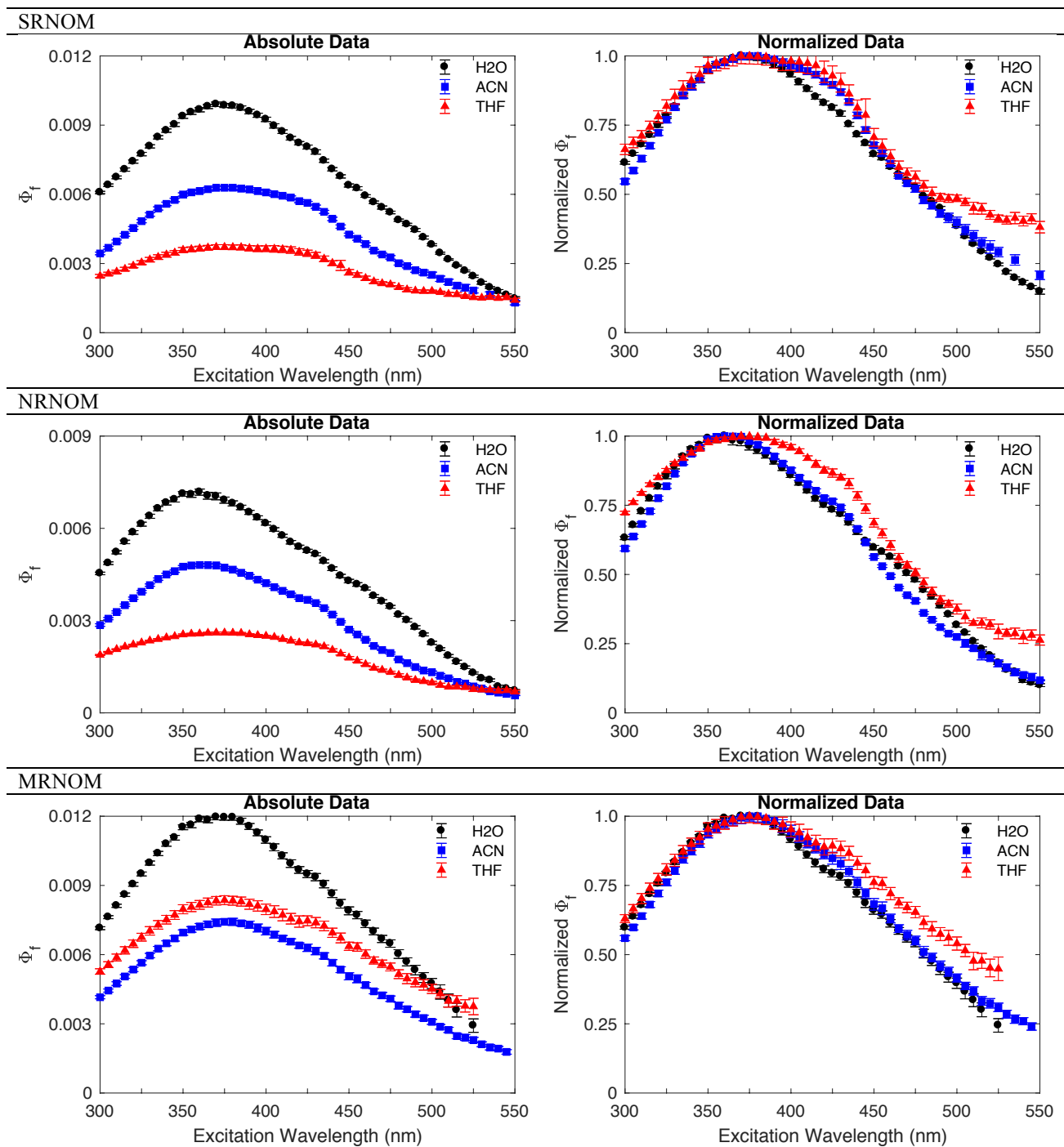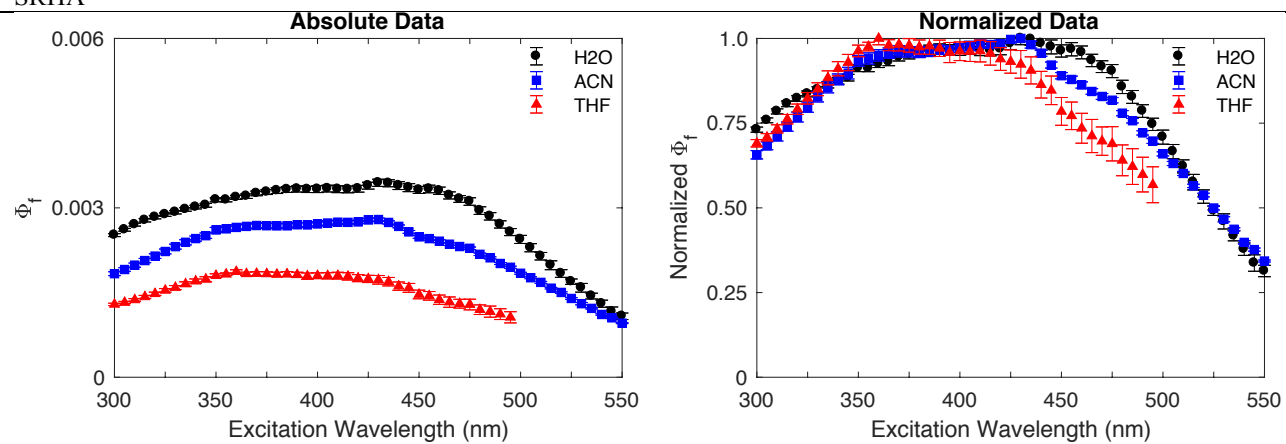
Figure B.20. Effect of solvent on fluorescence quantum yields for SRHA presented as both measured quantum yields (left pane) and quantum yields normalized to the maximum in each solvent (right pane).
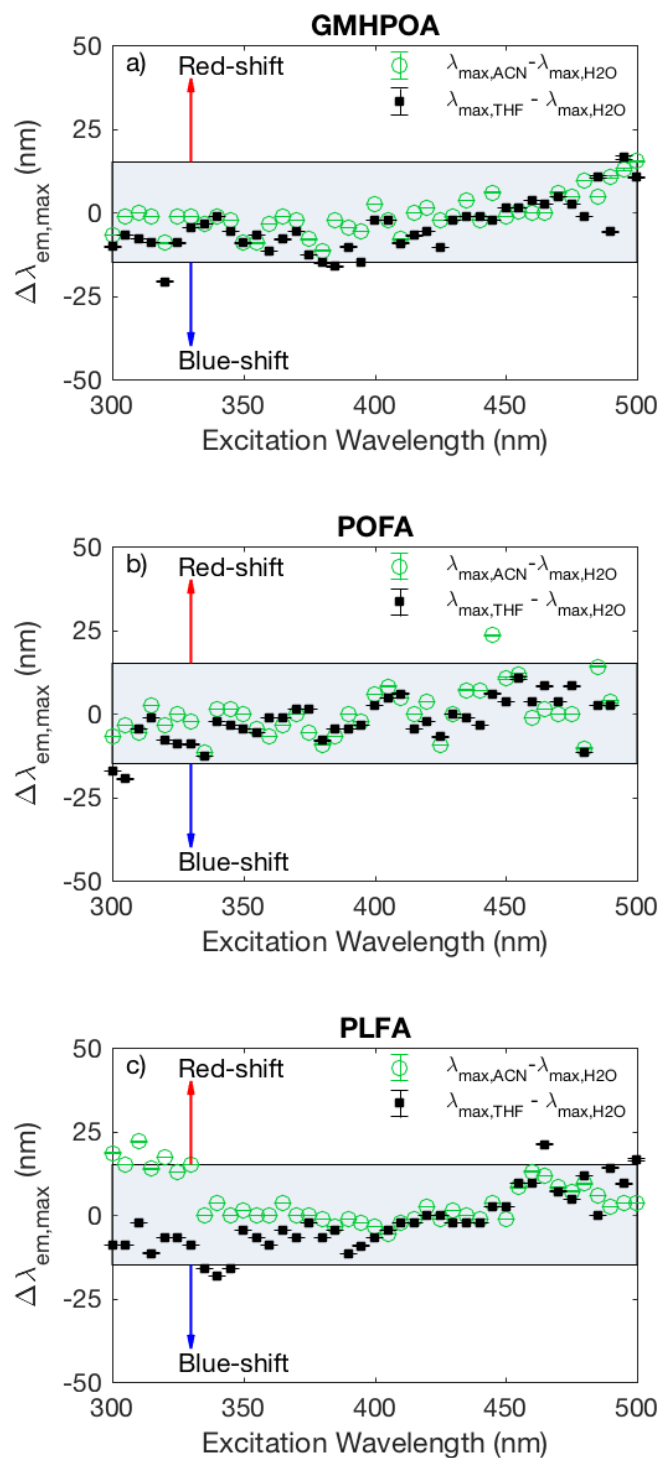
Figure B.21. Solvatochromic shift in peak emission wavelength in ACN and THF relative to water as a function of excitation wavelength for a) GMHPOA, b) POFA, and c) PLFA.
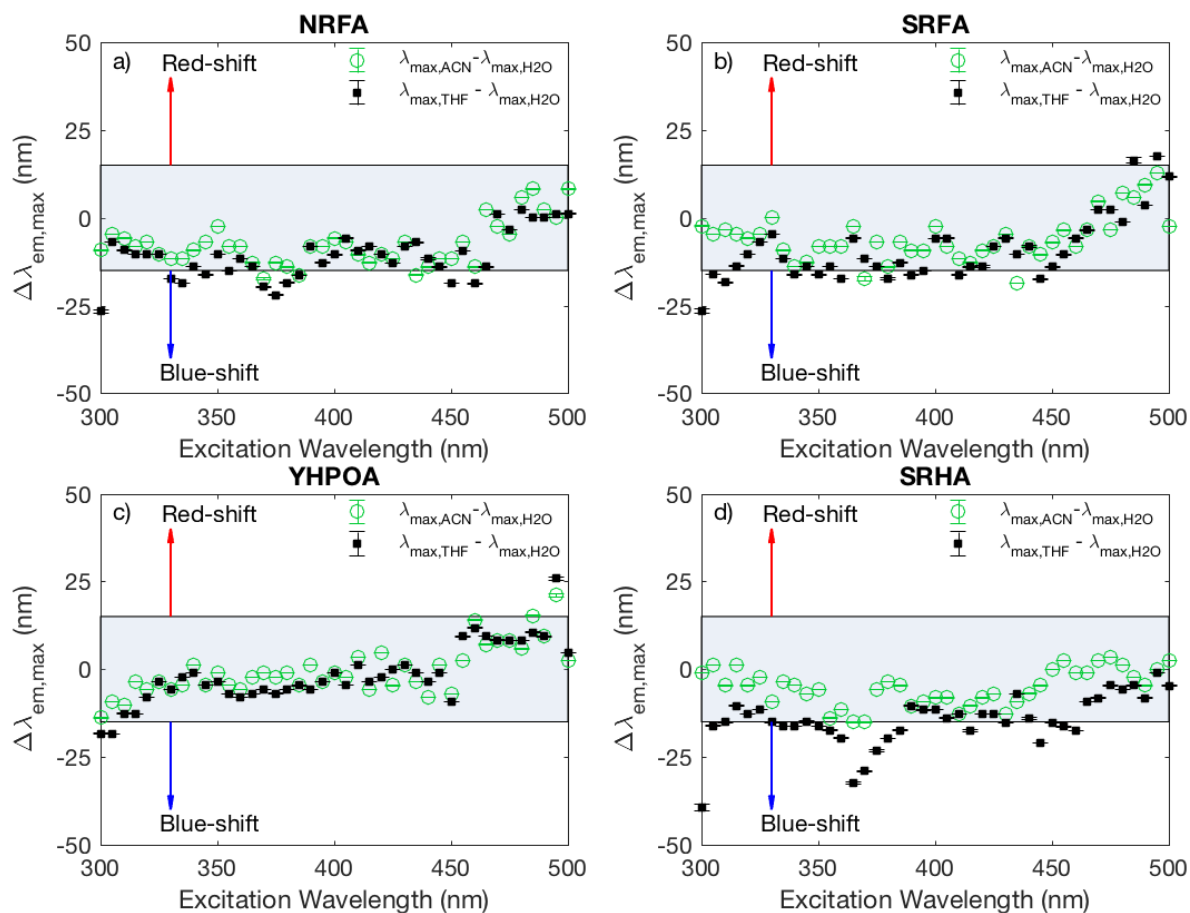
Figure B.22. Solvatochromic shift in peak emission wavelength in ACN and THF relative to water as a function of excitation wavelength for a) NRFA, b) SRFA, c) YHPOA and d) SRHA.
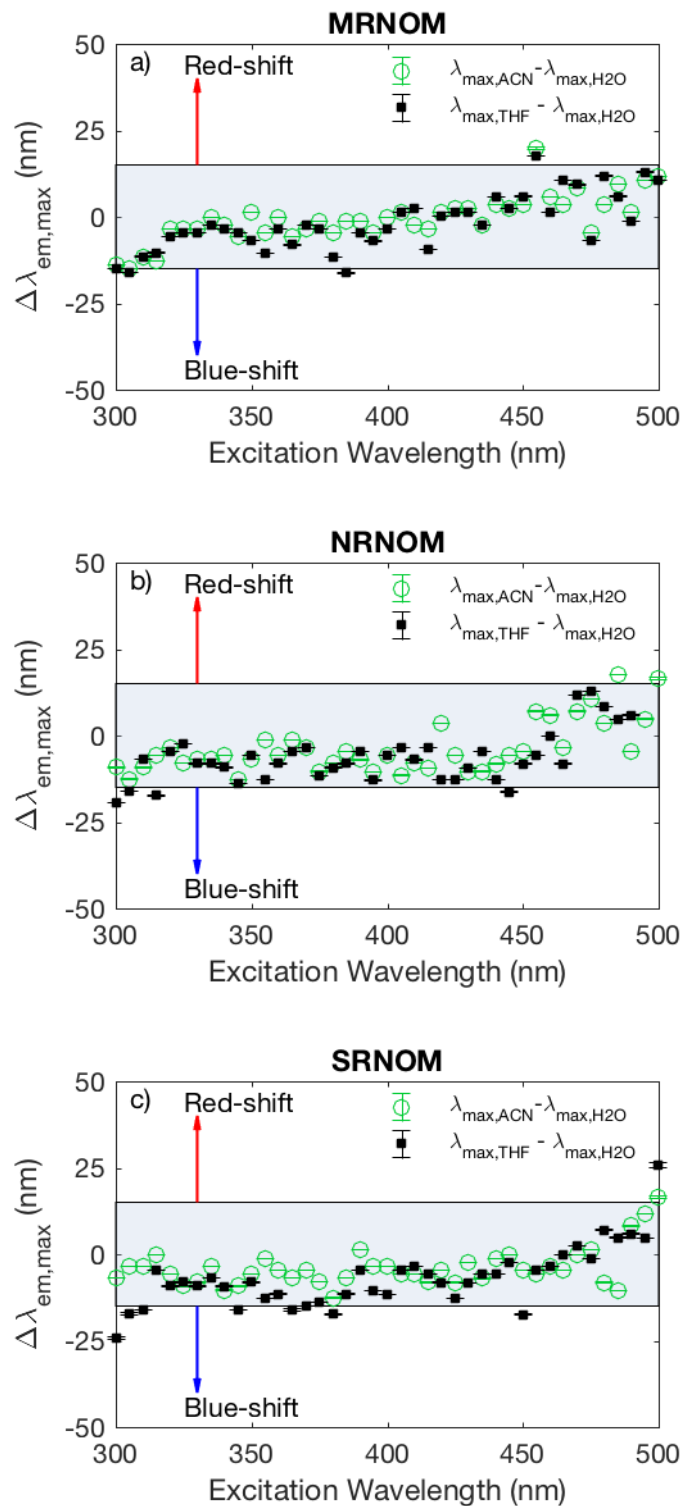
Figure B.23. Solvatochromic shift in peak emission wavelength in ACN and THF relative to water as a function of excitation wavelength for a) MRNOM, b) NRNOM, and c) SRNOM.
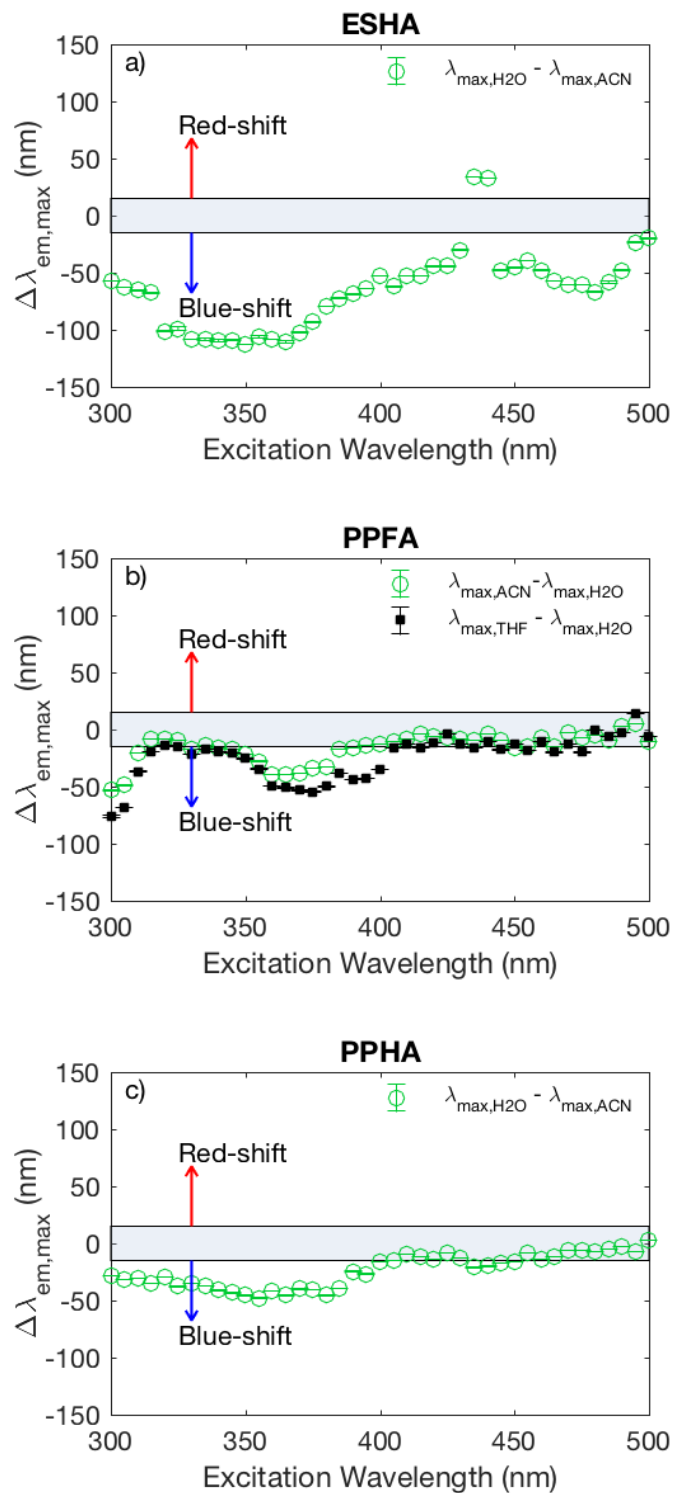
Figure B.24. Solvatochromic shift in peak emission wavelength in ACN and THF (PPFA only) relative to water as a function of excitation wavelength for a) ESHA, b) PPFA, and c) PPHA. ESHA and PPHA were not evaluated in THF due to instability and precipitation of isolate.

213

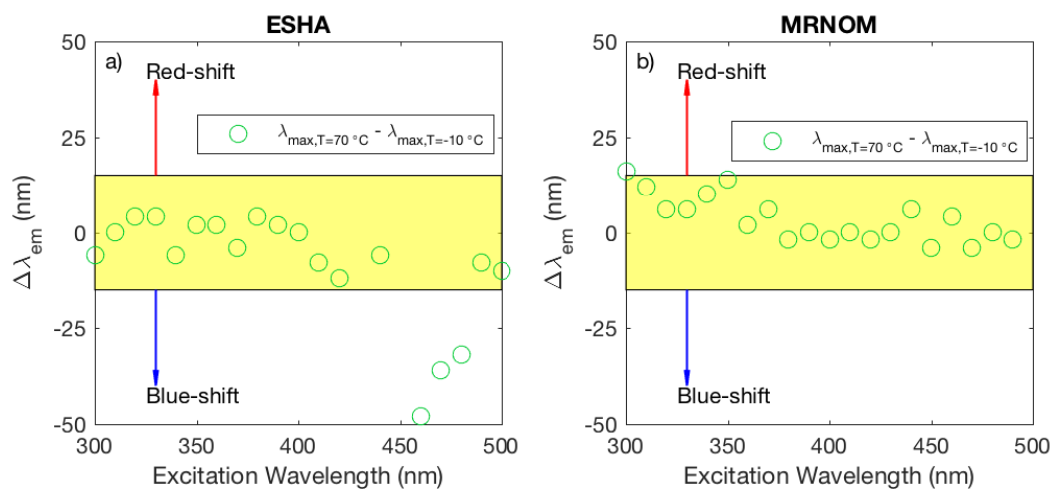Figure B.25. Solvatochromic shift in peak emission wavelength in 70:30 (%v/v glycerol:water) at 70 °C relative to -10 °C as a function of excitation wavelength.
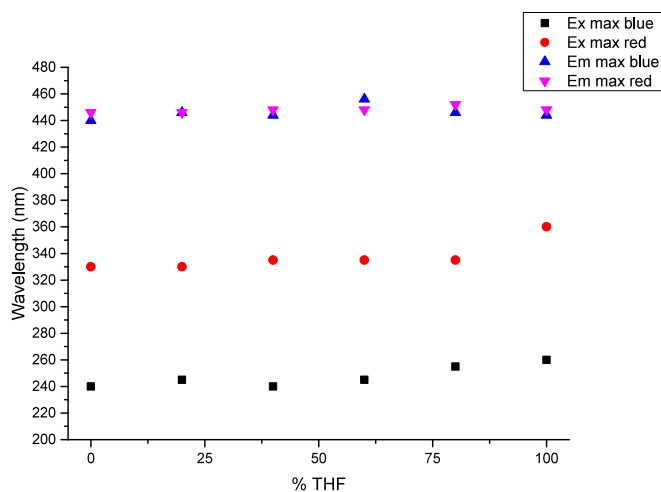

Figure B.26. Solvatochromic shifts in peak emission and excitation wavelength as a function of solvent composition (% THF in water) for SRFA.

214

Appendix C Supplemental Information for Chapter 5

C.1. Quantum yield calculations

The fluorescence quantum yield (Φ_f) was determined using steady state fluorescence data and quinine sulfate in 0.1 N H_2SO_4 as a reference (Φ_f of 0.51). Equation C.1 is the most general expression for fluorescence quantum yield. This method calculates the ratio of the integrated DOM sample fluorescence intensity (I_{DOM}) across all emission wavelengths (λ_{em}) at a given excitation wavelength (λ_{ex}) divided by the DOM absorbance at this excitation wavelength (Abs_{ex}). This ratio is divided by the same ratio for the quantum yield standard ($I_{ref}f$ and Abs_{ref}), in this case quinine sulfate. The first term corrects for differences in refractive index between the sample and quantum yield reference.

$$\frac{\Phi_{DOM}(\lambda_{ex})}{\Phi_{ref}(\lambda_{ex})} = \frac{n^2}{n_{ref}^2} \frac{\int_0^\infty I_{DOM}(\lambda_{ex},\lambda_{em})d\lambda_{em}}{Abs_{ex}(\lambda_{ex})} \frac{Abs_{ref}(\lambda_{ex})}{\int_0^\infty I_{ref}(\lambda_{ex},\lambda_{em})d\lambda_{em}}$$

Equation C.1.

Quinine sulfate does not absorb at wavelengths > 400 nm, which are of interest to DOM fluorescence. Thus, the reference term in the above equation was fixed to an excitation wavelength of 350 nm. This approach has been used before and is justified by the fact that instrument-specific correction factors are applied to the fluorescence data. Finally, the dependence of refractive index on wavelength and solvent was assumed to be negligible. In aqueous samples, the wavelength dependence is due to the fixed quinine sulfate standard excitation wavelength compared to sample excitation wavelength. For aqueous samples, the maximum refractive index range between all excitation and temperature combinations tested is 1.33 to 1.36. Based on Equation C.1, the maximum systematic error due to neglecting the refractive index term is 10%. With these assumptions, Equation B.1 simplifies to Equation B.2.

215

$$\frac{\Phi_{DOM}(\lambda_{ex})}{\Phi_{ref}(350 \text{ nm})} = \frac{\int_0^\infty I_{DOM}(\lambda_{ex},\lambda_{em})d\lambda_{em}}{Abs_{ex}(\lambda_{ex})} \frac{Abs_{ref}(350 \text{ nm})}{\int_0^\infty I_{ref}(350 \text{ nm},\lambda_{em})d\lambda_{em}}$$

Equation C.2

The upper bound of the integral in Equation B.2 is given by the maximum emission wavelength for which the sample emits. For measurements performed on the Fluoromax-4, the maximum emission wavelength measured was 700 or 800 nm, depending on the sample (red-shifted samples such as soil HA and SRHA were analyzed out to 800 nm). For measurements performed on the Aqualog, all samples were analyzed with a maximum emission wavelength of 800 nm.

Some additional details need to be mentioned regarding quantum yield determined with the Fluoromax-4 instrument. First, due to second order diffraction of fluorescence signal by the emission gratings, it was necessary to extrapolate (first order) fluorescence to zero using a single exponential function at excitation wavelengths less than 400 nm before integrating the signal. The difference in area between this method and simply stopping the integration when second order diffraction appeared was typically < 10% at excitation wavelengths > 300 nm. Second, past work comparing quantum yield profiles determined on a Fluoromax-4 and Aqualog showed systematically higher values for the Fluoromax-4 as compared to the Aqualog at excitation wavelengths < 350 nm. This difference is due to the poorer quality excitation gratings in the Fluoromax-4 (plane ruled gratings) that lets more stray light pass than the gratings in the Aqualog excitation system (concave holographic). For these reasons, quantum yields determined on the Fluoromax-4 are only reported at excitation wavelengths greater than 350 nm, which did not exhibit this systematic bias. At excitation wavelengths greater than 350 nm, there was good agreement in quantum yields measured on both instruments.

C.2. Temperature-dependence of DOM absorbance

Figure 1b in the main manuscript demonstrates that absorbance is unaffected by changes in temperature over 10 to 40 °C. Although absorbance data for only one sample (SRFA) is shown in Figure 1a, this same result was obtained for all isolates at all temperatures examined. In brief, as discussed in McKay et al. (McKay et al., n.d.), the constancy of absorbance with temperature suggests that DA complexes, if present, do not play a significant role in the absorbance properties of DOM. This is because absorbance due to these DA complexes depends on their concentration, which in turn depends on the equilibrium constant for formation of the complex (K_{DA}), which is temperature-dependent as described by the van't Hoff equation (Birks, 1970). For a typical enthalpy of complex formation of -2 kcal mol^{-1} (e.g. for p-benzoquinone and benzene is -1.8 kcal mol^{-1}) (Kuboyama and Nagakura, 1955), an ~25% decrease in absorbance between 10 and 40 °C is expected. Thus, the observed lack of change in absorbance with temperature is inconsistent with what would be predicted by the CT model.
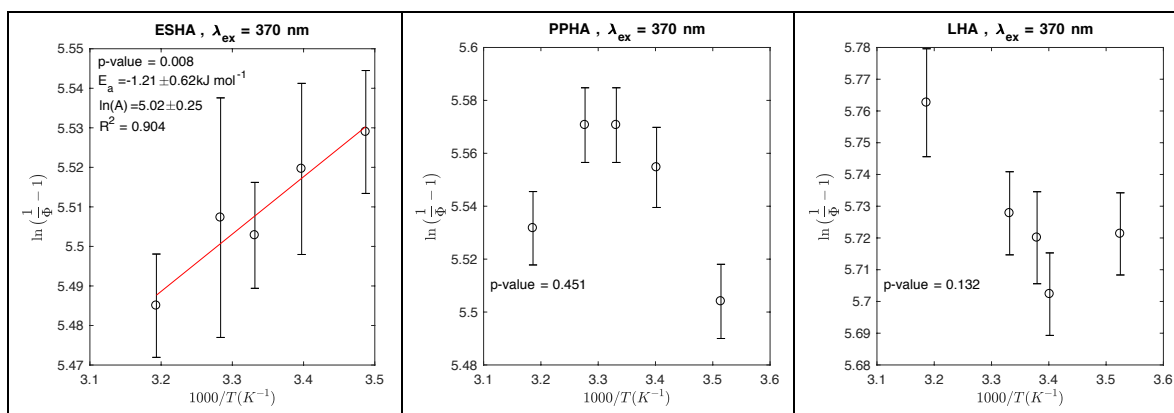
Figure C.1. Arrhenius-type plots for ESHA (top), PPHA (middle), and LHA (bottom) at an excitation wavelength of 370 nm. These data were regressed and slope p-values are displayed in the plots. Arrhenius parameters are displayed for ESHA due to the significant slope p-value (i.e. p-value < 0.05). Note that this trend observed for ESHA (increasing Φ_f with increasing temperature) is opposite that observed for aquatic isolates (decreasing Φ_f with increasing temperature). This is an interesting observation and should be explored in more detail in future studies. Note that Φ_f for ESHA is 0.0041 and 0.0043 at 10 and 40 °C (a 5% increase) where as this difference is much larger for aquatic isolates (e.g. 0.0118 and 0.0092 for MRNOM at 10 and 40 °C, i.e. a 22% decrease).
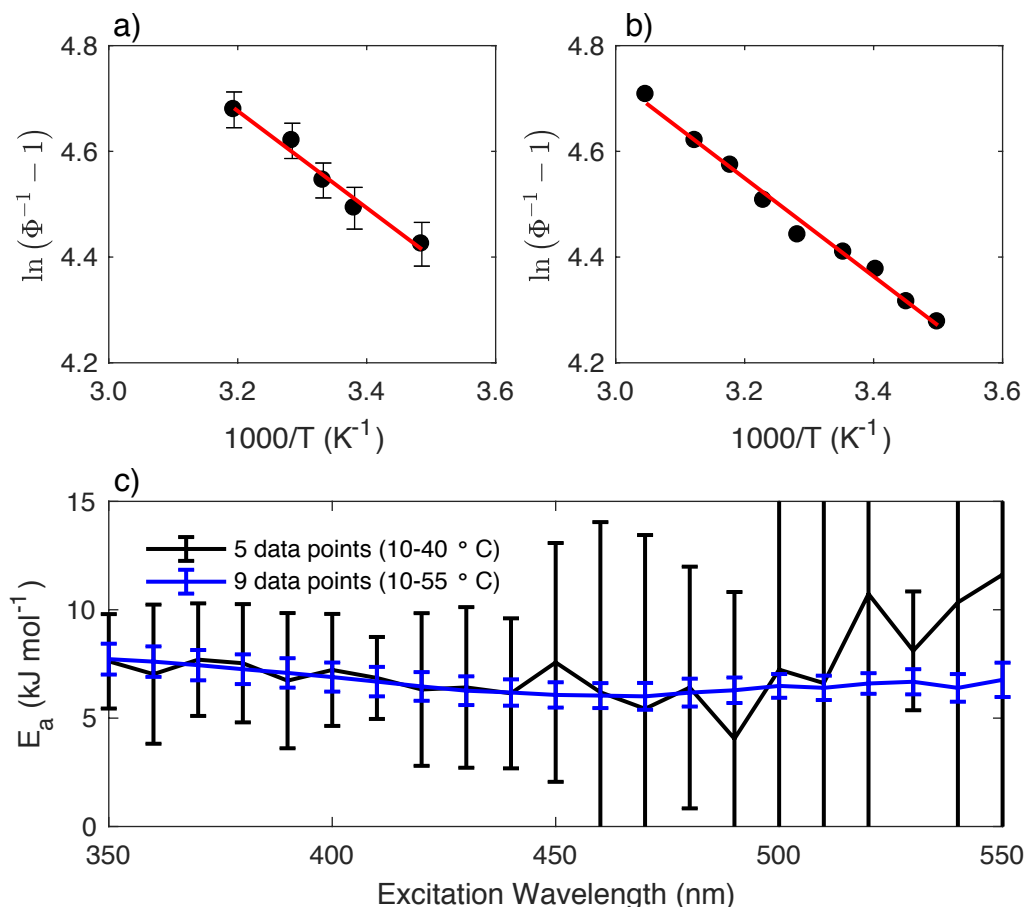
Figure C.2. Arrhenius-type plots for Mississippi River NOM (MRNOM, 1R110N) using 5 data points between 10-40 °C (a) and 9 data points between 10-55 °C (b) at an excitation wavelength of 350 nm. Error bars in a) represent propogated error from triplicate absorbance and fluorescence measurements on the sample and quinine sulfate reference standard. Subplot c) shows activation energies, Ea, as a function of excitation wavelength for MRNOM obtained via these two different experiments. Error bars in c) represent 95% confidence intervals based on a linear fit of Equation 5.9 in Chapter 5 to the transformed data. Note that data in subplot b) were obtained in 30% v/v glycerol and that no error bars are shown because only a single replicate was measured. Linear regression of E_a versus excitation wavelength between 350 and 440 nm yields slope p-values of 1.52×10^{-10} and 0.0017 for the 9 and 5 data point experiments, respectively.
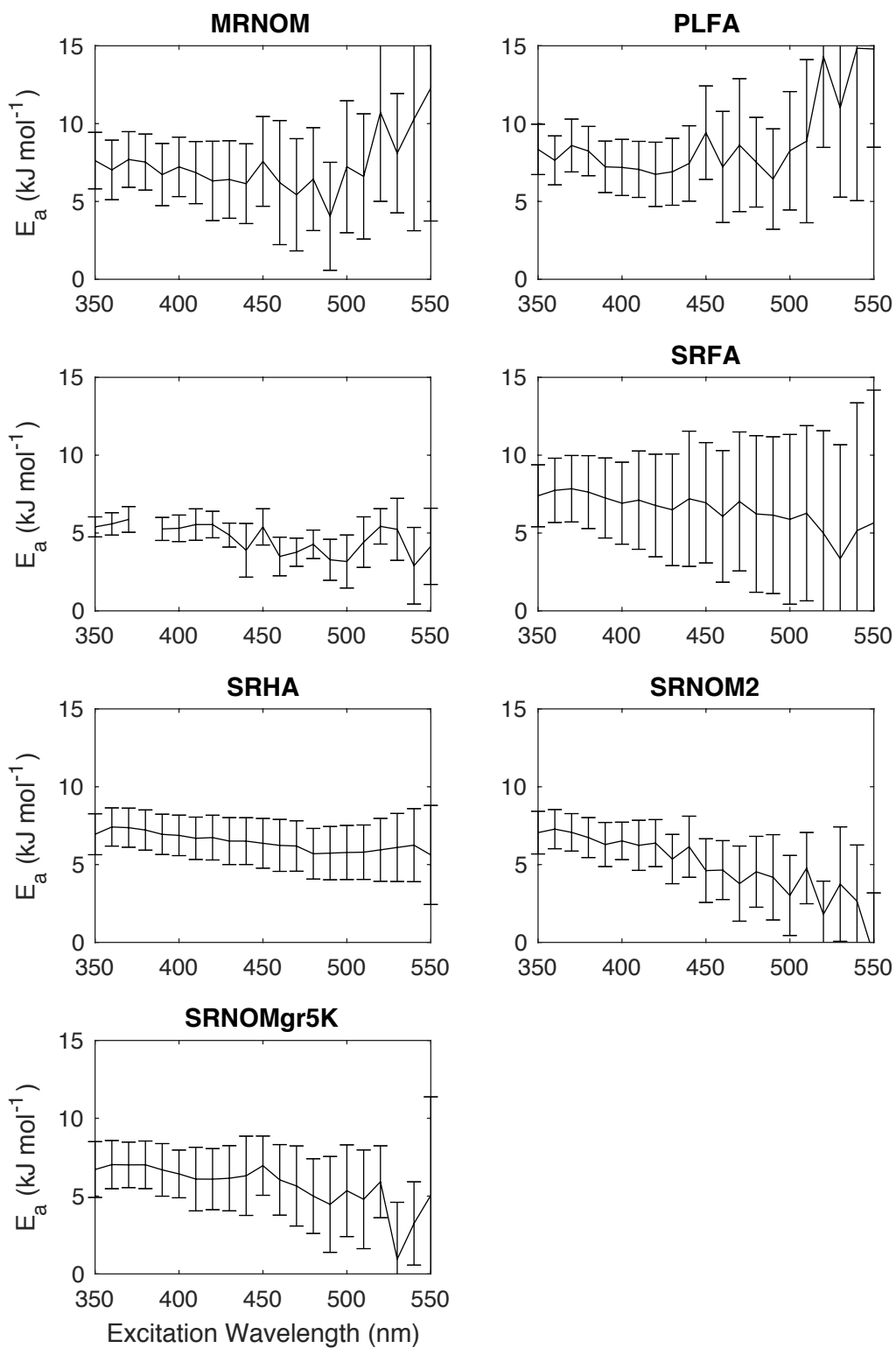
Figure C.3. Plots of activation energy versus excitation wavelength for all samples in this study.
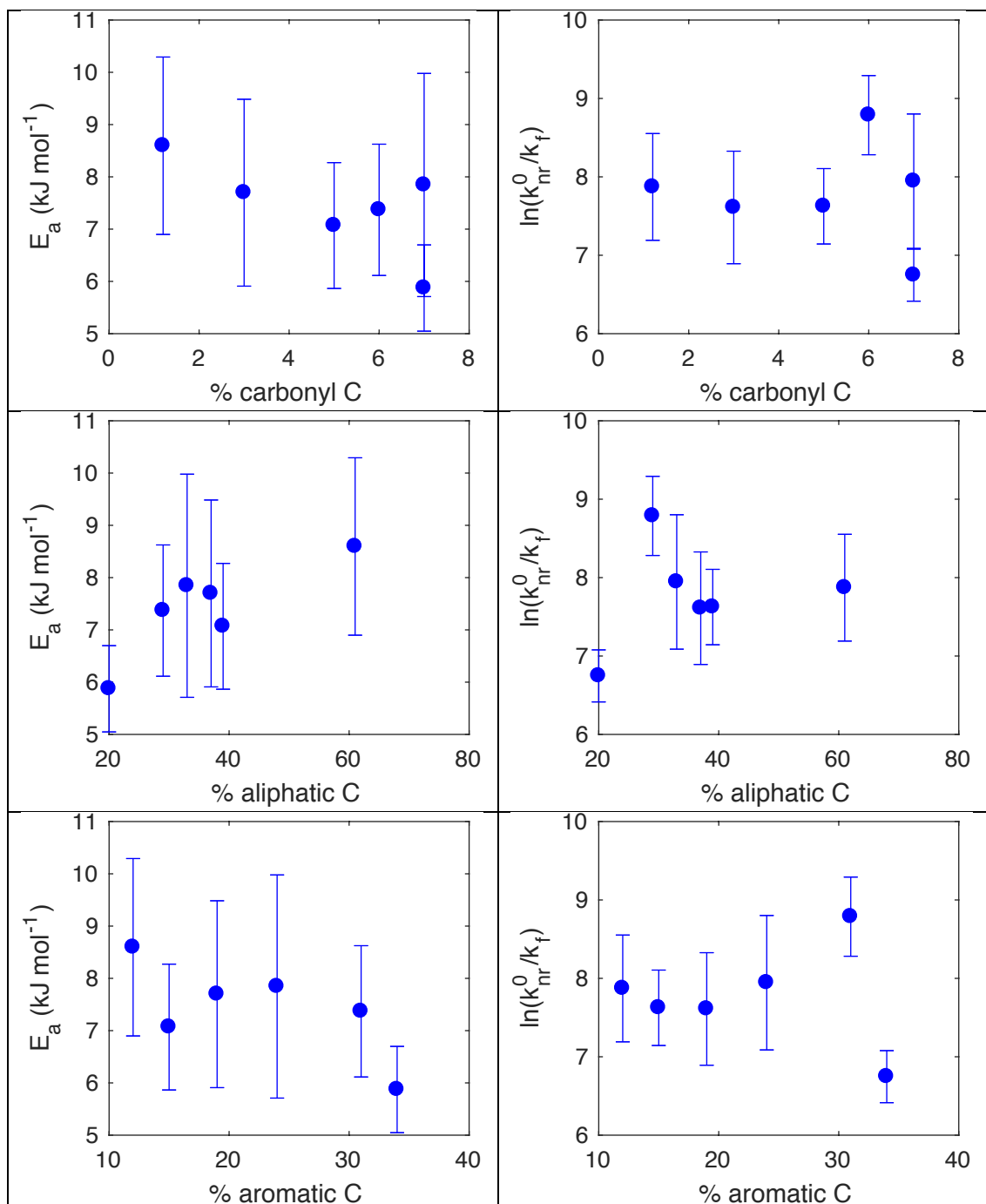
Figure C.4. Correlations between activation energy values, Ea, and optical properties for different organic matter isolates. Errorbars represent 95% confidence intervals based on a linear fit of Equation 5.9 in Chapter 5 to the transformed data.
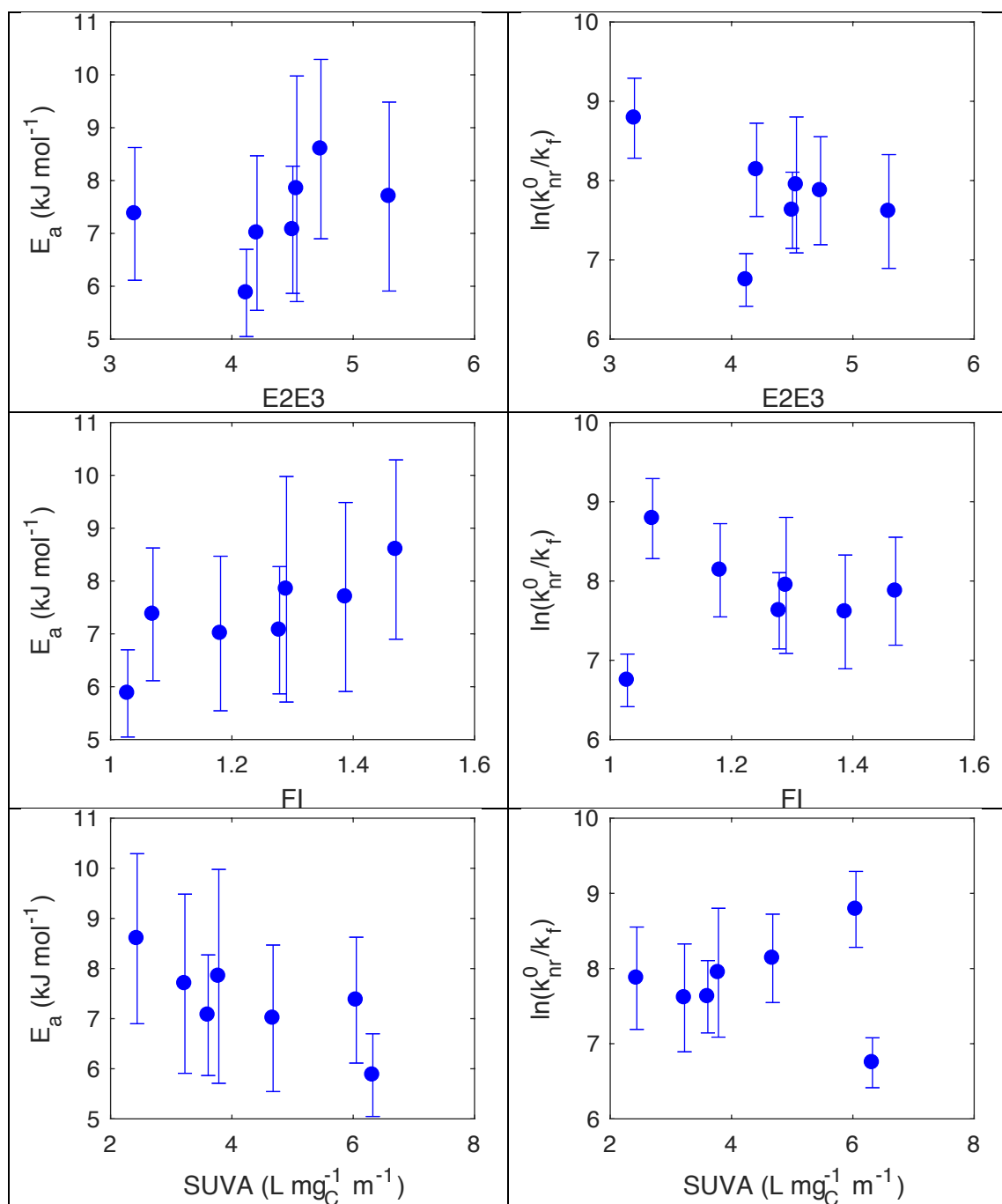
Figure C.5. Correlations between activation energy values, Ea, and optical properties for different organic matter isolates. Errorbars represent 95% confidence intervals based on a linear fit of Equation 5.9 in Chapter 5 to the transformed data.
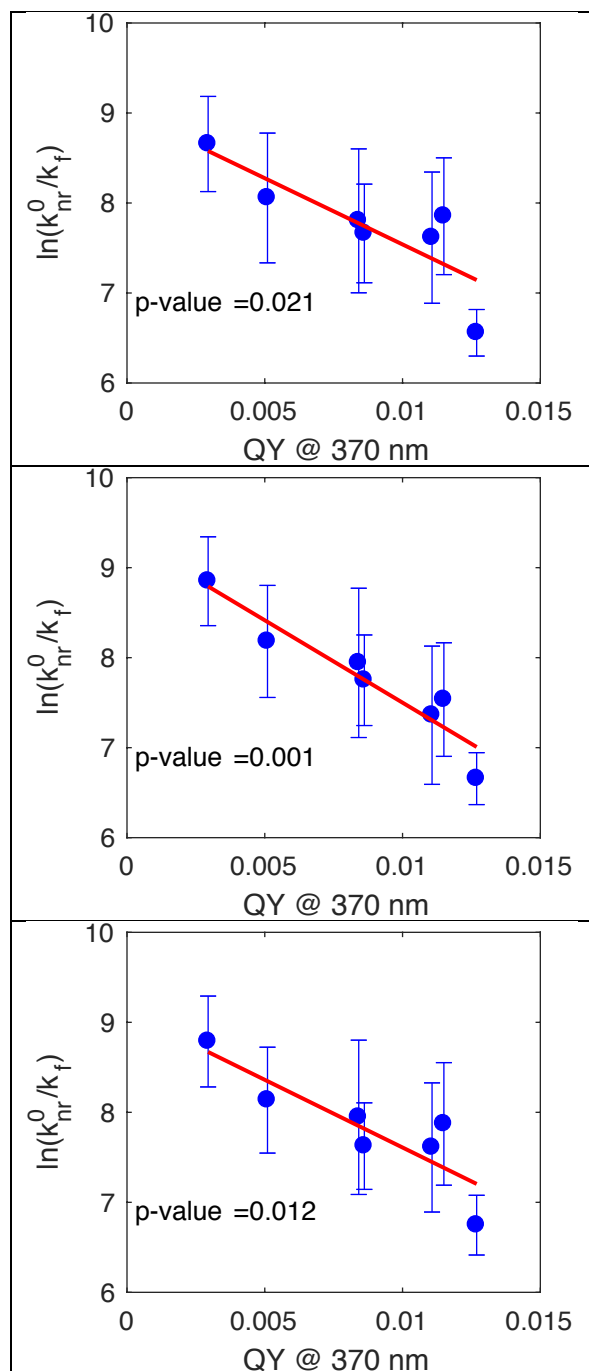
Figure C.6. Correlations between intercept term, $\ln(k_{nr}^0/k_f)$, and quantum yield at 370 nm for organic matter isolates. Intercept term derived from fit to Equation 5.9 in Chapter 5 at excitation wavelengths of 350 nm (top), 360 nm (middle) and 370 nm (bottom). Error bars represent 95% confidence intervals based on a linear fit of Equation 5.9 in main manuscript to the transformed data.

Table C.1. Source, acronym, identification #, and isolation method of DOM isolates used tin this study.

Sample	Classification	Source	Acronym	Identification #	Isolation method
Suwannee River Fulvic Acid	Terrestrial, aquatic	IHSS	SRFA	2S101F	Thurman and Malcolm (1981, EST)(Thurman and Malcolm, 1981)
Suwannee River Humic Acid	Terrestrial, aquatic	IHSS	SRHA	2S101H	Thurman and Malcolm (1981, EST)
Pony Lake Fulvic Acid	Microbial, aquatic	IHSS	PLFA	1R109F	Thurman and Malcolm (1981, EST)
Suwannee River Natural Organic Matter	Terrestrial, aquatic	IHSS	SRNOM	2R101N	Sun, Perdue and McCarthy (1995, Water Res)(Sun et al., 1995)
Upper Mississippi River Natural Organic Matter	Terrestrial, aquatic	IHSS	MRNOM	1R110N	Sun, Perdue and McCarthy (1995, Water Res)
Elliot Soil Humic Acid	Soil	IHSS	ESHA	1S102H	base extracted from solid material, XAD-8
Pahokee Peat Humic Acid	Soil	IHSS	PPHA	1S103H	base extracted from solid material, XAD-8
Pahokee Peat Fulvic Acid	Soil	IHSS	PPFA	2S103F	base extracted from solid material, XAD-8

Table C.2. Activation energies, E_a, for model organic compounds.

Compound	Solvent	E_a (kJ mol^{-1})	Ref.
Benzene	Ethanol	21.23	(Birks, 1970)
Toluene	Ethanol	24.12	(Birks, 1970)
Toluene	Hexane	17.37	(Birks, 1970)
p-Xylene	Ethanol	10.61	(Birks, 1970)
Napthalene	Ethanol	7.72	(Birks, 1970)
Napthalene	Hexane	5.79	(Birks, 1970)
2-Napthol	H2O	11f	(Robinson et al., 1986)
Tyrosine	H2O	29.71a	(Gally and Edelman, 1962)
Tryptophan	H2O	33.89a	(Gally and Edelman, 1962)
Tryptophan	H2O, D2O	29.29b	(Eisinger and Navon, 1969)
N-methyl tryptophan	H2O, D2O	27.20b	(Eisinger and Navon, 1969)
N-methyl tryptophan	H2O, D2O	27.20b	(Eisinger and Navon, 1969)
Tyrosine	0.5 M CH3COOH	9.1c	(Menter, 2006)
1-methyl anthroate	Acetonitrile	7.6d	(Matsumoto et al., 1972)
9-methyl anthroate	Ethanol	6.2d	(Matsumoto et al., 1972)
4-methyl-n-alkoxy coumarins	H2O	16.8-34.3e	(Giri, 1992)
Skh-1 (citrate-soluble calf skin)	0.5 M CH3COOH	6.2-8.4c	(Menter, 2006)
Collagen	0.5 M CH3COOH	10.3-11.4c	(Menter, 2006)
H2O viscosity		16.8	Calculated from wtt-pro.nist.gov/wtt-pro
Ethanol viscosity		14.3	Calculated from wtt-pro.nist.gov/wtt-pro
Tetrahydrofuran viscosity		7.6	Calculated from wtt-pro.nist.gov/wtt-pro

Appendix D Supplemental Information for Chapter 6

D.1. p-benzoquinone photolysis measurements using UV/Vis absorbance spectrophotometry

Irradiations of 70 µM p-benzoquinone spiked with 3 mM benzene were performed and analyzed by UV/Vis spectrophotometry to confirm this compounds rate of decay as observed by HPLC. Solutions were made at lower concentrations here to keep the maximum absorbance around 1 using a 1 cm path length

Spectra showing the loss of p-benzoquinone, and growth of hydroxy-p-benzoquinone and hydroquinone are shown in Figure D.5. By plotting the absorbance at 250 nm as a function of time, an initial decay rate of p-benzoquinone of 2.46×10^{-8} M s^{-1} was estimated. Performing the same analysis on data obtained by HPLC for 92.5 µM solutions of p-benzoquinone gives a decay rate of 6.24×10^{-8} M s^{-1}. Dividing each of these values by their respective concentrations yields first order rate constants of 3.6×10^{-4} s^{-1} and 6.7×10^{-4} s^{-1} for the UV/Vis and HPLC method, respectively. This factor of two difference can be reconciled by considering that the presence of benzene results in the formation of phenol. Because phenol absorbs at 250 nm, its growth in concentration (causing an increase in absorbance) would decrease the rate of p-benzoquinone loss.

D.2. Analysis of temperature dependent data using the Eyring equation:

Quantum yields were plotted according to the Eyring equation:

$$\ln\left(\frac{\Phi_a}{T}\right) = -\frac{\Delta H^{\ddagger}}{RT} + \ln\left(\frac{k_B}{h}\right) + \frac{\Delta S^{\ddagger}}{R}$$

Equation D.1

where Φ_a is the apparent quantum yield of $^{\bullet}$OH formation, $\Delta H^{\ddagger}$ is the enthalpy of activation, $\Delta S^{\ddagger}$ is the entropy of activation, k_B is Boltzman's constant, h is Planck's constant, and R is the

ideal gas constant. Values of $\Delta H^{\ddagger}$ and $\Delta S^{\ddagger}$ are summarized in Table D.1, and, as expected $\Delta H^{\ddagger}$ is approximately equal to the Arrhenius activation energy (Table 6.1). It is difficult to interpret the meaning of $\Delta S^{\ddagger}$ for the multistep reaction sequence that forms $^{\bullet}OH$ from DOM photolysis. Nevertheless, it is interesting to note that the DOM samples having the largest Arrhenius activation energy (SRFA, SRNOM < 5K and <1K) all have the largest values of $\Delta S^{\ddagger}$ (notice especially the trend with SRNOM).

Table D.1. Summary of enthalpy and entropy of activation values obtained via the Eyring equation.

Sample	$\Delta H^{\ddagger}$ (kJ mol^{-1})	$\Delta S^{\ddagger}$ (J mol^{-1} K^{-1})
Nitrate	14.1	-66.0
PLFA	19.1	-97.4
SRFA	38.3	-48.5
ESHA	15.1	-123.5
SRHA	13.5	-124.8
SRNOM	15.3	-112.9
SRNOM 5K	24.1	-83.0
SRNOM 1K	33.0	-55.6

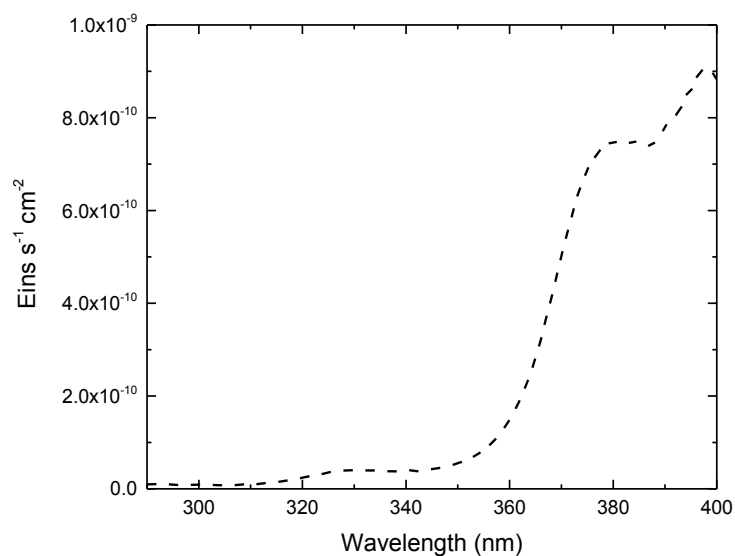Figure D.1. Photon irradiance as a function of wavelength obtained using the experimental setup (xenon lamp in Oriel solar simulator) taken using Ocean Optic spectrometer.
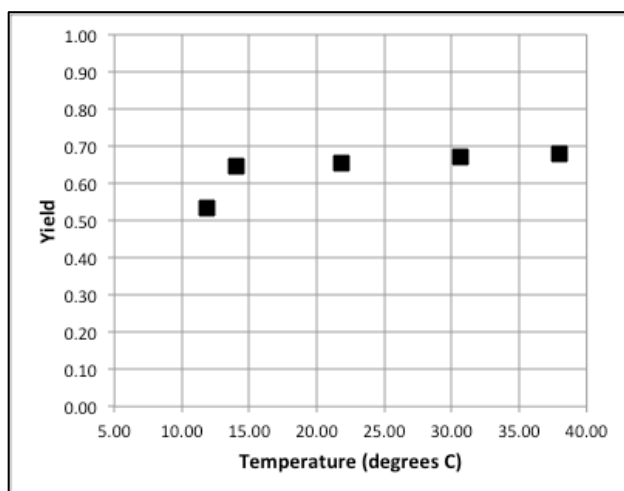
Figure D.2. Plot of phenol yield from the hydroxylation of benzene as a function of temperature. Experiments were performed using H_2O_2 as a $^•$OH radical source and detailed discussion of the calculations is located in the main text.
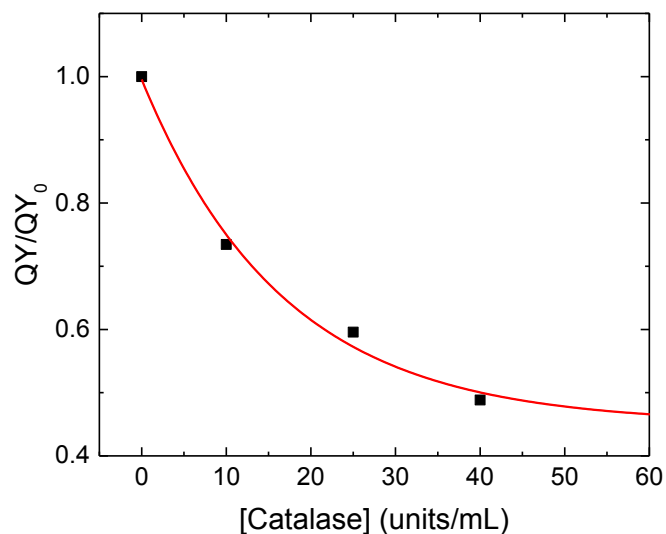
Figure D.3. Plot of $^{\bullet}$OH radical quantum yield at a given concentration of catalase normalized to the quantum yield at zero catalase concentration. Data were fitted with a first order exponential decay to estimate the baseline (0.456), which represents the maximum amount of quenching.
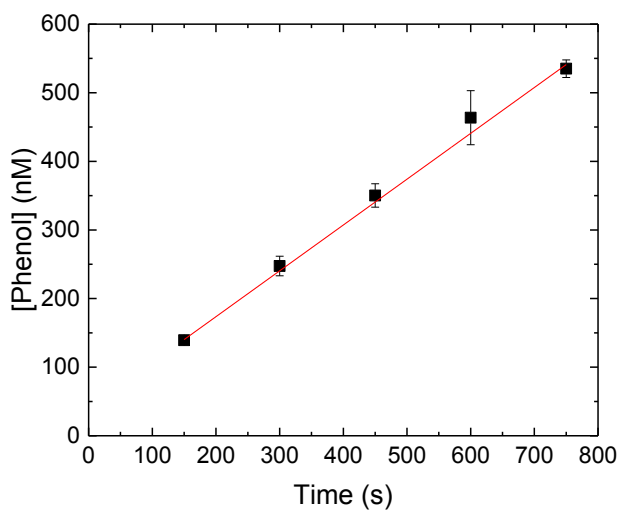
Figure D.4. Plot of phenol concentration against time for irradiation of 92.5 μM p-benzoquinone in the presence of 3 mM benzene. Linear fit of the data gives a rate of phenol production of 6.72 × 10^{-11} M s^{-1}. Dividing by the rate of light absorption yields the quantum yield for phenol production from p-benzoquinone photolysis.
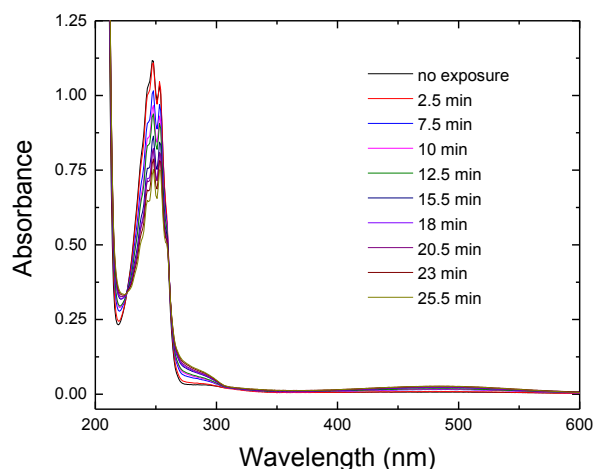
Figure D.5. Absorption spectra of 70 µM p-benzoquinone solutions over the course of 25.5 minutes of irradiation. The decrease at 250 nm, and growth at 290 nm and 500 nm represent the loss of p-benzoquinone, and growth of hydroquinone and hydroxyl-p-benzoquinone, respectively.
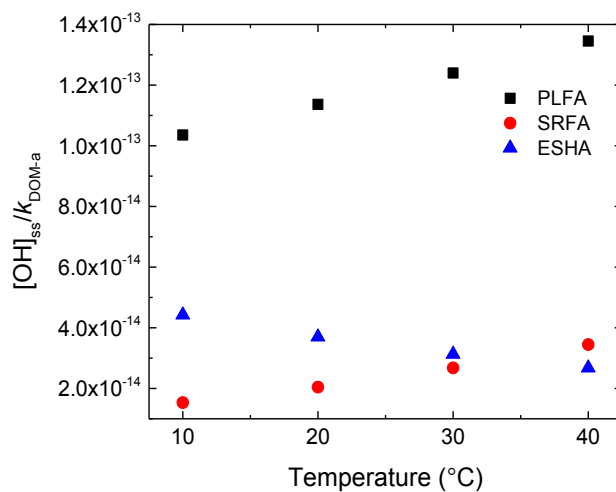
Figure D.6. Plot of steady state concentration of $^{\bullet}$OH radical as a function of temperature due to both photochemical production of and scavenging by DOM. Note that the steady state concentration is normalized to the specific rate of light absorption.

Appendix E Supplemental Information for Chapter 7

E.1. Hierarchal Cluster Analysis

As described in the main text, hierarchal cluster analysis was performed on samples using optical property and reactive intermediate (RI) formation rates and quantum yields (Φ_{RI}) in order to determine relationships between samples. Figure E.1 shows the results of this analysis for all samples (a) and monthly averages (b). Detailed interpretation of these results is given in the main text.
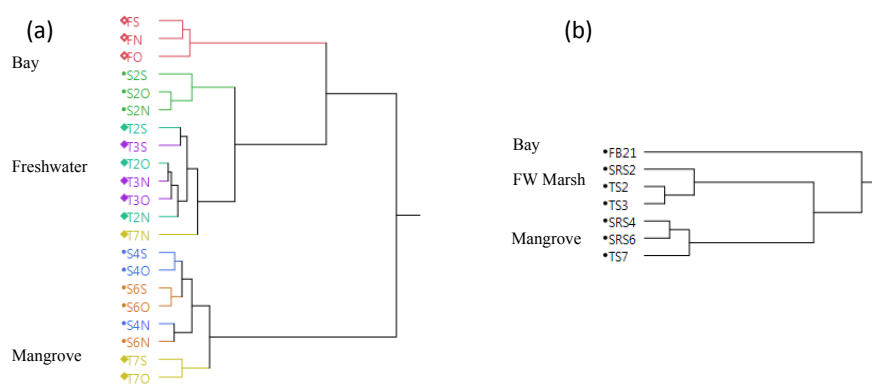
Figure E.1. Cluster analyses for ENP samples: (a) all samples and (b) monthly averages. In (a), sample name is a combination of sampling site and month. For example, FB stands for Florida Bay September sample and T7N stands for TS7 November sample. Φ_{RI}, optical properties, and $A_{\times}A_{50}$ were used in this analysis.

E.2. Reactive oxygen species measurement

Samples were irradiated with an Oriel solar simulator (94041A, Newport Corp, USA) as described in the main text. Figure E.2 shows an example lamp spectrum and calculation of the rate of light absorption in this system.

Quantum yields for $^1O_2$ (Φ_{1O2}), $^{\bullet}OH$ (Φ_{OH}), and initial TMP loss (f_{TMP}, a surrogate for $^3DOM^*$) were calculated using the measured rate of RI formation (or in the case of $^3DOM^*$, TMP loss) and the rate of light absorption:

$$\Phi_{RI} = \frac{R_{RI,form}}{R_{a-DOM}}$$

<div align="right">Equation E.1</div>

$R_{a\text{-}DOM}$ is the rate of light absorption by DOM and is a function of the solution absorbance and irradiance, both of which are functions of wavelength:

$$R_{a-DOM} = \sum_{\lambda=290nm}^{400nm} \frac{E_{p,\lambda}^0 \left(1-10^{-Abs_\lambda l}\right)}{l} \Delta\lambda$$

<div align="right">Equation E.2</div>

$E_{p,\lambda}^0$ is the surface irradiance (measured with an Ocean Optics USB2000 spectroradiometer), Abs_λ is the solution absorbance at wavelength λ, l is the optical path length (0.84 cm for our system) (Dong and Rosario-Ortiz, 2012), and $\Delta\lambda$ is the step in wavelength used in the sum (1 nm). Sample absorbance for photochemical experiments was measured in triplicate using a Cary 100 Bio UV-Vis spectrophotometer (Varian, USA). Samples were irradiated (only one replicate) in borosilicate vials laid flat in a water-jacketed petri dish cooled to 20 ± 2 °C. Probe compound's disappearance (or appearance of reaction product) was quantified by HPLC (Agilent 1200 Series) as described below. The sample standard deviation for measurement of each Φ^{RI} was assessed by measuring Φ_{RI} for SRNOM (1R101N) at least three times for each RI over the experimental campaign. Coefficient of variance was less than 10% for these measurements (Table E.1). Details on the use of probe compounds to measure RI formation rates are as follows.
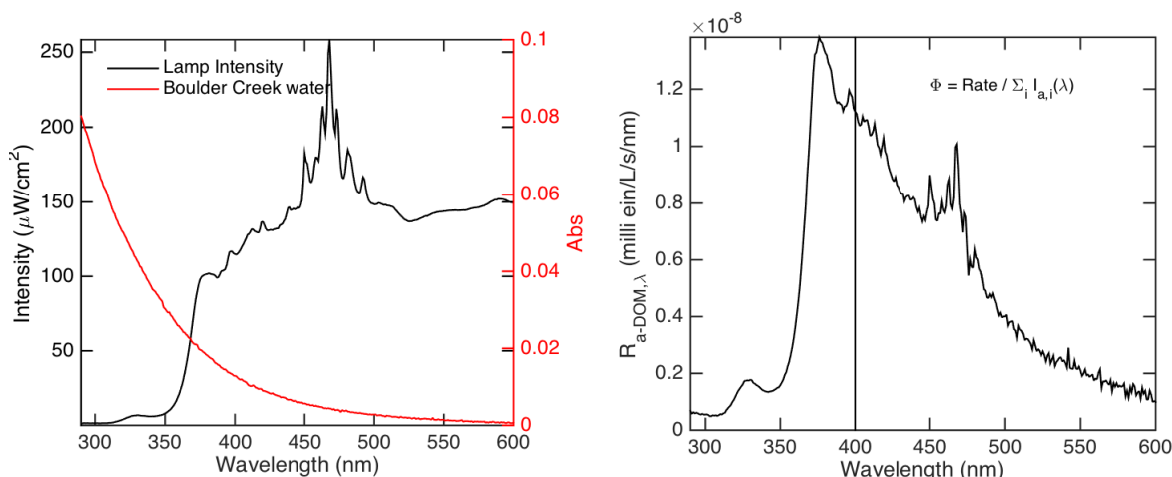
Figure E.2. (Left) Lamp spectra (black, left axis) for Oriel 94041 A solar simulator described in main text and absorbance spectra (red, right axis) for Boulder Creek non-base-modified. (Right) calculation of the rate of light absorption by DOM.

Table E.1. Quality control/quality assurance parameters for RI measurement

Parameter \ RI	ΦTMP	Φ_{1O2}	Φ_{OH}
n	3	3	5
Average Φ	1.32×10^{-4}	0.0266	2.37×10^{-5}
S	1.06×10^{-5}	0.0019	1.31×10^{-6}
CV (%)	8.0	7.2	5.5

Triplet States: ^{3}DOM* formation was assessed using the electron transfer probe 2,4,6-trimethylphenol (TMP) (Canonica and Freiburghaus, 2001; McCabe and Arnold, 2016). Briefly, because DOM has a spectrum of triplet states, all of which react at different rate constants with TMP, exact quantification of ^{3}DOM* formation rates are not attainable. However, the pseudo-first order rate for TMP loss can be used (at a fixed TMP concentration) to calculate the quantum efficiency for TMP loss, f_{TMP} (M^{-1}), which is proportional to the quantum yield for ^{3}DOM* (Bodhipaksha et al., 2015). This analysis works under the assumption that both k_{TMP} and Σk_{3DOM*} are constant, which represent the second order rate constant between ^{3}DOM* and TMP and the sum over all first- and pseudo-first order ^{3}DOM* loss reactions, respectively. Thus, for the above reasons, we have not calculated ^{3}DOM* steady state concentrations or quantum yields based on

our data. For the purposes of this study, we report the quantum yield coefficient of ^{3}DOM* (f_{TMP}) at an initial [TMP] of 3.7 μM. Analyzing the data in this way allows for comparison to previous studies and Φ^{1O2} values. f_{TMP} was calculated via:

$$f_{TMP} = \frac{k_{TMP\,loss}}{R_{a-DOM}}$$

Equation E.3

where k_{TMP} loss is the first order rate constant for TMP loss. This method has been explained in detail previously (Andrew et al., 2016; Bodhipaksha et al., 2015; Green and Blough, 2003).

TMP loss was monitored by HPLC with UV detection at 219 nm. Previous studies have shown that TMP degradation due to ^{3}DOM* is slowed at high ionic strength (~0.54 M) compared to freshwater (Parker et al., 2013; Sharpless and Blough, 2014). Some control experiments were performed to assess if this occurred in our system (see Text S5) and this possibility is considered in the analysis and conclusions presented in Chapter 7.

<u>Singlet Oxygen:</u> ^{1}O$_2$ formation was measured by monitoring the first order disappearance of FFA ([FFA]$_0$ = 22.5 μM) with 0.1 M methanol to quench $^\bullet$OH (k_{FFA-OH} = 1.5 × 10^{10} M^{-1} s^{-1}) (Buxton et al., 1988; Peterson et al., 2012). The first order rate constant for FFA loss was multiplied by the second order rate constant for the reaction between ^{1}O$_2$ and FFA ($k_{FFA-1O2}$ = 1.2 × 10^8 M^{-1} s^{-1}) to obtain the steady state singlet oxygen concentration, [^{1}O$_2$]$_{ss}$ (Dalrymple et al., 2010; Haag and Höigne, 1986). To calculate Φ_{1O2}, [^{1}O$_2$]$_{ss}$ was multiplied by the first order quenching rate constant of ^{1}O$_2$ by water (k_d = 2.5 × 10^5 s^{-1}):

$$[^1O_2]_{ss} = \frac{R_{1O2}}{k_d + k_{FFA-1O2}[FFA]} \simeq \frac{R_{1O2}}{k_d}$$

$$R_{1O2} = [^1O_2]_{ss} k_d$$

Equation E.4

FFA loss was monitored by HPLC with UV detection at 219 nm.

Hydroxyl Radical: $^\bullet$OH formation was quantified using benzene as a probe under conditions such that all photochemically formed $^\bullet$OH radicals were scavenged by the probe ([benzene] ~ 3 mM) (Bodhipaksha et al., 2015; Dong and Rosario-Ortiz, 2012; Vione et al., 2010). Benzene reacts with $^\bullet$OH via ring addition, forming the hydroxycyclohexadienyl radical, which is then oxidized to phenol by oxygen ($[^1O_2]$ ~ 250 µM). Phenol was quantified using HPLC with UV detection at 210 nm. The rate of phenol formation is related to the rate of $^\bullet$OH formation by $R_{phenol} = Y \times R_{OH}$ where Y is the reaction yield. A yield of 0.63 previously determined by our lab was used (McKay and Rosario-Ortiz, 2015; Mostafa and Rosario-Ortiz, 2013).

DOM is the major source of $^\bullet$OH for the samples in this study. Nitrate (NO_3^-) concentrations were measured (see main text) for all samples and the highest measured concentration was 0.056 mM. Based on work by Vione et al. (2006), NO_3^- becomes the dominant $^\bullet$OH source in DOM-containing waters at a ratio of 3.3×10^{-5} mol NO_3^- mg_C^{-1} (McCabe and Arnold, 2016; Vione et al., 2006). Thus, for the sample containing 0.056 mM NO_3^-, the dissolved organic carbon (DOC) concentration, [DOC], required for DOM to become the primary $^\bullet$OH source is 1.70 ppm:

$$\frac{[NO_3^-]}{[DOC]} \leq 3.3 \times 10^{-5} \left[\frac{mol\ NO_3^-}{mg_C} \right] \Rightarrow [DOC] \geq \frac{[NO_3^-]}{3.3 \times 10^{-5}}$$

$$\Rightarrow [DOC] \geq \frac{0.056\ \text{mmol}\ NO_3^-/L}{3.3 \times 10^{-5} \left[\dfrac{mol\ NO_3^-}{mg_C} \right]} \Rightarrow [DOC] \geq 1.70\ mg_C\ L^{-1}$$

Equation E.5

The lowest [DOC] for any sample was ~5.5 $mg_C\ L^{-1}$, thus, DOM was the main source of $^\bullet$OH for these samples.

E.3. Single linear regression modeling

Single linear regression models referenced in the main text are presented below. These include correlations between RI formation rates and extrinsic predictors (Figure E.3) as well as

Φ_{RI} and intrinsic predictors (Figure E.4 and Figure E.5). Correlations between Φ_{RI} and E2:E3 or $S_{300-600}$ have been most often presented in the literature. Figure E.3 demonstrates, as expected, that the rate of RI formation is determined by the amount of CDOM. The results demonstrate that all optical properties besides S_R are good predictors of Φ_{1O2} and f_{TMP}, but not Φ_{OH}.
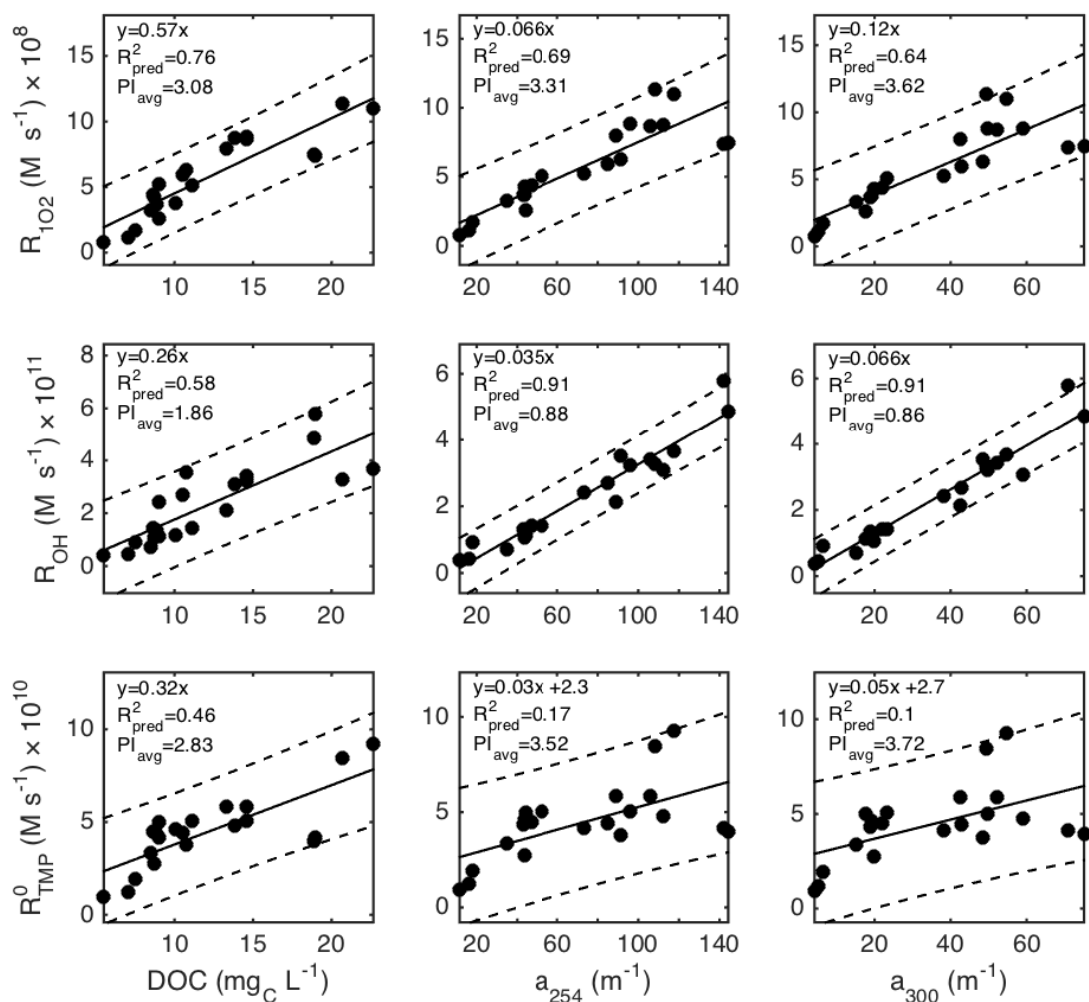
Figure E.3. Regression models for the three extrinsic predictors used in estimating rates of RI formation. Solid line indicates the model prediction and dashed lines indicate the 95% prediction interval. The fitted model equation, R^2_{pred} , and average prediction interval are shown for each prediction-regressor pair.
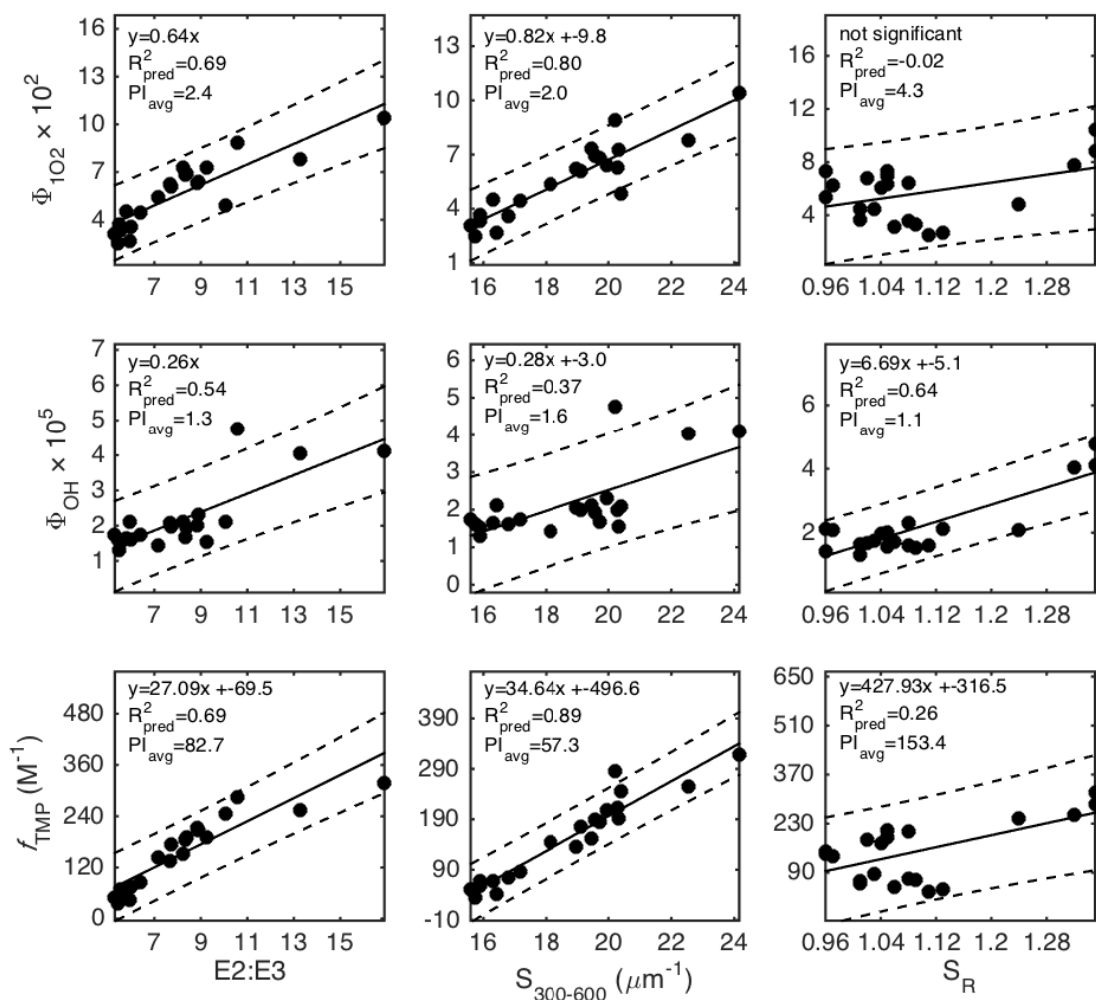
Figure E.4. Regression models for the intrinsic absorbance predictors used in estimating RI quantum yields. Solid line indicates the model prediction and dashed lines indicate the 95% prediction interval. The fitted model equation, R^2_{pred}, and average prediction interval are shown for each prediction-regressor pair.
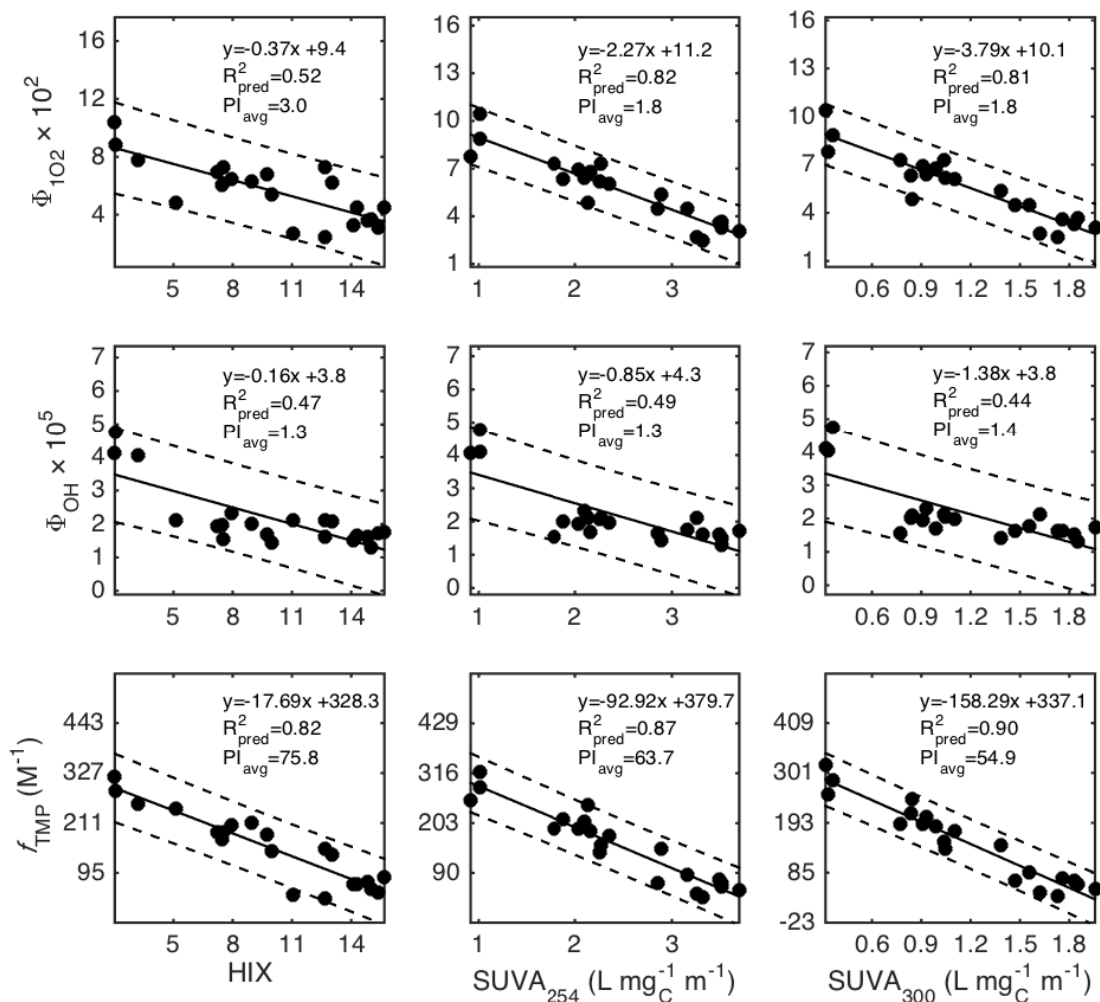
Figure E.5. Regression models for the intrinsic absorbance and fluorescence predictors used in estimating RI quantum yields. Solid line indicates the model prediction and dashed lines indicate the 95% prediction interval. The fitted model equation, R^2_{pred}, and average prediction interval are shown for each prediction-regressor pair.

E.4. Multiple linear regression models for RRI and ΦRI

As described in the main text, attempts were made at using multiple linear regression to better predict R_{RI} and Φ_{RI}. The results and discussion regarding this attempt is given here. In addition, Table E.2 through Table E.6 present Pearson's correlation coefficients between the standardized and non-standardized predictors. Multiple linear regression was carried out with R_{RI} as observations and DOC, a_{254}, and a_{300} as predictors. Stepwise regression was used to determine

a statistically significant model in which single regressor and interaction terms were allowed. Fitted versus modeled results, model equations, and R^2_{pred} values are shown in Figure E.6 and show improved prediction capability for R_{1O2}, R_{OH}, and R^0_{TMP} degradation (average $R^2_{pred}=0.92$, $0.90< R^2_{pred} <0.93$) compared to single linear regression models (average $R^2_{pred}=0.58$, $0.1< R^2_{pred} <0.91$) for our dataset. As noted above, R^2_{pred} is a more robust diagnostic for model predictability than R^2, as it does not necessarily increase when terms are added to the model.

Multiple linear regression was also carried out with Φ_{RI} as observations and two different sets of predictors: one that was absorbance- and DOC-based (E2:E3, $S_{300\text{-}600}$, SUVA$_{254}$ and SUVA$_{300}$) and one with two additional parameters (HIX and A$_x$A$_{50}$). Stepwise regression was used to determine a statistically significant model in which single regressor and interaction terms were allowed. Fitted versus modeled results, model equations, and R^2_{pred} values are shown in Figure E.7 and Figure E.8 and show improved predictive capability for Φ_{1O2}, Φ_{OH}, and f_{TMP} for the absorbance- and DOC-based predictors (average $R^2_{pred}=0.89$) and full predictor set (R^2_{pred} =0.92) compared to single linear regression models (average $R^2_{pred}=0.66$ and 0.68 for the two predictor sets, respectively). Correlations for Φ_{OH} were weaker for all predictor sets examined compared to Φ_{1O2} and f_{TMP}.

Although multiple linear regression provided better predictability (i.e. R^2_{pred}) for the samples in this study, all regressors were intercorrelated, even when standardized (i.e. $\bar{x}=0$, $\sigma=1$). To test whether multiple linear regression models led to better predictability, we developed models with $S_{300\text{-}600}$, E2:E3, and SUVA$_{254}$ as regressors and Φ_{RI} as observations (from ENP samples) and

240

used these (Figure E.9 and Figure E.10) to calculate Φ_{RI} values based on optical property data from the study of McCabe and Arnold (2016). A comparison of calculated to measured Φ_{RI} is shown in Figure E.11, which demonstrates that the multiple linear regression models are unsuccessful at predicting Φ_{RI}. Thus, although the multiple linear regression models built here exhibited high R^2_{pred} values within the ENP samples, they are not applicable in general (Figure E.11b). More work should be done to clarify the potential use of multiple linear regression for predicting Φ_{RI}. Conversely, use of single linear regression models built with data from the ENP adequately modeled Φ_{1O2} and f_{TMP} (but not Φ_{OH}) values determined by McCabe and Arnold (Figure E.11a) (Canonica and Freiburghaus, 2001; McCabe and Arnold, 2016).

Table E.2. Pearson correlation coefficients for HIX, E2:E3, $S_{300\text{-}600}$, S_R, SUVA$_{254}$, SUVA$_{300,}$ and A$_x$A$_{50}$ with standardized regressor. The p-value on all non-diagonal elements was < 0.05.

	HIX	E2:E3	S	SUVA254	SUVA300	AA50
HIX	1.00000	-0.86305	-0.86478	0.89477	0.90192	0.54231
E2:E3	-0.86305	1.00000	0.95296	-0.89282	-0.89450	-0.60403
S	-0.86478	0.95296	1.00000	-0.94222	-0.95532	-0.78540
SUVA254	0.89477	-0.89282	-0.94222	1.00000	0.99571	0.72213
SUVA300	0.90192	-0.89450	-0.95532	0.99571	1.00000	0.76017
AA50	0.54231	-0.60403	-0.78540	0.72213	0.76017	1.00000

Table E.3. Pearson correlation coefficients for HIX, E2:E3, $S_{300\text{-}600}$, S_R, SUVA$_{254}$, SUVA$_{300,}$ and A$_x$A$_{50}$ with non-standardized regressor. The p-value on all non-diagonal elements was < 0.05.

	HIX	E2:E3	S	SUVA254	SUVA300	AA50
HIX	1.00000	-0.86297	-0.86476	0.89478	0.90196	0.54220
E2:E3	-0.86297	1.00000	0.95292	-0.89280	-0.89447	-0.60378
S	-0.86476	0.95292	1.00000	-0.94225	-0.95533	-0.78531
SUVA354	0.89478	-0.89280	-0.94225	1.00000	0.99573	0.72207
SUVA300	0.90196	-0.89447	-0.95533	0.99573	1.00000	0.76006
AA50	0.54220	-0.60378	-0.78531	0.72207	0.76006	1.00000

Table E.4. Pearson correlation coefficients for DOC, a_{254}, and a_{300} with non-standardized regressors. The p-value on all non-diagonal elements was < 0.05.

	DOC	a254	a300
DOC	1.00000	0.88524	0.84275
a254	0.88524	1.00000	0.99515
a300	0.84275	0.99515	1.00000

Table E.5. Pearson correlation coefficients for DOC, a_{254}, and a_{300} with standardized regressors. The p-value on all non-diagonal elements was < 0.05.

	DOC	a254	a300
DOC	1.00000	0.88524	0.84270
a254	0.88524	1.00000	0.99515
a300	0.84270	0.99515	1.00000

Table E.6. Pearson correlation coefficients for E2:E3, $S_{300-600}$, and SUVA$_{254}$. The p-value on all non-diagonal elements was < 0.05.

	Non-standardized regressor			Standardized regressors		
	E2E3	S	SUVA254	E2E3	S	SUVA254
E2E3	1.000000	0.952960	-0.892825	1.000000	0.952918	-0.892796
S	0.952960	1.000000	-0.942224	0.952918	1.000000	-0.942248
SUVA254	-0.892825	-0.942224	1.000000	-0.892796	-0.942248	1.000000

Figure E.6. Multiple linear regression models for the extrinsic predictors used in estimating RI formation rates. The one to one line is shown for comparison. The fitted model equation and R^2_{pred} are shown for each R_{RI}. Stepwise elimination was used to obtain only significant ($\alpha=5\%$) model terms.

Figure E.7. Multiple linear regression models for the intrinsic absorbance-based predictors used in estimating RI quantum yields. The one to one line is shown for comparison. The fitted model equation and R^2_{pred} are shown for each R_{RI}. Stepwise elimination was used to obtain only significant (α=5%) model terms.

$$\Phi_{1O2} \times 10^2 = 110.29 \times \text{E2E3}$$
$$-211.81 \times \text{S}$$
$$-10.45 \times \text{SUVA254}$$
$$-108.05 \times \text{E2E3:SUVA300}$$
$$206.04 \times \text{S:SUVA300}$$
$$10.75 \times \text{SUVA254:SUVA300}$$
$$R^2_{pred} = 0.95$$

$$\Phi_{OH} \times 10^5 = 16.27 \times \text{(Intercept)}$$
$$0.56 \times \text{HIX}$$
$$-22.78 \times \text{S}$$
$$-0.46 \times \text{SUVA254}$$
$$0.55 \times \text{IP100}$$
$$-0.03 \times \text{HIX:IP100}$$
$$2.56 \times \text{E2E3:S}$$
$$R^2_{pred} = 0.84$$

$$f_{TMP} = -698.74 \times \text{(Intercept)}$$
$$-6.24 \times \text{HIX}$$
$$602.77 \times \text{E2E3}$$
$$-490.33 \times \text{S}$$
$$13.28 \times \text{SUVA254}$$
$$817.02 \times \text{SUVA300}$$
$$-16.80 \times \text{IP100}$$
$$-440.68 \times \text{E2E3:SUVA300}$$
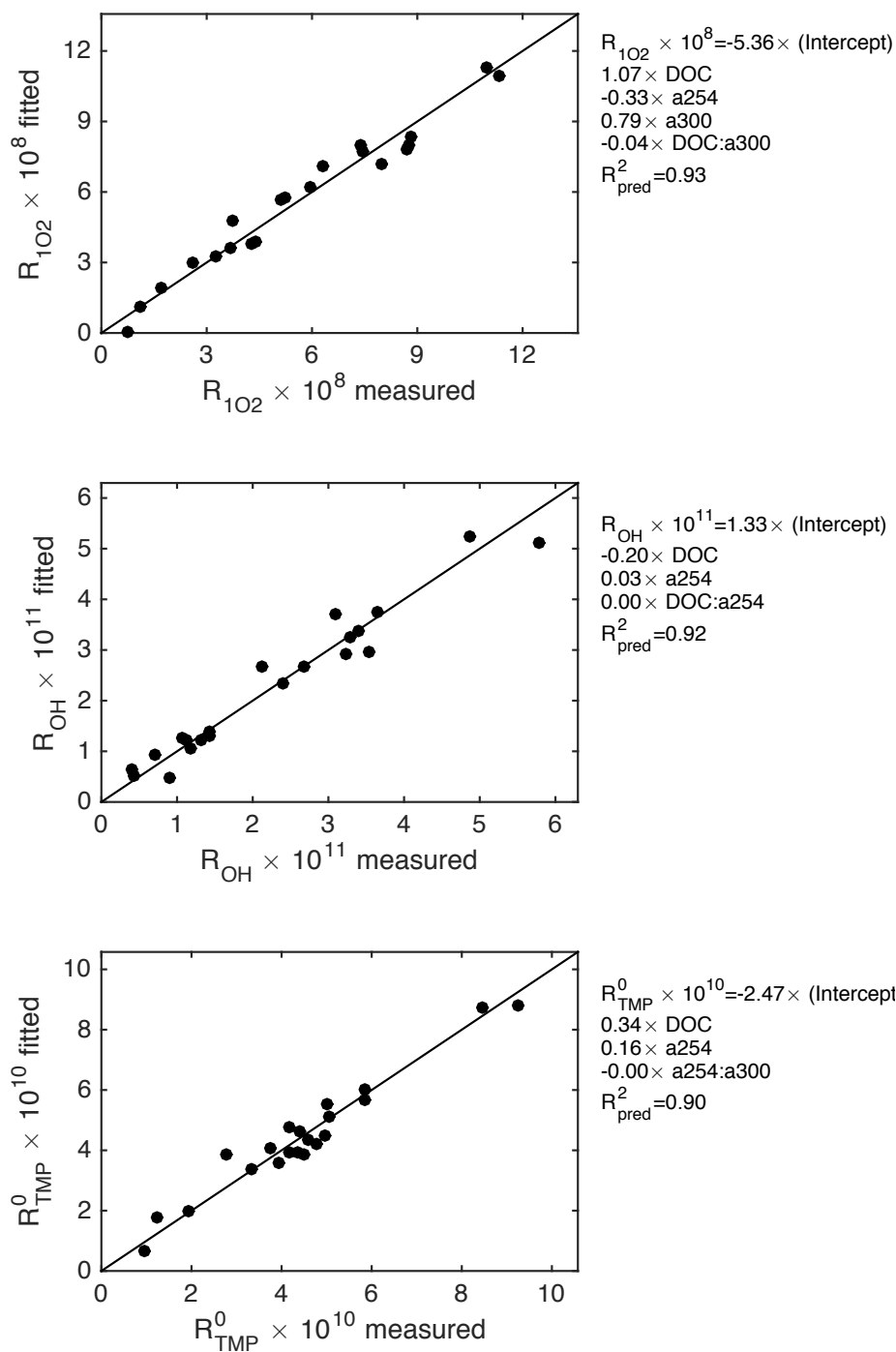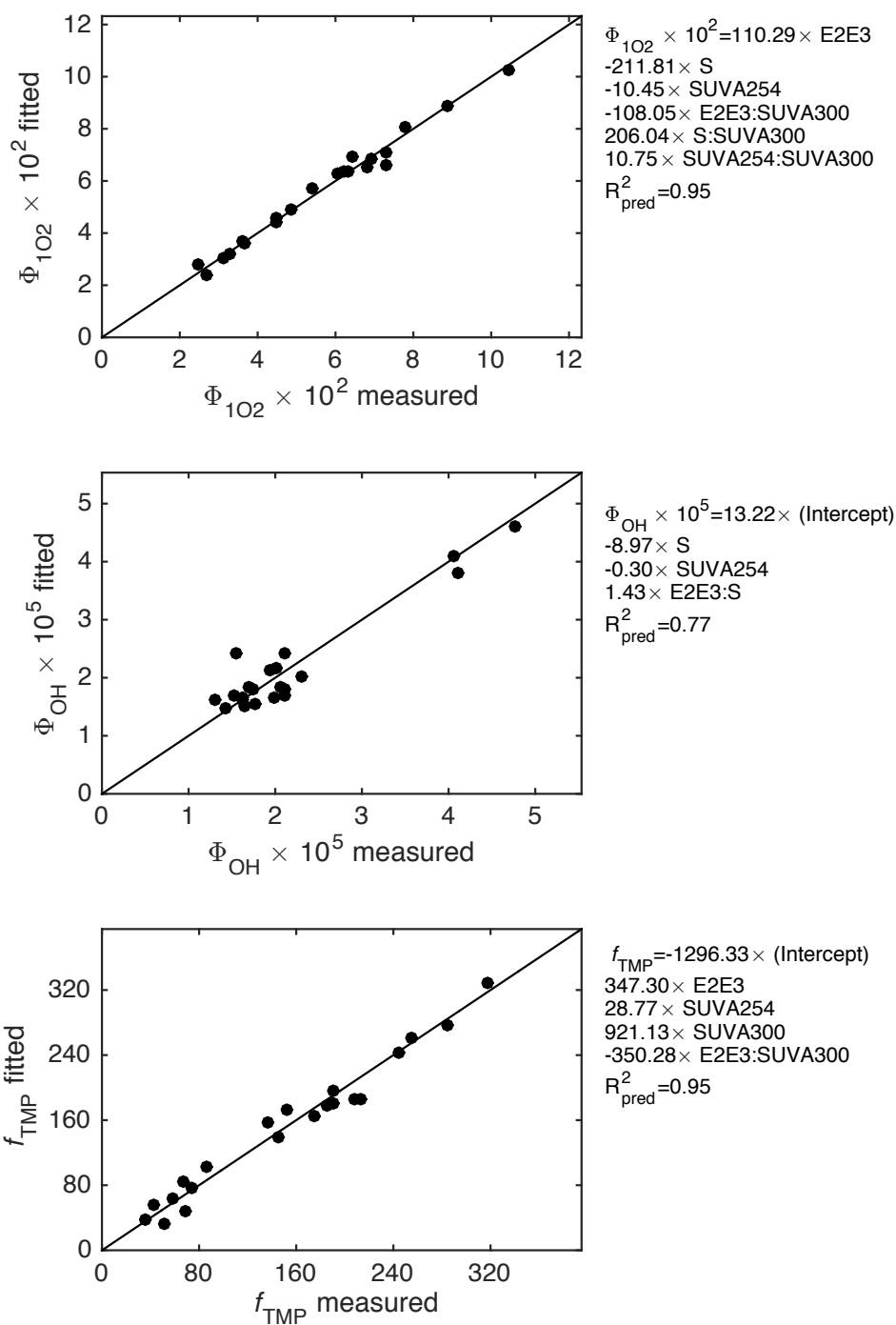$$7.23 \times \text{E2E3:IP100}$$
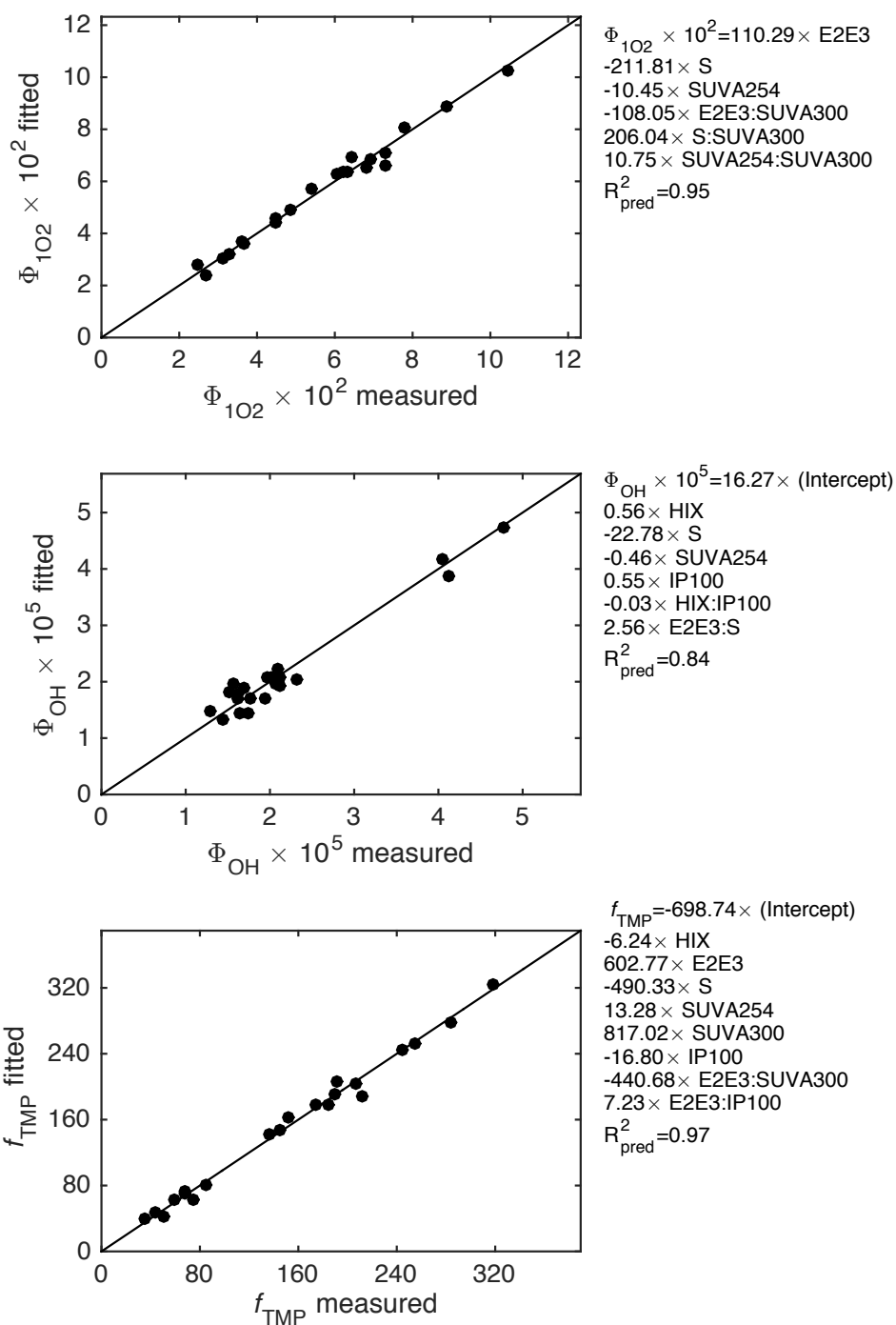$$R^2_{pred} = 0.97$$

Figure E.8. Multiple linear regression models for all intrinsic predictors used in estimating RI quantum yields. The one to one line is shown for comparison. The fitted model equation and R^2_{pred} are shown for each Φ_{RI}. Stepwise elimination was used to obtain only significant ($\alpha = 5\%$) model terms.

Figure E.9. Multiple linear regression models with non-standardized regressors used in modeling the dataset of McCabe and Arnold. The one to one line is shown for comparison. The fitted model equation and R^2_{pred} are shown for each R_{RI}. Stepwise elimination was used to obtain only significant (α=5%) model terms.
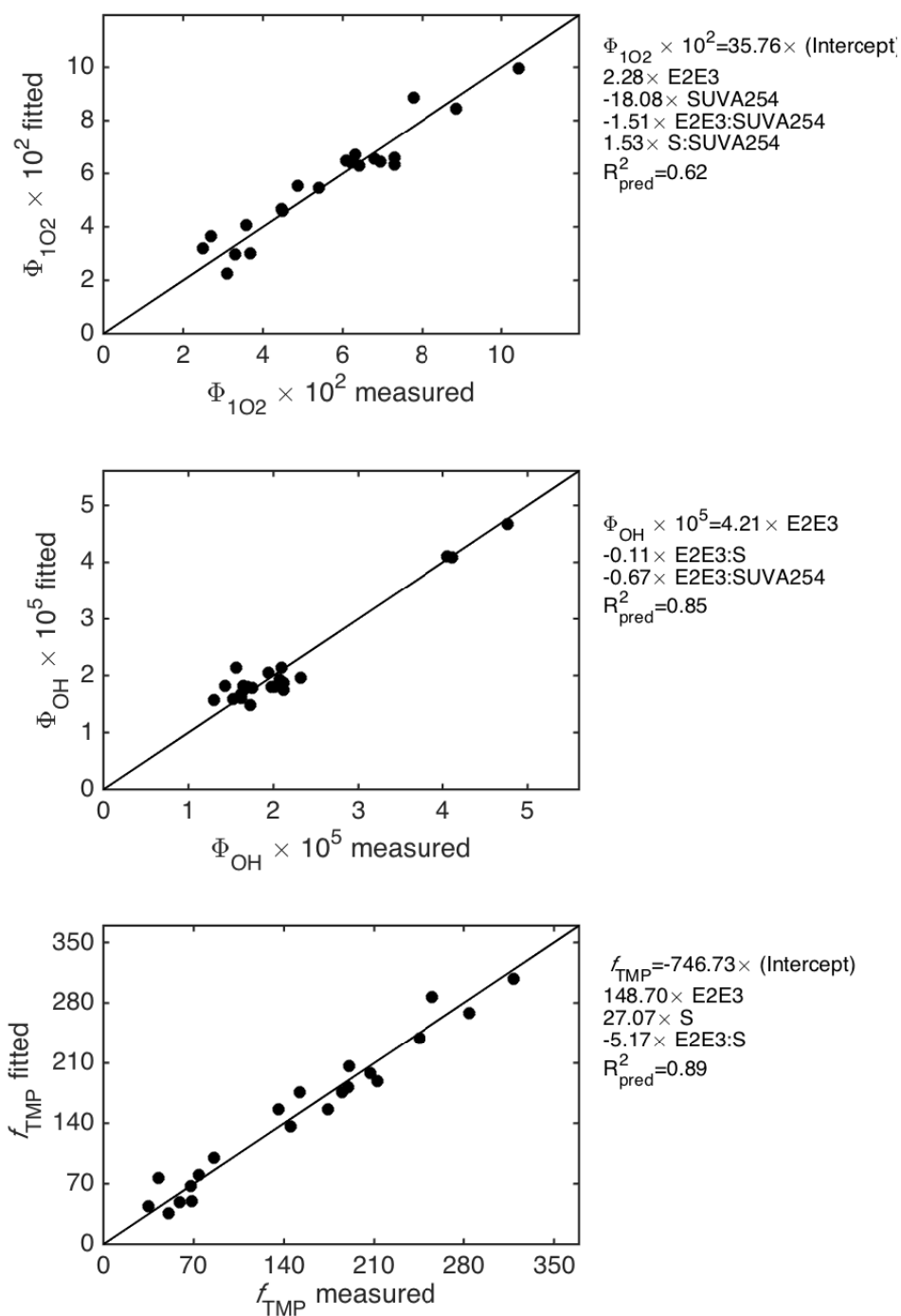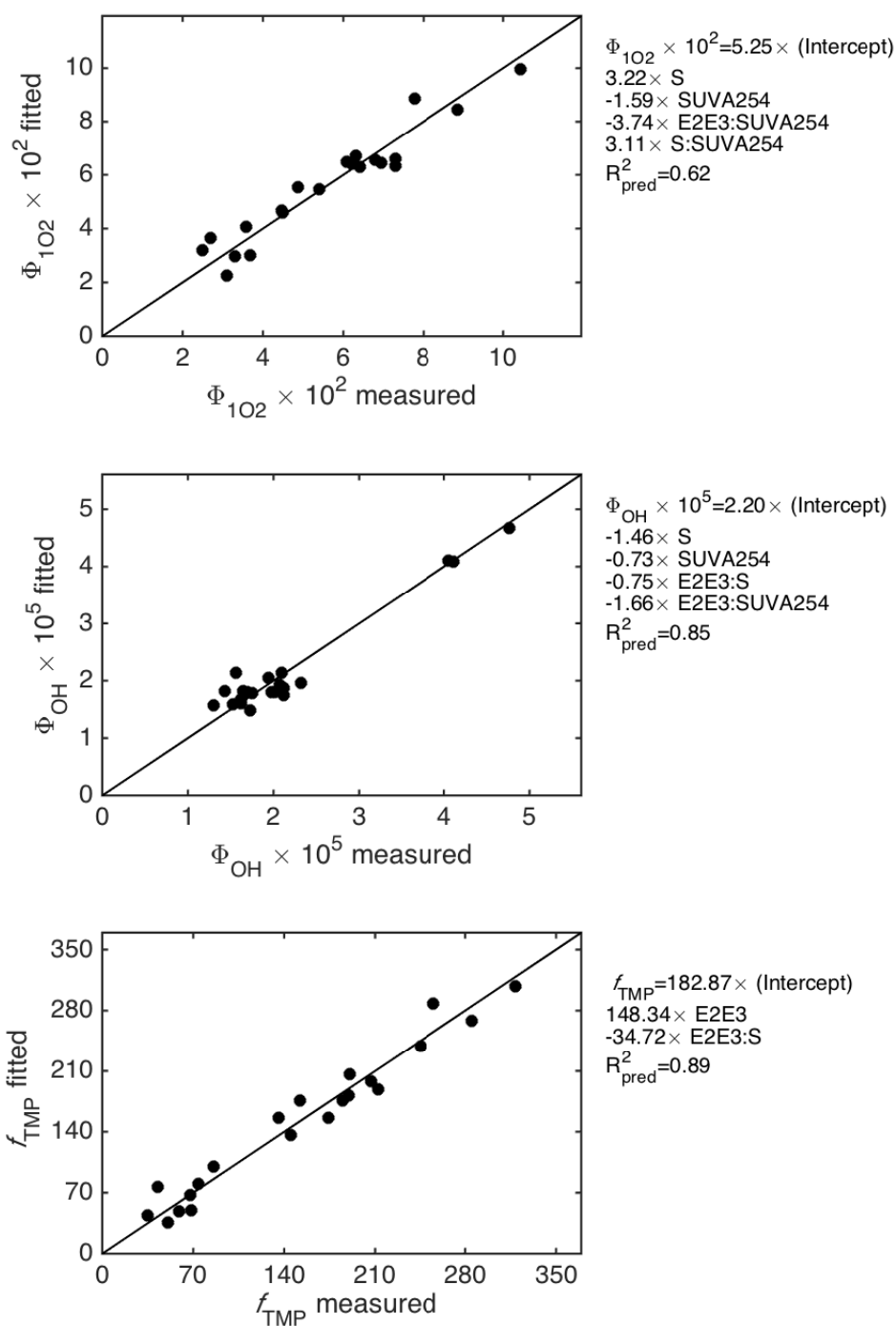
Figure E.10. Multiple linear regression models with standardized regressors used in modeling the dataset of McCabe and Arnold. The one to one line is shown for comparison. The fitted model equation and R^2_{pred} are shown for each R_{RI}. Stepwise elimination was used to obtain only significant ($\alpha=5\%$) model terms. Note that the above regression coefficients are standardized.
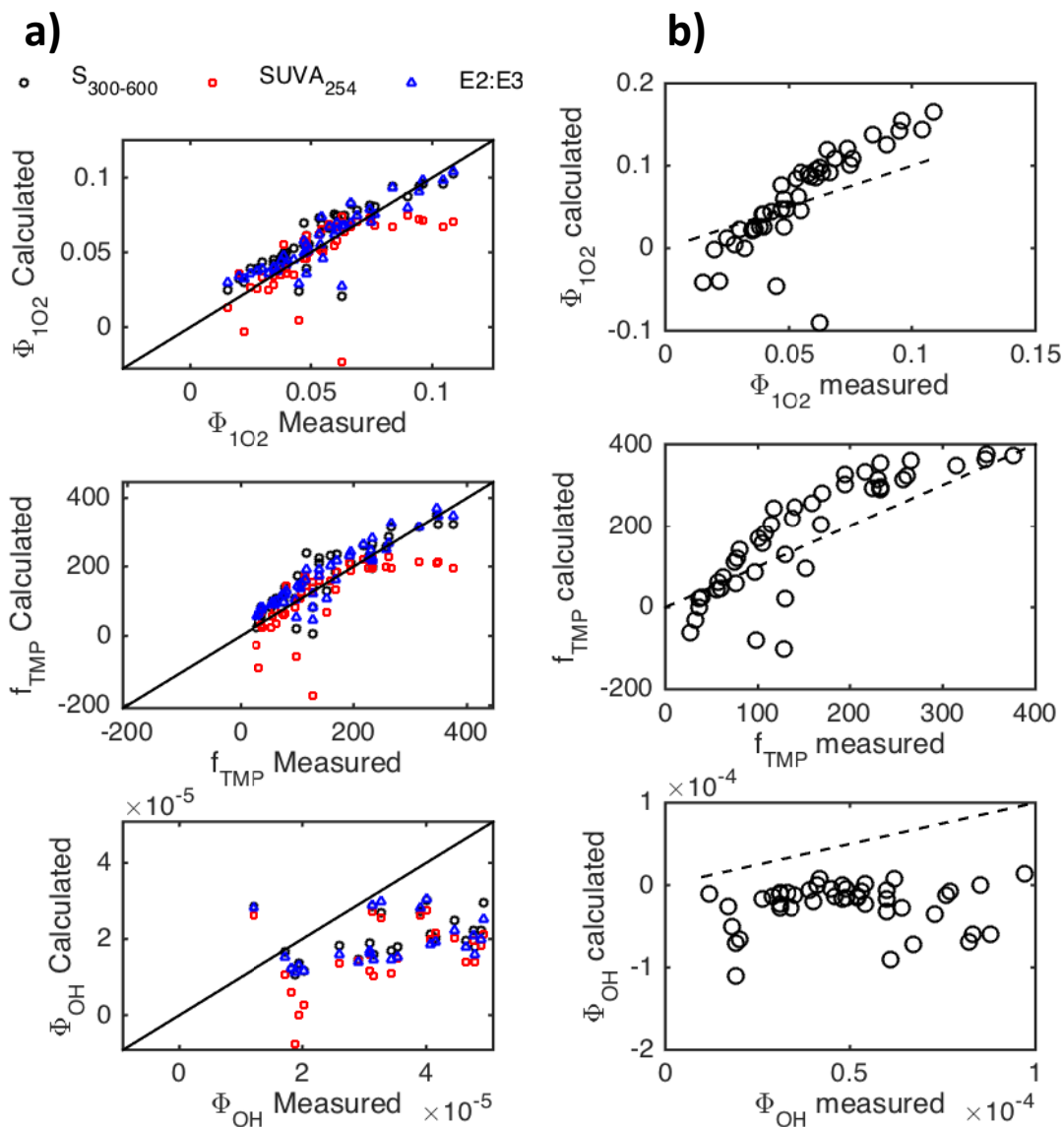
Figure E.11. Plots of calculated versus measured Φ_{RI} for data from McCabe and Arnold (2016) with a one to one line shown for comparison. a) Calculations based on single linear regressions (developed with the dataset from the Florida Everglades) presented in Figure E.4. Legend indicates the regressor that was used in the model. b) Calculations based on multiple linear regressions (developed with the dataset from the Florida Everglades) presented in Figure E.10.

E.5. Comparison of whole water and PPL extract optical properties and ΦRI

It is well known that isolation using solid phase extraction (SPE) does not capture 100% of the DOC (Bodhipaksha et al., 2015), and so we performed a control experiment in which E2:E3 and Φ_{RI} values were measured for a subset of our samples (*n*=8). These results are shown in Figure E.12 along with a one to one line for comparison. The general agreement between whole water and PPL extract's E2:E3 and Φ_{RI} values supports comparison of Φ_{RI} measured on whole water samples to $A_{\times}A_{50}$ values measured on extracts (Andrew et al., 2016; Bodhipaksha et al., 2015; Green and Blough, 2003). As noted above, TMP oxidation by ^{3}DOM* can be influenced by ionic strength. The general one to one agreement between whole water and PPL extract f_{TMP} values suggests that differing ionic strength is not the source of the observed variability. This conclusion is further supported by the fact that two of the points (TS2 and TS3 collected in October) above the one to one line (f_{TMP}, whole water ~ 225 and 250 M^{-1}) had zero salinity. We note, however, that the sample exhibiting the greatest deviation is FB21 collected in October, which is estuarine and thus has a very high salinity (38.4 practical salinity units) relative to other samples.

To further verify this finding, we plotted R_{RI} and Φ_{RI} versus total salinity (in practical salinity units) and concentrations of Cl- and Br- measured by ion chromatography (Figure E.14 and Figure E.15). There were significant negative correlations between R_{RI} and salinity, which likely reflects the decreasing [DOC] from freshwater to estuarine sites (i.e. north to south; Figure 7.1). Importantly, correlations between Φ_{RI} and salinity, [Cl-], and [Br-] were weak, and a number of the relationships were not significant. This provides good evidence that general and specific ion effects are not influencing measured Φ_{RI}.
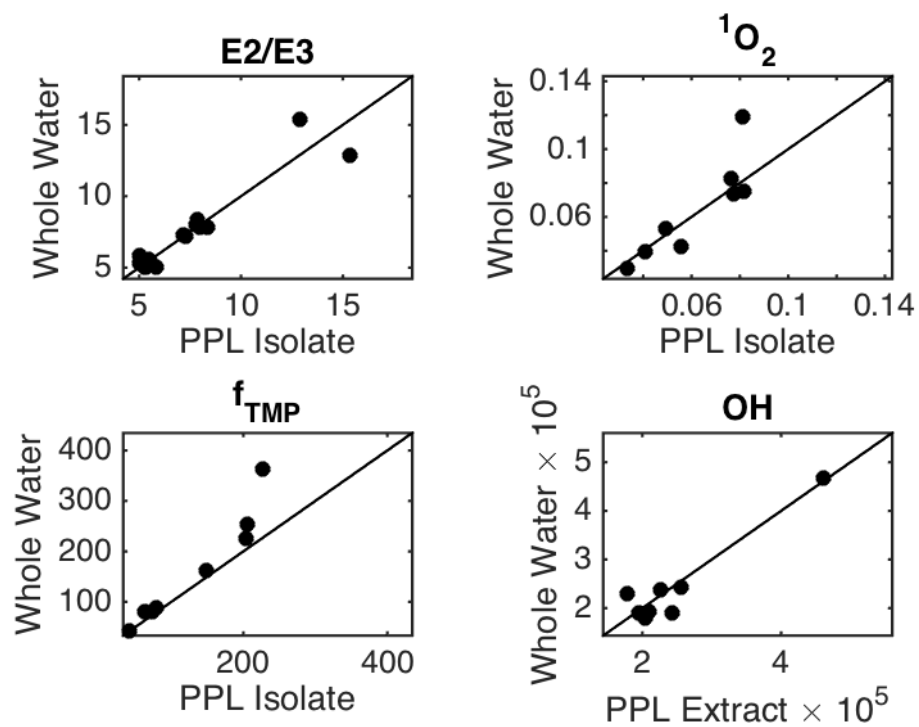
Figure E.12. Whole water versus PPL extract Φ_{RI} values for select (n=8) number of samples from this study. One to one line is shown for comparison.

Figure E.13. Relationship between R_{RI} and salinity for whole water samples. Solid line indicates the model prediction and dashed lines indicate the 95% prediction interval. The fitted model equation and R^2_{pred} are shown for each prediction-regressor pair. Note that R_{RI} values for samples with zero salinity (and thus a zero concentration of Cl^- and Br^-) were averaged in the above plot and analyses.
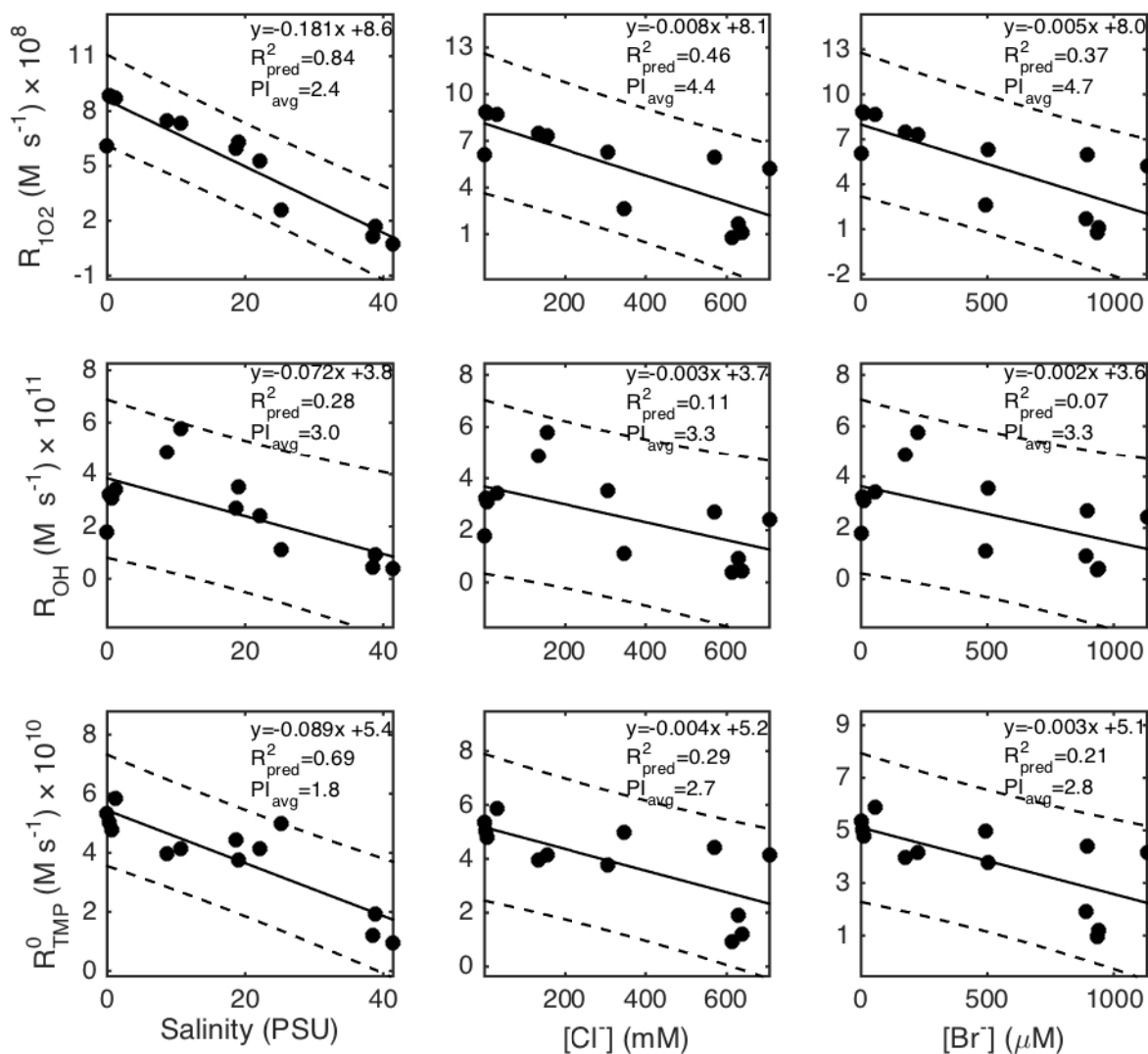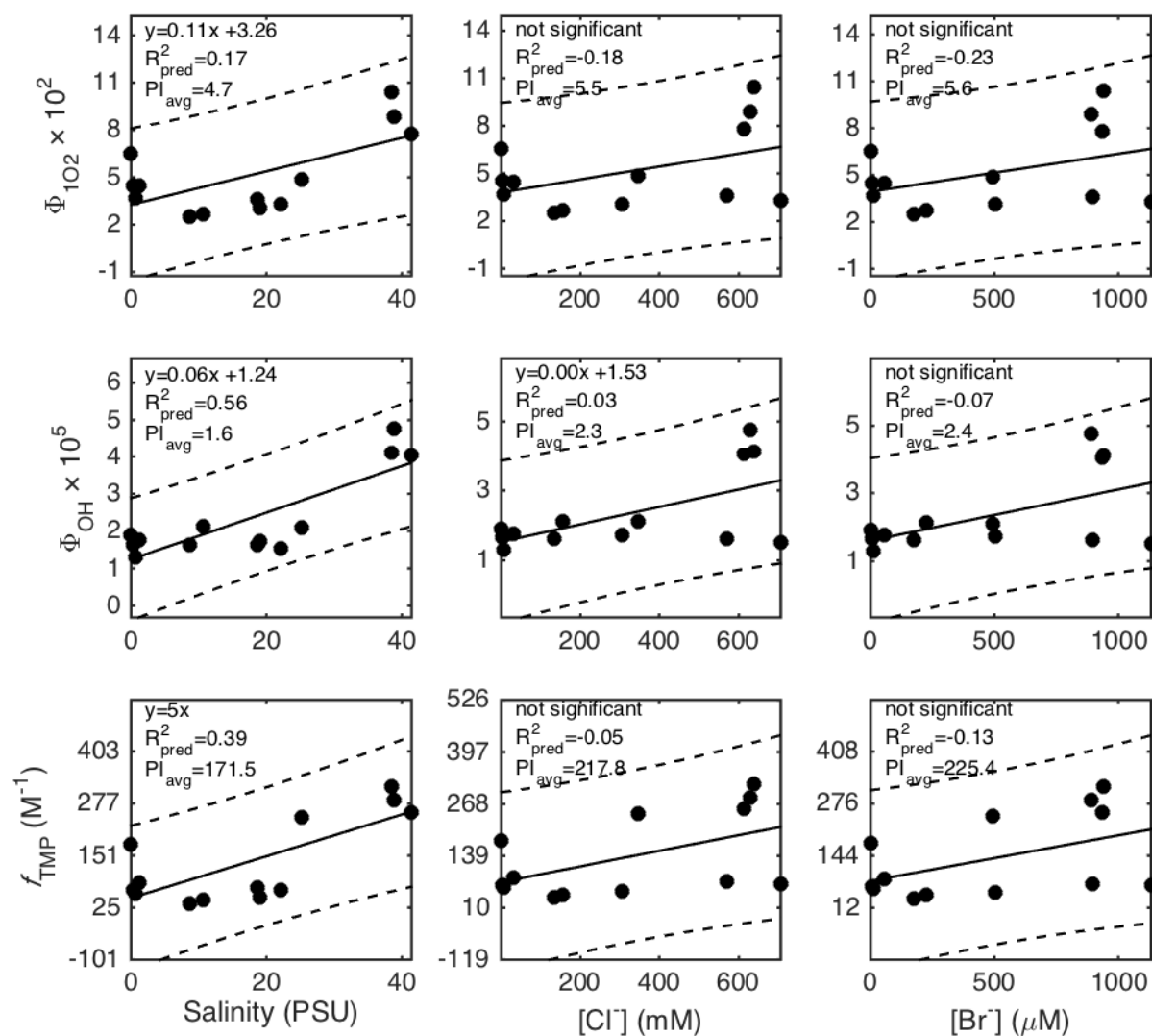
Figure E.14. Relationship between Φ_{RI} and salinity for whole water samples. Solid line indicates the model prediction and dashed lines indicate the 95% prediction interval. The fitted model equation and R^2_{pred} are shown for each prediction-regressor pair. Note that Φ_{RI} values for samples with zero salinity (and thus a zero concentration of Cl^- and Br^-) were averaged in the above plot and analyses.

E.6. Analysis of single linear regression for combined dataset

As discussed in the main text, the slope of the linear relationship between Φ_{1O2} and E2:E3 for the pooled dataset seemed to have a dependence on the range of E2:E3 values used in the regression. This was verified by repeating the regression analysis for this dataset with a

decreasingly narrower range of E2:E3 values. Although the intercepts from the regression analyses are shown in Table E.7, they are not statistically different from zero. Thus, the maximum error associated with use of different regression parameters is about a factor of ~2. Although this value is fairly good, it is greater than the prediction interval error for this model (factor of ~0.5 for a $\Phi_{1O2} \approx 4\%$).

We next discuss the use of different irradiance bases for determining Φ_{RI}. We are specifically interested in dealing with data from McCabe and Arnold (McCabe and Arnold, 2016) because the rate of light absorption was calculated by summing all the way out to 800 nm. Many of these wavelengths do not correspond to photochemically productive excitations (i.e. $\Phi_{RI} \rightarrow 0$ as $\lambda_{ex} \rightarrow \approx 400$ nm) (Sharpless and Blough, 2014), which ultimately results in a lower Φ_{RI} than if the sum were cut off at shorter wavelengths. To examine the effect of varying methods in calculating the rate of light absorption on the regressions shown in Figure 7.2, we sought to convert the Φ_{RI} measured by McCabe and Arnold into the 290-400 nm irradiance basis. To do this, we calculated absorbance spectra for each of the samples generated by McCabe and Arnold by using the spectral slope ($S_{300-500}$) for each sample location/date in their study and the average absorption coefficients at 350 nm for each of their sampling sites:

$$a(\lambda) = a(\lambda_{350})e^{-(\lambda - \lambda_{350})S}$$
$$Abs(\lambda) = \frac{a(\lambda)}{2.303}$$

Equation E.6

An important point to mention here is that absorbance values < 0.005 (an estimate for the detection limit of the spectrophotometer) were made equal to zero. This is important because small, non-zero absorbance will still contribute to the rate of light absorption in a significant way as the irradiance is more intense at longer wavelengths. Specific rates of light absorption were calculated with a short (290-400 nm) and long (290-800 nm) irradiance basis

$$k_{a,long} \propto \sum_{\lambda=290}^{800} E_{p,\lambda}^{0}(1-10^{-Abs_{\lambda}})$$

$$k_{a,short} \propto \sum_{\lambda=290}^{400} E_{p,\lambda}^{0}(1-10^{-Abs_{\lambda}})$$

Equation E.7

and used to derive apparent quantum yields for the 290-400 nm basis

$$\Phi_{RI,short} = \Phi_{RI,long} \times \frac{k_{a,long}}{k_{a,short}}$$

Equation E.8

Note that $E_{p,\lambda}^{0}$ above was derived from an Oriel 94041 A Class ABB solar simulator. The relationship between the quantum yield calculated over the long and short irradiation bases, Φ (290-800) and Φ (290-600), respectively, is shown in Figure E.15.

We have applied the corrections in Figure E.15 to the data used to generate Figure 7.2. These results are shown in Figure E.16 and indicate little change in the slopes of the linear regressions, but in some cases substantial changes in the intercepts. Table E.7 presents calculations using the regressions from different and same irradiance basis and shows modestly similar quantitative results, although this depends on the E2:E3 and S test values.
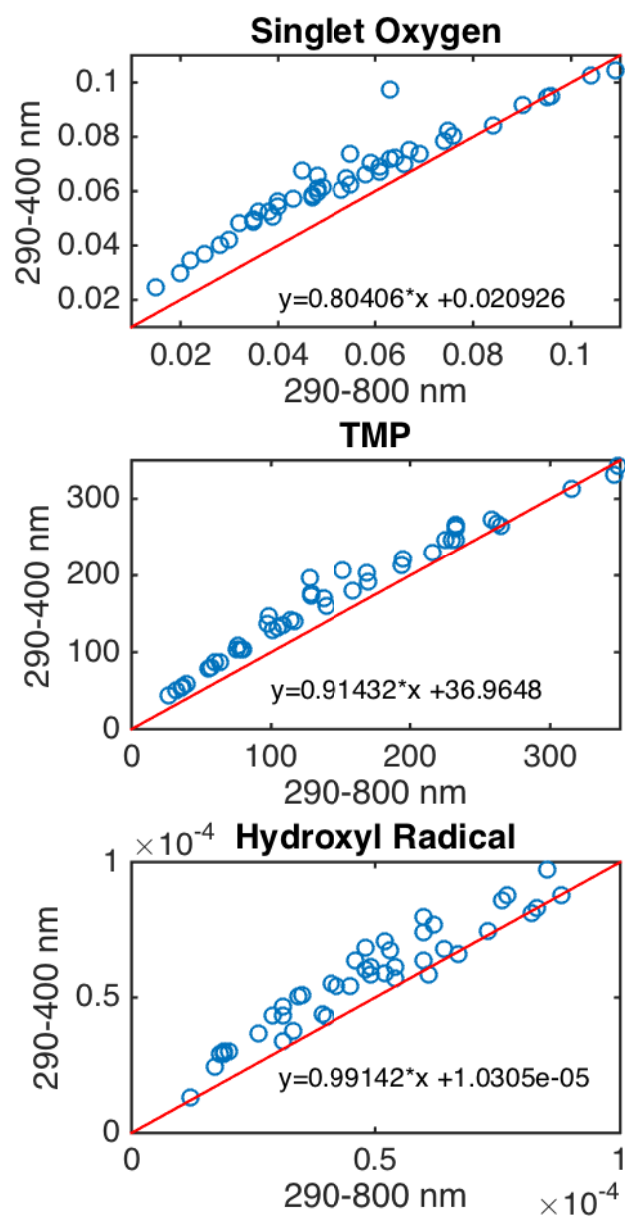
Figure E.15. Correlation between Φ_{RI} calculated using a rate of light absorption derived by summing over 290-800 nm and 290-400 nm for the data of McCabe and Arnold (McCabe and Arnold, 2016).
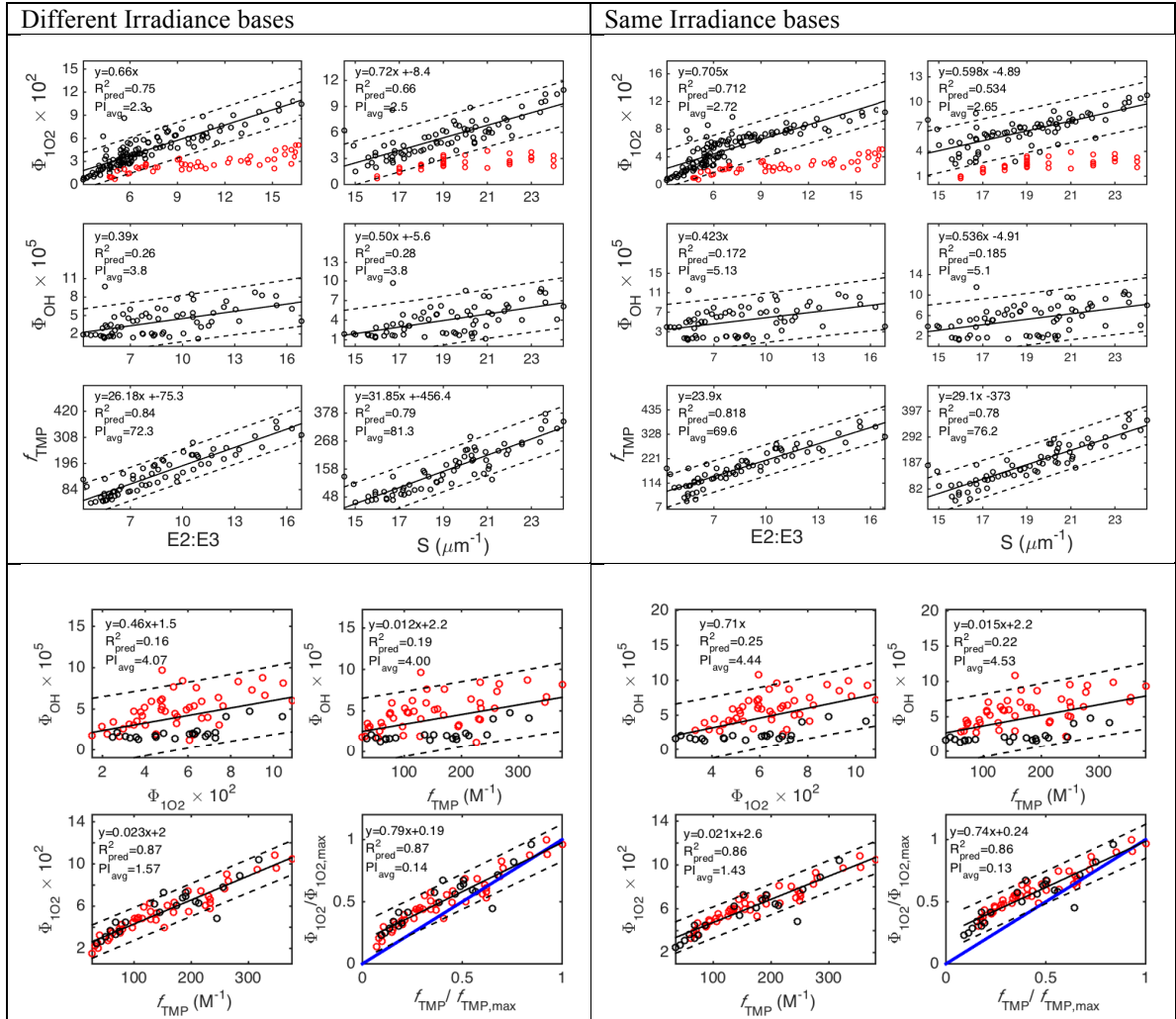
Figure E.16. (First row) Comparison of linear regressions for compiled dataset with different (left) and same (right) wavelength range used to calculate the rate of light absorption. (Second row) Comparison of linear regressions for Φ_{RI} intercorrelations with different (left) and same (right) wavelength range used to calculate the rate of light absorption.

Table E.7. Sensitivity analysis of predicted Φ_{RI} to regression parameters using the same (new) and different (old) wavelength ranges to compute the rate of light absorption.

					E2:E3 test value =		9
	Old		*New*		*Analysis*		
Species	**Slope**	**Intercept**	**Slope**	**Intercept**	**Calc Old**	**Calc New**	**% difference**
Singlet Oxygen	0.66	0	0.7	0	5.94	6.3	6.1%
Hydroxyl Radical	0.39	0	0.423	0	3.51	3.807	8.5%
Trimethyl phenol	26.18	-73	23.9	0	162.62	215.1	32.3%

					S test value =		21
	Old		*New*		*Analysis*		
Species	**Slope**	**Intercept**	**Slope**	**Intercept**	**Calc Old**	**Calc New**	**% difference**
Singlet Oxygen	0.72	-8.4	0.598	-4.89	6.7	7.7	14.1%
Hydroxyl Radical	0.5	-5.6	0.536	-4.91	4.9	6.3	29.5%
Trimethyl phenol	31.85	-456	29.1	-373	212.9	238.1	11.9%

Table E.8. Parameters for Φ_{1O2}-E2:E3 regression as a function of E2:E3 range grouped by percent of data included or by study.

Data Included	Range of E2:E3 values	Range of SO values	Slope	Intercept	R^2
100%	3.06-16.9	0.59-10.87	0.661	-0.211	0.755
83%	3.06-10.04	0.59-9.8	0.813	-1.055	0.574
68%	3.06-7.65	0.59-9.8	1.005	-2.054	0.472
49%	3.06-6	0.59-8.59	1.160	-2.724	0.424
All - Peterson	3.06-16.9	0.59-10.87	0.661	-0.211	0.755
Bodhipaksha, Mostafa, McCabe, ENP	3.07-117	0.83-66	0.565	0.570	0.964
Mostafa, McCabe, ENP	4.3-117	1.52-66	0.560	0.689	0.975
McCabe, ENP	4.3-117	1.52-66	0.561	0.618	0.982
ENP	5.3-117	2.49-66	0.556	1.107	0.993
Dalyrmple, Bodhipaksha, Mostafa	3.06-7.85	0.59-9.8	1.279	-3.297	0.635
Peterson(Buxton et al., 1988; Peterson et al., 2012)	4.7-21.4	0.7-5.5	0.198	0.580	0.592
Dalyrmple(Dalrymple et al., 2010; Haag and Höigne, 1986)	3.06-7	0.59-4.5	0.871	-1.534	0.654
Bodhipaksha(Bodhipaksha et al., 2015; Dong and Rosario-Ortiz, 2012; Vione et al., 2010)	3.1-7.2	0.83-9.8	1.640	-4.922	0.817
Mostafa(McKay and Rosario-Ortiz, 2015; Mostafa and Rosario-Ortiz, 2013)	5.3-7.9	2.77-8.59	0.581	0.990	0.056
McCabe(McCabe and Arnold, 2016; Vione et al., 2006)	4.3-16.3	1.52-10.87	0.619	-0.105	0.825
ENP	5.3-16.9	2.49-10.43	0.644	0.392	0.755

E.7. Correlation of Φ_{RI} with antioxidant capacity

Figure E.17 shows linear regression analysis for Φ_{RI} with antioxidant capacity ($A_{\times}A_{50}$) as the predictor. Note that the relationship between $A_{\times}A_{50}$ and Φ_{OH} is not significant. $A_{\times}A_{50}$ has been correlated to the (electrochemically measured) electron donating capacity (DOC) for a select number of DOM isolates (Romera-Castillo and Jaffé, 2015).
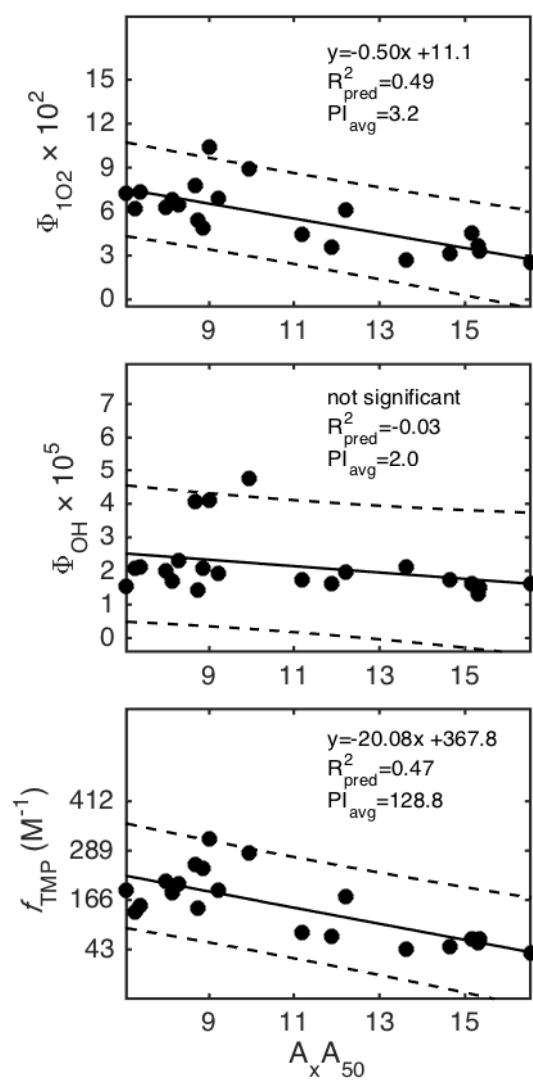
Figure E.17. Regression models for Φ_{RI} with A_xA_{50} as a predictor. Solid line indicates the model prediction and dashed lines indicate the 95% prediction interval. The fitted model equation and R^2_{pred} are shown for each prediction-regressor pair.